ISSN: 0120-1425 • Junio de 2020

SERVICIO GEOLÓGICO COLOMBIANO

46

Boletín Geológico

revistas.sgc.gov.co

Boletín Geológico
Núm. 46, 2020
Periodicidad anual
ISSN impreso: 0120-1425
ISSN digital: 2711-1318

SERVICIO GEOLÓGICO COLOMBIANO
Diagonal 53 N.º 34-53
Bogotá D. C., Colombia
Teléfono: 220 0200, ext.: 3048
boletingeologico@sgc.gov.co

CORRECCIÓN DE ESTILO
Édgar Ordóñez

DISEÑO Y DIAGRAMACIÓN
Leonardo Cuéllar V.

EDITORA GENERAL
Carolina Hernández O.

FOTO DE CARÁTULA
Afloramiento de granito
Estación de reconocimiento geológico, comunidad indígena Bogotá Cachivera, sector caño Abiyú, departamento del Vaupés.
Tomada por el geólogo y geofísico Ernesto Gómez

FOTO DE CONTRACARÁTULA
Río Caquetá, La Pedrera, departamento de Amazonas
Tomada por el geólogo y geofísico Ernesto Gómez

INCLUIDA EN LOS SIGUIENTES ÍNDICES Y BASES DE DATOS:
Ulrich

PÁGINA WEB:
https://revistas.sgc.gov.co/index.php/boletingeo

IMPRESIÓN
Imprenta Nacional de Colombia
Carrera 66 N.º 24-09
PBX: 457 8000
www.imprenta.gov.co
Bogotá, D. C., Colombia

Junio, 2020

CONTENTS

Boletín Geológico

SERVICIO GEOLÓGICO COLOMBIANO

EDITORIAL

Boletín Geológico number 46 (2020) has published three articles in the disciplines of economic geology, hydrocarbon genesis, and basin evolution in several zones of Colombia. The following passages have been taken from these articles and introduce their contents.

The Servicio Geológico Colombiano (SGC) has carried out a large geophysical exploration campaign to acquire data and make it available to the academic community and mining industry. The SGC overflew the Andean and eastern parts of Colombia and obtained more than 700,000 km of high resolution airborne geophysical data (magnetometry and gamma spectrometry). Moyano et al. present an interpretation of isolated magnetic anomalies located in three different geologic environments in Colombia: the San Lucas range, the Andes Cordillera, and the Amazonian craton (Figure 1).

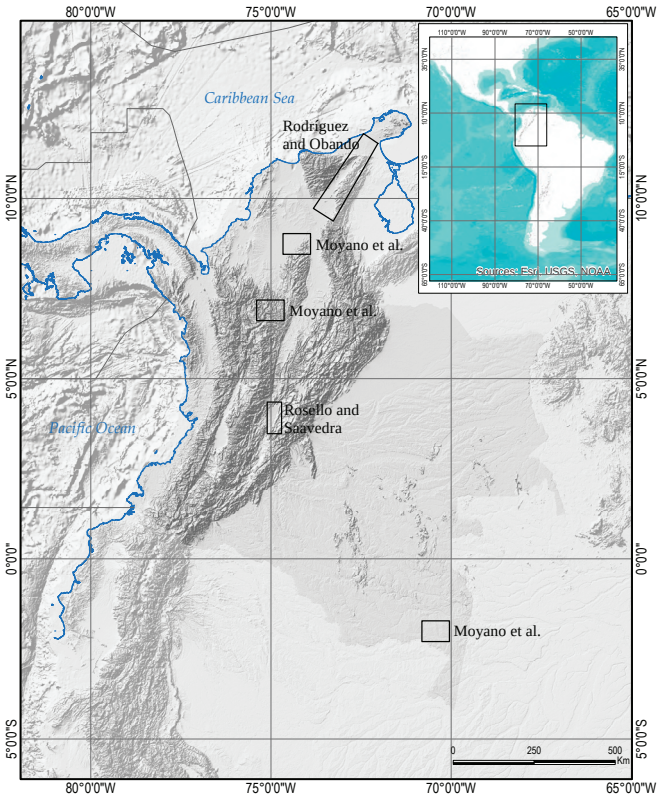

Figure 1. Location of the areas with geological contributions presented in this issue

Rossello and Saavedra present a discussion about the structural aspects that contribute to the creation of the genetic and morphological characteristics of the bedding surfaces underlying the petrophysical potential of the Matachines field located in the Girardot subbasin, within the Upper Magdalena Valley basin (VSM, *Valle Superior del Magdalena*), Colombia (Figure 1). The authors focus on sectors where the primary permeability and porosity values are usually too low to meet economic expectations for hydrocarbon exploration or production activities.

Rodríguez and Obando report new petrography, total rock chemistry and U-Pb zircon geochronology data for the La Quinta Formation, Serranía de Perijá, in the northern Andes of Colombia (Figure 1). This new information is correlated with other volcano-sedimentary sequences, specifies the distribution of arc volcanism and the analysis of inherited zircons in the volcanic rocks to improve the understanding of the basement distribution on which the arc is founded.

The editor acknowledges the efforts of the following reviewers whose comments and recommendations, on the eleven manuscripts submitted contributed to the improvement of the three articles that were ultimately approved: Ana Ibis Despaigne, Andrés Cárdenas, Ariel Cadena, Barbara Martiny, Camilo Bustamante, César Mora, Germán Bayona, Gustavo Córdoba, Hermann Bermúdez, Hugo Murcia, Jhon Jairo Sánchez, José Luis Arce, Juan Carlos Molano, Juan Diego Colegial, Luis Castillo, Luis Enrique Cruz, Mario Moreno, Mauricio Bermúdez, Umberto Cordani, Natalia Pardo, Oswaldo Ordóñez, Thomas Cramer, and Yamirka Rojas. We recognize that the final content of the articles does not necessarily reflect the thoughts of the reviewers and editors.

Mario Maya
Editor
Boletín Geológico
mmaya@sgc.gov.co
boletingeologico@sgc.gov.co

Boletín Geológico

SERVICIO GEOLÓGICO COLOMBIANO

Boletín Geológico, 46, 5–22, 2020
https://doi.org/10.32685/0120-1425/boletingeo.46.2020.514

Received: December 10, 2019
Accepted: March 6, 2020
Published online: June 30, 2020

Interpretation of geophysical anomalies for mineral resource potential evaluation in Colombia: Examples from the northern Andes and Amazonian regions

Interpretación de anomalías geofísicas para la evaluación del potencial de recursos minerales en Colombia: ejemplos del norte de los Andes y Amazonía

Ismael Enrique **Moyano Nieto**[1], Renato **Cordani**[2], Lorena Paola **Cárdenas Espinosa**[1], Norma Marcela **Lara Martínez**[1], Oscar Eduardo **Rojas Sarmiento**[1], Manuel Fernando **Puentes Torres**[1], Diana Lorena **Ospina Montes**[1], Andrés Felipe **Salamanca Saavedra**[1], Gloria **Prieto Rincón**[1]

1 Servicio Geológico Colombiano, Mineral Resources Direction.

2 Reconsult Geofisica, São Paulo – Brazil.

Email: imoyano@sgc.gov.co

Abstract

This paper focuses on presentation of the methodology used by geophysicists at the Servicio Geológico Colombiano (SGC) for the processing, anomaly selection and interpretation of airborne magnetometry and gamma spectrometry data. Three (3) selected magnetic anomalies from different geological settings (Andes Cordillera, San Lucas Range and Amazon region) are presented as examples. 3D magnetic vector inversion (MVI) modeling of each of the selected magnetic anomalies shows magnetic sources less than 100 m deep or exposed with sizes from 2.5 to 6 km. The magnetic data interpretation also allows the identification of linear features that could represent structural control for fluid migration and/or ore emplacement. Additionally, the integration of the geophysical data with other geoscientific information (geologic, metallogenic and geochemical data) leads to the proposition of an exploration model for each anomaly: intrusion-related/VMS deposits for the Andes, porphyry/intrusion-related/epithermal deposits for San Lucas and carbonatite/kimberlite for Amazonas. The methodology used and examples presented illustrate the potential of SGC airborne geophysical data for mineral resource evaluation and as input for the design of fieldwork for geological, geophysical, geochemical and metallogenic characterization of an area of interest.

Key words: Geophysical data processing, 3D modeling, magnetic anomalies, mineral resources.

Resumen

Este documento se centra en la presentación de la metodología usada por los geofísicos del Servicio Geológico Colombiano (SGC) para el procesamiento, selección de anomalías e interpretación de datos de aeromagnetometría y gamma-espectrometría. Se presentan como ejemplo tres anomalías localizadas en diferentes ambientes geológicos (cordillera de los Andes, serranía de San Lucas y Amazonia). La modelación 3D a partir de la inversión del vector magnético (MVI) de cada una de las anomalías seleccionadas muestra fuentes magnéticas a menos de 100 m de profundidad, o aflorantes, y con tamaños de 2.5 a 6 km. La interpretación de los datos magnetométricos también permitió identificar rasgos lineales que pueden representar controles estructurales para el ascenso o emplazamiento de mineralizaciones. Adicionalmente, la integración de los datos geofísicos con otra información geocientífica (geología, metalogenia y datos geoquímicos) permitió proponer posibles modelos de exploración de cada anomalía: depósitos asociados a intrusivos/sulfuros masivos vulcanogénicos (VMS), en el caso de la anomalía de los Andes, pórfido/asociado a intrusivo/epitermal para la de San Lucas, y carbonatita/kimberlita para la del Amazonas. La metodología empleada y los ejemplos presentados ilustran el potencial de los datos geofísicos del SGC para evaluar el potencial de recursos minerales y como un insumo para la definición del trabajo de campo enfocado en la caracterización geológica, geofísica, geoquímica y metalogénica de un área de interés.

Palabras clave: Procesamiento de datos geofísicos, modelado 3D, anomalías magnéticas, recursos minerales.

1. Introduction

Airborne geophysics is the easiest and most economical way to improve geological knowledge of large areas and to detect direct anomalies for further interpretation and subsequent drilling. The presence of an isolated magnetic anomaly attracts the attention of a mineral explorer. Once found, the next step is to estimate the physical and geometric parameters of the magnetic rock that produces the anomaly. Magnetic interpretation techniques such as detailed processing, 2D filters and 3D modeling can be applied to better understand the anomaly and suggest new exploration methods or target drilling. Magnetic anomalies can be the expression of several types of mineral deposits, such as iron oxide-gold-copper (IOCG) deposits, porphyries (Au and Cu), kimberlites (diamonds), alkaline complexes (phosphate and niobium), nickel deposits (both sulfide and laterite), volcanogenic massive sulfide deposits (VMS), and banded iron formations (BIFs). In this context, the absence of a radiometric anomaly coincident with the magnetic anomaly is a strong clue that we will not find any evidence of the rock at the surface.

The geophysical data used for the present work correspond to surveys carried by the Servicio Geológico Colombiano (SGC), separated in blocks that cover broad areas of the Andean and eastern parts of Colombia, including more than 900,000 linear km of high-resolution airborne magnetometric and gamma spectrometric data (Moyano et al., 2018). Each block is surveyed with a line separation of 500 or 1,000 m and data sampling of 10 Hz (magnetometry) and 1 Hz (gamma spectrometry), which yield spatial resolutions of 7-9 m and 70-90 m, respectively. These sampling rates and flight line separations allow the interpolation of grids with spatial resolutions of 125 x 125 m and 250 x 250 m, providing details not previously available in Colombia, considering the broad coverage of the surveys.

This document presents the interpretation of three magnetic anomalies located in three different geologic environments in Colombia: one in the Andes Cordillera, with some surface expression and a gold geochemical anomaly; one in the San Lucas Range area without any surface expression; and one in the Amazonian craton without surface expression or rock outcrops. Each area has different levels of previous geologic and mineral potential knowledge, from a lack of data other than the magnetic anomaly in the Amazon region to good geological control, geochemistry and metallogenic characterization for the Andes anomaly. These three anomalies illustrate the

potential of the geophysical data acquired by the SGC for the assessment of mineral resource potential in Colombia.

2. Geological setting

Colombia is located northwestern South America, an area with specific tectonic features and a physiographic landscape modeled by the complex interactions among the Nazca, South American and Caribbean plates (Figure 1). The Colombian Andes are considered a mixture of many fragments of parautochthonous and allochthonous crustal fragments and tectonic wedges of continental, peri-cratonic and oceanic affinities. These fragments were accreted by strike-slip faults and subduction zones along the NW margin of the Guyana shield during many periods, with some of the major periods occurring in the Permo-Triassic, Jurassic and Late Cretaceous (Bustamante et al., 2017). This highly fertile metallotectonic environment is supported by the significant production of gold, silver, emeralds, platinum group elements (PGE), ferronickel and other commodities such as copper, lead and zinc as principal or secondary products at a modest scale. All of these elements are found in a wide variety of geological environments, combined with hundreds of manifestations, occurrences of active or abandoned mines and showings (Au, Ag, Pb, Zn, Cd, Cu, Mo, Sb, Hg, Cr, Ni, Pt, Pd, Ti, Mn and Fe); the majority of them have no historical exploration, and minimal academic studies are available (Shaw et al., 2019).

The convergent margin regime that was present throughout the Phanerozoic and the multiple occurrences of mineral deposits related to this tectonic regime led to the identification of at least three "copper belts" (Sillitoe et al., 1982), delimited in the metallogenic map of Colombia (López et al., 2018) as different "metallogenic belts" with Jurassic, Miocene and Eocene ages (Figure 1).

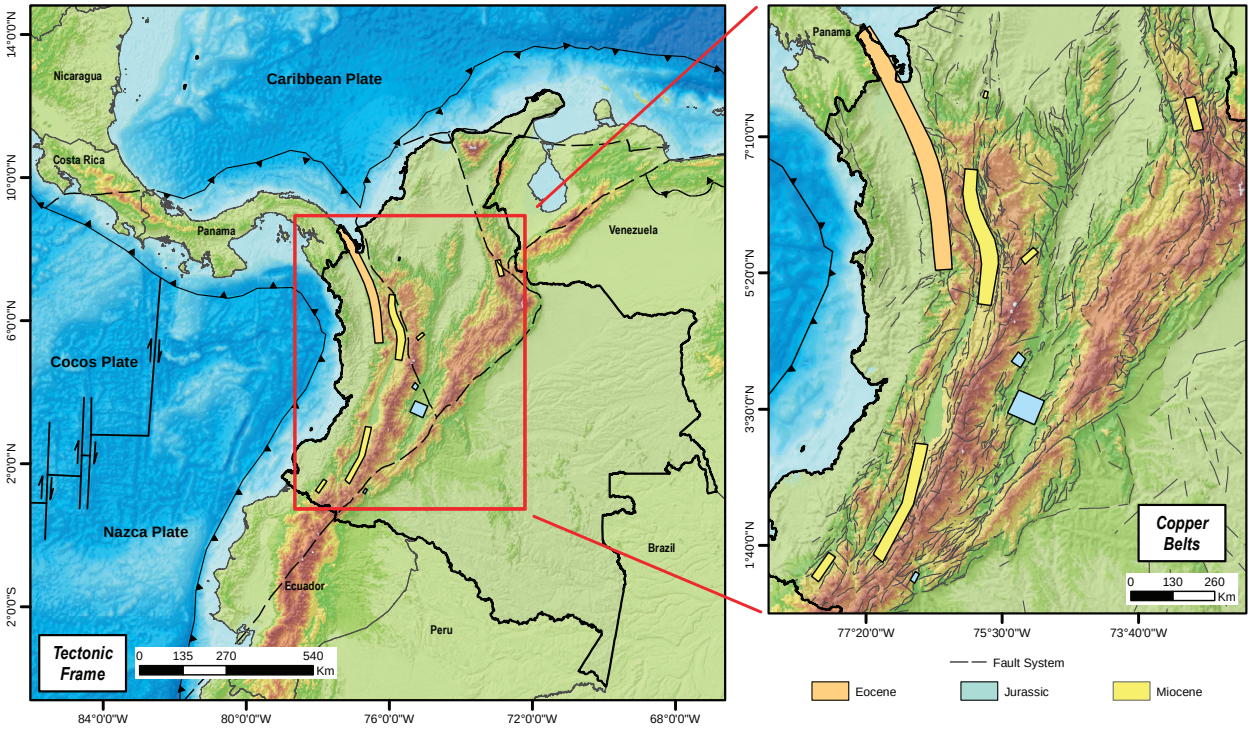

Figure 1. Tectonic setting of NW South America; the inset shows the copper belts and the main geological faults (dashed black lines) Modified from López et al. (2018)

Additionally, recent data have defined at least seven magmatic/mineralization events with a NNE trend and distributed all across the country (Leal, 2011), which occurred between the early Paleozoic and the Pleistocene and were related to magmatic belts, island arcs of variable composition and intracratonic environments.

3. Geophysical methods used

Airborne geophysics is a very useful method to increase geological knowledge of large and remote areas such as the Amazonian region of Colombia, not only for geological mapping but also for potential assessment of mineral resources. For this purpose, the SGC began an extensive airborne geophysical survey that, by the end of 2019, had accumulated a coverage of nearly 550,000 km^2 in the Andean, Caribbean and Amazonian regions, collecting more than one million linear kilometers of high-quality magnetometry and gamma spectrometry within specified polygons, herein referred to as blocks (Figure 2).

Data acquisition was performed with instruments mounted on "fixed wing" aircraft, with line spacings of 500 m (Andes and Bolivar regions) and 1,000 m (Amazon) and a flight height of 100 m above terrain over flat areas. In the mountainous areas, a "drape" survey design was used with heights between 100 and 300 m or more, securing aircraft safety and good data quality. The onboard geophysical equipment included high-sensitivity magnetometers that recorded the variations in the Earth´s magnetic field, 512- to 1,024-channel gamma spectrometers with 2,056 in^3 of downward-detection crystals and high-definition GPS and radar altimeters to ensure the quality of the raw data. The sampling rates were 10 Hz for magnetometry and 1 Hz for gamma spectrometry, measu-

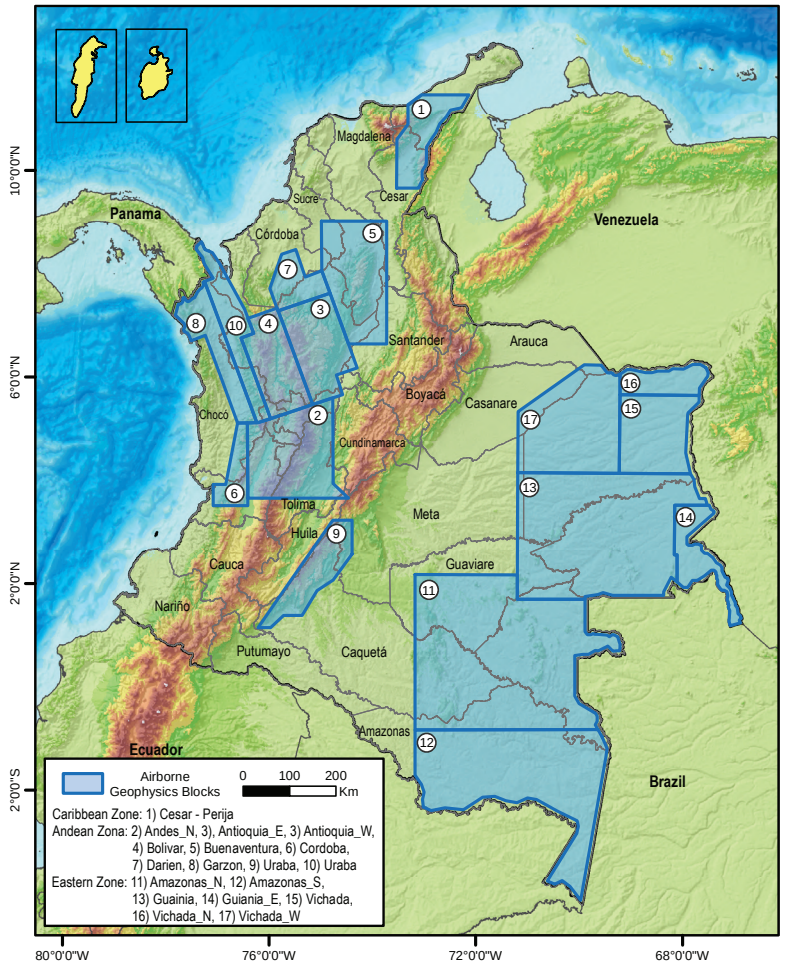

Figure 2. Blocks selected for airborne geophysics surveys

ring geophysical data every 7 to 9 m and 70 to 90 m, respectively. The 500 m flight line blocks were processed into 125 x 125 m grids, and the 1,000 m blocks were processed into 250 x 250 m grids. The processed grids included total magnetic field anomaly (TFA) and concentrations of potassium (K, %), uranium (U, ppm) and thorium (Th, ppm). All postprocessing and interpretation were performed by geophysicists and external advisors of the SGC.

The magnetometry method, used as an exploration tool, evaluates the lateral variations in the Earth's magnetic field that are assumed to be a response to the variations in the amounts of magnetic minerals contained in the rocks. These changes in magnetic mineral content could mark variations in the rock type or internal changes due to other geological processes, such as hydrothermal alteration or metamorphism. Therefore, magnetometry data are useful to identify magnetic bodies covered by nonmagnetic lithologies, to delineate geological structures and to target exploration on the increase/decrease in magnetic mineral content related to the most common geological mechanisms for ore formation: magma intrusion, faulting and hydrothermal alteration processes.

Gamma spectrometry data reflect the relative concentrations of the common radioactive elements uranium (U), thorium (Th) and potassium (K) that are naturally concentrated through magmatic differentiation. This process generates the highest concentrations of these elements in acidic rocks as well as in its metamorphic and sedimentary-related lithologies. Because of the relation between natural radioactivity and the mineralogy of lithological units, gamma spectrometry helps in the "lithogeophysical" characterization of surface materials and allows the determination of secondary alteration processes; such processes change the geochemical composition of the rocks because of the emplacement of magma bodies, which triggers processes that result in ore deposits.

4. Data processing and anomaly selection methodology

The analysis of the magnetometry information aims to detect and describe data attributes such as geometry, intensity and orientation that may represent anomalies reasonably related to geological features. For this purpose, it is useful to reduce the natural complexity of the magnetic anomalies by reduction to pole transformation (RTP; Baranov 1957) or by computation of the analytical signal (AS, Nabighian 1972). Additionally, other transformations, such as the tilt derivative (Miller and Singh, 1994) and composite ternary images of different order vertical derivatives (1, 1.25, and 1.5 order), are used to locate anomalies and magnetic domains from a consistent interpretation of the data and to relate these anomalies to a geological framework, such as intrusions, dikes, shear zones, kimberlites, carbonatites, etc., that may host mineral resources.

Gamma spectrometry data are useful to identify and correlate outcropping lithologies and anomalies in radioactive element distributions that may be related to secondary geological processes of mineral enrichment or depletion, such as hydrothermal alteration zones and weathering zones. The use of gamma spectrometry images (potassium, uranium or thorium) and ternary red, green, blue (RGB) images (red = K, green = Th, blue = U) with lithological information and magnetic anomalies enhances the geological interpretation and the possible types of related mineralization.

For the data processing, interpretation and target selection from geophysical airborne data, a procedure to generate standardized information for the entire area covered is established. The suggested steps are as follows:

- Calculate the RTP and/or the analytical signal of the TFA
- Calculate the tilt angle derivative.
- Calculate vertical derivatives of the RTP and display them on a ternary RGB image (R = lowest order, G = middle order and B = highest order)
- Make a ternary image (RGB) of the relative distributions of the concentrations of radioactive elements potassium (R), thorium (G) and uranium (B).
- Select magnetic anomalies and create a regular window (polygon) around each anomaly.
- Run inverse 3D modeling of each selected anomaly. For this case, the algorithms used are those included in Oasis Montaj "magnetization vector inversion (MVI, Ellis et al., 2012)" included with the VOXI extension using iterative reweighting inversion (IRI) focusing with 2 passes to sharpen positives.

Considering this information, every 3D model is described (geometry of the magnetic source, depth to top, etc.); then, radiometric data and topography are checked to identify whether the source crops out or whether a

feature related to the source is modeled. In addition, the available geology is checked to see if the calculated source has already been mapped, and other mining (deposits, occurrences) and geochemical (soil, sediment, rock) data are integrated to refine the interpretation.

5. Examples of anomalies targeting and interpretation

The procedure presented above was applied to three anomalies located in different tectonic and geological settings (Figure 3): the first one in the Central Andes Cordillera, the second one in the western foothills of the San Lucas Range and the last one in the Guyana shield. These anomalies were used not only to demonstrate the potential of airborne magnetometry and gamma spectrometry for increasing the geoscientific knowledge of wide areas but also to generate multiple exploration targets to aid in the development of the mineral potential of Colombia.

5.1 Andes anomaly

The Andes anomaly is located on the eastern flank of the Central Cordillera of Colombia, where the Triassic core of the Andes Cordillera and the Cretaceous Antioquia Batholith form a block limited by the nearly N-S trending Palestina Fault System to the east and the Romeral Fault System to the west (Gómez et al., 2015).

5.1.1 Geology

Locally, the southern part of the area corresponds to the northernmost outcrop of the Antioquia Batholith (Kgd, Figure 4), with some mafic bodies to the north (Kg), cataclastic granites (Kgn), altered lava flows (Krv) and the

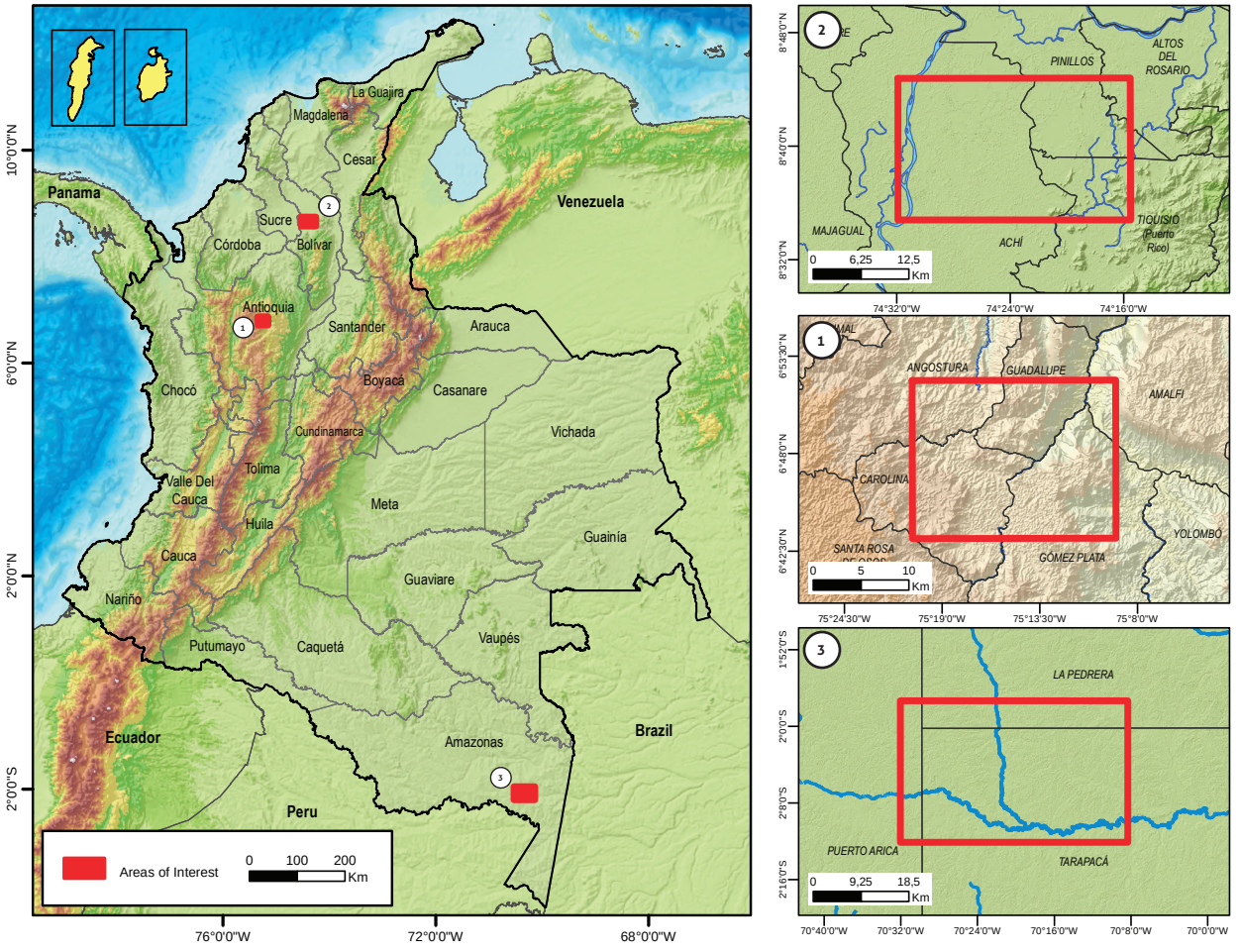

Figure 3. Locations of the selected anomalies: Andes (1), San Lucas (2) and Guyana shield (3)

nonmagnetic San Pablo Formation (Kap), a Cretaceous sedimentary unit frequently intruded by the batholith. Specifically, the anomaly is related to a quartz-rich dacitic porphyry (Kda), strongly linked to the edge facies of the batholith (Hall et al., 1972).

5.1.2 Anomaly description and 3D modeling

The Andes anomaly is detected as a strong (326 nT peak-to-peak amplitude in the TFA) and large (6 km diameter) magnetic anomaly located in an area containing several mineral deposits (López et al., 2018). The gold anomaly occurrence (yellow dot, Figures 5a and 5b) in the center of the anomaly is important to prioritize its study. Furthermore, on the tilt derivative image (Figure 5c), dominant nearly NE-SW lineaments are identified, which may represent a structural control on possible fluid migration and/or emplacement.

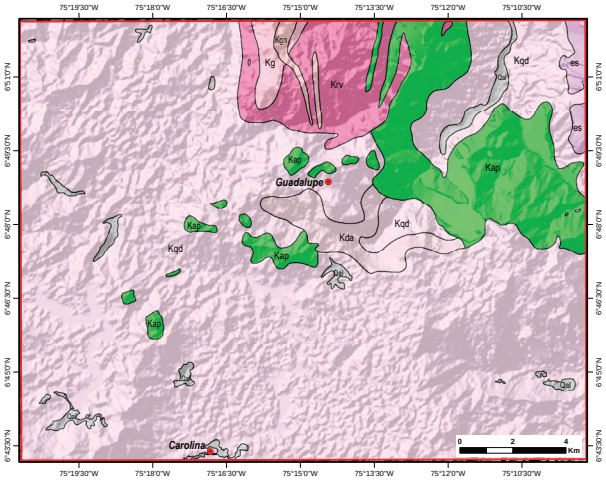

Figure 4. Geology of the area containing the Andes anomaly: Antioquia Batholith (Kgd), mafic bodies (Kg), cataclastic granites (Kgn), altered lava flows (Krv) and the nonmagnetic San Pablo Formation (Kap) and quartz-rich dacitic porphyry (Kda) Modified from Hall et al. (1972)

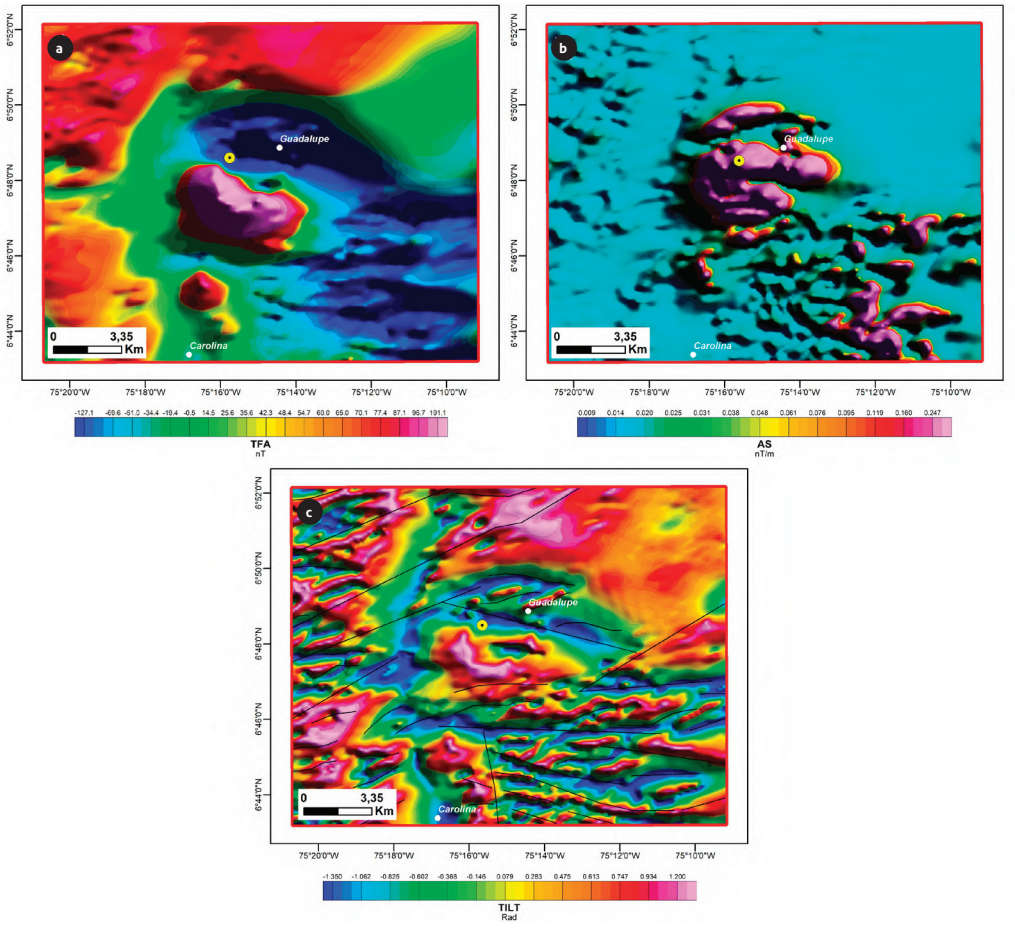

Figure 5. Magnetometry images of the Andes anomaly: a) Total field anomaly (TFA), b) analytical signal (AS) of the TFA, c) tilt derivative image with magnetic lineaments. The yellow circle represents the location of the sample with a high gold content

The ternary radiometric image (Figure 6) shows that the magnetic anomaly is coincident with a rock outcrop that presents high grades of Th, U and K, generating a white color in the image.

The 0.03 SI cutoff isosurface from the 3D magnetic susceptibility MVI model depicts a large (7 x 3.5 km) E-W elongated magnetic body (Figure 7). The model shows some portions close to the surface or cropping out, but clearly, a large part of the body is below the surface.

The follow-up procedure for this anomaly could include fieldwork for rock sampling and a regular sampling grid for geochemical analysis. The data obtained can guide the next steps in the evaluation of the anomaly.

5.1.3 Mineral resource potential

The Andes anomaly is located within the Guadalupe Au-(Ag) metallogenic district and east of the Amalfi-Anorí metallogenic district (López et al., 2018). The Guadalupe district is characterized by the presence of intrusive-related deposits and includes a copper volcanogenic massive sulfide (VMS) deposit known as the Guadalupe project (Figure 8). For this area, geochemical data report 144,000 ppb of gold from a vein inside the most magnetic portion of the anomaly and 58.2 ppm of silver within a neighboring dike. Due to the metallogenic context and known deposits/occurrences in the area of the Andes anomaly, the exploration target could be an intrusion-related/VMS and/or epithermal deposit.

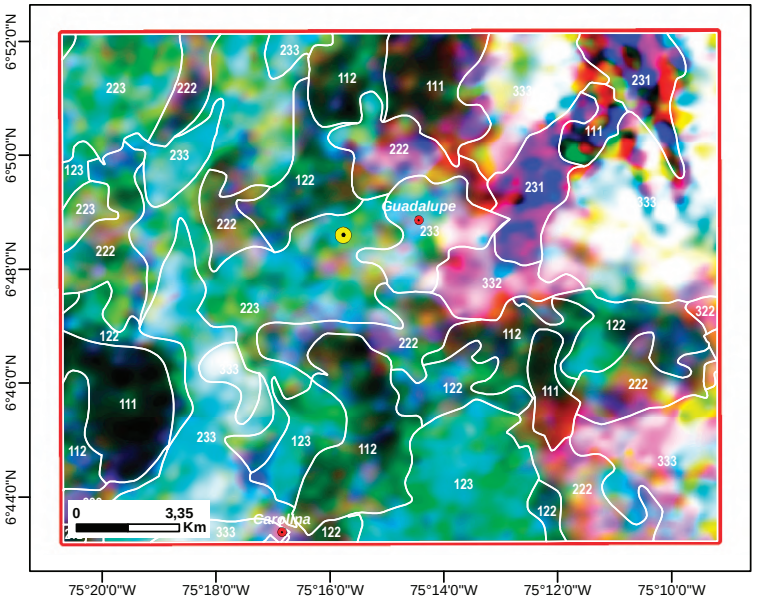

K	U	Th	Combination	Code
Low	Low	Low	Kl-Ul-Thl	111
Low	Low	Medium	Kl-Ul-Thm	112
Low	Medium	Medium	Kl-Um-Thm	122
Low	Medium	High	Kl-Um-Thh	123
Medium	Low	Medium	Km-Ul-Thm	212
Medium	Medium	Medium	Km-Um-Thm	222
Medium	Medium	High	Km-Um-Thh	223
Medium	High	Low	Km-Uh-Thl	231
Medium	High	High	Km-Uh-Thh	233
High	Low	Medium	Kh-Ul-Thm	312
High	Medium	Medium	Kh-Um-Thm	322
High	High	Medium	Kh-Uh-Thm	332
High	High	High	Kh-Uh-Thh	333

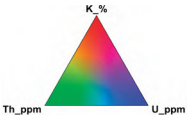

Figure 6. Ternary radiometric image of the Andes anomaly with contoured radiometric domains. The yellow circle represents the location of the 144.000 ppb Au sample

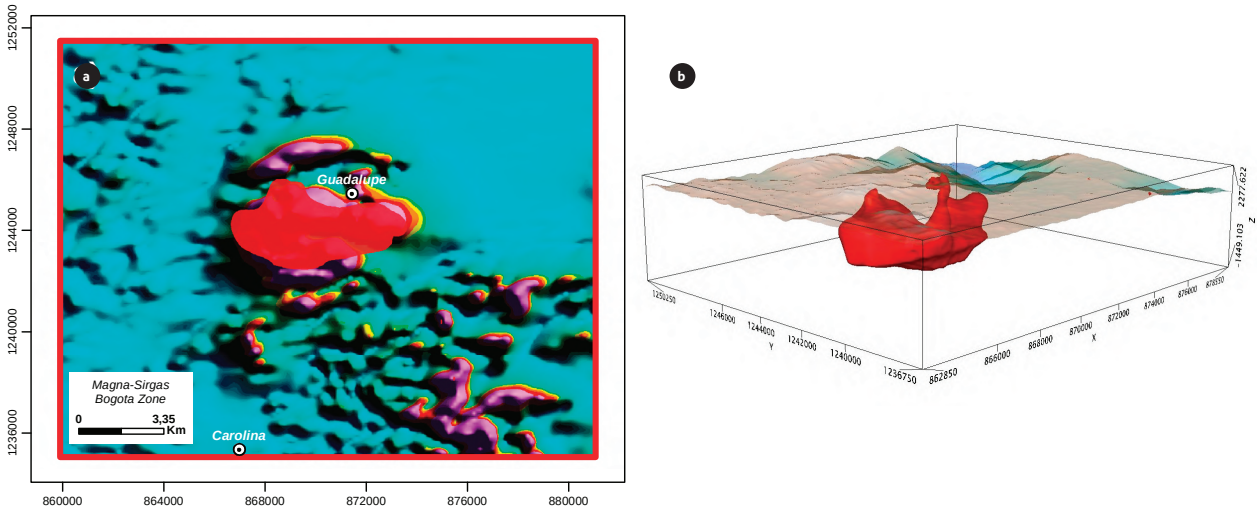

Figure 7. 3D model of the Andes anomaly: a) Analytical signal from the TFA with 0.3 SI MVI model, b) 0.3 SI isosurface of the 3D magnetic susceptibility model from MVI inversion

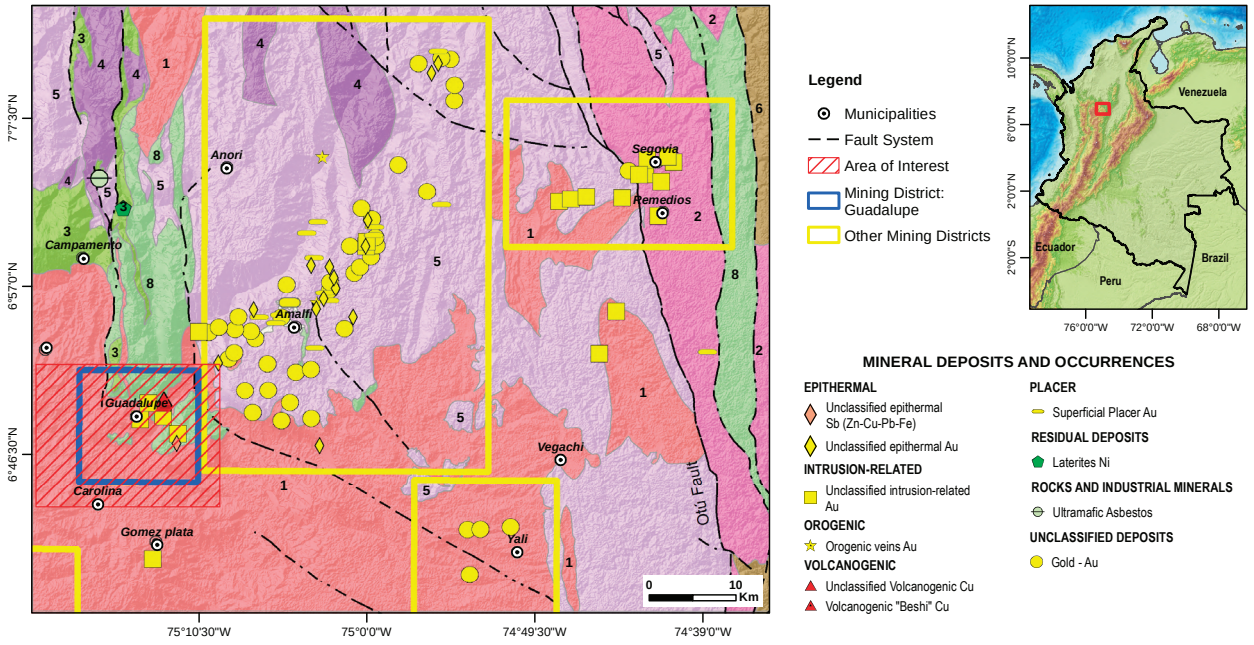

Figure 8. Mineral deposits and metallogenic districts near the Andes anomaly (yellow boxes); the numbers represent the local geology: 1) Felsic igneous rocks (Cretaceous), 2) felsic igneous rocks (Jurassic), 3) mafic and ultramafic igneous rocks (Cretaceous), 4) gneiss and intrusive rocks (Permian-Triassic), 5) low-grade metamorphic rocks (Triassic), 6) high-grade metamorphic rocks (Proterozoic), 7) sedimentary rocks (Cenozoic), 8) volcanic and volcanic-sedimentary mafic rocks (Cretaceous)
Modified from López et al. (2018)

5.2 San Lucas Range Anomaly

This anomaly is located in the northernmost part of the Central Cordillera in the western foothills of the San Lucas Range at the confluence of the Magdalena and Cauca rivers.

5.2.1 Geology

Nonmagnetic floodplain and lacustrine deposits bounded to the south by the last outcrops of the Central Cordillera and some Cenozoic deposits cover the San Lucas Range anomaly. To the east of the Palestina Fault is mapped the gneiss of the San Lucas Formation (MPsl), a gneiss often intruded by igneous bodies and covered by Quaternary deposits and the Sudan Formation (T3s), which consists of very thick beds of conglomerates intercalated with intervals of clay limestone and beds of tuffaceous sandstones (Figure 9).

5.2.2 Anomaly description and 3D modeling

The magnetic anomaly corresponds to an isolated dipole with a 1,000 nT peak-to-peak amplitude (TFA) within an area of low magnetic contrast related to the sedimentary cover; the anomaly is limited to the east by a strong gradient area related to the Palestina fault-controlled transition to the San Lucas Range crystalline rocks (Figures 10a and 10b). The tilt derivative image (Figure 10c) shows predominantly NNE-SSW-oriented lineaments, one of which delineates the Palestina Fault located east of the anomaly and other of which is located west of the anomaly. This structural trend interpreted from the geophysical data suggests that the magnetic source "emplacement" was probably controlled between these structures.

There is no relation between the gamma spectrometry data and the magnetic anomaly, which suggests that there could not be a surface expression of the causative magnetic body (Figure 11). However, gamma spectrometry data themselves reflect changes in the surface materials that are useful for lithogeophysical mapping, such as changes in the radioactive element contents of the sedimentary deposits, delineation of crystalline rocks cropping out to the east of the Palestina Fault and even fault delineation itself.

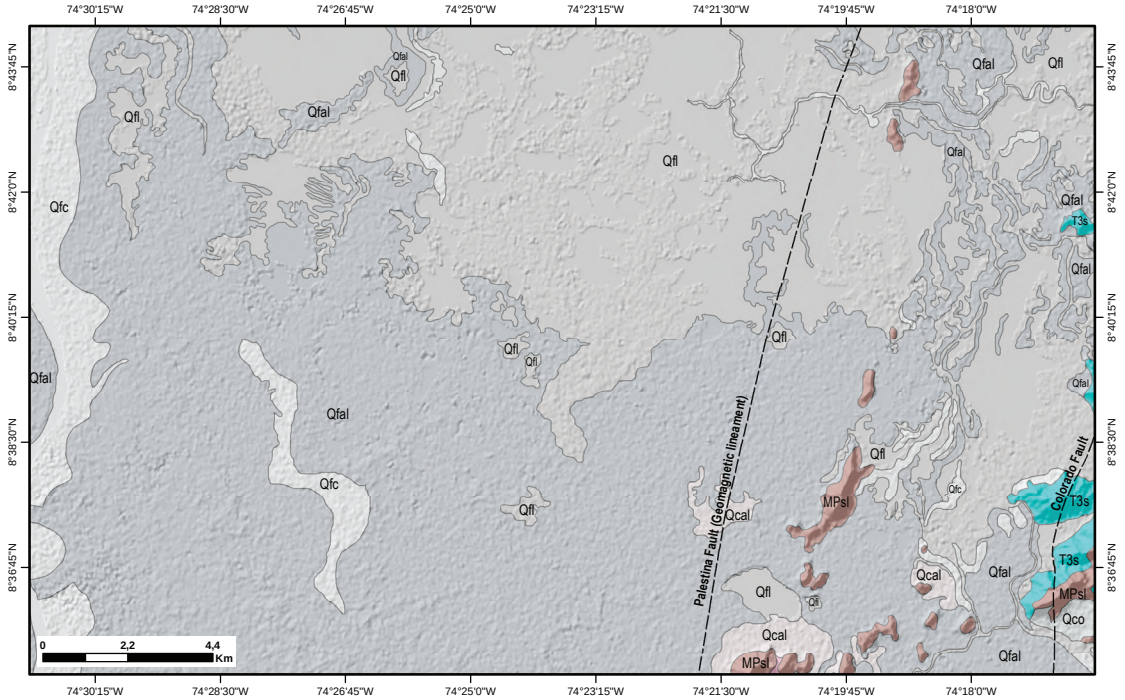

Figure 9. Geology of the San Lucas anomaly: Floodplain (Qfal) and fluvio-lacustrine (Qfl) deposits, fluvial channel (Qfc) deposits, fan and terraces (Qcal) deposits, San Lucas gneiss (MPsl), Sudán Formation (T3s)
Modified from Ingeominas (2006)

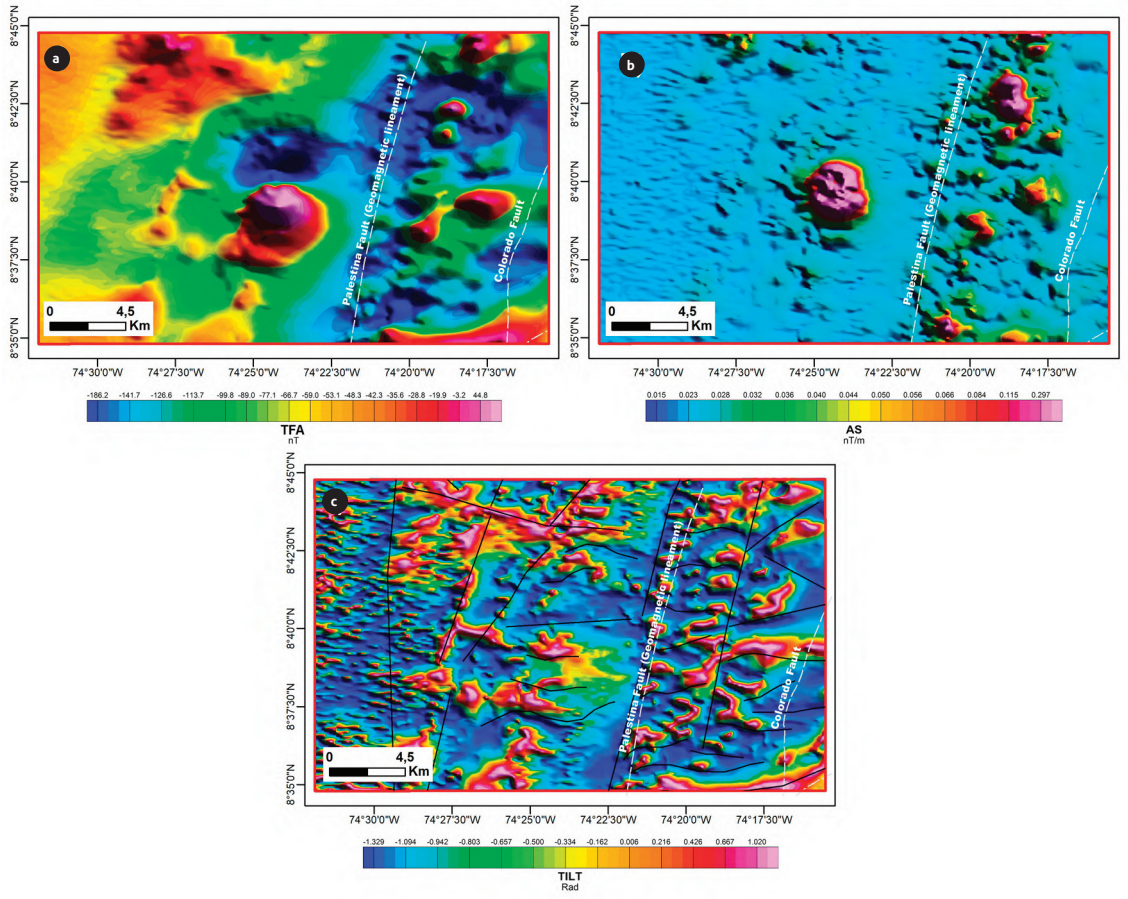

Figure 10. Magnetometry images of the San Lucas anomaly: a) Total field anomaly (TFA), b) analytical signal of the TFA, c) tilt derivative image with magnetic lineaments (black lines) and Palestina Fault (yellow line)

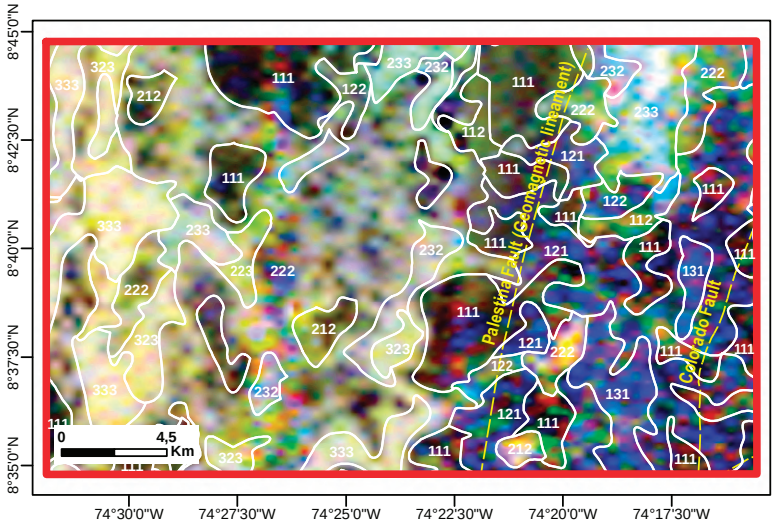

K	U	Th	Combination	Code
Low	Low	Low	Kl-Ul-Thl	111
Low	Low	Medium	Kl-Ul-Thm	112
Low	Medium	Low	Kl-Um-Thl	121
Low	Medium	Medium	Kl-Um-Thm	122
Low	High	Low	Kl-Uh-Thl	131
Medium	Low	Low	Km-Ul-Thl	211
Medium	Low	Medium	Km-Ul-Thm	212
Medium	Medium	Medium	Km-Um-Thm	222
Medium	Medium	High	Km-Um-Thh	223
Medium	High	Medium	Km-Uh-Thm	232
Medium	High	High	Km-Uh-Thh	233
High	Medium	High	Kh-Um-Thh	323
High	High	High	Kh-Uh-Thh	333

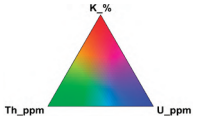

Figure 11. Ternary radiometric image of the San Lucas anomaly with contoured radiometric domains

Since there are no outcrops and no topographic or radiometric expressions, magnetic 3D modeling is the only choice to estimate the parameters of a possible buried body of interest. The MVI model with a cutoff magnetic susceptibility of 0.03 SI shows a "pipe-like" body of 2 x 3 km (Figures 12a and 12b), located at 100 m depth.

5.2.3 Mineral resource potential

The San Lucas anomaly is located 25 km to the west of the Au-(Ag) metallogenic district of Barranco de Loba (López et al., 2018). This district is characterized by the presence of Au/Cu porphyries such as the San Carlos Project and intrusion-related and epithermal deposits (Figure 13). The metallogenic context of the area and the semicircular pipe-like shape of the magnetic source allows us to estimate that the corresponding target of this anomaly is more likely to be a porphyry system than a kimberlite/carbonatite-related body. Therefore, additional exploration programs for this anomaly should be airborne gradiometric gravity or ground gravity and airborne or ground EM.

5.3 Amazonas anomaly

This anomaly is found in the southeastern part of Colombia, in an area of low relief with a drainage system that flows into the Amazon River and is covered by a dense tropical rainforest.

5.3.1 Geology

The surface geology corresponds to nonmagnetic Neogene rocks with ferruginous matrixes (conglomerates, sandstones, claystone, and in some cases coal) that are poorly consolidated and dissected by the principal drainages of the area (Figure 14). The magnetic basement rock can be related to the Mitú Complex (Rodríguez et al., 2011), composed of subalkaline high-potassium rocks, in some places with enrichments in rare earth element (REE) minerals.

5.3.2 Anomaly description and 3D modeling

This single magnetic anomaly has a very strong (2,000 nT) peak-to-peak amplitude (TFA) and lacks surface expression (Figures 15a and 15b). Through a flight with 1,000 m line spacing, it appears in four flight lines. Because such anomalies are not expected in the sedimentary rocks that crop out and because there is neither radiometric signature nor geological evidence of a causative body coincident with the magnetic anomaly (Figure 16), 3D modeling of the magnetometry is used to estimate the shape, depth and other parameters of the subsurface body.

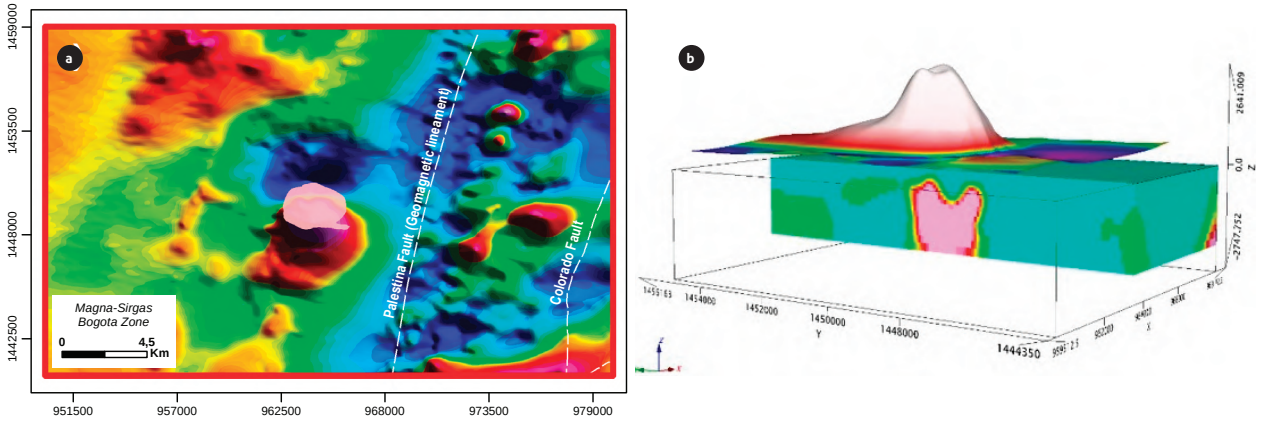

Figure 12. 3D model of the San Lucas anomaly: a) TFA superimposed with the 3D framework of the susceptibility model with a cutoff of 0.3 SI, b) cross section of the magnetic susceptibility model from 3D MVI inversion with the 3D image of the RTP

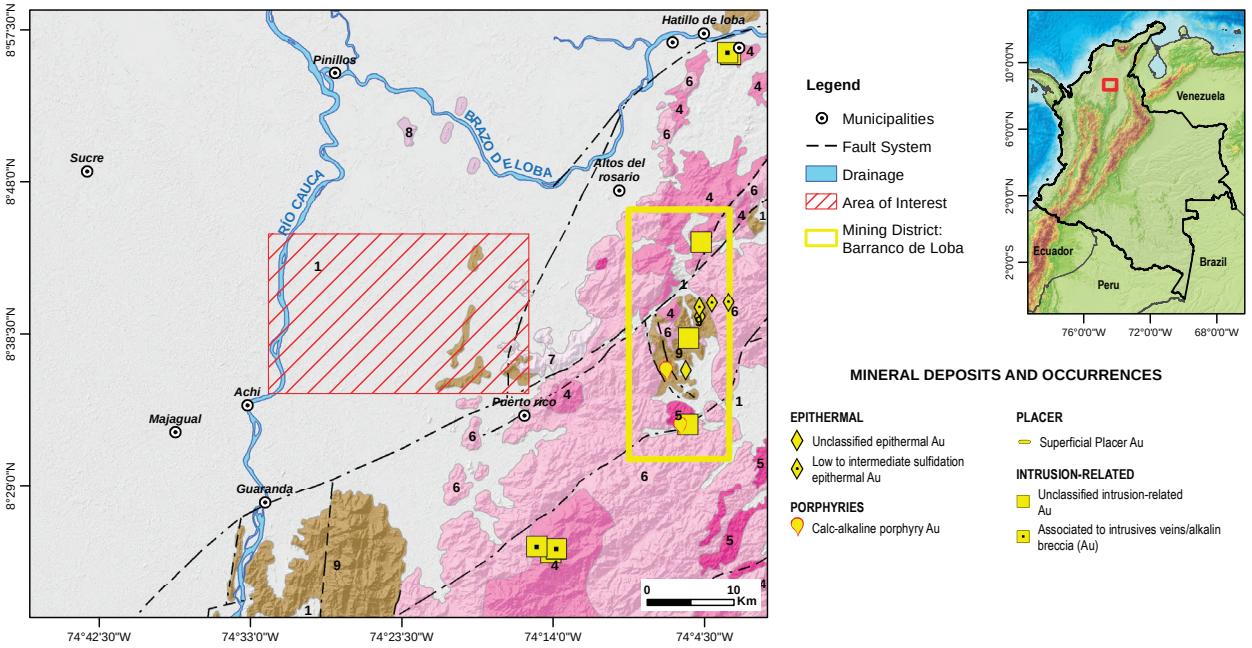

Figure 13. Mineral deposits and occurrences near the San Lucas anomaly (red box); the numbers represent the local geology: 1) Surface deposits (Quaternary), 2) Cenozoic sedimentary rocks (Paleocene-Pliocene), 3) Cretaceous sedimentary rocks (Berriasian-Albian), 4) felsic igneous rocks (Jurassic), 5) subvolcanic rocks (Jurassic), 6) volcanic and volcanic-sedimentary rocks (Permian–Upper Jurassic), 7) continental siliciclastic rocks (Triassic?), 8) metamorphic rocks (Triassic), 9) high-grade metamorphic rocks (Proterozoic)
Modified from López et al. (2018)

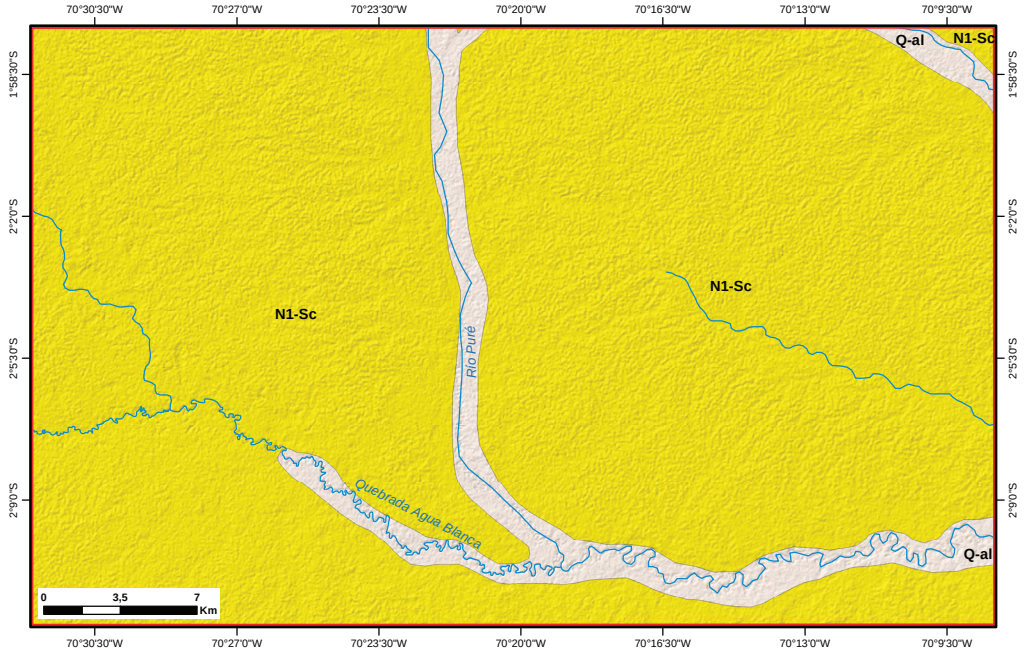

Figure 14. Geology of the Amazonas anomaly: Neogene deposits with ferruginous matrix (N1-Sc), alluvial and alluvial plain deposits (Q-al)
Modified from Gómez et al. (2015)

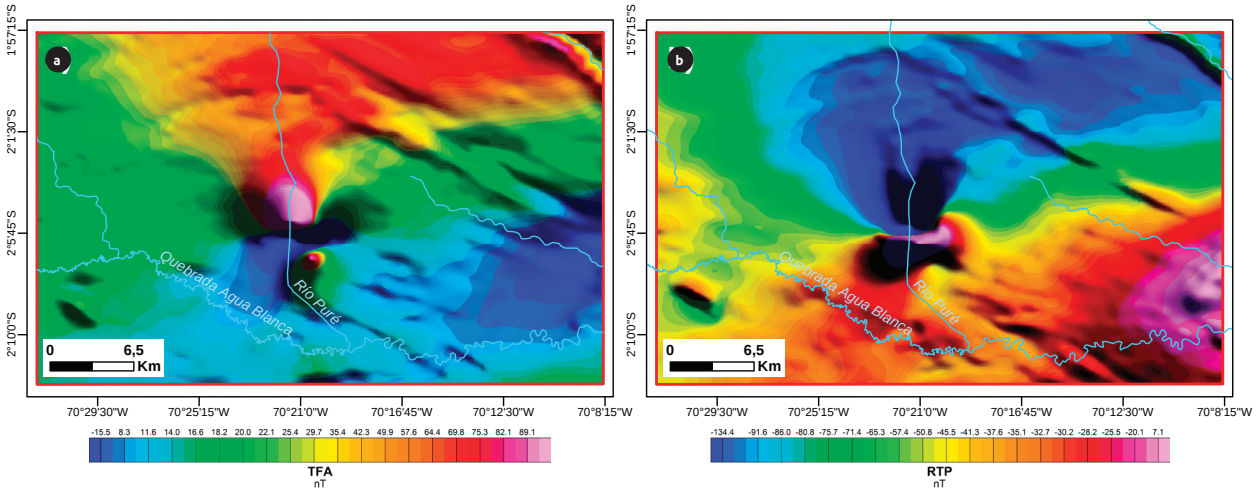

Figure 15. Magnetometry images of the Amazonas anomaly: *a) Total field anomaly (TFA), b) reduction to magnetic pole (RTP) of the TFA*

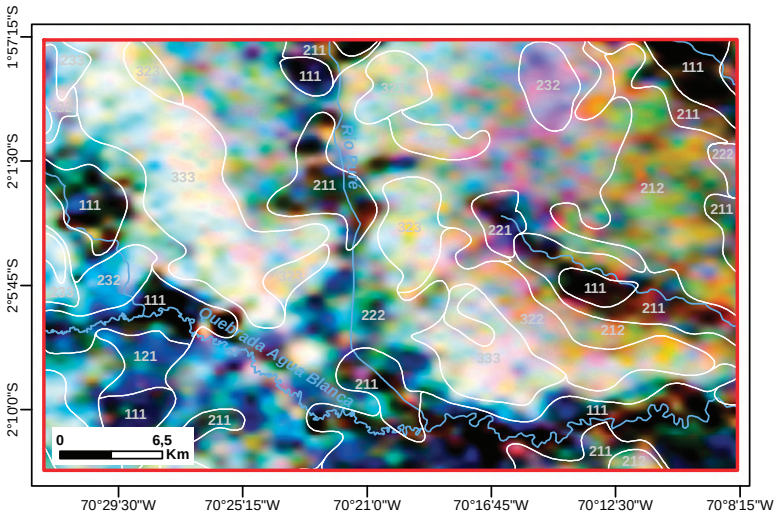

K	U	Th	Combination	Code
Low	Low	Low	Kl-Ul-Thl	111
Low	Medium	Low	Kl-Um-Thl	121
Medium	Low	Low	Km-Ul-Thl	211
Medium	Low	Medium	Km-Ul-Thm	212
Medium	Medium	Low	Km-Um-Thl	221
Medium	Medium	Medium	Km-Um-Thm	222
Medium	High	Medium	Km-Uh-Thm	232
Medium	High	High	Km-Uh-Thh	233
High	Medium	Medium	Kh-Um-Thm	322
High	Medium	High	Kh-Um-Thh	323
High	High	High	Kh-Uh-Thh	333

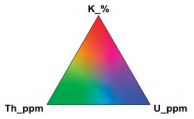

Figure 16. Ternary radiometric image of the Amazonas anomaly with contoured radiometric domains

Figures 17a and 17b show the results of the 3D MVI inversion with a magnetic susceptibility cutoff of 0.003 SI. The isosurface shows a 4 km x 3.5 km magnetic source located close to the surface. Additionally, the shape of the dipole in the TFA anomaly (Figures 15a and 17b) could indicate that the magnetic body has a complex magnetization (remanence).

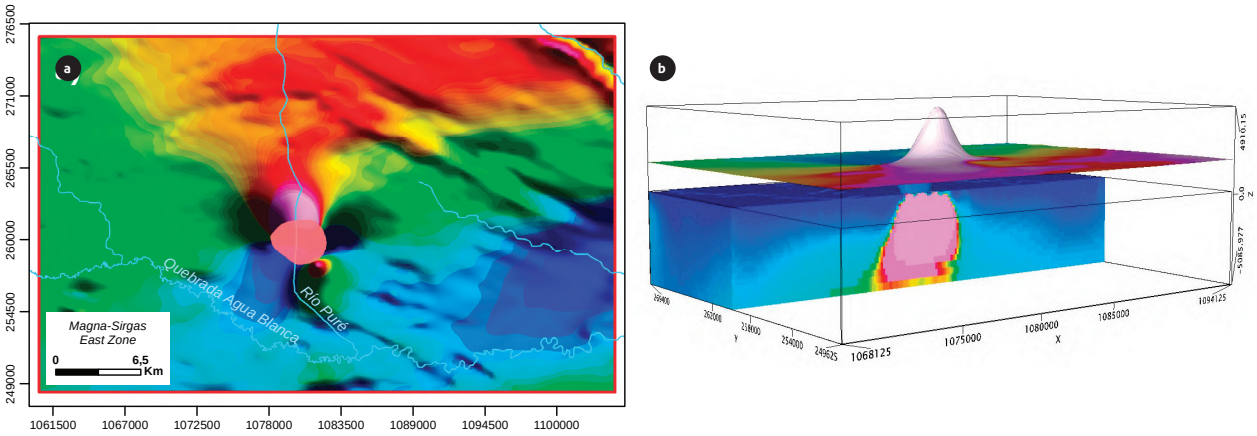

Figure 17. 3D model of the Amazonas anomaly. a) TFA superimposed with the 3D framework of the susceptibility model, b) cross section of the magnetic susceptibility model from 3D MVI inversion and the 3D image of the RTP

5.3.3 Mineral resource potential

The average depth of the modeled source (top of the body) is 40 m, and it is not possible to determine either the source petrology of the source or the economic value. Additionally, the anomaly is in an area with poor geological knowledge due to the dense rainforest coverage and lack of infrastructure.

However, isolated magnetic bodies located within the sedimentary cover in the Amazonian Craton have the potential to be alkaline rocks. Kimberlites (diamonds) and carbonatites (phosphate, niobium, and REEs) are the main economic targets of anomalies. In this case, rocks of the Mitú Complex have REEs, niobium (Nb), and tantalum (Ta) minerals associated principally with granitic pegmatites, dikes and acidic stocks, which intrude the complex and could also be the source of tin (Sn) and tungsten (W) (López and Cramer, 2012).

A mineral exploration program should apply other methods and then drill the anomaly to find the source. The additional methods suggested for this anomaly are i) ground magnetics and ii) airborne gradiometric gravity or ground gravity.

6. Discussion

As explained above, the metallotectonic environment and known mineral deposits in the NW Andes and Colombia reflect a subduction-related affinity with magma generation and emplacement. For exploration purposes in this kind of geological setting, magnetometry has advantages over other geophysical methods due to the strong correlation between magnetic mineral contents and ore-deposit generation. In this work, the processing and interpretation of the magnetometric data focus on going beyond the anomaly detection itself to more specialized modeling of the magnetic source geometrical parameters and structural framework, integrated with gamma spectrometry and available geological, geochemical and metallogenic data. This integration methodology helps in the identification, characterization and fieldwork prioritization of the magnetic anomalies found in the blocks covered by the airborne surveys.

The Andes anomaly is located at the northern edge of the Antioquia Batholith. The MVI magnetic susceptibility model shows a nearly 7 km E-W elongated body located mostly at depth but with some possible outcrops related to a radiometric signature. The local geology identifies a Qz-rich dacitic porphyry (Kda, Figure 4) in the area of the anomaly, so it is possible that the magnetic source corresponds to the subsurface extent of this intrusive rock. This indication should increase the potential for mineral resource exploration beyond the outcropping portion of the rock. The presence of 144,000 ppb gold value in a vein sample that is located at the center of the magnetic source also suggests important potential but demands more detailed work. The location of intrusion-related/VMS Au/Cu deposits close to the anomaly and the delimitation of a metallogenic district in the area are key facts to priori-

tize the study of this anomaly. The data processing also allows the identification of NE-SW lineaments that represent a structural control on a possible fluid migration and/or emplacement of a potential ore.

The San Lucas Range anomaly is covered by nonmagnetic fluvial and lacustrine deposits of recent age. To the east of the anomaly, separated by the Palestina Fault (NNE-SSW), metamorphic rocks of the San Lucas gneiss (MPsl, Figure 9) crop out. There is no surface or gamma spectrometric expression related to the anomaly, which supports the idea that the magnetic source is buried under recent sediments. Magnetometry interpretation marks predominantly NNE-SSW lineaments such as the Palestina Fault trend and suggests possible structural control on the emplacement of the magnetic source, which appears to be limited by these lineaments to the west and by the Palestina Fault to the east. The MVI magnetic susceptibility model shows a 2 km x 3 km "pipe-like" body located close to the surface, which could indicate that the magnetic source is not related to the magnetic igneous-metamorphic basement and probably is a magmatic body intruded within less magnetic rocks. There is no direct evidence of fertile rocks or mineralization over the anomaly, but 25 km to the east, the Barranco de Loba metallogenic district is delimited, characterized by the presence of several Au (Cu) porphyry, intrusion-related and epithermal deposits and occurrences. The size and shape of the MVI model of the magnetic source and the regional metallogenic context allow us to estimate that this anomaly could be related to an intrusive body with exploration potential for porphyry, intrusion-related and/or epithermal deposits.

The Amazonas anomaly is located in a very remote area of the Amazon rainforest where geological and metallogenic knowledge is restricted to regional extrapolation from sparse observation points. There is no surface or gamma spectrometry evidence that can be related to the anomaly. The magnetic anomaly shows a complex dipole with a very strong (2,000 nT) amplitude that suggests that the magnetic source could have strong remnant magnetization and be located within almost nonmagnetic rocks. Additionally, the dipole shows sharp lobes, suggesting that the source is buried very close to the surface. The MVI magnetic susceptibility model shows a 2.5 km x 3 km source located close to the surface. Even in the absence of detailed geological, geochemical or metallogenic information, it is possible to extrapolate the evidence and deposits discovered in other cratonic areas (Brazil and Venezuela) and expect that this kind of nearly cylindrical and isolated magnetic anomaly is related to alkaline rocks, kimberlites or carbonatites.

It is important to remember that geophysical data, for mineral exploration purposes, imply the estimation of physical properties of the rocks and materials of the subsurface by indirect measurement of the perturbation of a natural field or an induced signal due to contrasts in these properties. Furthermore, the use of mathematical modeling to quantitatively estimate the distribution of the selected physical property that corresponds to the observed perturbation has almost infinitely many different solutions (the nonuniqueness principle) that can be reduced to more geologically related models when integrated with field data.

In this context, the magnetic susceptibility cutoff used to represent the dimension and geometry of each of the magnetic sources (0.03 SI for the Andes and San Lucas anomalies and 0.003 SI for the Amazonas anomaly) from the MVI are estimated with the analytical signal (AS) of the TFA. The AS is a mathematical transform that reduces the dipolar signature of a magnetic anomaly and has the effect of strengthening at the edges of the magnetic source (Nabighian, 1972). Using this attribute, the magnetic susceptibility from the model is chosen so that the surface expression of the isosurface is close to the borders of the AS of the anomaly. For this reason, the magnetic susceptibility used for this work must be considered only a reference parameter estimated by mathematical criteria and has to be compared with petrophysical data. However, it is still a reliable and useful approximation in the absence of petrophysical data collected from rocks in the field.

For the anomalies and models presented in this work, the Andes anomaly has strong geological, geochemical and metallogenic controls that allow us to demonstrate the mineral potential in this area, and the 3D modeling of the magnetic source reinforces this potential. For the San Lucas and Amazonas anomalies, the lack of other geoscientific data must encourage exploration in these areas because geophysical modeling shows that there are magnetic sources that have to be explained, and given our

actual knowledge of the area, there is no evidence of potential other than the geological setting and, in the case of the San Lucas anomaly, the known mineral deposits in the surroundings.

The results presented in this work illustrate the methodology used to manage geophysical data (magnetometry and gamma spectrometry) for the evaluation of the mineral resource potential in Colombia. The three anomalies presented are located in different geological contexts within the country and represent strong evidence that the integration of available geological, geochemical and metallogenic data with advanced geophysical modeling will provide a better understanding of the nature, geometry and subsurface distribution of potential targets and hence optimize efforts and resources in the fieldwork phase.

7. Conclusions

The acquisition of high-resolution airborne magnetometry and gamma spectrometry generates valuable information to increase the geoscientific knowledge of Colombia and allows target identification and interpretation for mineral resource exploration. For this purpose, three magnetic anomalies were selected to illustrate the data processing methodology used for the identification of areas of interest for future investigation.

The Andes anomaly is interpreted as a magnetic (0.03 SI) source 3.5 km x 7 km wide and located at depth with some surface expression correlated with gamma spectrometry. The geological data correlate this anomaly at the surface with a Qz diorite porphyry, suggesting that the subsurface extent of the intrusion is wider. This anomaly is located within the Guadalupe (Au/Ag) metallogenic district and is a potential target for intrusion-related, epithermal or VMS deposits. The evidence of magnetic lineaments and a vein sample with gold suggest structural control for fluid migration and ore deposition.

The San Lucas anomaly is modeled as a magnetic (0.03 SI) "pipe like" source 2 km x 3 km wide, located close to the surface and surrounded by almost nonmagnetic rocks. There is no surface expression related to the anomaly, and the geological data indicate the presence of recent fluvio-lacustrine deposits. The magnetometry suggests a possible control by NNE-SSW lineaments on the emplacement of the source; one lineament is correlated with the Palestina Fault in the east. The presence of the Barranco de Loba Au (Cu) metallogenic district 25 km to the east and the regional metallogenic context mark this anomaly as a target for porphyry/intrusion-related and epithermal deposits.

The Amazonas anomaly MVI model (0.003 SI) shows a nearly cylindrical 2.5 km x 3 km body, surrounded by almost nonmagnetic rocks and located close to the surface but with no topographic or gamma spectrometric correlation. Geological knowledge about the area is minimal, but evidence from deposits identified in other areas of the Amazonian Craton and the potential estimated for rocks of the Mitú complex allow us to consider this anomaly a potential target for carbonatite/kimberlite deposits.

Considering that there must be very few outcrops of mineral deposits yet to be found, the supply for the mineral market must be obtained from underground deposits. This fact, added to the global requirements of environmental protection, means that geophysical methods are increasingly fundamental in mineral prospecting.

Acknowledgments

The authors would like to acknowledge the Servicio Geologico Colombiano (SGC) for allowing the use of airborne geophysical data from ongoing surveys and the interpretations presented in this document.

References

Baranov, V. (1957). A new method for interpretation of aeromagnetic maps: pseudo-gravimetric anomalies. *Geophysics*, 22 (2), 359-382. https://doi.org/10.1190/1.1438369.

Bustamante, C., Archanjo, C. J., Cardona, A., Bustamante, A., and Valencia, V. A. (2017). U-Pb Ages and Hf Isotopes in Zircons from Parautochthonous Mesozoic Terranes in the Western Margin of Pangea: Implications for the Terrane Configurations in the Northern Andes. *The Journal of Geology*, 125 (5), 487-500. https://doi.org/10.1086/693014.

Ellis, R. G., Wet, B., and Macleod, I. N. (2012). Inversion of Magnetic Data from Remanent and Induced Sources. 22nd International Geophysical Conference and Exhibition, Australia.

Gómez, J., Montes, N., Nivia, A., and Diederix, H. (2015). *Mapa Geológico de Colombia 2015. Escala 1:1000000*. Bogotá: Servicio Geológico Colombiano.

Hall, R., Álvarez, J., and Rico, H. (1972). Geología de los departamentos de Antioquia y Caldas (Subzona II-A). *Boletín Geológico*, 20 (1), 1-85.

Ingeominas. (2006). *Memoria Explicativa Plancha 64 Barranco de Loba Sur Del Departamento de Bolívar*.

Leal, H. (2011). Phanerozoic Gold Metallogeny in the Colombian Andes: A Tectono-Magmatic Approach (Ph.D. Thesis). Universidad de Barcelona.

López, J. A., Leal, H., Luengas, C. S., Velásquez, L. E., Celada, C. M., Sepúlveda, M. J., Prieto, D. A., Gómez, M., and Hart, C. J. R. (2018). *Mapa Metalogénico de Colombia*. Bogotá: Servicio Geológico Colombiano.

López, J., and Cramer, T. (2012). Ambiente geológico del Complejo Mitú y perspectivas de ocurrencias minerales de Niobio y Tantalio en el territorio colombiano. *Geología Colombiana*, 37. https://revistas.unal.edu.co/index.php/geocol/article/view/40483.

Miller, H. G., and Vijay, S. (1994). Potential field tilt—a new concept for location of potential field sources. *Journal of Applied Geophysics*, 32 (2-3), 213-217. https://doi.org/10.1016/0926-9851(94)90022-1

Moyano, I., Lara, N., Ospina, D., Salamanca, A., Arias, H., Gómez E., Puentes, M., and Rojas, O. (2018). *Mapa de anomalías Geofísicas de Colombia para Recursos Minerales, Versión 2018*. Bogotá: Servicio Geológico Colombiano.

Nabighian, M. N. (1972). The analytic signal of two-dimensional magnetic bodies with polygonal cross-section: its properties and use for automated anomaly interpretation. *Geophysics*, 37 (3), 507-517. https://doi.org/10.1190/1.1440276

Rodríguez, G., Sepúlveda,J., Ramírez, C., Ortiz, F. H., Ramos, K., Bermúdez, J. G., and Sierra, M. I. (2011). Unidades, petrografía y composición química del Complejo Migmatítico de Mitú en los alrededores de Mitú. *Boletín de Geología*, 33 (1), 27-42.

Shaw, R., Leal-Mejia, H., and Melgarejo, J. (2019). Phanerozoic Metallogeny in the Colombian Andes: A Tectono-magmatic Analysis in Space and Time. In: F. Cediel, R. P. Shaw (eds.), *Geology and Tectonics of Northwestern South America, Frontiers in Earth Sciences*. Switzerland: Springer. https://doi.org/10.1007/978-3-319-76132-9_6

Sillitoe, R. H., Jaramillo, L., Damon, P. E., Shafiqullah, M., and Escovar, R. (1982). Setting, characteristics, and age of the Andean Porphyry Copper Belt in Colombia. *Economic Geology*, 77 (8), 1837-1850. https://doi.org/10.2113/gsecongeo.77.8.1837

Boletín Geológico

SERVICIO GEOLÓGICO COLOMBIANO

Boletín Geológico, 46, 23–49, 2020
https://doi.org/10.32685/0120-1425/boletingeo.46.2020.534

Received: June 26, 2019
Accepted: April 13, 2020
Published online: June 30, 2020

Contribution of bedding to the petrophysical characterization of naturally fractured reservoirs: Example of the Matachines fields, Upper Magdalena Valley (*Valle Superior del Magdalena* – VSM) Colombia

Contribución de la estratificación en la caracterización petrofísica de reservorios naturalmente fracturados: ejemplo de los campos Matachines (VSM, Colombia)

Eduardo A. **Rossello**[1] and José Luis **Saavedra**[2]

1 CONICET (National Scientific and Technical Research Council) – IGEBA (Institute of Basic, Applied and Environmental Geosciences of Buenos Aires) – UBA (University of Buenos Aires) – FCEN (Faculty of Exact and Natural Sciences). Buenos Aires, Argentina

2 Hocol Petroleum Limited, Bogotá, Colombia

Email: ea_rossello@yahoo.com.ar

Abstract

The Matachines field, located in the Girardot subbasin, Upper Magdalena Valley (*Valle Superior del Magdalena* – VSM) basin, has a morphology characterized by antiforms arranged along a N–S axis. These antiforms involve multiphase tectono-sedimentary sequences with half-graben geometries associated with Mesozoic sequences reactivated by at least three Andean phases. Bedding surfaces are mechanically active planes that contribute to the flexural slip that is generated by the folding of multilithologic sequences. In the Matachines field, the bedding planes help to improve the petrophysical characteristics of the reservoirs by incorporating a significant number of discontinuities, which complement the fluid connectivity. Thus, the subhorizontal planes are linked to subvertical fractures preferentially arranged in the ENE–WSW direction, generated by horizontal compressive stress. In particular, these effects are magnified on the western flank and hinge zone of the anticline structure, where they contribute greatly to the connectivity of the production wells. In naturally fractured reservoirs, the correct 4D technical and economic evaluation of the quality and arrangement of discontinuities is essential to determine their actual contribution to improving the petrophysical

properties of such reservoirs. Accordingly, many methods often used to study wells from core samples or images identify, along with different types of fractures, the presence of bedding surfaces, although they evaluate them separately, so they overlook petrophysical factors that affect the porosity and permeability of the wells. The present study discusses the genetic and morphological aspects of bedding surfaces that enhance the petrophysical potential of reservoirs, which usually have limited primary values of permeability and porosity, to meet the economic expectations of specific resources in hydrocarbon exploration and/or production activities.

Keywords: Petrophysics, unconventional reservoirs, hydraulic fracturing, Matachines field, VSM, Colombia.

Resumen

Los campos Matachines, localizados en la subcuenca de Girardot (cuenca del valle superior del Magdalena), presentan una morfología antiformal con su eje dispuesto en rumbo submeridianal que involucra secuencias tectosedimentarias multifásicas en las que pueden reconocerse geometrías de hemigraben asociadas con las secuencias mesozoicas que han sido reactivadas por al menos tres fases andinas. Las superficies de estratificación son planos mecánicamente activos contribuyentes de los flexodeslizamientos que genera el plegamiento de secuencias multilitológicas. En los campos Matachines, la estratificación contribuye a mejorar las características petrofísicas de sus reservorios al incorporar una importante participación de discontinuidades que complementan la conectividad de los fluidos. Así, desde sus posiciones subhorizontales se vincula con los planos de fracturas subverticales dispuestos preferencialmente en dirección ENE-WSW, generados por los esfuerzos compresionales horizontales. En particular, estos efectos se magnifican sobre el flanco occidental y charnelar de la estructura anticlinal, donde exhiben una mayor participación en la conectividad de los pozos productivos. En los reservorios considerados naturalmente fracturados, la correcta evaluación técnico-económica 4D de la calidad y disposición de las discontinuidades es fundamental para determinar las mejoras petrofísicas que determinan. En este sentido, muchas metodologías habitualmente aplicadas en el estudio de pozos a partir de núcleos o imágenes reconocen, además de distintos tipos de fracturas, la presencia de superficies de estratificación. Sin embargo, se las evalúa separadamente, lo que no incide estadísticamente en las consideraciones petrofísicas que contribuyenan evaluar su porosidad y permeabilidad. Se discuten los aspectos genéticos y morfológicos de las superficies de estratificación que contribuyen a aumentar la potencialidad petrofísica de los reservorios, cuyos valores primarios de permeabilidad y porosidad suelen ser limitados, para sostener expectativas económicas satisfactorias de ciertos recursos en actividades de exploración o producción de hidrocarburos.

Palabras clave: petrofísica, reservorios no convencionales, fracturación, campo Matachines, VSM, Colombia.

1. Introduction

In naturally fractured hydrocarbon reservoirs, the correct 4D technical and economic evaluation of the quality and arrangement of fractures is essential to determine their actual contribution to improving the petrophysical properties of such reservoirs. Many petrophysical methods that are often used to study wells from core samples of images (Aguilera and Aguilera, 2004; Bratton et al., 2006; Serra, 2008) identify and quantify the presence of bedding surfaces, but they evaluate them in separate statistical analyses and not within the petrophysical model. Thus, by analyzing them separately from discordant fractures, they are overlooked in geo-economics considerations of their reservoirs.

Naturally fractured reservoirs often present a production paradox because their initially high productivity tends to decline rapidly. Many are also responsible

for early gas or water penetration. However, they include some of the largest and most productive reservoirs, explaining the growing industry efforts to learn more about them and to more accurately model them.

The Matachines field (03°49' N–74°53' W) is located in the Girardot subbasin, within the Upper Magdalena Valley (*Valle Superior del Magdalena* – VSM) basin, similarly to the Purificación, Chenche, and Guando oilfields (Figure 1). The structure of these oilfields is generally characterized by tight and faulted anticlines and by wide synclines with an axis that runs roughly NNE–SSW, related to west-vergence thrust faults that are linked to the uplift of the Eastern Cordillera of Columbia (Campbell and Burgl, 1965; Corrigan, 1967; Anderson, 1972; Butler and Schamel, 1988; Cooper et al., 1995; Barrero et al., 2007 and Higuera, 2012, among many others).

In the present study, the structural aspects that contribute to creating the genetic and morphological characteristics of the bedding surfaces underlying the petrophysical potential of the Matachines field reservoirs are discussed. We focus on sectors where the primary permeability and porosity values are usually too low to meet economic expectations in hydrocarbon exploration or production activities. These analyses and interpretations may be used to evaluate oilfields with similar characteristics that will be subjected to exploration and/or production.

2. Methods

A multidisciplinary study was conducted to correctly evaluate deformation features associated with fractures. This study included the analysis of well core or borehole samples, borehole image logs, and a field study aimed at characterizing the physical attributes of the fractures, such as their geometry, direction, aperture, length, and spacing, to classify them into sets. All discontinuity surfaces analyzed in the present study ranged in size from meters to decimeters.

The seismic data were analyzed on a WorkStation mounted on the Petrel platform to spatiotemporally characterize the deformations by horizon flattening of sequences related to the study area, thereby establishing a relative

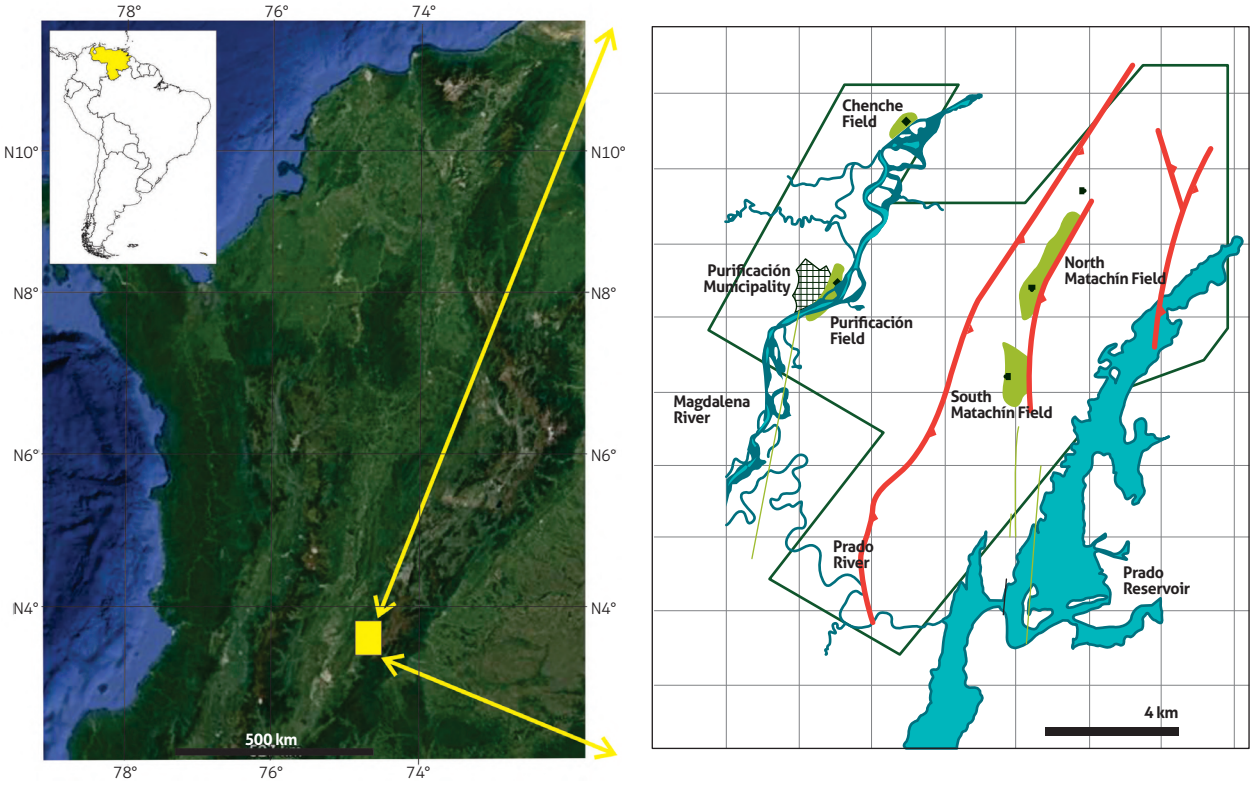

Figure 1. Location of the Matachines field in the VSM

criterion to recognize structures before and after the units that make up the oil system of the Matachines field.

Core samples were analyzed considering the above, as extensively described by Nelson (1985), Aguilera (2001), and by Kubik and Lowry (1993), among others. The available core samples were tentatively arranged and spatially oriented according to strike and dip data of the corresponding wells. The structures were qualitatively and quantitatively analyzed, organoleptically identifying some of their mineralogical components, using magnifying glasses in more detailed cases.

Ultrasonic borehole images are electronic records of well images that provide information on the slope and azimuth of layers and fractures. These data were tabulated, analyzed, and grouped as a function of slope and azimuth (Ekstrom et al., 1987) using the algorithm proposed by Fisher (Fisher et al., 1987) because, in general, this method yields data that are quasi-normally distributed and requires the mean direction and a concentration parameter for input. The main direction data of the fractures and microfaults were plotted on stereograms (lower hemisphere) to assess the vertical configuration of the fractures in the reservoirs.

This analysis generated a set of characteristic attributes of each fracture pattern, which were tabulated in data-processing software to quantify their occurrence percentages, particularly focusing on the identification of friction surfaces (slickensides), to determine the direction of the movements in the discontinuity surfaces.

Data were collected from two study areas in a structural position analogous to the field to analyze fractures in outcrops, primarily measuring representative fracture sets by microtectonics to contrast them with the structures observed in ultrasonic borehole images and core samples.

3. Geological Framework Of The Matachines Field

From the standpoint of regional tectonics, VSM is bordered to the west, in the Cordillera Central (Central Andes), by the Calarma thrust fault system with eastward vergence, and to the east, in the Cordillera Oriental (East Andes), by faults with opposite vergence, such as the Magdalena fault system (Schamel, 1991; Cooper et al., 1995; Toro et al., 2004).

Morphostructural features derived from surface and subsoil data indicate the multiphase evolution of the Matachines field, which is like that of other regions of VSM (Figure 2). The main stages of its history, based on our own data and on interpretations compiled from the abundant related bibliography, are listed below (*e.g.*, Irving, 1975; Kroonenberg and Diederix, 1982; Mojica and Franco, 1990; Bayona et al., 1994; Villamil et al., 1999; Sarmiento, 2001; Gómez et al., 2003; Sarmiento and Rangel, 2004; Montes et al., 2005; Mora et al., 2010).

3.1 First pre-Andean extensional stage

The tectonic history of the VSM basin started in the Triassic–Jurassic as a retroarc depocenter, which may have been controlled, at least partly, by pre-existing Paleozoic anisotropies (De Freitas, 2001). Half-graben geometries are fairly well preserved, albeit usually modified by the reactivation of at least three Andean phases, which are described below. Then, during the Cretaceous–Early Tertiary, the VSM basin continued as an intracratonic depocenter with the marine sequences of seals of the Caballos Formation (Duarte et al., 2018), generating the hydrocarbons of the Villeta and Guadalupe Groups, resulting in the seals of the Guaduas Formation (Higuera, 2012). Marine transgression and basin subsidence continued during the late Albian until the Santonian, with the VSM basin reaching its maximum extension during the Turonian–Coniacian period (limestones of the La Luna Formation), with the deposition of sediments very rich in organic matter, such as limestones from the Tetuán Formation, pelites from the Bambucá Formation, and pelites and limestones from the Luna Formation, from oldest to youngest (Buitrago, 1994).

Subsequent basin shallowing led to the development of the shallow marine detrital facies of the Guadalupe Group, which is the main producer of several fields (Matachines, Purificación, and Guando) in the Girardot subbasin and of the Monserrate Formation in the Neiva subbasin (Barrero et al., 2007). Marine regression during the Late Cretaceous, with coastline progradation, caused the deposition of fluvio-deltaic sediments of the Guaduas Formation (Late Maastrichtian?–Paleocene), but uplifts during the early-to-middle Eocene eroded these sediments in the highest sections of the basin (Cooper et al., 1995).

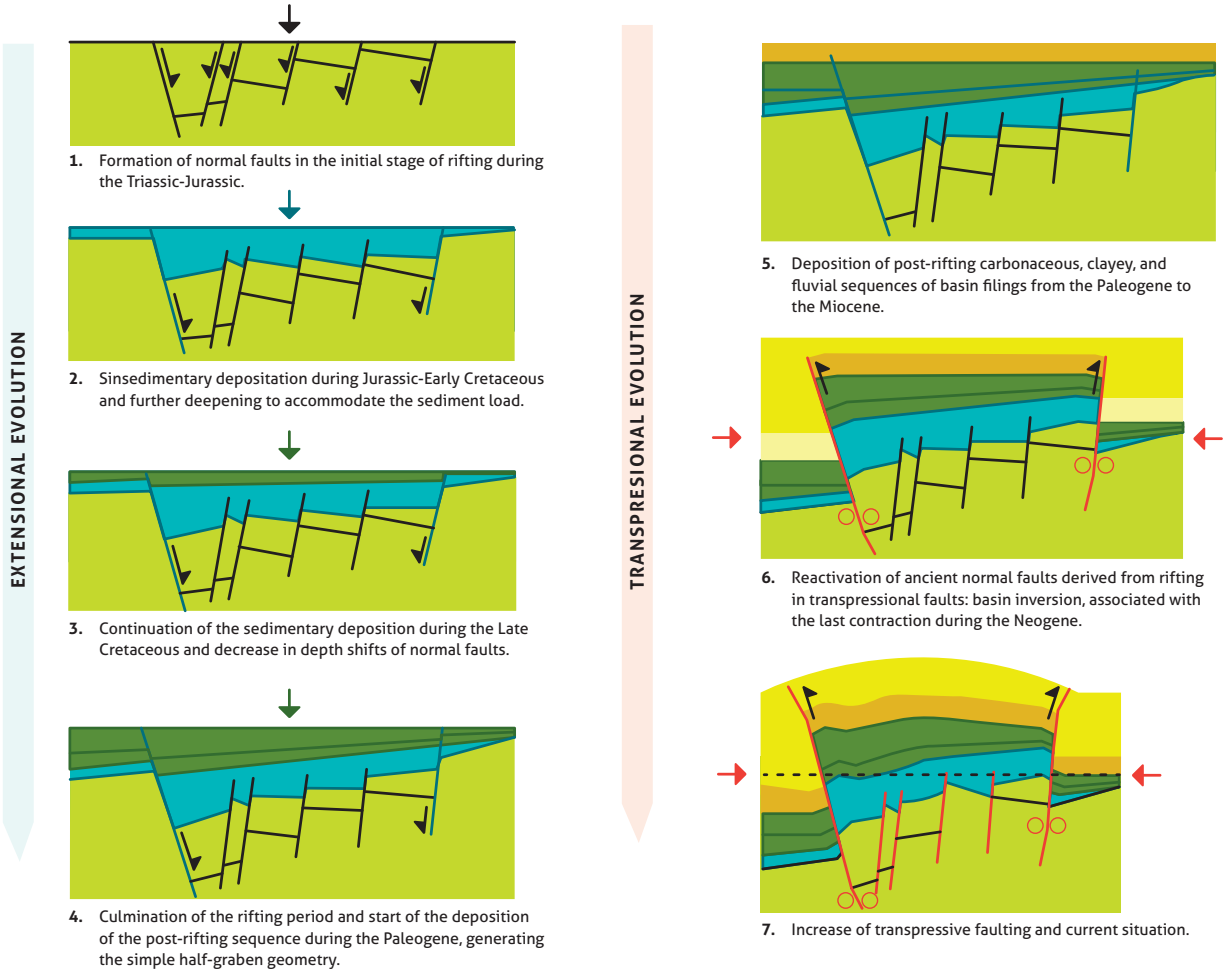

Figure 2. Idealized scheme of the structural evolution of VSM

3.2 Peruvian phase (first stage of compressional inversion)

The Peruvian phase (Cobbold et al., 2007), or the "Mochica event" (De Freitas et al., 2006), has been in general overlooked in Colombia, despite its comprehensive characterization in the rest of the Andes (Pindell and Tabbutt, 1995). In VSM, the Peruvian phase overlaps with the Albian–Cenomanian, as discussed by Jaimes and De Freitas et al. (2006), based on observations by Van der Wiel (1991) in the Garzón massif. De Freitas et al. (2006) recognized evidence of this phase in the Balcón region, where they observed half-graben geometries with clear mild inversions, which occurred during the Late Albian–Cenomanian, as shown by thinning and overlap of pelites of the Bambucá Formation. The NNW–ESE direction of the faulting suggests that compression primarily occurs in the WSW–ENE direction, which would transpressionally reactivate the Jurassic faulting in the ENE direction. Thus, they suggested that an early uplift of the Balcón area during this phase may have positively affected the oil system by generating secondary porosity in the Caballos Formation and by controlling subsequent deformations and migration patterns.

3.3 Incaic phase (second stage of compressional inversion)

The Incaic phase of Andean orogeny started during the early Eocene (for further details, please refer to Cobbold et al., 2007), with the increase in the speed of convergence between the Nazca plate and the South American plate, a determinant of crustal shortening structures expressed by thrust faults involving the basement, especially in the

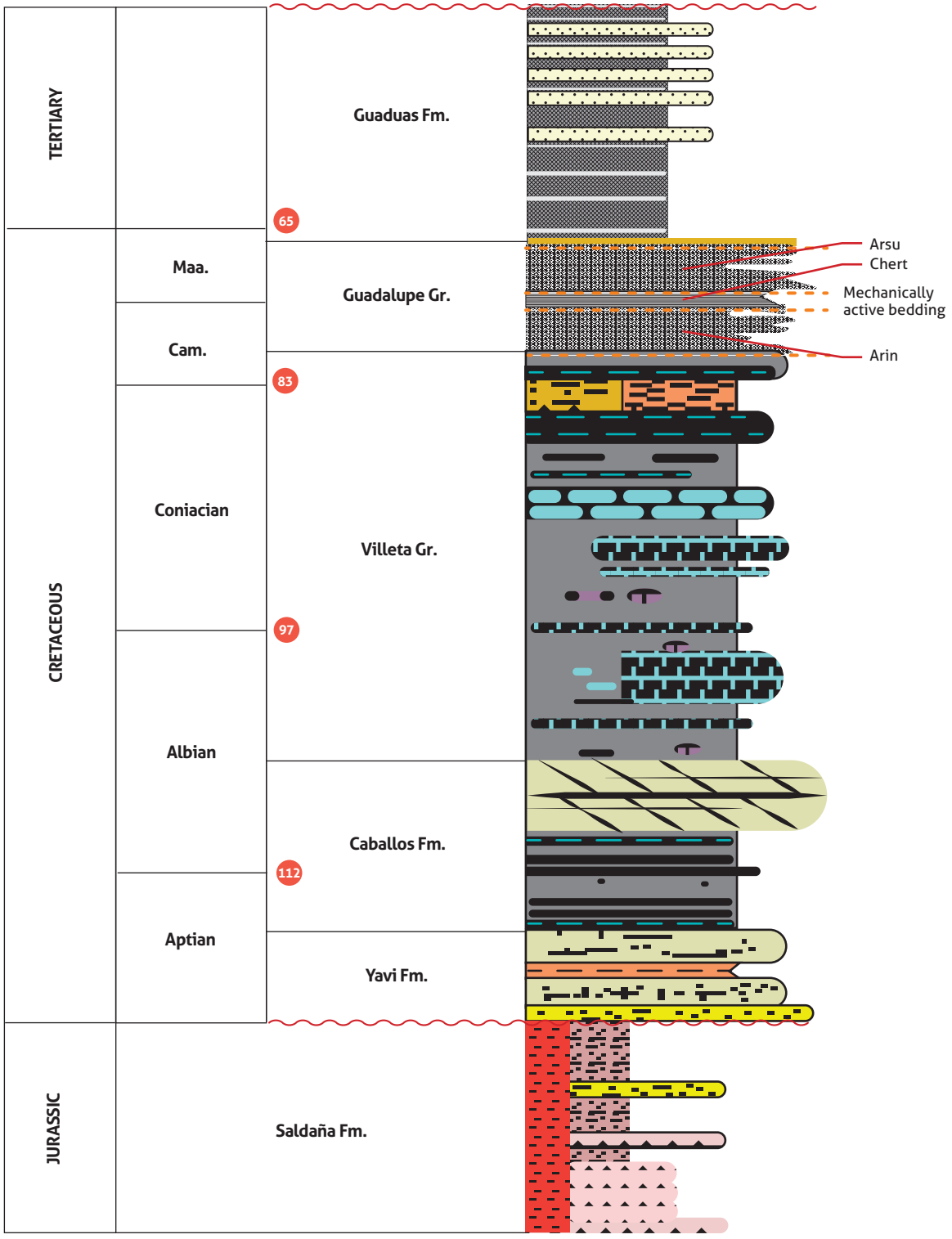

Figure 3. Generalized stratigraphic column of VSM, related to the oil system of the Matachines field

areas neighboring or on the western and eastern margins of the Cordillera Central. The continental sediments of the Gualanday Group were deposited from the late Eocene until the late Oligocene. The Incaic phase, the "Early Andean event" (De Freitas et al., 2006), is identified in the Balcón area by Cenomanian horizon flattening (top of the Bambucá Formation) in seismic interpretation, where the angular discordance postdates the most intense deformation pulse of the area. This event is widely distributed in VSM and has been partly obliterated by the most modern Andean tectonic phases. Despite generating controversy, the age of this discordance is most often attributed to the Middle Eocene (*e.g.*, Schamel, 1991; Cooper et al., 1995; George et al., 1997). However, De Freitas et al. (2006), in line with Buitrago (1994), consider that this discordance is younger, with an Oligocene age in the Neiva subbasin because it is immediately superimposed by the Barzalosa Formation (late Oligocene to early Miocene) by the basal section of the Honda Group, attributed to the middle Miocene (Guerrero, 2002). The configuration produced during this phase persists until the late Miocene, when the oil generation peaks, and is thus a key controlling factor of hydrocarbon entrapment (Higuera, 2012).

3.4 Quechua phase (last stage of compressional-transpressional inversion)

Between the late Miocene and the present Quechua phase of Andean orogeny (Cobbold et al., 2007), the deformation and uplift of the Cordillera Oriental led to another compression period, with new thrust faults with westward vergence, which correspond to the Boquerón fault system, and subsequent deposition of continental sediments of the Honda Formation. The Quechua phase, or the "Andean" event of De Freitas et al. (2006), caused the main uplifts of the region, including those of the Cordillera Oriental, which through thrust faults such as the Garzón fault superimpose these mountain ranges on VSM and produce the exhumation of Jurassic rocks exceeding 8,000 feet. In the Neiva region, an ENE–WSW compression is suggested by numerous folds, whose axes are arranged perpendicularly, preferentially in the WSW direction. This deformation succeeded the deposits of the Honda Formation, dated to the middle Miocene (Guerrero, 2002). Similarly, a discordance is observed at the base of the Gigante (or Mesa) Formation, which was presumably formed between the late Miocene and the Pliocene and which is gently uplifted in the eastern flank of the basin (De Freitas and Vallejo, 2000). During the Pliocene, strike-slip faults developed along the NW–SE direction, involving the basement and displacing the axes of the folds and of the main faults, due to differential movements of large blocks. Later, from the middle Tertiary, the VSM basin became a marginal foreland basin with continental deposits of the Gualanday Group and Barzalosa Formation, and finally, from the late Tertiary to the present, it became an intermountain basin with the deposits of the Honda Formation (Barrero et al., 2007).

The Neiva and Girardot subbasins of VSM are structural depocenters of the late Cenozoic staggered between the Columbian Cordillera Central and Oriental, which contain three main depositional sequences up to 9,000 m thick on a Paleozoic crystalline basement, which are summarized as follows: 1) Triassic to Jurassic nonmarine siliciclastic rocks and underlying carbonate sequences; 2) Middle Cretaceous to Paleogene marine to nonmarine clastic and carbonate sequences; and 3) a Neogene potent nonmarine molasse-like sequence. According to Beltrán and Gallo (1979), to Buitrago (1994) and to Higuera (2012), the sandstones of the Guadalupe Group (Campanian-Maastrichtian) were deposited in a marine environment from the shallow shelf through the continental shelves to marine-influenced coastal shelves (Figure 3).

The Guadalupe formation contains the main productive reservoirs with petrophysical characteristics, according to observations of outcrops and core samples available in and collected from the various exploration and production wells. These make it possible to differentiate an Upper Guadalupe or "Arup" alloformation (upper sandstones) and a Lower Guadalupe or "Arlo" alloformation (lower sandstones), separate from the Middle Guadalupe or "chert" alloformation (Figure 4).

The pelites of the Villeta Group (late Albian to Santonian) are the main hydrocarbon-generating rocks, and the oil extracted from the fields may come from generation areas located in the nearest synclines or from the vertically deepest areas of production structures (Barrero et al., 2007; Higuera, 2012).

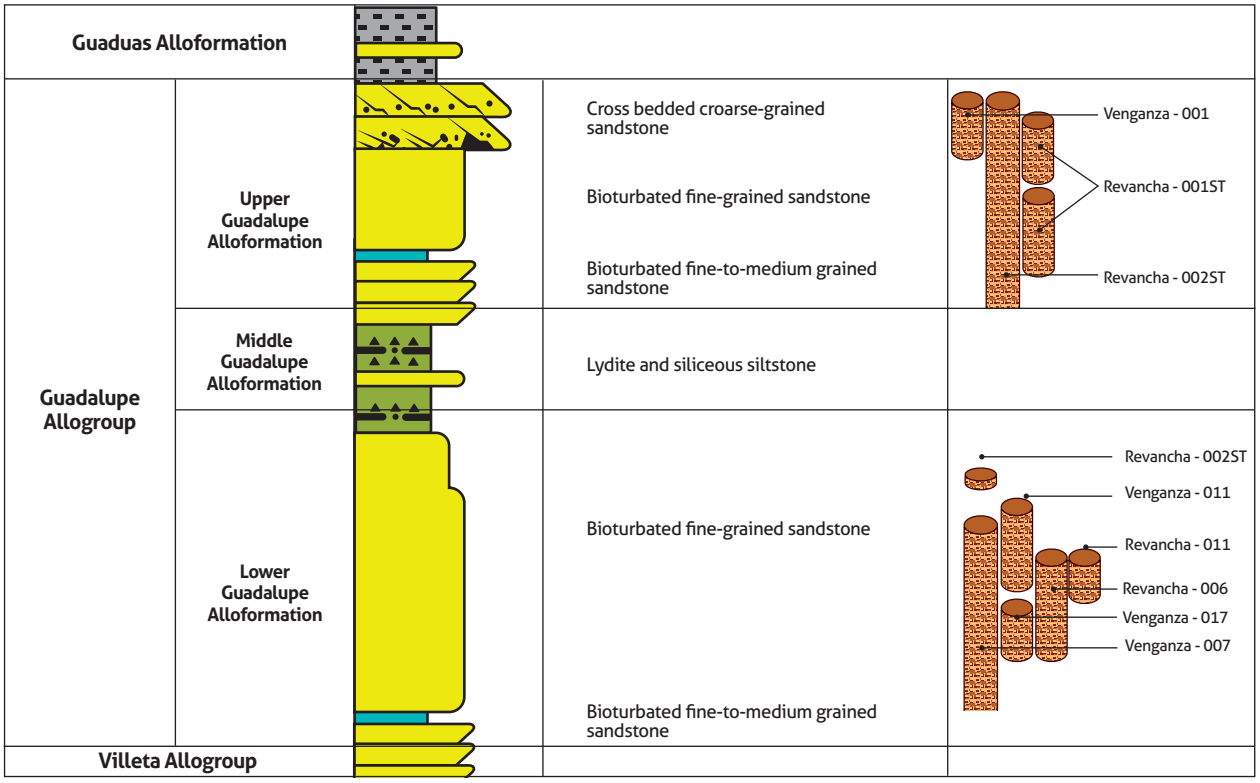

Figure 4. Petrophysical characteristics of the Guadalupe Allogroup, based on outcrop data and core samples

4. Structural Observations of the Matachines Field

The Matachines field is located immediately west of the southern end of the Prado syncline and west of the prominent reliefs of the Guadalupe Formation (Figure 5).

The main hydrocarbon production zone is associated with horizons of the Guadalupe Formation, consisting of structural traps with effective closures located in the hinge area of an asymmetric anticline (with a flatter western flank and a steeper eastern flank) and with a N–S axis, gently dipping towards both ends. The Venganza fault is arranged immediately above the hydrocarbon production zone, differentially bisecting the upper flanks, so that the upper ranges of the Guadalupe Formation (Arup) are partly absent in the eastern section (Figure 6).

A plan view of the Matachines field shows the asymmetric anticline that generates this field, with a steeper eastern flank than western flank. The South Matachines Field is not a simple structural continuation of the North Matachines Field and is related to the gradual change in subsidence of the Vengeance fault plane, to the southward tilt of the reservoir layers and to the presence of structural imbrications (Saavedra, 2013). The westward change in direction of the South Matachines Field in relation to the North Matachines Field results from the action of a structural transfer in the sinistral transverse direction (intra-Matachines transverse zone) to the main fold structure (Figure 7).

In a sublatitudinal section, a differentially eroded asymmetric fold affected by compressional faulting is identified, showing a two-scale model based on the South Matachines Field (Figure 8).

Secondary reverse faults increase the structural complexity of the area of interest in such a way that the Guadalupe Formation is repeated in structural units, as found in well REV 09; thus, other reservoir horizons most likely exist in the area. Based on the interpretation of the well logs, the Guadalupe Formation would have been affected by the second detachment and saturated with oil in the REV 01 well. From a morphological standpoint, the hydrocarbon-producing horizons of the Guadalupe For-

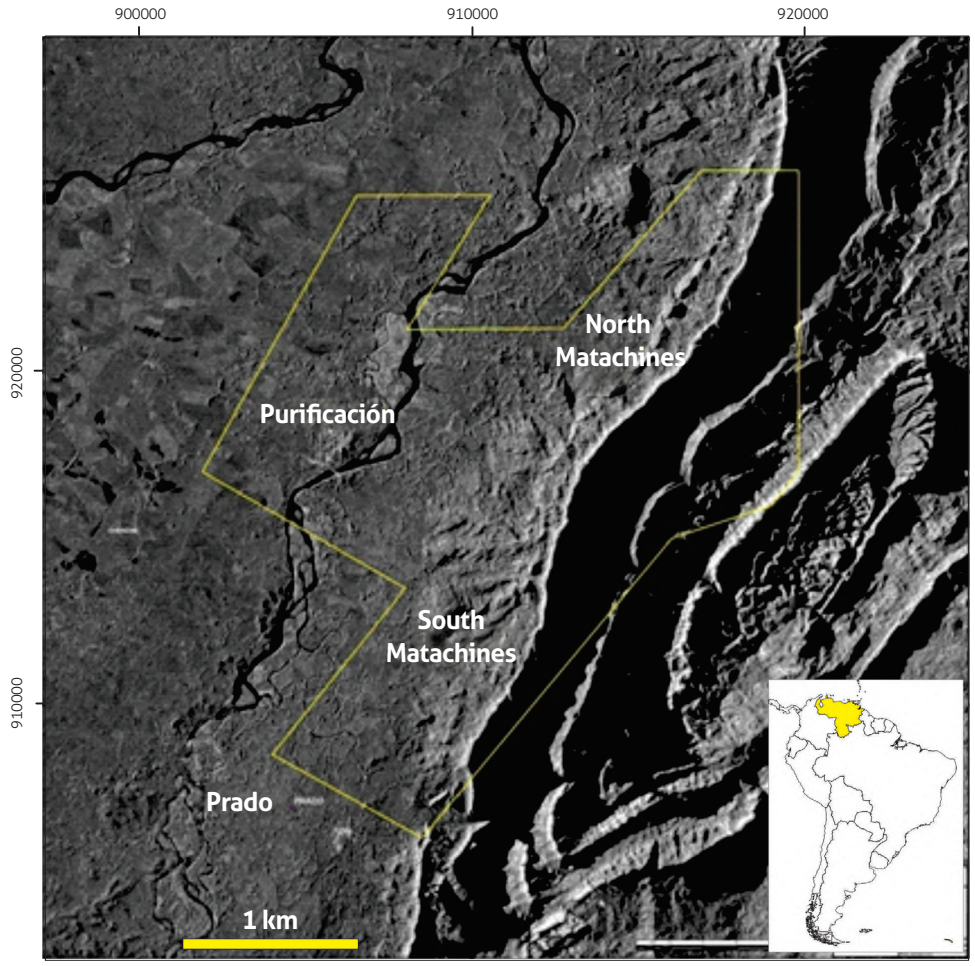

Figure 5. Digital topographic map of the South and North Matachines Field and Purificación, located between the Prado syncline and the Magdalena River

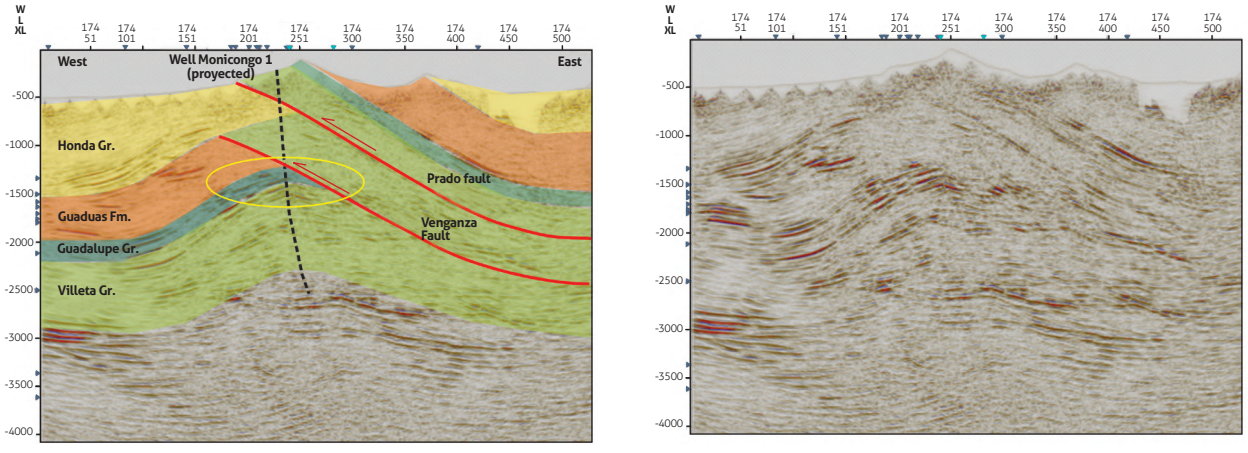

Figure 6. Characteristic sublatitudinal seismic cross-section of a Matachines field. Extracted from a project in WorkStation in which the main structural characteristics were represented (for the location, see Figure 4)

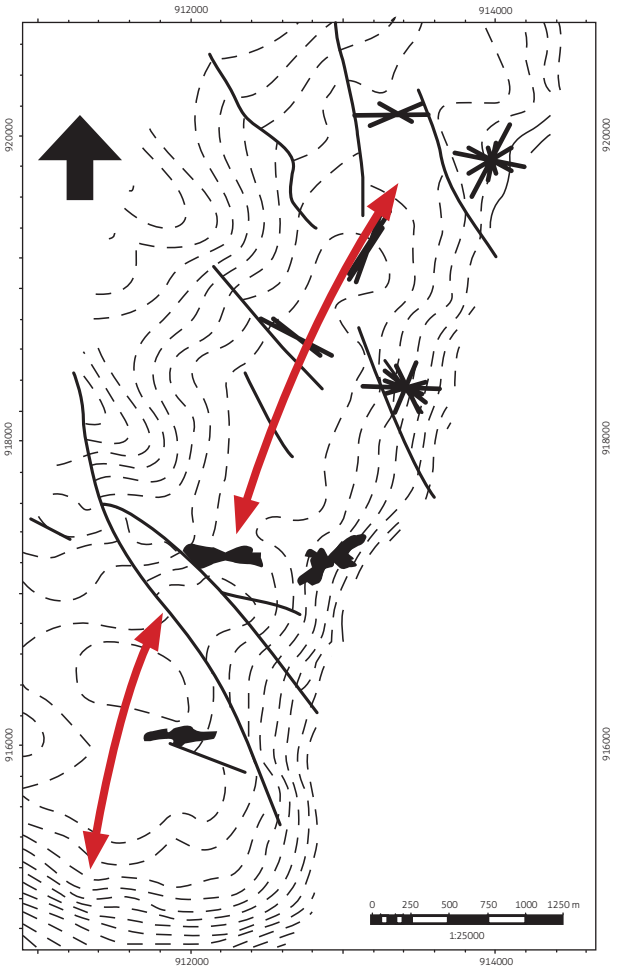

Figure 7. Plan-view map of the Venganza fault structure showing the distribution of the fractures based on well log data

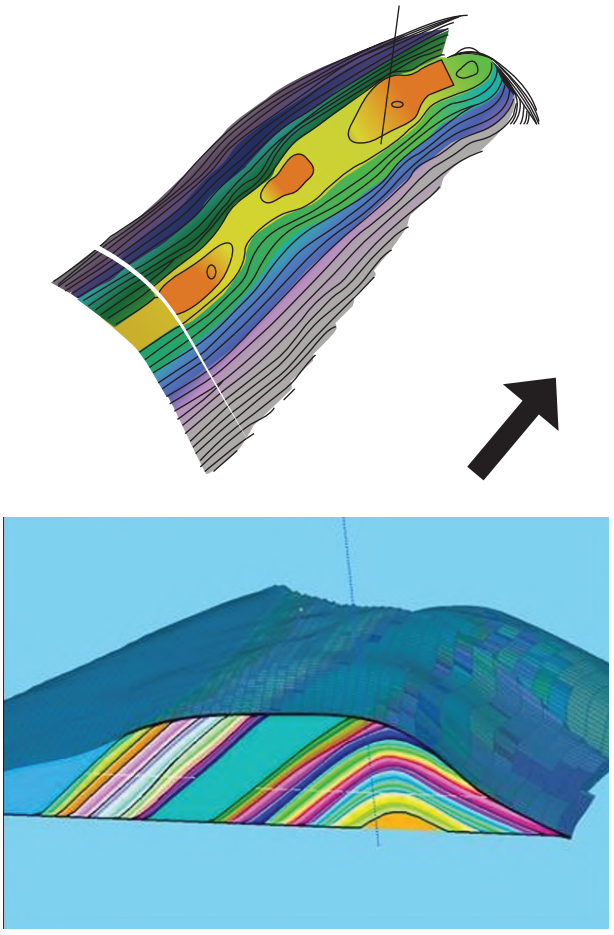

Figure 8. Hydrocarbon-producing horizons of the Guadalupe Formation partly truncated by the Paleocene discordance of the basement of the Gualanday Formation and intersected by the thrust fault Revancha (blue surface), which overlaps Mesozoic sequences (example of the VEN 7 well)

mation are discontinuous due to the truncation of the Paleocene discordance. These horizons are intact in the western flank, but only the lower Guadalupe Formation (Arlo) horizons are preserved in the eastern flank.

According to the available GPS data on the tectonic movement (Tremkamp et al., 2002; Acosta et al., 2004), the current horizontal maximum principal stress field is arranged sublatitudinally due to the sublatitudinal convergence between the Nazca and South America plates, albeit with variable rates and directions. The maximum horizontal principal effort is oblique to the Caribbean margin, indicating a dextral transpressional component, highlighting dextral strike-slip components in the faults of the NE–SW quadrant and sinistral strike-slip components in the faults of the NW–SE quadrant.

The overlap pattern of the Honda Formation across the discordance and the direction of its layers indicates a clockwise rotation of the compressive stress, now oriented in the NW–SE direction, which would have caused an uplift of approximately 2,500 feet from an intra-Honda Formation reference level (De Freitas et al., 2006). Fault kinematics data collected south of the Balcón area corroborate this direction of transportation (Blanco and de Freitas, 2003).

5. Naturally Fractured Reservoirs

Based on the fracture evidence, the Guadalupe Formation reservoirs can be characterized as "naturally fractured" reservoirs because their timely and persistent fractures may also help to accumulate hydrocarbons. Formation micro-imaging (FMI) and petrographic analyses of limestones of the Villeta Group in the Monicongo-1 well suggest the presence of a good reservoir. In addition, despite the low density of these fractures, their aperture (considering Aguilera, 2001) suffices to reach a permeability higher than 1,000 mD.

As the Guadalupe Formation does not adequately outcrop in the Matachines field sectors, to acquire microtectonic data, surveys were conducted near the access road to the Prado dam, where the wide and clear artificial cut made it possible to perform semiquantitative observations (Figure 9).

The outcrops show fractures that, depending on the granulometric characteristics of the horizons of the affected Guadalupe Formation, develop differential spacing and magnitude patterns (Figure 10 and Figure 11).

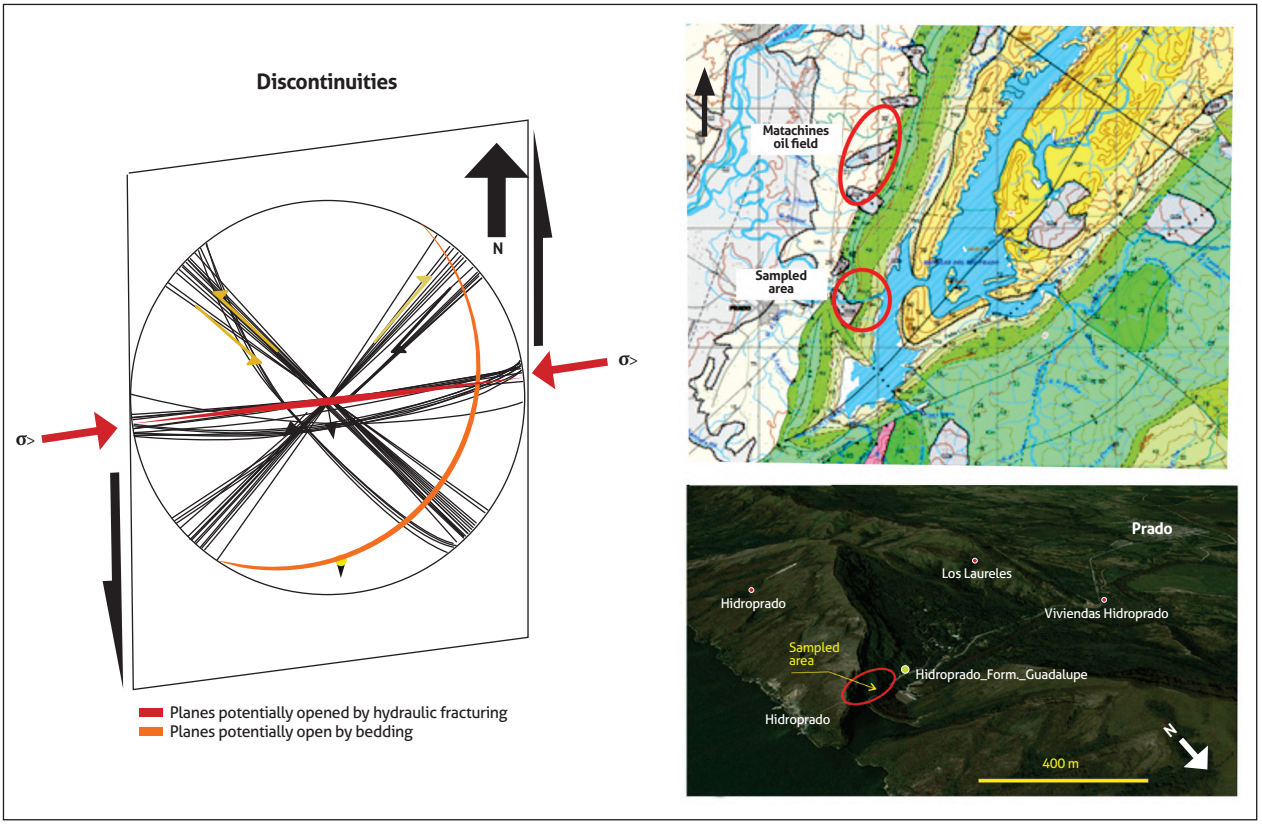

Figure 9. Diagram of fractures surveyed on the access road to the Prado dam. Interpretation of planes potentially opened by hydraulic fracturing and by bedding on the access road to the Prado dam correlated with the Matachines fields (geological map retrieved from Cossio et al., 1995)

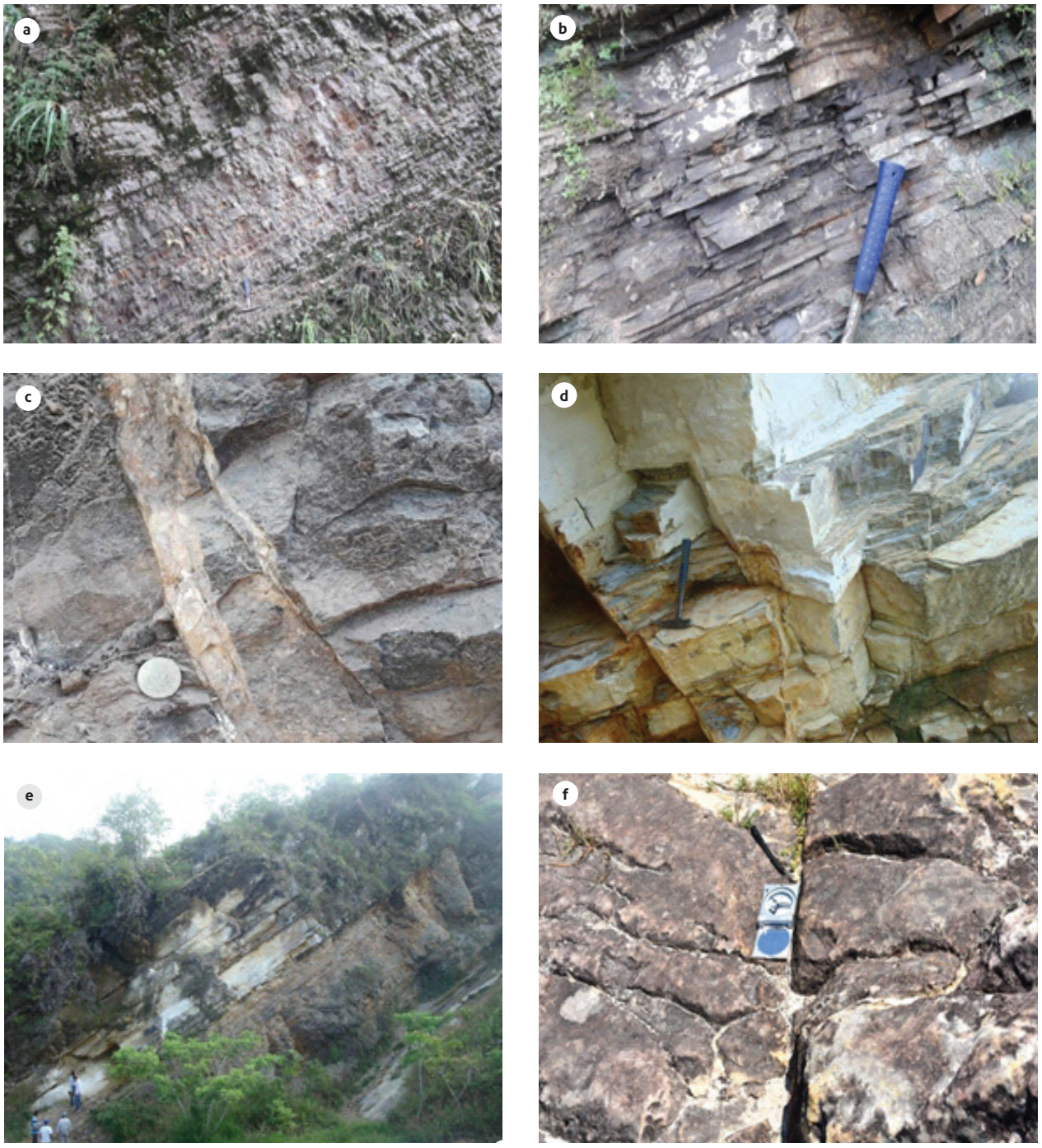

Figure 10. Photographs of the Guadalupe Formation. a) Detail of pelite sequences on the access road to the Prado dam. b) Detail of sequences of fine sandstones on the access road to the Prado dam. c) Detail of subvertical fractures filled with carbonates, arranged sublatitudinally. d) Detail of discordant and concordant fractures with sandstone bedding (chert) on the access roadcut to the Prado dam. e) View of the sequences tilted eastward on the road between Melgar and Icononzo. f) Detail of E–W fractures in the Guadalupe Formation (Arup), on the top of the mountain range of the Tres Mesetas camp

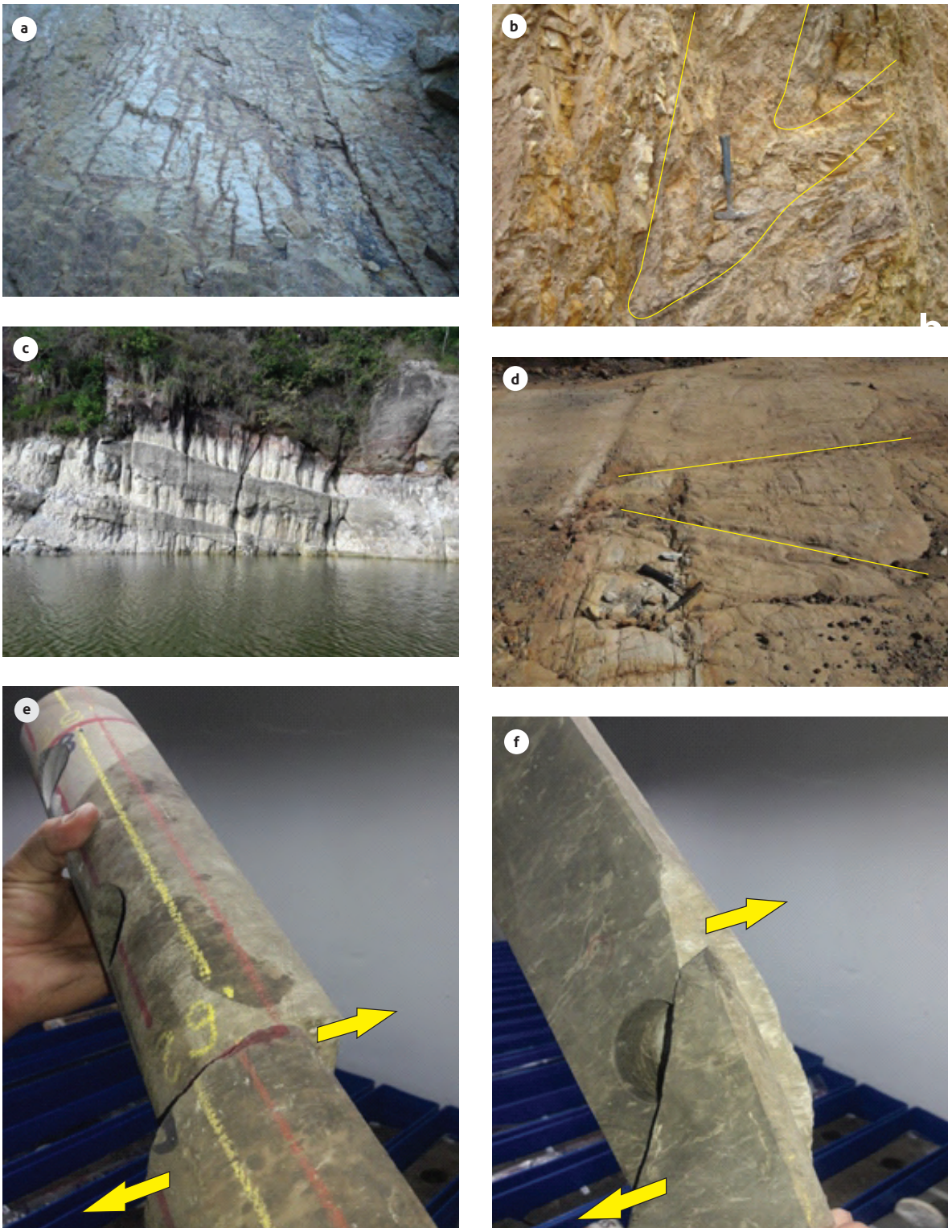

Figure 11. Photographs: a) fractures in sandstone strata of the Guadalupe Formation on a quarry stone road between Guando and Icononzo. b) Folds in pelite horizons of the Guadalupe Formation on the pass of the Melgar-Icononzo route. c) Fractures located in Tertiary sandstone horizons in the Prado reservoir. d) Fractures of the Caballos Formation, on the road to Tomogó. e) Dextral strike-slip fault in a REV1-ST1 well core sample; a 38° plunge in the 107° azimuth direction in layers of the Guadalupe Formation, with bedding at a 34°-35° angle in the 274-284° azimuth direction, approximately located by 3D analysis. f) Subvertical Dextral strike-slip fault with a N–S axis in a REV1-ST1 well core sample, approximately located by 3D analysis

6. Results

Bedding surfaces are mechanically active planes that can considerably enhance the flexural slip produced by the folding of multilithologic sequences (Jamison, 1997). In the Matachines field, bedding also improves the petrophysical characteristics of its reservoirs by incorporating a significant number of discontinuities, thereby complementing fluid connectivity from subhorizontal positions through planes of subvertical fractures generated by the horizontal compressional stresses, which are preferentially arranged in the ENE–WSW direction. In particular, these effects are magnified on the western flank of the anticline structure and to a large extent participate in the connectivity of production wells (Figure 12).

The images of the available wells of fine sand horizons, in light-gray colors, with rhythmic laminations with bioturbations, show microfractures concurrent with postsedimentary structures, which were used by subsequent faults. Thus, for example, one of the main characteristics of fractures interpreted in the VEN-40 well is that they are conductive, preferentially with an axis along the E–W direction and rarely in the NE–SW direction. The highest fracture density, accounting for 67% of the total data (722), ranges from 0 to 1.6 fractures per foot, distributed between hydrocarbon-producing horizons (Arlo-2, Arlo-3, and Arlo-4). In the other 23 % of the data, fracture density ranges from 2 to 3 fractures per foot. The microfractures have planes with E–W and NNE–SSW directions, on average, and are preferentially located on an upper chert (from 6,970 to 7,021' MD), at a 60° angle (to the axis of the well) and with angles of inclination ranging from 70° to 90°. The main characteristic of the fractures interpreted in the VEN-15 well is that they are conductive, with an axis preferentially in the E–W direction and with rare NE–SW fractures (Figure 13).

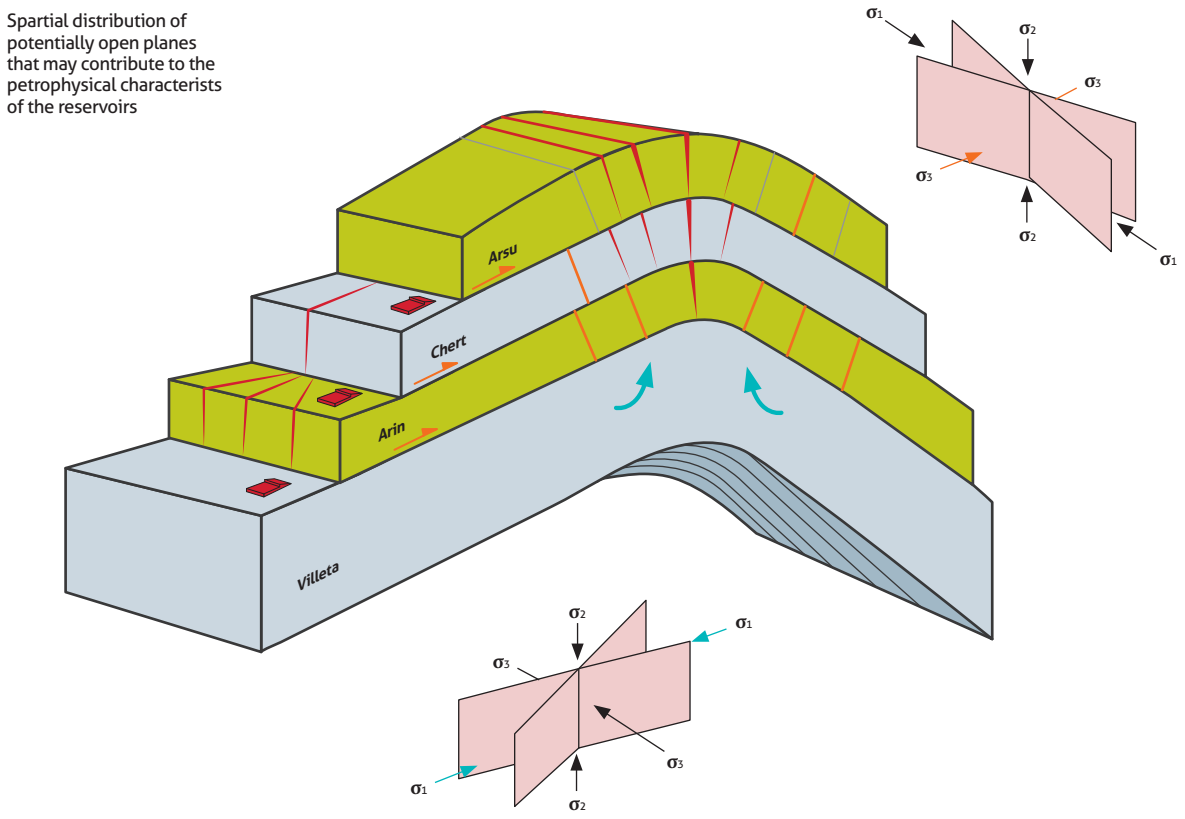

Figure 12. Idealized diagram of the planes potentially responsible for improving the petrophysical quality of unconventional reservoirs

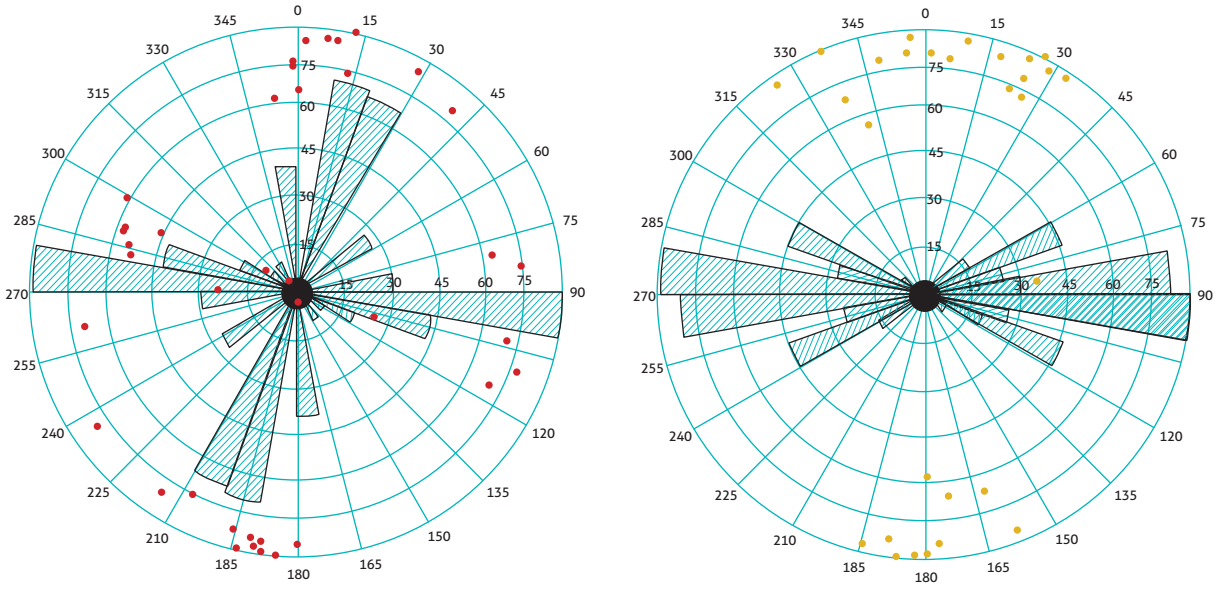

Figure 13. Examples of fracture diagrams. *Left*: Pozo VEN-40 Arup, microfaults 5440-6084' MD. *Right*: Pozo VEN-15 Arlo, conductive fractures 5496-5760' MD

The apertures of some fractures were also measured in core samples with simple techniques such as by using gauges. Most apertures were smaller than 2 mm, and most values were approximately 1 mm or less (Figure 14).

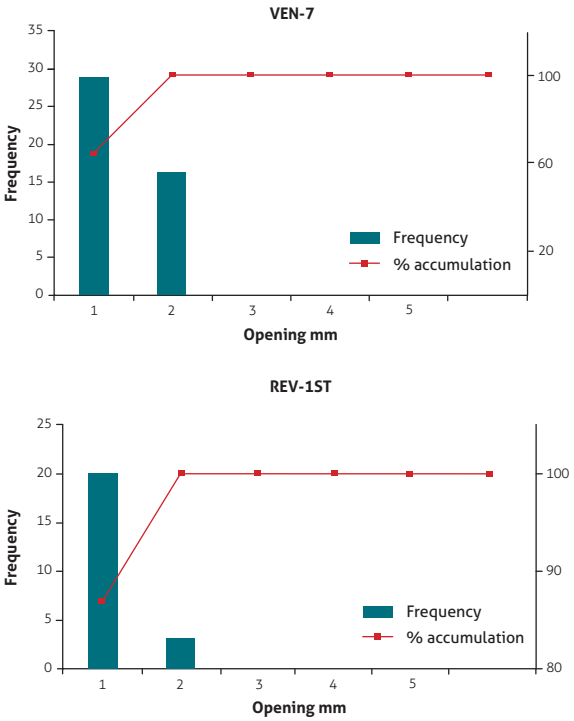

MD	VEN-7	ARIN 3	
	#FRAC Natu	Observations	Opening mm
5321	1	Subhorizontal	2
5320	1	30°	1
5319	0		
5318	0		
5317	0		
5316	1	30°	1
5315	0		
5314	2	1. Parallel to bedding 2. 20-25°	2
5313	1	30°	1
5312	2	30°	1
5309	2	1. Parallel to bedding 2. 20-25°	2
5308	1	30°	2
5307	1	Subhorizontal	1
5306	1	Parallel to bedding	2
5305	1	30°	1
5303	3	30° Conjugated	1
5302	1	Parallel to bedding	2
5300	2	1. Parallel to bedding 2. 20-25°	1

MD	REV-1ST	ARSU 2-3	
	#FRAC Natu	Observations	Opening mm
5683	1	Subhorizontal	2
5680	1	Subhorizontal	2
5673	0	1 vein subvertical	
5668	0	1 vein subvertical	
5667	0	Carbonaceous nodule (no HC)	
5666	1	Subvertical (fault plane)	1
5665	0	Veins parallel to fractal	
5660	1	Subhorizontal close bedding	1
5659	1	Subhorizontal close bedding	1
5658	1	Subhorizontal cercar estratification	1
5656	1	Subhorizontal	1
5654	1	Subhorizontal	1
5653	1	Subhorizontal	1
5651	0	Subvertical veins in calcareous bedding 0.5'-1'	0.5'-1'
5650	1	Subhorizontal	2
5645	1	Subhorizontal	1
5644	1	Subhorizontal, veins	1
5643	0	Conjugated veins, 30-40°	

Figure 14. Graphs of the aperture of fractures in millimeters measured in core samples. *Top*: VEN-7 well. Total fractures: 45; parallel to the bedding: 13 (28 %). *Bottom*: REV-1ST well. Total fractures: 24; parallel to the bedding: 4 (17 %)

In the reservoirs that, in addition to their primary characteristics, are considered naturally fractured (Hennings et al., 2000), a correct 4D technical and economic evaluation of the quality and arrangement of discontinuities is essential to determine their actual contribution to improving the petrophysical properties of such reservoirs (Figure 15).

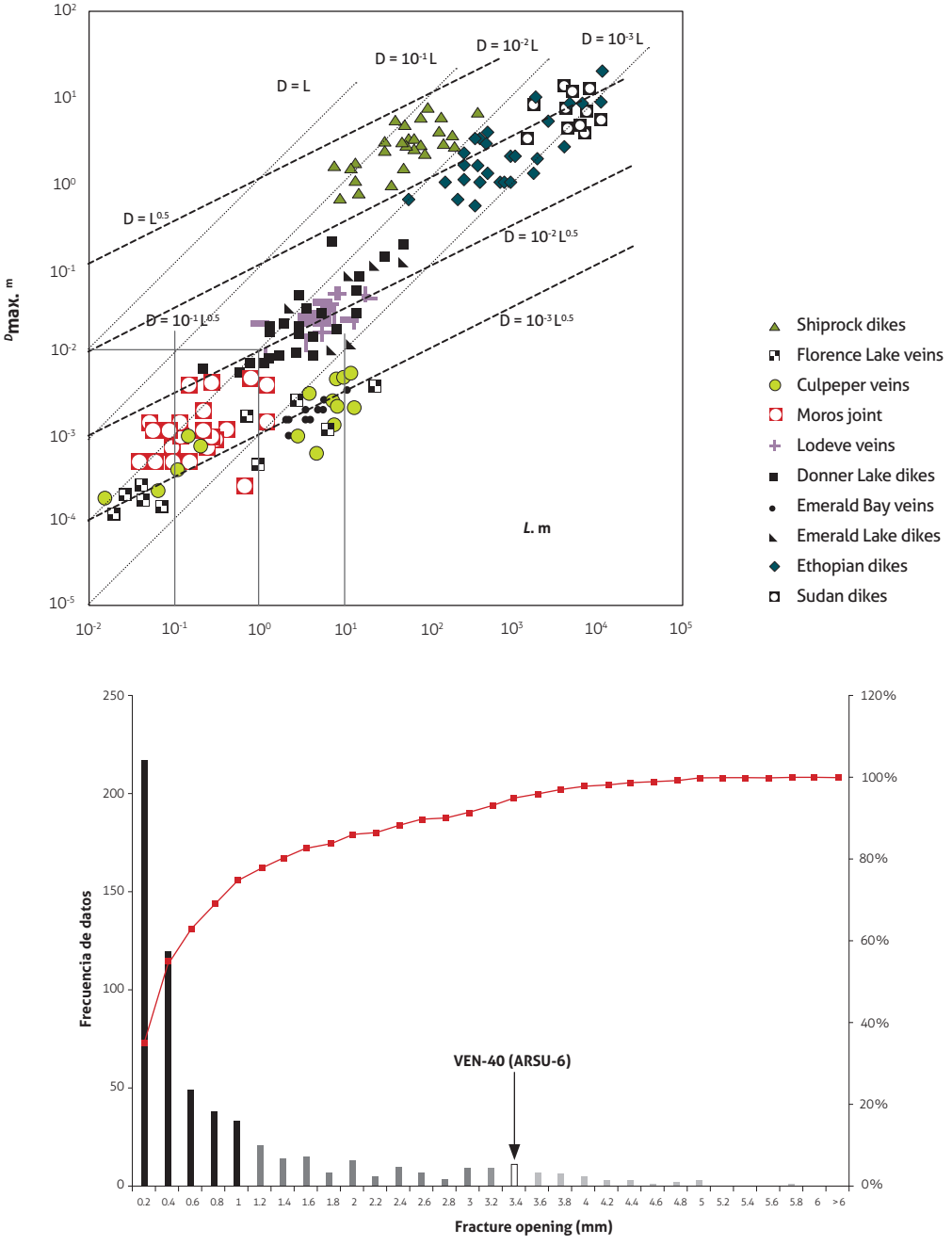

Figure 15. Fracture aperture in millimeters from BHI records
Left: compilation of D/L ratios of ten fracture aperture sets. Fracture length vs. fracture aperture as a function of n- 0.5 exponents. The dashed black lines represent square root functions. Gray dashed lines are linear functions (retrieved from Klimczak et al., 2009). *Right*: histogram of fracture aperture vs. frequency

The relationships between the permeabilities and porosities of hydrocarbon-producing horizons of the Guadalupe Formation in some wells derived from the South and North Matachines Fields show fairly regular behaviors, albeit with different dispersions, most likely due to the direction of the intersecting boreholes (Figure 16).

The relationships between porosity and horizontal permeability in core samples corresponding to the levels of the Arup and Arlo horizons in the VEN-1, VEN-17, REV-1ST, REV-2ST, and REV-6 wells of North and South Matachines clearly show that bedding-lamination produced mechanical boundaries that increased permeability (Figure 17).

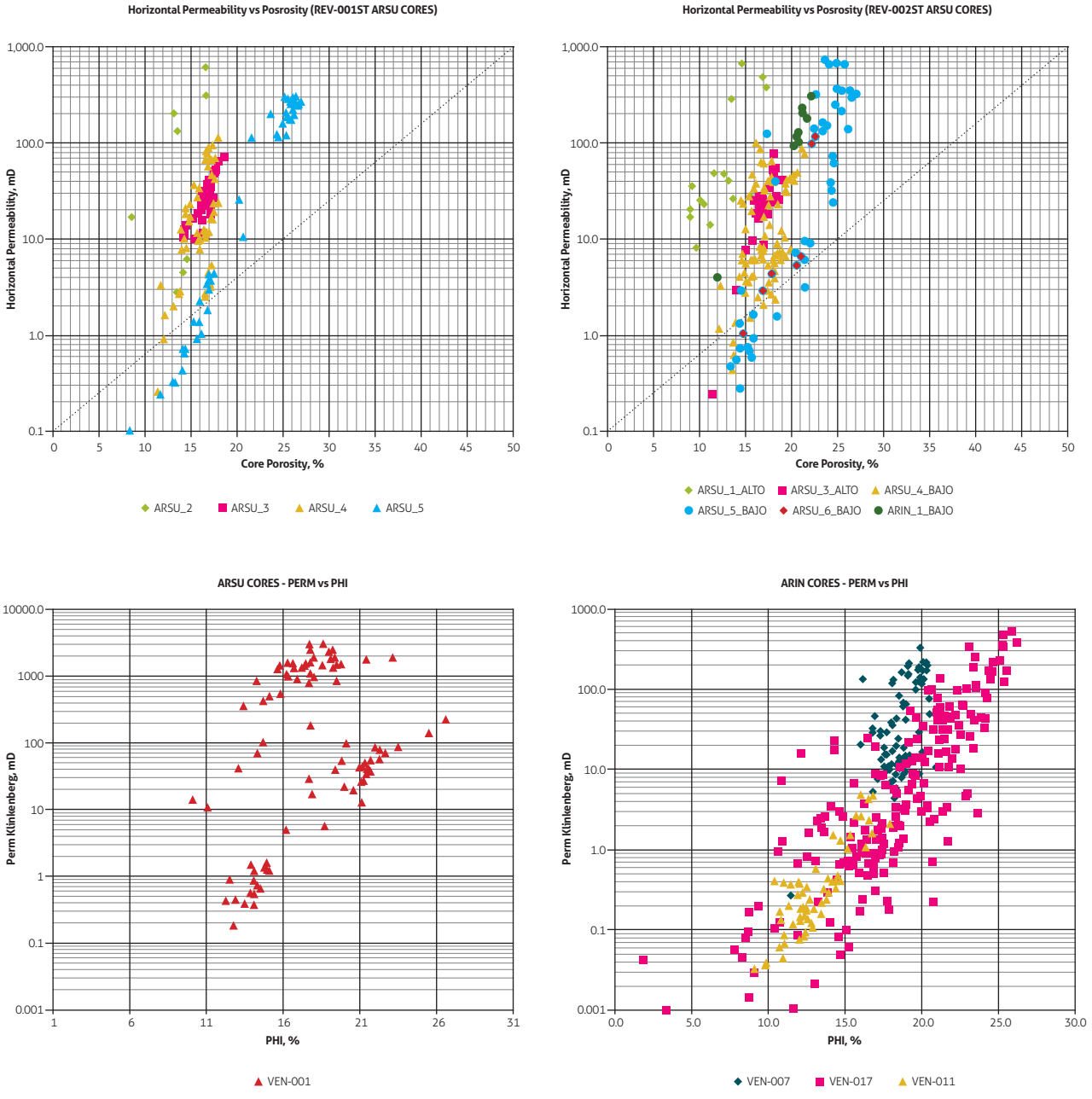

Figure 16. Graphs of relationships between porosity and permeability in core samples from wells
Top: Arup horizons in the South Matachines Field. *Bottom*: Arup and Arlo horizons in the North Matachines Field

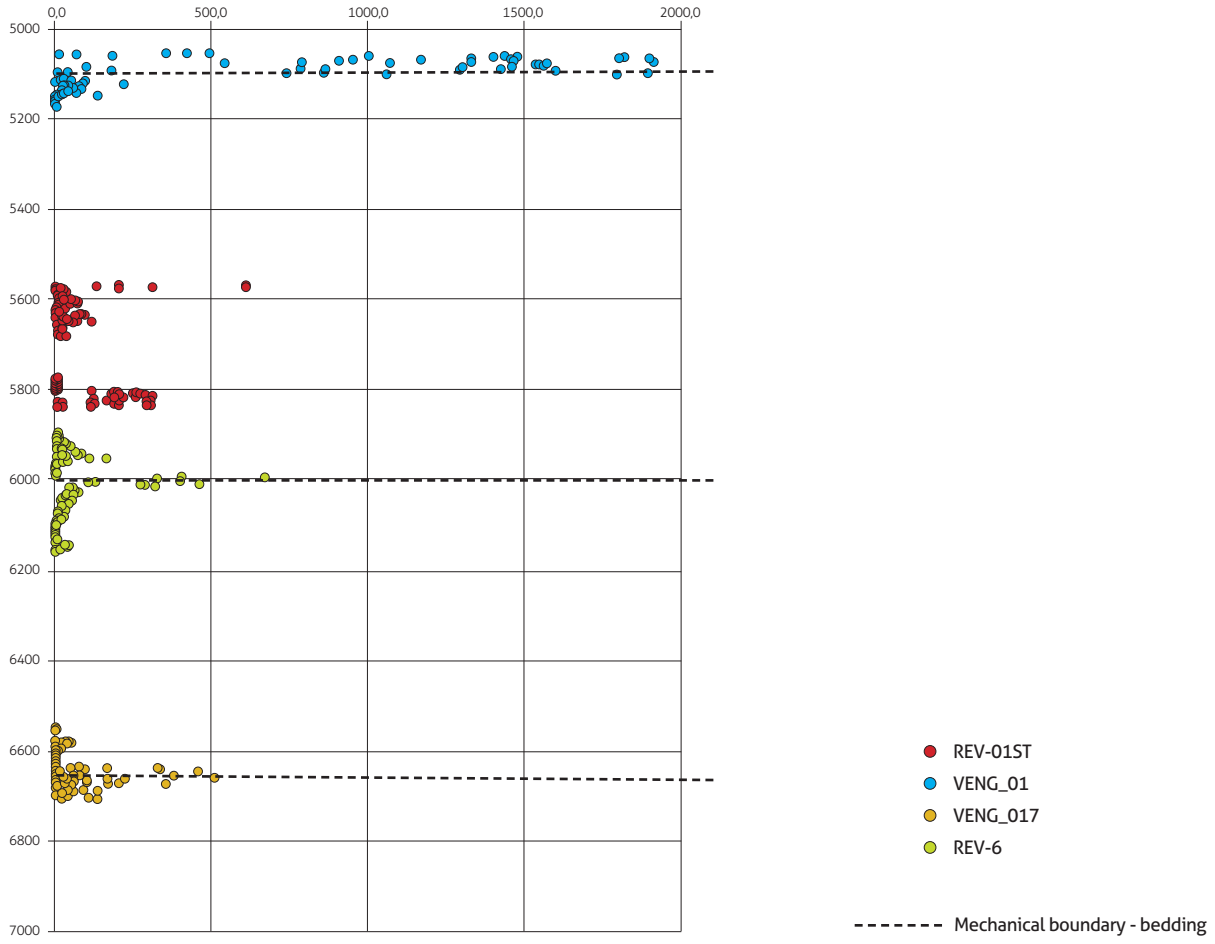

Figure 17. Relationship between core depth and permeability of hydrocarbon-producing horizons, wherein permeability increases at the mechanical boundaries between layers

Permeability was compared between vertical and horizontal wells, considering permeability data in hydrocarbon-producing horizons within stratigraphic units expressing mechanically active boundaries, showing that permeability is higher in horizontal wells than in vertical wells (Figure 18).

The greater permeability of horizontal wells should have been generated by their location in the top hinge section of the main structure of the field (Figure 12), which in turn has higher flexural slip folding and therefore higher permeability in the stratigraphic mechanical boundaries. For this reason, horizontal wells parallel to the bedding in the hinge areas are more likely to intersect dilating sectors with better porosity and secondary permeability characteristics. Furthermore, when they are located in the top sections of the hinges, the locally more extensional conditions favor their development.

Based on the morphostructural features identified in the surface and subsoil data, the Matachines fields shows a multiphase evolution, which may have been controlled, at least partly, by pre-existing Paleozoic anisotropies. The new structural interpretation on the geologic time scale shows a main fault in the WNW–ESE direction in the North Matachines field, which is consistent with the fracture data from the BHI analyses (Figure 19).

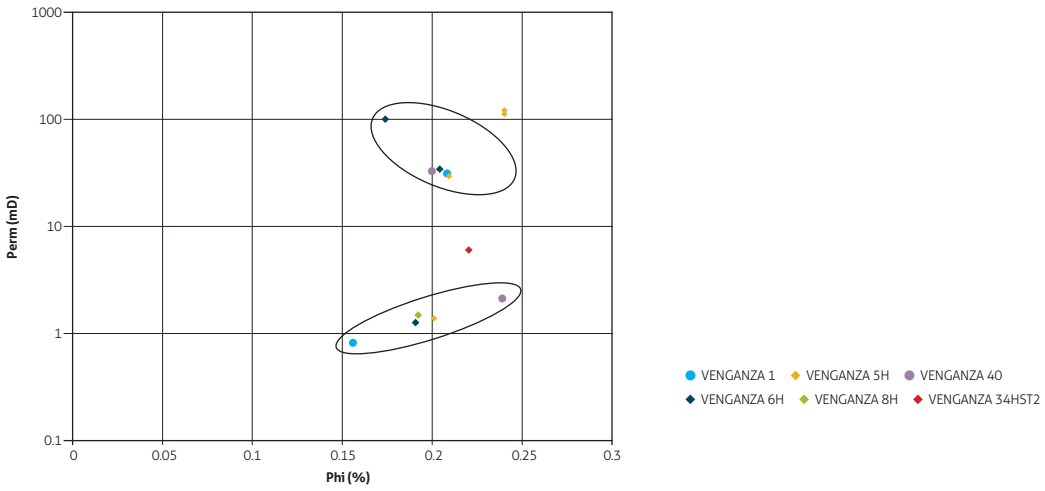

Figure 18. Comparative graph of the permeabilities of the same sands or stratigraphic units (mechanical boundaries) of vertical and horizontal wells

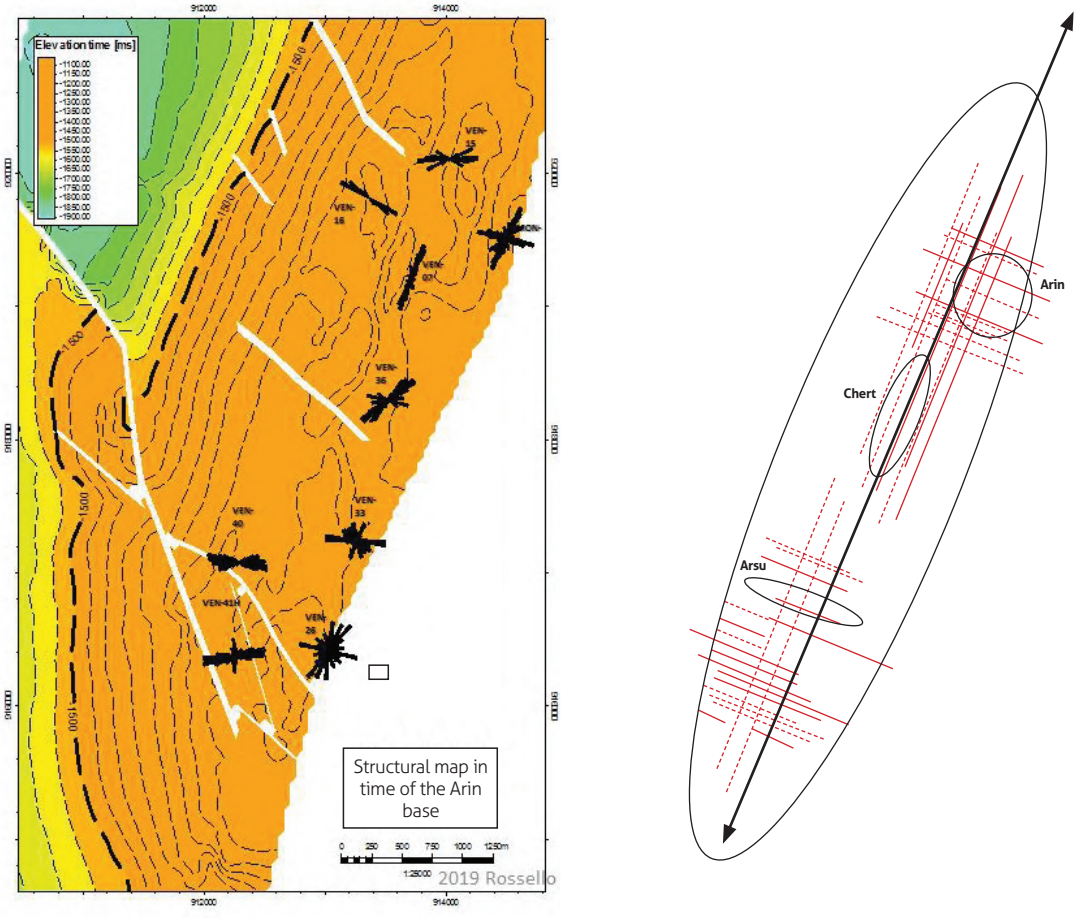

Figure 19. Plan view of the conceptual model of the permeability domains related to the interpreted fracture patterns. Areas with numerous fracture intersections highlight interconnected fracture patterns determining a likely circular drainage. Areas where fractures lack intersections show a more elliptical drainage pattern because they run parallel to the fractures

Accordingly, many commonly used methods for studying wells from core samples or images (Nelson, 1985; Nelson and Serra, 1995; Rider, 1986; Ortega and Marret, 2000; Laongsakul and Dürrast, 2011) identify different types of discordant fractures, but the bedding surfaces are evaluated separately, which does not statistically consider the petrophysical effects that contribute to porosity and permeability (Figure 20). Discontinuities due to bedding planes are highly important because they control the distribution of fluids running parallel to the main axis of folding.

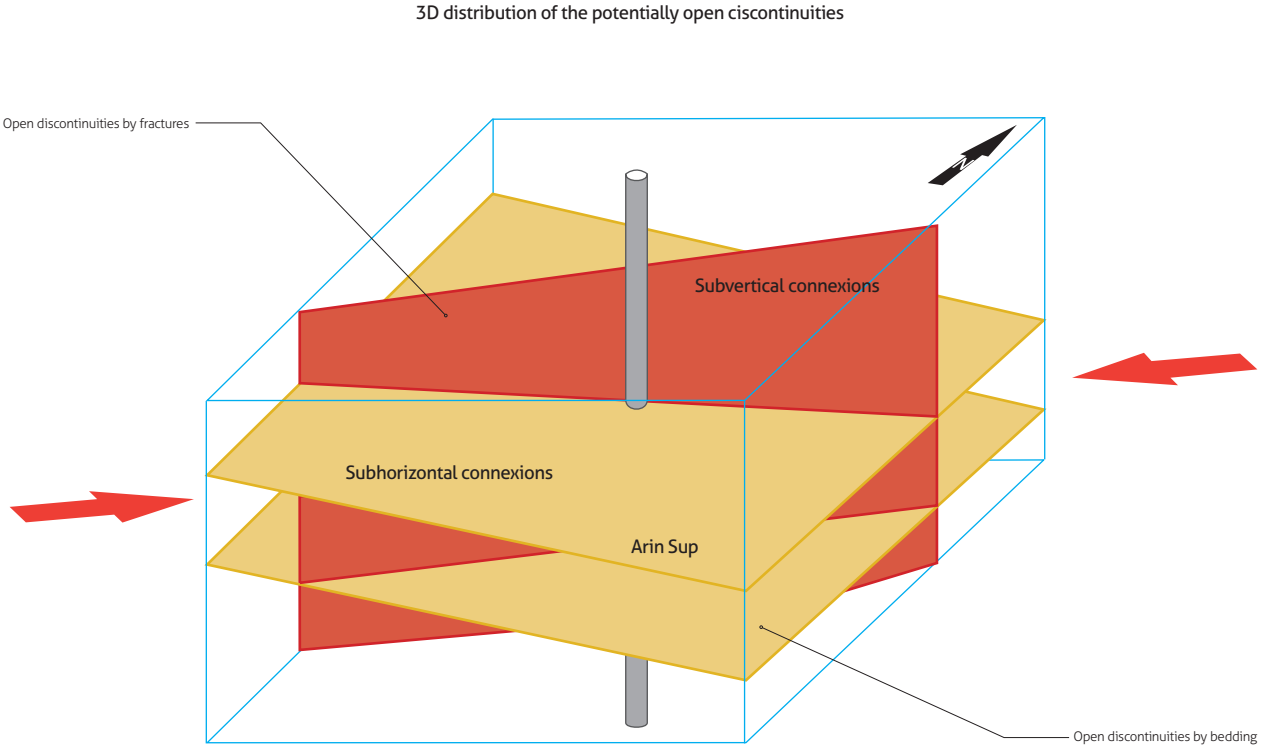

Figure 20. Idealized diagram of spatial relationships of subvertical fracture and bedding planes that contribute to fluid circulation in the Upper Arlo horizons of the Guadalupe Formation

7. Discussion

The action of a compressive stress field is responsible for the structural style of this basin, characterized by the successive action of the Incaic and Quechua phases between the Eocene and recent times, which started with the reactivation of the pre-existing normal fault planes during the distensive tectonics between the late Paleozoic and the early Cretaceous (Figure 21).

The tensional state produced by successive Andean tectonic phases has remained active for a long time, as shown by the differential deformation of sedimentary sequences, which was more intense in those deposited earlier because they have accumulated deformations from this stage to now (overlapping phases). Thus, these earlier (Cretaceous) horizons may exhibit a more pronounced clockwise rotation of fractures than those generated in the later (Neogene) sequences of the study area (Figure 22).

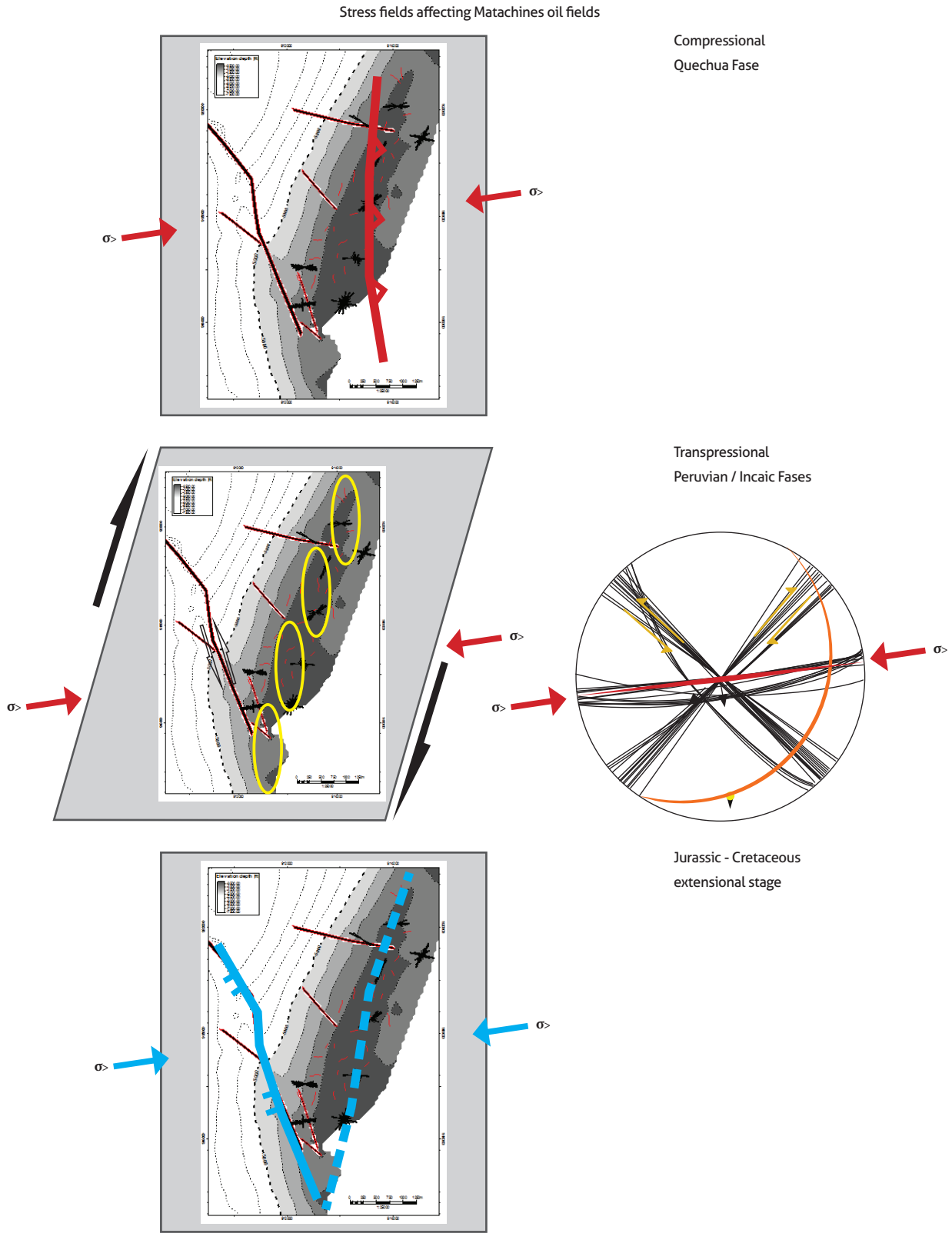

Figure 21. Evolutionary diagrams of the position of the active stress fields of the Jurassic–Cretaceous and Andean phases on the Matachines field

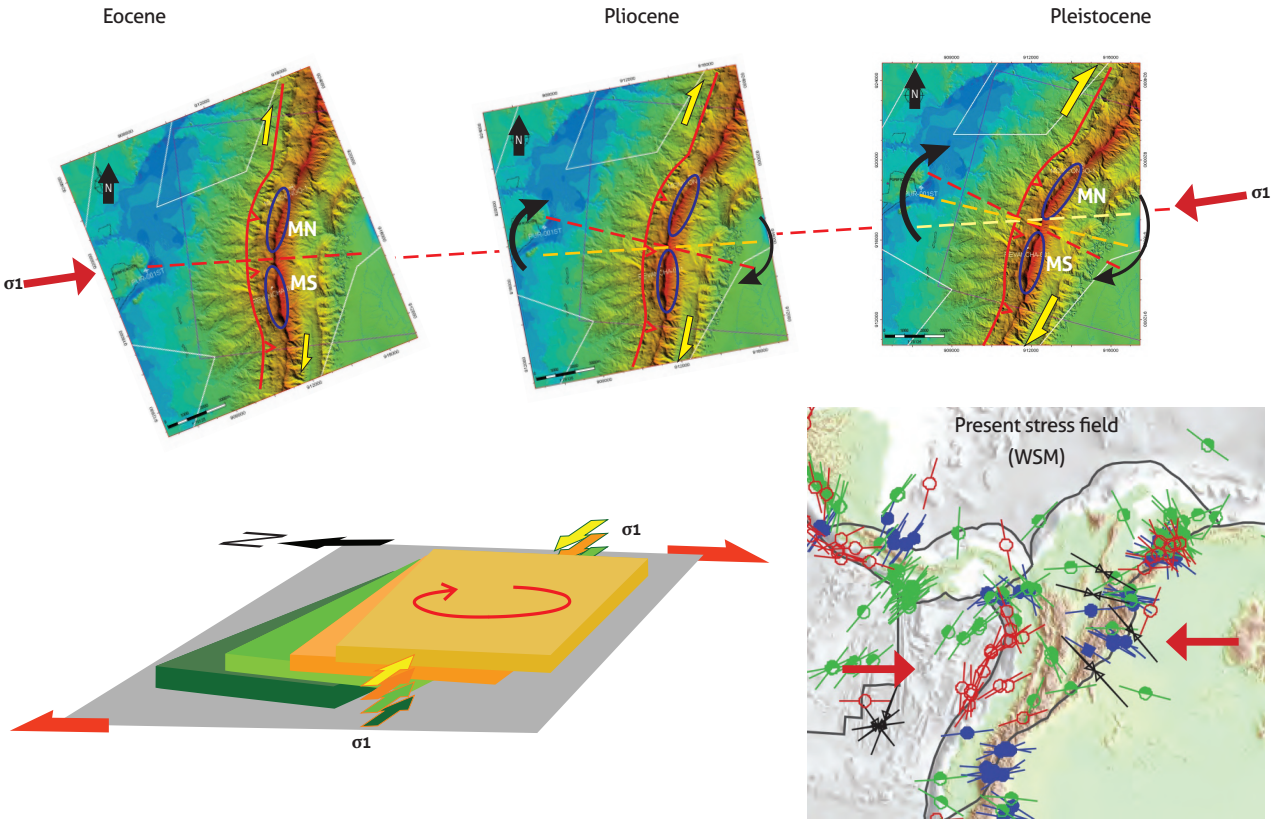

Figure 22. Evolutionary diagram of the invariable arrangement of the stress field during Andean tectonics and clockwise rotation of the study area. *Top*: three ideal states of the model with the invariant stress field (s_1). Red, the Prado faulting; dashed yellow line, the transfer zone that separates the Matachines fields, which are indicated by blue ellipses (MN and MS). Yellow arrows indicate dextral strike-slip components. *Bottom left*: rotational model whose older levels accumulate greater rotation. *Bottom right*: focal mechanism data (circles) retrieved from the World Stress Map indicating an approximately WSW–ENE direction of convergence (red arrows)

Thus, a simplified scheme highlights discontinuous tectonic features with warped surfaces, suggesting an increase in (clockwise or counterclockwise) rotation with depth (Figure 23). These sigmoidal warps, regardless of possible stress changes due to localized and variable effective geologic overpressures, would be based on the fact that sequences deposited earlier accumulate more rotational deformation than sequences deposited later within an invariant stress field in space throughout a contemporary span with all sequences involved (Rossello, 2018).

Due to the structuring characteristics of the Matachines field, the boreholes are concentrated in the NNW–SSE quadrant (subvertical fractures), mostly with a slightly plunging direction due to bedding surfaces, so it is more likely for there to be a higher number of potentially open fractures per linear meter of their trajectory in the reservoir horizons of the Guadalupe Formation (Figure 24).

CONCLUSIONS

In reservoirs with primary sedimentological characteristics that are considered naturally fractured, a correct 4D technical and economic evaluation of the quality and arrangement of discontinuities should include the effect of the bedding. Many commonly used methods for studying hydraulic fracturing from core samples or images identify bedding surfaces. However, the bedding surfaces, when evaluated separately, are not sufficiently accounted for in the petrophysical considerations that contribute to porosity and permeability.

The seismic data collected in a WorkStation and mounted on the Petrel platform make it possible to spa-

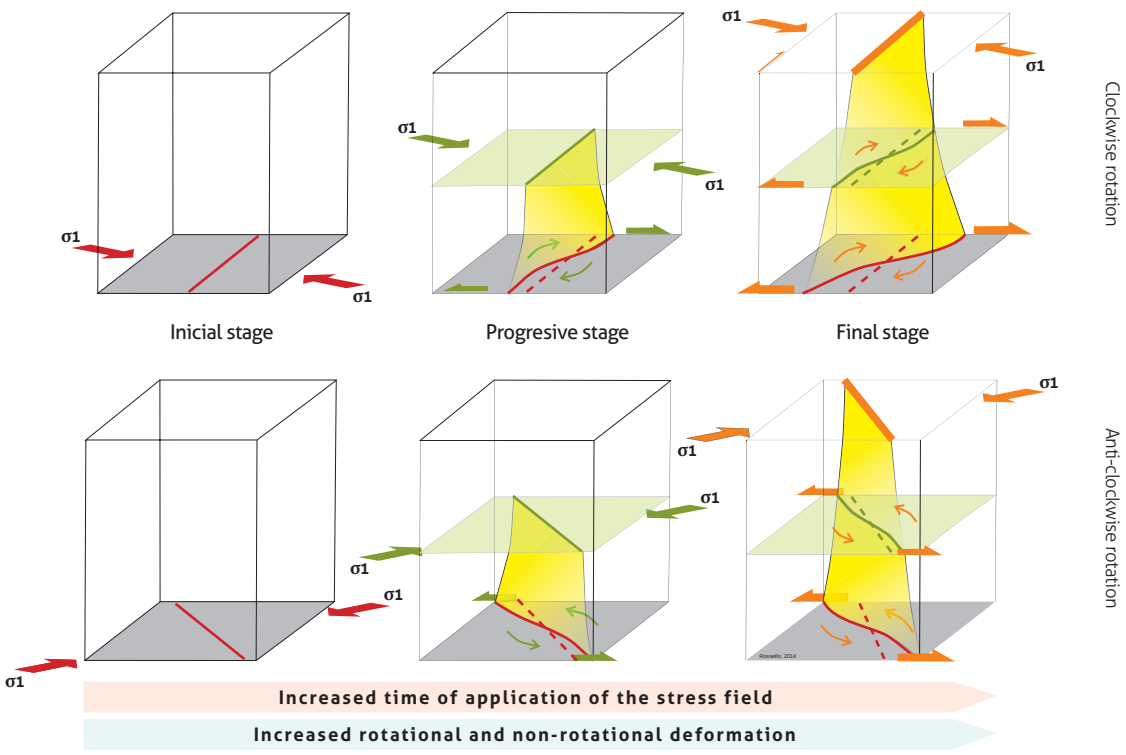

Figure 23. Evolutionary diagram of fault rotation as a function of depth within a long-term stress field. Earlier sequences exhibit greater rotations than later sequences, as a function of the time they remain in a syntectonic stress field (retrieved from Rossello, 2018)

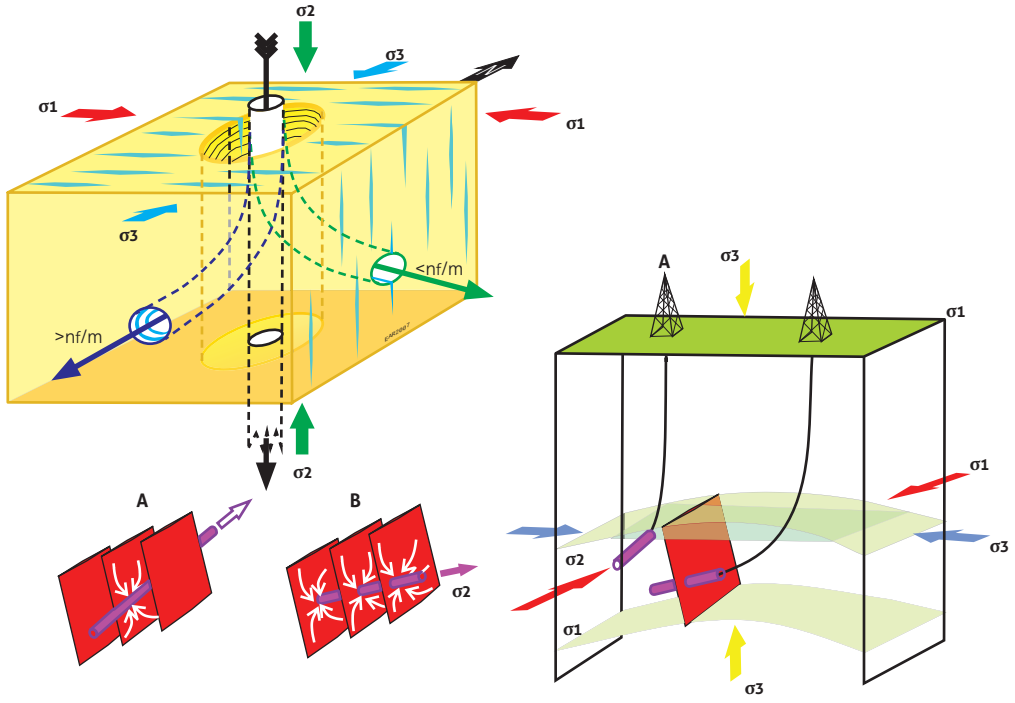

Figure 24. Schematic diagram of the preferential direction of a borehole with the highest likelihood of finding potentially open fractures along the borehole. The direction perpendicular to the dilating fractures corresponds to the minimum principal stress σ_3 (retrieved from Rossello, 2018)

tiotemporally characterize, with a mechanical criterion of deformation, a series of pre- and postdiscordance structures preceding the Honda Group. This tectonic context favors the development of deformations that tend to express clockwise rotations as a function of the time in this stress field. Thus, early generated structures have a higher clockwise rotation rate than structures generated later.

The NW–SE transverse zone that separates the two Matachines fields is considered a transfer zone resulting from an initially normal fault subjected to a sinistral strike-slip reactivation that has been timely and efficient to compartmentalize the oil system.

All the available tectosedimentary data on the Matachines field and on the spatial characteristics of the hydraulic fracturing assessed in the wells show that the evolution of the oil system is based on the following processes: 1) extensional tectonics, as shown by the normal growth of the faults that accommodated the deposition of the Lower Cretaceous sequences; 2) the transpressional deformation that occurred during the late Cretaceous, which reactivated pre-existing normal faults; 3) burial due to deposition and erosion from the Tertiary; and 4) the structuring that occurred during the Miocene, which caused the uplift of the area, and the resulting erosion and reactivation of previous structures. Therefore, the most important and efficient traps, in terms of timeliness, are those that formed during the late Cretaceous, before the maturation of the hydrocarbons.

Bedding surfaces are mechanically active planes that have enhanced the flexural slip produced by the folding of multilithological sequences. In the Matachines field, bedding improves the petrophysical characteristics of its reservoirs by incorporating a significant number of discontinuities, thereby complementing fluid connectivity from subhorizontal positions through planes of subvertical fractures generated by the horizontal compressional stresses preferentially arranged in the ENE–WSW direction. In particular, these effects are magnified on the western flank of the anticline structure and near its top hinge, resulting in their strong effect on the connectivity of production wells from their subhorizontal positions, with the action of subvertical fracture planes generated by the compressional efforts preferentially arranged in the ENE–WSW direction.

Acknowledgments

The colleagues at Hocol Petroleum Limited are thanked for their valuable discussions throughout this study, which helped us understand the technical and regional aspects of the Matachines field. The meticulous editorial work and thoughtful comments and suggestions from the anonymous referees greatly improved the clarity of this work.

References

Acosta, J., Lonergan, L., & Coward, M. P. (2004). Oblique transpression in the western thrust front of the Colombian Eastern Cordillera. *Journal of South American Earth Sciences*, 17 (3), 181-194. https://doi.org/10.1016/j.jsames.2004.06.002

Aguilera, R. (2001). *Naturally fractured reservoirs* (2nd ed.). Tulsa: Penn Well Publishing Company.

Aguilera, R., & Aguilera, R. (2004). A triple porosity model for petrophysical analysis of naturally fractured reservoirs. *Petrophysics*, 45 (2), 157-166.

Anderson, T. A. (1972). Paleogene non-marine Gualanday Group, Neiva Basin, Colombia, and regional development of the Colombian Andes. *GSA Bulletin*, 83 (8), 2423-2438. https://doi.org/10.1130/0016-7606(1972)83[2423:PNGGNB]2.0.CO;2

Barrero, D., Pardo, A., Vargas, C. A., & Martínez J. F. (2007). *Colombian sedimentary basins: Nomenclature, boundaries and petroleum geology, a new proposal*. Bogotá: Agencia Nacional de Hidrocarburos y B&M Exploration Ltda.

Bayona, G. A., García, D. F., & Pabón, G. M. (1994). La Formación Saldaña: producto de la actividad de estratovolcanes continentales en un dominio de retro-arco. In F. Etayo Serna (ed.), *Estudios geológicos del Valle Superior del Magdalena* (cap. I, pp. 1-121). Bogotá: Universidad Nacional de Colombia.

Beltrán, N., & Gallo, J. (1979). The geology of the Neiva Sub-Basin, Upper Magdalena Basin, southern portion. In *ACGGP, Geological field trips Colombia, 1959-1978* (pp. 253-275). Bogotá: Geotec.

Blanco, M. A., & De Freitas, M. G. (2003). Geología estructural de la zona de Yaguará-Palermo, piedemonte

de la cordillera Central, valle superior del Magdalena, Colombia. In *Memorias del 8.º Simposio Bolivariano de Exploración Petrolera en las Cuencas Subandinas* (Cartagena) (t. I, pp. 21-33).

Bratton, T., Viet Canh, D., Van Que, N., Duc, N. V., Gillespie, P., Hunt, D., Li, B., Marcinew, R., Ray, S., Montaron, B., Nelson, R., Schoderbek, D., & Sonneland, L. (2006). The nature of naturally fractured reservoirs. *Oilfield Review*, 18, Summer, 4-23.

Buitrago, J. (1994). Petroleum systems of the Neiva area, Upper Magdalena Valley, Colombia. In L. Magoon, & W. G. Dow (eds.), *The petroleum system: From source to trap* (pp. 483-497). Tulsa: American Association of Petroleum Geologists.

Butler, K., & Schamel, S. (1988). Structure along the eastern margin of the Central Cordillera, Upper Magdalena Valley, Colombia. *Journal of South American Earth Sciences*, 1 (1), 109-120. https://doi.org/10.1016/0895-9811(88)90019-3

Campbell, C. J., & Burgl, H. (1965). Section through the Eastern Cordillera of Colombia, South America. *GSA Bulletin*, 76 (5), 567-590. https://doi.org/10.1130/0016-7606(1965)76[567:STTECO]2.0.CO;2

Cobbold, P. R., Rossello, E. A., Roperch, P., Arriagada, C., Gómez, L. A., & Lima, C. (2007). Distribution, timing, and causes of Andean deformation across South America. In A. C. Ries, R. W. H. Butler, & R. H. Graham (eds.), *Deformation of the continental crust: The legacy of Mike Coward* (pp. 321-343). Special Publications, 272. Geological Society of London,

Cooper, M. A., Addison, F. T., Álvarez, R., Coral, M., Graham, R. H., Hayward, A. B., Howe, S., Martínez, J., Naar, J., Peñas, R., Pulham, A. J., & Taboada, A. (1995). Basin development and tectonic history of the Llanos Basin, Eastern Cordillera and Magdalena Valley, Colombia. *American Association of Petroleum Geologists, Bulletin*, 79 (10), 1421-1443. https://doi.org/10.1306/7834D9F4-1721-11D7-8645000102C1865D

Corrigan, H. T. (1967). The geology of the Upper Magdalena Basin. In ACGGP, *Geological fieldtrips, Colombia 1959-1978* (pp. 221-251). Reprinted by Geotec, 1992, Bogotá.

Cossio, U., Rodríguez, G., & Rodríguez, M. (1995). *Geología de la plancha 283, Purificación. Escala 1:100.000*. Bogotá: Ingeominas.

De Freitas, M. G. (2001). Exploring for subthrust traps in a transpressional setting: A review of unsuccessful results and strategies for improvement in the Upper Magdalena Valley of Colombia. AAPG Hedberg Conference (Mendoza), extended abstract.

De Freitas, M. G., & Vallejo, J. (2000). Condicionantes estructurales y estratigráficos en el yacimiento terciario de río Ceibas, cuenca alto Magdalena, Colombia. In *Memorias del 7.º Simposio Bolivariano de Exploración Petrolera en Cuencas Subandinas* (Caracas) (pp. 207-217).

De Freitas, M. G., Vidal, G., & Mantilla, M. (2006). Structural evolution and hydrocarbon entrapment in the Balcon field area, Upper Magdalena Valley, Colombia. In *Actas del 9.º Simposio Bolivariano de Exploración en Cuencas Subandinas* (Bogotá) (pp. 253-275). Asociación Colombiana de Geólogos y Geofísicos del Petróleo.

Duarte, E., Cardona, A., Lopera, S., Valencia, V., & Estupiñán, H. (2018). Provenance and diagenesis from two stratigraphic sections of the Lower Cretaceous Caballos Formation in the Upper Magdalena Valley: Geological and reservoir quality implications. *Ciencia, Tecnología y Futuro*, 8 (1), 5-29.

Ekstrom, M. P., Dahan, C. A., Chen, M. Y., Lloyd, P. M., & Rossi, D. J. (1987). Formation imaging with microelectrical scanning arrays. *The Log Analyst*, 28, 294-306.

Fisher, N. I., Lewis, T. L., & Embleton, B. J. (1987). *Statistical analysis of spherical data*. Cambridge: Cambridge University Press.

George, R. P., Pindell, J. L., & Cristancho, J. (1997). Eocene paleostructure of Colombia and implications for history of generation and migration of hydrocarbons. Exploración petrolera en las cuencas subandinas. In *Memorias del 6.º Simposio Bolivariano* (Bogotá) (t. II, pp. 133-140). Asociación Colombiana de Geólogos and Geofísicos del Petróleo.

Gómez, E., Jordan, T. E., Allmendinger, R. W., Hegarty, K., Kelley, S., & Heizler, M. (2003). Controls on architecture of the Late Cretaceous to Cenozoic Southern Middle Magdalena Valley Basin, Co-

lombia. *GSA Bulletin*, 115 (2), 131-147. https://doi.org/10.1130/0016-7606(2003)115<0131:COAOTL>2.0.CO;2

Guerrero, J. (2002). Proposal on the classification of systems tracts: Application to the allostratigraphy and sequence stratigraphy of the Cretaceous Colombian Basin. Part 2: Barremian to Maastrichtian. *Geología Colombiana*, 27, 27-49.

Hennings, P., Olson, J., & Thomson, L. (2000). Combining outcrop data and three dimensional structural models to characterize fracture reservoirs: An example from Wyoming. *AAPG Bulletin*, 84 (6), 830-849. https://doi.org/10.1306/A967340A-1738-11D7-8645000102C1865D

Higuera, D. A. (2012). *Modelo petrofísico integrado del Grupo Guadalupe, aplicado al campo Matachín Norte* (M.Sc. thesis). Universidad Nacional de Colombia.

Irving, E. M. (1975). Structural evolution of the northernmost Andes, Colombia. *U. S. Geologial Survey Professional Paper*, 846, 1-47. https://doi.org/10.3133/pp846

Jaimes, E., & De Freitas, M. G. (2006). An Albian-Cenomanian unconformity in the Northern Andes: Evidence and tectonic significance. *Journal of South American Earth Sciences*, 21 (4), 466-492. https://doi.org/10.1016/j.jsames.2006.07.011

Jamison, W. (1997). Quantitative evaluation of fractures on Monkshood Anticline, a detachment fold in the foothills of Western Canada. *AAPG Bulletin*, 81 (7), 830-849. https://doi.org/10.1306/522B-49FB-1727-11D7-8645000102C1865D

Klimczak, C., Schultz, R. A., Parashar, R., & Reeves, D. M. (2009). Cubic law with aperture-length correlation: Implications for network scale fluid flow. *Hydrogeology Journal*, 18 (4), 851-862. https://doi.org/10.1007/s10040-009-0572-6

Kroonenberg, S. B., & Diederix, H. (1982). Geology of the uppermost Magdalena Valley. In Geotec, *Geological field trips: Colombia, 1980-1989* (pp. 73-89). Bogotá: Asociación Colombiana de Geólogos and Geofísicos del Petróleo.

Kubik, W., & Lowry, P. (1993). Fracture identification and characterization using Cores, FMS, CAST, and Borehole Camera: Devonian shale, Pike County, Kentucky. Paper SPE 25897 presented at the 1993 SPE Rocky Mountain Regional/Low Permeability Reservoirs Symposium, Denver, CO, 12-14 April.

Laongsakul, P., & Dürrast, H. (2011). Characterization of reservoir fractures using conventional geophysical logging. *Songklanakarin Journal of Science and Technology*, 33 (2), 237-246.

Mojica, J., & Franco, R. (1990). Estructura y evolución tectónica del valle medio y superior del Magdalena, Colombia. *Geología Colombiana*, 17, 41-64.

Montes, C., Hatcher, R., & Restrepo, P. (2005). Tectonic reconstruction of the Northern Andean blocks: Oblique convergence and rotations derived from the kinematics of the Piedras-Girardot area, Colombia. *Tectonophysics*, (1-4), 399, 221-250. https://doi.org/10.1016/j.tecto.2004.12.024

Mora, A., Mantilla, M., & De Freitas, M. G. (2010). Cretaceous paleogeography and sedimentation in the Upper Magdalena and Putumayo Basins, Southwestern Colombia. *Search and Discovery Article*, 50246.

Nelson, R. A. (1985). *Geologic analysis of naturally fractured reservoirs*. Houston: Gulf Publishing Co.

Nelson, R. A., & Serra, S. (1995). Vertical and lateral changes in fracture spacing in several folded carbonate sections and its relation to locating horizontal wells. *Journal of Canadian Petroleum Technology*, 34 (6), 51-56. https://doi.org/10.2118/95-06-05

Ortega, O., & Marret, R. (2000). Prediction of macrofracture properties using microfracture information: Mesaverde Group Sandstones, San Juan Basin, New Mexico-Texas. *Journal of Structural Geology*, 22 (5), 571-588. https://doi.org/10.1016/S0191-8141(99)00186-8

Pindell, J., & Tabbutt, K. D. (1995). Mesozoic-Cenozoic Andean paleogeography and regional controls on hydrocarbon systems. In A. J. Tankard, R. Suárez, & H. J. Welsink (eds.*), Petroleum Basins of South America* (pp. 101-128). American Association of Petroleum Geologists, Memoir 62.

Rider, M. H. (1986). *The geological interpretation of well logs*. New York: John Wiley & Sons, Inc.

Rossello, E. A. (2018). Interpretaciones estructurales dinámicas a partir del análisis de ovalización (breakouts) de pozos: aplicaciones a perforaciones en la Formación Vaca Muerta (cuenca neuquina, Argentina).

Revista de la Asociación Geológica Argentina, 75 (2), 252-264.

Saavedra, J. L. (2013). *Geometría y evolución cinemática del sector que separa los campos Matachín Norte y Matachín Sur, bloque Espinal-valle superior del Magdalena, Colombia* (M.Sc. thesis). Universidad Nacional de Colombia.

Sarmiento, L. F. (2001). *Mesozoic rifting and Cenozoic Basin inversion history of the Eastern Cordillera, Colombian Andes: Inferences from tectonic models* (Ph. D. thesis). Vrije Universiteit, Amsterdam.

Sarmiento, L. F., & Rangel, A. (2004). Petroleum systems of the Upper Magdalena Valley, Colombia. *Marine and Petroleum Geology*, 21 (3), 373-391. https://doi.org/10.1016/j.marpetgeo.2003.11.019

Schamel, S. (1991). Middle and Upper Magdalena Basins, Colombia. In K. T. Biddle (ed.), *Active margin basins* (pp. 283-301). American Association of Petroleum Geologists, Memoir, 52.

Serra, O. (2008). *Well logging handbook*. Paris: Technip Editions.

Toro, J., Roure, F., Bordas Le Floch, N., Le Cornec Lance S., & Sassi, W. (2004). Thermal and kinematic evolution of the Eastern Cordillera fold and thrust belt, Colombia. In R. Swennen, F. Roure, & J. W. Granath (eds.), *Deformation, fluid flow, and reservoir appraisal in foreland fold and thrust belts* (pp. 79-115). Hedberg Series, 1. American Association of Petroleum Geologists.

Trenkamp, R., Kellogg, J. N., Freymueller, J. T., & Mora, H. P. (2002). Wide plate margin deformation, Southern Central America and Northwestern South America, CASA GPS observations. *Journal of South American Earth Sciences*, 15 (2), 157-171. https://doi.org/10.1016/S0895-9811(02)00018-4

Van der Wiel, A. M. (1991). *Uplift and volcanism of the SE Colombian Andes in relation to Neogene sedimentation in the Upper Magdalena Valley* (Ph. D. thesis). University of Wageningen.

Villamil, T., Arango, C., & Hay, W. W. (1999). Plate tectonic paleoceanographic hypothesis for Cretaceous source rocks and cherts of Northern South America. In E. Barrera, & C. C. Johnson (eds.), *Evolution of the Cretaceous ocean: climate system* (Boulder, Colorado), vol. 332. Geological Society of America. https://doi.org/10.1130/0-8137-2332-9.191

Capas muy gruesas de rocas volcano-sedimentarias de la Formación La Quinta. Vía Uramita - Sector La Esperanza, serranía de Peñas.
Fotografía de Gabriel Rodríguez.

Boletín Geológico

SERVICIO GEOLÓGICO COLOMBIANO

Boletín Geológico, 46, 51–94, 2020
https://doi.org/10.32685/0120-1425/boletingeo.46.2020.535

Received: October 10, 2019
Accepted: January 17, 2020
Published online: June 30, 2020

Volcanism of the La Quinta Formation in the Perijá mountain range

Vulcanismo de la Formación La Quinta en la serranía del Perijá

Gabriel **Rodríguez García** and Gloria **Obando**[1]

1 Servicio Geológico Colombiano.

Email: grodriguez@sgc.gov.co

Abstract

This study reports new data on the petrography, total rock chemistry and U-Pb zircon geochronology of volcanic rocks of the La Quinta Formation that outcrop the western flank of the Perijá mountain range and the Cesar and La Guajira departments. The volcanic rocks consist of basaltic, andesitic, dacitic and rhyolitic lavas, and the volcaniclastic rocks consist of crystal-vitric and crystal-lithic tuffs and agglomerates of calc-alkaline affinity, formed in a continental margin arc setting. Geochronological data suggest that the La Quinta Formation was volcanically active for approximately 25 Ma, during which its composition varied from basaltic trachyandesites to rhyolites. U-Pb dating suggests that the volcanism began in approximately 191 Ma (Sinemurian age) and continued until approximately 164 Ma, with at least three periods of increased volcanic activity. The inherited zircons contain Triassic, Permian, Neoproterozoic and Mesoproterozoic populations, indicating that this arc was emplaced on rocks of the Chibcha Terrane along the South American paleomargin and that it is part of the same arc that formed the Jurassic volcanic rocks of the Sierra Nevada de Santa Marta, Cocinas and San Lucas mountain ranges and the Upper Magdalena Valley.

Keywords: Jurassic; U-Pb geochronology; volcanic rocks; Perijá mountain range.

Resumen

Este trabajo presenta nuevos resultados de petrografía, química de roca total y geocronología U-Pb en circón de rocas volcánicas de la Formación La Quinta que afloran en el flanco occidental de la serranía de Perijá, en los departamentos de Cesar y La Guajira. Las rocas volcánicas corresponden a lavas basálticas, andesíticas, dacíticas y riolíticas, y las rocas volcanoclásticas corresponden a tobas cristalo-vítreas, cristalo-líticas y aglomerados de afinidad calcoalcalina, formadas en un ambiente de arco de margen continental. Los datos geocronológicos sugieren que el vulcanismo de la Formación La Quinta estuvo activo aproximadamente 25 Ma, intervalo en el que varió su composición de traquiandesitas basálticas a riolitas. Las edades U-Pb obtenidas sugieren que el vulcanismo se inició aproximadamente a 191

Ma (Sinemuriense) y se extendió hasta aproximadamente 164 Ma, con al menos tres periodos de mayor actividad volcánica. Los circones heredados presentan poblaciones del Triásico, Pérmico, Neoproterozoico y Mesoproterozoico, lo que sugiere que este arco se emplazó en rocas del Terreno Chibcha a lo largo de la paleomargen Suramericana y que son parte del mismo arco que formó las rocas volcánicas jurásicas de la Sierra Nevada de Santa Marta, la serranía de Cocinas, la serranía de San Lucas y el valle superior del Magdalena.

Palabras clave: Jurásico; geocronología U-Pb; rocas volcánicas; serranía de Perijá.

1. Introduction

The volcanic rocks of the La Quinta Formation outcrop at the northern end of the Colombian Cordillera Oriental [Eastern Ranges] in the Perijá mountain range, and they are part of the Jurassic volcanism that outcrops in the Upper Magdalena Valley in the San Lucas and Sierra Nevada de Santa Marta mountain ranges and in the Upper Guajira. The ages of these volcanic sequences range from 195 to 164 Ma (Cediel et al., 1980, 1981; Bustamante et al., 2010; Villagómez, 2010; Leal Mejía, 2011; Zapata et al., 2016; Rodríguez et al., 2018; Correa et al., 2019; Leal et al., 2019).

Most authors agree on the model of formation of the lower-to-middle Jurassic volcanism and plutonism of the northern Andes, which is considered to be continental margin arc magmatism. The following variations in the model and arc development have been proposed: 1) an arc formed by a single subduction zone located west of the South American margin, which was formed between 209 and 114 Ma (Spikings et al., 2015); 2) a stationary continental margin arc formed by oblique convergence between the Farallón plate (an ancient oceanic plate) and the NW of South America that has been active for at least 40 Ma (Bustamante et al., 2016); 3) a continental arc and back-arc comprising Jurassic rock blocks of the Upper Magdalena Valley, Colombian Cordillera Central [Central Andes], and San Lucas and Sierra Nevada de Santa Marta mountain ranges (Villagómez et al., 2015; Bayona et al., 2010); 4) an erosive continental margin arc that was active for ~30 Ma exhibiting a compositional migration in a west-east direction (Rodríguez et al., 2018); and 5) a continental margin arc that fragmented and scattered along the paleomargin after its formation (Bayona et al., 2010; Villagómez et al., 2015; Zapata et al., 2016; Zuluaga et al., 2015).

This study reports new petrography (9), total rock chemistry (8) and U-Pb zircon geochronology (laser ablation inductively coupled plasma mass spectrometry (LA-ICP-MS)) (5) data, which, together with published geochronology data (González et al., 2015a; González et al., 2015b) and with total the rock chemistry of the La Quinta Formation, supplement the basic information on this unit and on the volcanism associated with the arc dated to the Lower-Middle Jurassic.

This new information is correlated with other volcano-sedimentary sequences that outcrop in Colombia, specifies the distribution of arc volcanism and, together with the analysis of the inherited zircons in volcanic rocks, improves our understanding of the basement distribution on which the arc is founded and of the geological evolution of the northern Andean volcanism during the Jurassic while furthering our knowledge of the Jurassic tectonic blocks that were scattered along the paleomargin and their distribution, according to Bayona et al. (2010), Villagómez et al. (2015), Zapata et al. (2016) and Zuluaga et al. (2015).

2. Regional Geological Framework

The Perijá mountain range, which is located in the northern Cordillera Oriental [Eastern Ranges], uplifts from the Cerrejón and Yaya faults on its western edge, culminating in the Oca fault northward and forming a block bordered to the west by the Cesar-Rancherías river valley, which is a drainage basin filled with Mesozoic and Cenozoic sediments covered by recent alluvial deposits that separates the Perijá mountain range from the Sierra Nevada de Santa Marta block; to the north, the Oca fault separates the basin from the Cocinas mountain range in Upper Guajira (Figure 1).

The core of the Perijá mountain range consists of Precambrian gneissic metamorphic rocks, such as those observed in the Cachirí river, on the eastern slope of the mountainous range; the Río Cachirí Group rests on this gneiss basement (Pastor Chacón et al., 2013), although the gneiss basement has not been found on the western slope of the Perijá mountain range (Miller, 1960 and Forero, 1970). In the northern sector, the Perijá mountain range is essentially composed of Jurassic and Cretaceous units that cover Paleozoic units. The oldest rocks are Cambro-Ordovician metamorphic rocks and Devonian, Carboniferous and Permian sedimentary rocks (Forero, 1970; Pastor Chacón et al., 2013). On the western slope, the oldest unit of the Perijá mountain range contains Devonian sedimentites consisting of argillites, sandstone siltstones and limestones (Weisbord, 1926; Trumpy, 1943; Miller, 1960; Forero, 1970 and Pastor Chacón et al., 2013).

The Jurassic volcano-sedimentary sequences of the La Quinta Formation rest on Paleozoic outcrops of the western slope of the Perijá mountain range. These sequences consist of red beds of sandstones, siltstones, argillites, conglomerates, subordinate lavas and subaerial pyroclastic rocks, where the former are similar to those exposed on the eastern slope of Sierra Nevada de Santa Marta, where abundant Jurassic volcanic rocks outcrop (Tschanz et al., 1969).

Cretaceous sedimentary sequences appear on both banks of the Cesar-Rancherías valley (Molino Formation, Cogollo Group and La Luna and Portales formations). These sequences rest on the La Quinta Formation and Jurassic Vulcanites of the Sierra Nevada de Santa Marta (SNSM). Similarly, Paleocene-to-Miocene sedimentary sequences, such as the Cerrejón Formation, rest on the Cretaceous units.

3. History of La Quinta Formation

The La Quinta Formation consists of red sediments that stratigraphically lie above Paleozoic units and below Mesozoic units. This unit was described by Kundig (1938) in the state of Táchira on the Seboruco-La Grita road near the La Quinta hamlet in Venezuela. The sequence, towards the base, is made up of compact dark red conglomerates with well-cemented rims and with sandstone and red clay intercalations.

In Colombia, Miller (1960) coined the term *La Quinta Formation* to refer to the likely Jurassic sediments that are found on the western slope of the Perijá mountain range, on the western slope of the Ranchería and Cesar rivers, and on the Majuyura Ridge (Oca fault) at the northern end of the Perijá mountain range.

Radelli (1962) continues using the term *La Quinta Formation* coined by Miller (1960), considering the stratigraphic correspondence with the La Quinta Formation of the Venezuelan authors, the sedimentation environment and the presence of volcanic material. Radelli (1962) describes the sequence as a predominantly detrital succession, albeit noting the presence of volcanic material. This author distinguishes the following facies: a) conglomerates with volcanic pebbles, which form the basement; b) acidic volcanic rocks associated with sandstones; and c) the fine-grained red sandstones that make up most of the La Quinta Formation, with interbedded tuffs and with sandstones at the basement of the formation, together with andesitic lavas, where there are conformities and unconformities between the sediments described above.

Forero (1972) surveyed a stratigraphic column of the La Quinta Formation in Manaure, Cesar Department (Colombia), and identified the following five sets of rocks from bottom to top: a) conglomerates, red sandstones and volcanic rocks; b) red sandstones and lutites; c) red sandstones with tuff intercalations; d) conglomerate with volcanic pebbles; and e) rhyolitic tuffs.

Hernández (2003) describes the sequence of the La Quinta Formation in the Perijá mountain range east of the towns of La Jagua de Ibirico in the sector of La Victoria de San Isidro and southeast of Santa Isabel, which shows a succession along the western flank of the mountain range. Arias and Morales (1999) report that this unit outcrops near the municipality of Manaure and continues south to the San Antonio gorge, with a thickness ranging from 2,700 to 3,000 m, whereas its thickness markedly decreases in La Jagua de Ibirico due to local reverse faults that affected the unit through tectonic uplift in the Miocene during the Andean orogeny.

Geoestudios (2006) describes the La Quinta Formation as a sequence consisting of purple-red, aphanitic ash tuffs and welded ash-flow tuffs with pseudolamination, together with slightly calcareous mudstones, conglomerate sandstones and matrix-supported conglomerates,

with local interbedding of reddish mudstones and arkosic sandstones with cross-bedding.

González et al. (2015 a and b) describe volcanic and pyroclastic rocks throughout the sequence of the La Quinta Formation, consisting of basalts, andesites, dacites, rhyolites and calc-alkaline subalkaline pyroclastic rocks, formed in a continental volcanic arc setting and with Lower to Middle Jurassic U-Pb ages.

3. Methodology

Regional sampling was performed from the volcanic rocks of the La Quinta Formation in the Perijá mountain range and the Cesar and La Guajira departments for this study. In this sampling, sixteen rocks were taken, with eleven additional samples for zircon extraction; fifteen new thin sections were prepared, total rock chemical analysis was performed on eight rocks, and six samples were dated by zircon U-Pb LA-ICP-MS.

3.1 Petrography

Initially, petrographic analyses were performed from the mapping projects of the Servicio Geológico Colombiano; previously known as Ingeominas. In the present study, rock samples were selected for petrography from a larger number of samples collected in field work. The selection criteria used in this study were undisturbed rocks with defined spatial distribution representative of the volcanic rocks that make up the La Quinta Formation. Fifteen new samples were sent to the Thin Section Preparation Laboratory of the Servicio Geológico Colombiano, Bogotá headquarters. Once the thin sections were prepared, they were analyzed by the authors at the Petrography Laboratory of the Servicio Geológico Colombiano in Medellín, using SGC standards in the analysis with Leitz and Olympus petrographic microscopes and classifying the samples from 300 counting points, according to the quartz, alkali feldspar, plagioclase, feldspathoid (QAPF) diagrams by Streckeisen et al. (1978) and following the recommendations of Le Maitre et al. (2002).

3.2 Total rock chemical analysis

Eight fresh rocks were chosen, taking into account the previous petrographic analysis, which was followed by total rock chemical analysis at the Analytical Geochemistry Laboratory of the Servicio Geológico Colombiano, Bogotá headquarters. The major oxides and minor elements were analyzed with a Panalytical Axios Mineral X-ray fluorescence spectrometer; the major oxides were quantified using samples fused with lithium metaborate and lithium tetraborate, whereas the minor elements were quantified using pressed samples. The trace elements were analyzed using a Perkin Elmer Nexion inductively coupled plasma mass spectrometer (ICP-MS). The findings of González et al. (2015 a, b) were compared with the results from the present study since both were based on samples collected from the same region.
Petrographic and geochemical diagrams were prepared using the GCDkit software by Janoušek et al. (2006).

3.3 U-Pb geochronology

Eleven samples were chosen for zircon separation after petrographic and chemical analysis of the total rock. Of these samples, from only six samples of lava and pyroclastic volcanic rocks, enough zircons were obtained for LA-ICP-MS U-Pb zircon dating. The rock samples were crushed, pulverized and sieved following the separation procedure of Castaño et al. (2018) and analyzed by LA-ICP-MS according to the procedure described by Peña et al. (2018). Most zircons were concentrated at the Chemistry Laboratory of Geological Surveys, Medellín headquarters, using hydrodynamic and magnetic separation and others were concentrated in the field using a gold pan. The zircons were selected manually using an Olympus stereo microscope at the Petrography Laboratory, Medellín headquarters. Cathodoluminescence (CL) images of the zircon grain mounts were acquired under a Zeiss scanning electron microscope (SEM) with a GatCL miniCL detector to observe the internal structure of the selected grains.

The analyses were performed in a Photon Machines laser ablation system with a 193-nm excimer laser coupled to an Element 2 mass spectrometer. The isotopes used for manual integration were ^{238}U, ^{206}Pb and ^{204}Pb. Plešovice zircon (Sláma et al., 2008), FC-1 (Coyner et al., 2004), Zircon 91500 (Wiedenbeck et al., 1995; Wiedenbeck et al., 2004) and Mount Dromedary (Renne et al., 1998) were used as reference standards. The points analyzed in the zircons were 20 microns in diameter. Data reduction was performed using the Iolite v2.5® software

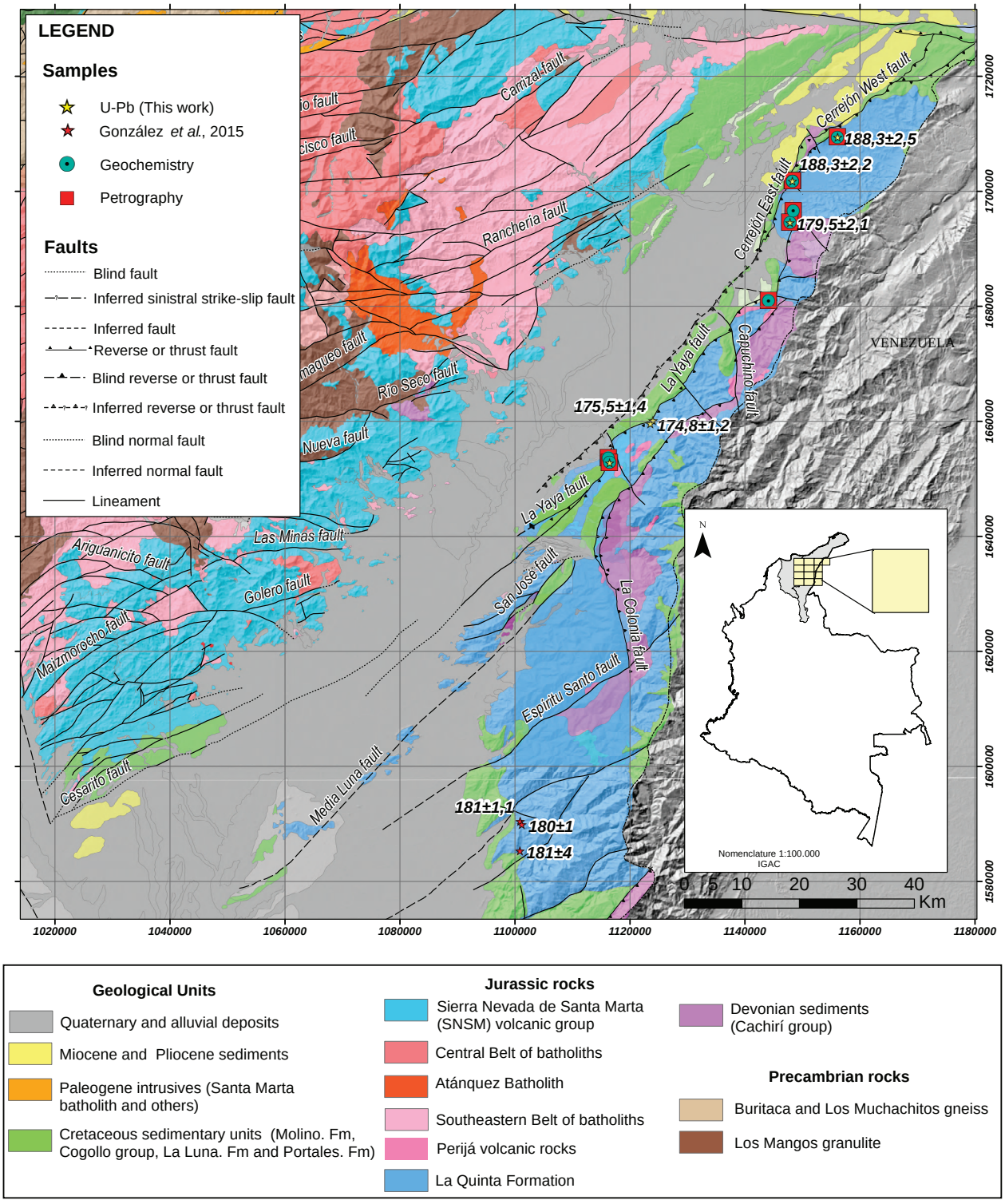

Geological Units

- Quaternary and alluvial deposits
- Miocene and Pliocene sediments
- Paleogene intrusives (Santa Marta batholith and others)
- Cretaceous sedimentary units (Molino. Fm, Cogollo group, La Luna. Fm and Portales. Fm)

Jurassic rocks

- Sierra Nevada de Santa Marta (SNSM) volcanic group
- Central Belt of batholiths
- Atánquez Batholith
- Southeastern Belt of batholiths
- Perijá volcanic rocks
- La Quinta Formation

- Devonian sediments (Cachirí group)

Precambrian rocks

- Buritaca and Los Muchachitos gneiss
- Los Mangos granulite

Figure 1. Geological map of the La Quinta Formation. Distribution of samples with thin sections, lithogeochemistry and geochronology with U-Pb dating
Source: González et al. (2015 a, b); Invemar et al. (2007)

in IGORPro 6.3.6.4® (Paton et al., 2010; Hellstrom et al., 2008). Common lead correction was performed using the evolution model according to Stacey and Kramers (1975). The final results corresponded to the mean of the data that fell within two standard deviations.

The ages were determined by the youngest results in each sample (assuming that this group of zircons crystallized during the same magmatic episode) because this provides the best estimate of the rapid crystallization of pyroclastic or volcanic material. The analysis was performed sample by sample when the youngest data corresponded to one or more populations by considering probability density plots and zircon by zircon when more than one population was identified by analyzing the ablation sites and the internal structure of each zircon, initially separating the ablations into cores and rims and then grouping them. This method was used to separate the populations of xenocrystals and inherited zircon cores. In the populations that defined the crystallization age and suggested the presence of antecrystals, the zircons were compared. Whether the ablation sites corresponded to cores or rims was analyzed, and the age of the entire population was calculated, which could define the crystallization age; additionally, the weighted average age of the antecrystals and the weighted average age of the younger zircons was calculated, which likely defined the crystallization age of the rock. The findings were compared with the crystallization episodes of the arc in both the plutonic and volcanic rocks (Rodríguez et al., 2018; Rodríguez et al., 2019b; Correa et al., 2019).

The $^{207}Pb/^{206}Pb$ ratios, ages and errors were calculated according to Petrus and Kamber (2012). The concentrations of U and Th were calculated according to Paton et al. (2010) using an external standard zircon. The ages and the geochronology plots were calculated and drawn, respectively, using the add-in program Isoplot v4.15 (Ludwig, 2012). The graphical representation in the article is a single weighted average age diagram showing the zircons that indicate the age of the crystals and the age of crystallization, albeit with the age calculated separately in the program.

4. Results

4.2 Petrography

The La Quinta Formation, located in the Perijá mountain range and the Cesar and La Guajira departments, primarily consists of conglomerates, conglomeratic sandstones and reddish and subordinately brown, gray and greenish gray sandstones, usually in thick-to-very-thick wavy layers, some of which include cross-bedding.

Less frequently, violet rhyolitic, dacitic, andesitic and basaltic lavas are identified, as well as thick interbedded layers of crystal-vitric and crystal-lithic tuffs and agglomerates with ash matrix and lapilli. The volcanic rocks of this study are violet. The petrographic results are summarized in Figure 2 and Table 1.

Basalts. The basalts have a fluid trachytic, porphyritic texture, and some of the basalts show irregular zeolite-filled amygdules, epidote and epidote and quartz. The

Table 1. Modal classifications in percentages for volcanic rocks of the La Quinta Formation

IGM	W	N	Qz	Pl	Fsp	Cpx	Ol	Hbl	Bt	Op	Ap	Zrn	Ep	Matrix	FR	Other	Classification
901373	1124017	1660152	16	12.1	10			1.5		1.9		0.4	0.8	29.2		30	Vitreous tuff
901609	1148285	1701812	3.6	15.8	0.8	7.1				2	0.8			69.9			Dacite
901377	1148433	1696644	1.4	21	0.7	1	tr			1				71.9		3	Andesite
901631	1123566	1659592	33	20.8						2.1			2.1	41.7			Dacite
901624	1156113	1709417		22.5				5.3		8.6	tr			63.6			Phenoandesite
901625	1116457	1652853		57.6			1			1.3				40.1			Basalt
901382	1116236	1653658		45.6			16.2			38.2							Olivine basalt
901437	1144105	1681005	0.1	79.9		8.4				11.6			3.1				Trachytic basalt
901623	1147831	1694625	1.2	8.4	2.1			0.5	0.6	2.4	Tr	Tr		32.4	50.6	1.8	Lithic tuff

Qz: quartz, Pl: plagioclase, Fsp: feldspar, Cpx: clinopyroxene, Ol: olivine, Hbl: hornblende, Bt: biotite, Op: opaque minerals, Ap: apatite, Zrn: zircon, Ep: epidote, FR: lithic fragments, tr: traces. Coordinates in Magna Sirgas, Bogotá

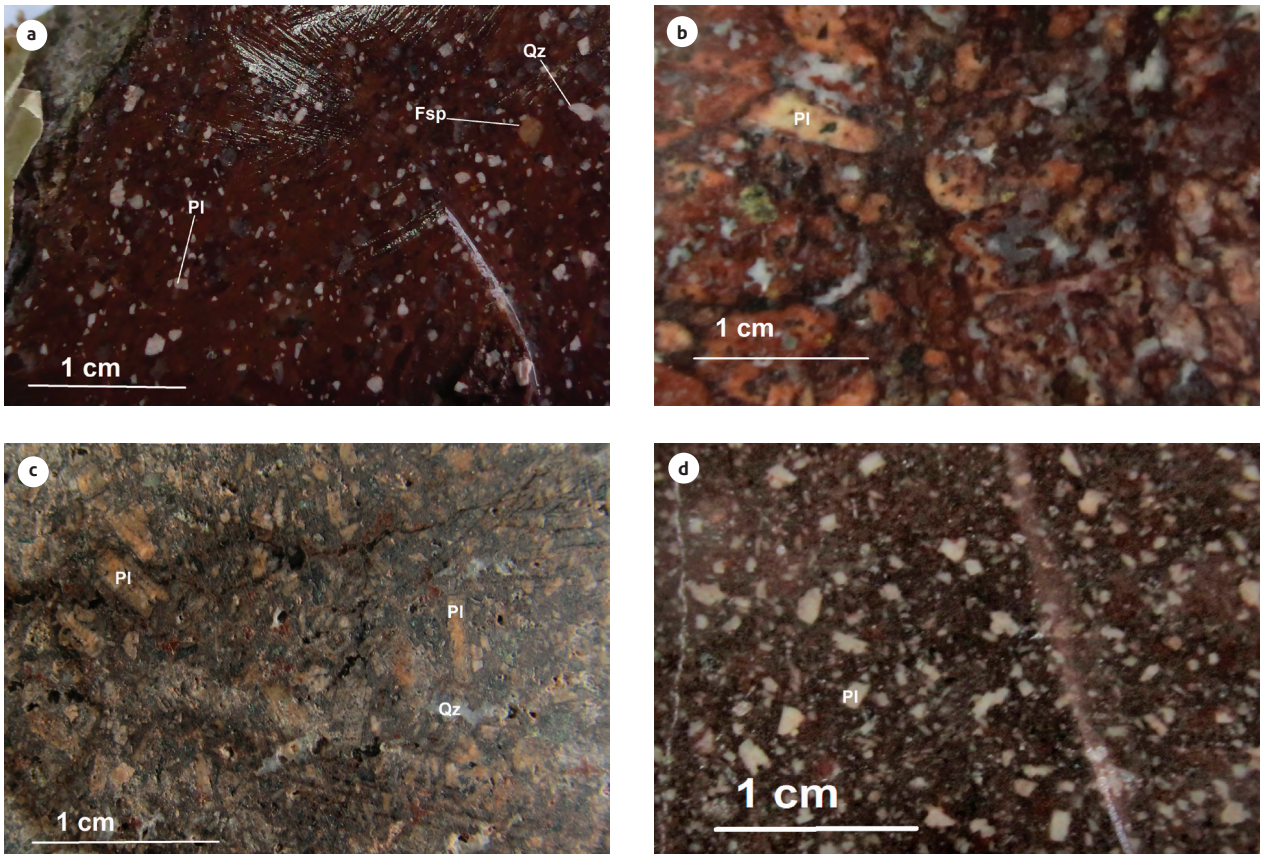

Figure 2. Macroscopic observations of lavas and tuffs of the La Quinta Formation
A) 901373-Tuff. B) 901377-Tuff. C) 901609-Dacite. E) 901624-Phenoandesite

phenocrysts are mainly skeletal olivine (0.1-16%) inside a trachytic matrix consisting of tabular plagioclase euhedral microcrystals (45.6%-79.9%), glass and intersertal opaque minerals (hematite 1.3%-11%), and some of the rocks contain clinopyroxene (0%-8.4%). The skeletal olivine phenocrysts are euhedral to subhedral, with sizes ranging from 700 μn to 3 mm and with irregular fractures marked by opaque minerals altered to hematite, and are completely replaced by serpentine and epidote inside the crystals. The accessory minerals are microcrystals of opaque minerals (hematite). The alteration minerals are serpentine and epidote from olivine; the plagioclase can be dusted due to an alteration to saussurite, and the glass, in some rocks, is altered to epidote and sericite (Figure 3A and B).

Rhyolites and dacites. Rhyolites and dacites are rocks with microporphyritic, porphyritic and sometimes seriate textures. These rocks consist of euhedral microphenocrysts to phenocrysts of quartz (6.6%-38%), plagioclase (12%-45%), sanidine (0%-10%) and may contain hornblende. The phenocrysts are dispersed in a matrix ranging from hyalocrystalline to fluidal microlithic; the matrix can be devitrified and altered to secondary sericite and epidote aggregates. The accessory rocks are ochre hematite, which accounts for the color of the rocks, apatite and zircon. The quartz can be euhedral-to-subhedral bipyramidal, with matrix corrosion bays and uneven internal matrix droplets. The plagioclase ranges from 3 to 0.1 mm and is found in euhedral crystals, with zonation. The alteration minerals are sericite and clay in plagioclase and feldspar and chlorite in amphiboles.

Pyroclastic rocks. The rocks correspond to red-to-violet, and less frequently greenish-gray, tuffs and volcanic agglomerates and consist of lithic fragments of crystals and altered glass.

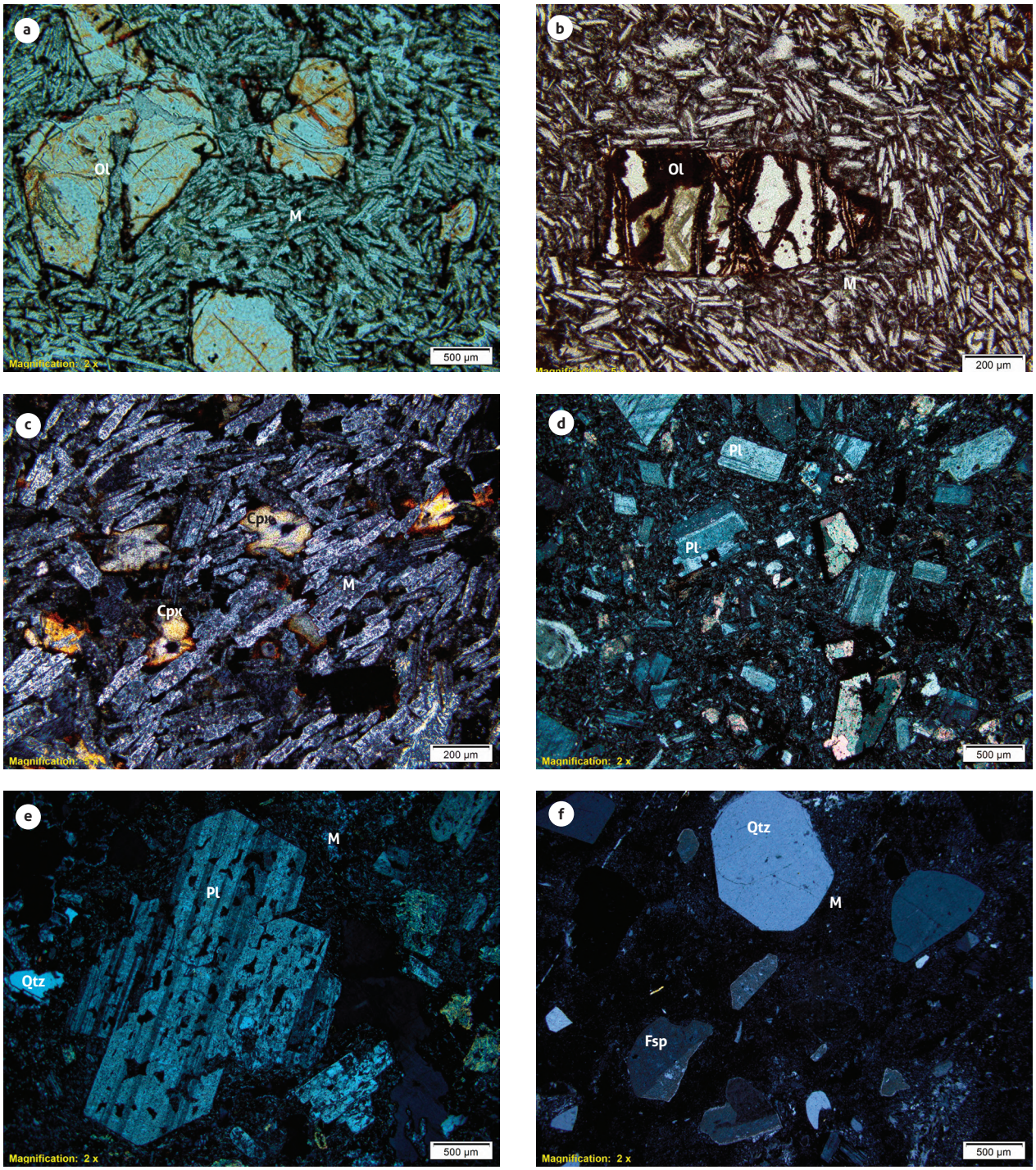

Figure 3. Microscopic observations of lavas and tuffs of the La Quinta Formation
A, B) Samples IGM 901382 and IGM 901625: basalts consisting of skeletal olivine (Ol) phenocrysts suspended in a trachytic plagioclase matrix (M). C) Sample IGM-901437: basaltic andesite with clinopyroxene (Cpx) phenocrysts suspended in a trachytic plagioclase matrix (M). D) Sample IGM 901624: andesite, seriate plagioclase (Pl) phenocrysts and skeletal hornblende (Hbl) suspended in a vitreous matrix (M). E) Sample IGM 901609: andesite with plagioclase (Pl) phenocrysts and quartz in a microlithic matrix (M). F) Sample IGM 901373: crystalline vitreous tuff with quartz (Qtz) and feldspar (Fsp) crystals suspended in a vitreous matrix (M)

The tuffs consist of volcanic lithic fragments of andesites and basalts with porphyritic textures and vitreous, trachytic, fluidal microlithic and devitrified matrix, with plagioclase phenocrysts and, less frequently, with skeletal mafic minerals replaced by opaque minerals and epidote, with sizes ranging from 300 microns to 6 mm (ash and lapilli). The suspended and scattered fragments range from angled and rounded to amorphous. Some crystal fragments of quartz, plagioclase, sanidine, hornblende and biotite range from 0.2 to 1.8 mm. The crystals and crystal fragments are anhedral to euhedral. The quartz can be bipyramidal and have corroded rims, with corrosion bays and paste or devitrified glass inclusions. The plagioclase and sanidine crystals are tabular euhedral and are covered with their alteration to kaolin; the hornblende and the biotite usually occur as skeletal crystals completely replaced by opaque minerals. The matrix consists of devitrified glass and fragments of quartz crystals and feldspars smaller than 80 microns, with widespread apatite, zircon and opaque minerals as accessory minerals (Figure 3F).

5. Geochemistry

Eight samples of lavas, agglomerates and tuffs were analyzed. The spatial distribution of the samples is shown in Figure 1. The contents of the major oxides and trace and rare-earth elements (REE) are presented in Tables 2 and 3.

The samples IGM 901610, IGM 901382 and IGM 901624 present 3.41%. 3.60% and 4.30% losses on ignition (LOIs), respectively. The sample IGM 901382, classified as basalt, shows olivine phenocrysts that are completely altered to serpentine; the sample IGM 901624, classified as andesite, shows skeletal hornblende that is altered to calcite and calcite veinlets, and the sample IGM 901377, classified as andesite, presents hydrothermal quartz veins. The analysis of the possible rock alterations from the diagram of Hughes (1972) demonstrated that the samples IGM 901624, IGM 901623, IGM 901610 and IGM 901377 show sodic alteration (Figure 4).

Table 2. Results for major oxides in lavas and pyroclastic rocks of the La Quinta Formation

IGM	901609	901610	901377	901382	901437	901623	901624	901625
Field No.	GOE-1045A	GOE-1045B	GOE-1048	GOE-1058	GR-6821	GR-6849	GR-6851	GR-6854
W	1148285	1148285	1148433	1116236	1144105	1147831	1156113	1116457
N	1701812	1701812	1696644	1653658	1681005	1694625	1709417	1652853
SiO2	60.57	59.55	58.24	51.27	51.29	70.43	55.66	57.75
TiO2	1.05	0.87	1.20	1.36	1.49	0.48	1.21	1.08
Al2O3	17.35	16.05	15.28	15.32	15.45	14.39	18.31	15.16
Fe2O3T	6.09	6.60	7.80	8.70	9.08	3.08	5.41	7.30
MgO	1.83	4.66	2.27	7.32	6.64	1.01	2.64	4.57
CaO	1.16	1.29	5.60	5.11	5.83	1.03	3.50	3.47
Na2O	6.19	5.59	5.30	4.38	4.53	6.23	7.53	5.21
K2O	3.42	1.49	1.10	2.24	1.82	1.84	0.81	2.64
P2O5	0.247	0.292	0.465	0.345	0.526	0.146	0.298	0.325
MnO	0.01	0.01	0.01	0.02	0.02	0.00	0.01	0.01
LOI	1.88	3.41	2.53	3.60	2.99	1.27	4.30	2.19

The SiO_2 values of lavas and pyroclastic rocks range from 51.3% to 70.4%, and the Fe_2O_3, MgO and CaO values decrease with increasing SiO_2 (Table 2); the Na_2O values increase with increasing SiO_2, and the K_2O content is variable and dispersed. The TiO_2 values are higher and lower than 1%, with most values > 1%, except for samples GOE-1045B and IGM- 901623 (GR-6849), with TiO_2 < 1%. The Al_2O_3 content ranges from 14.4% to 18.3%; Fe_2O_3 ranges from 3.1% to 9.1%; MgO ranges from 1 to 7.3%; CaO ranges from 1% to 5.8%; the alkali ($Na_2O + K_2O$) content is high, ranging from 6.3% to 9.6%, with K_2O/Na_2O ratios < 0.6%

Table 3. Results for trace elements of volcanic rocks of the La Quinta Formation

IGM	901382	901437	901609	901610	901624	901625	901377	901623
Field No.	GOE-1058	GR-6821	GOE-1045A	GOE-1045B	GR-6851	GR-6854	GOE-1048	GR-6849
Chemical classification	Basaltic trachyandesite	Basaltic trachyandesite	Trachydacite	Trachyandesite	Trachyandesite	Trachyandesite	Trachyandesite	Rhyolite
W	1116236	1144105	1148285	1148285	1156113	1116457	1148433	1147831
N	1653658	1681005	1701812	1701812	1709417	1652853	1696644	1694625
Y	27	25	24	26	27	21	22	18
Li	33.5	65.7	23.12	53.37	31.19	27.60	13.7	10.31
Be	1.70	2.01	1.77	2.37	1.57	1.38	1.79	2.07
Sc	24.82	21.60	20.7	20.5	22.0	21.5	17.78	5.8
Co	40.8	41.6					27.5	
Ga	17.3	18.3	21	34	20	18	17.9	20
As	2.82	9.14	4.5	5.2	4.7	2.5	3.88	4.7
In	0.06	0.08	0.05	0.06	0.05	0.06	0.05	0.03
Cs	0.29	0.22	0.80	1.35	0.62	1.12	0.38	0.13
Ba	618	829	1972	352	181	1359	442	241
La	23.6	30.0	40	24	36	30	28.3	112
Ce	55.7	75.1	88	68	76	71	69.9	119
Pr	7.6	11.6	10.6	8.8	9.4	8.5	9.6	14.2
Nd	27.1	46.2	13.0	18.4	14.1	11.7	35.9	5.1
Sm	6.7	9.4	7.12	7.03	6.79	6.70	7.7	6.77
Eu	2.0	2.8	2.01	1.85	1.21	2.03	2.1	1.58
Gd	6.3	7.9	6.48	6.39	6.41	6.14	6.9	6.64
Tb	0.92	1.16	0.85	0.88	0.90	0.89	0.89	0.77
Dy	4.94	5.90	3.93	4.73	4.77	4.63	4.48	3.58
Ho	1.01	1.14	0.73	0.87	0.90	0.87	0.83	0.67
Er	2.80	3.18	2.01	2.59	2.57	2.48	2.29	1.93
Tm	0.38	0.40	0.25	0.34	0.34	0.33	0.30	0.25
Yb	2.34	2.60	1.59	2.17	2.10	2.09	1.92	1.61
Lu	0.33	0.38	0.23	0.33	0.31	0.31	0.25	0.23
Tl	0.34	0.46	0.41	0.22	0.10	0.38	0.18	0.26
Pb	6.1	8.0	15.4	7.9	13.7	6.2	9.1	7.2
Th	2.83	2.82	4.94	3.48	4.65	4.51	3.82	10.18
U	0.73	0.62	1.15	0.67	1.09	1.27	1.05	1.51
Nb	12	14	8	7	9	11	13	8
V	< 66	123	131	125	148	167	101	74
Rb	56	44	63	58	16	153	23	41
Sr	439	518	261	232	483	406	335	186

In the total alkali–silica (TAS) diagram (Le Bas et al., 1986), the lava and pyroclastic rocks are located in the fields of basaltic trachyandesites, trachyandesites, trachydacites and rhyolites, with wide compositional variation

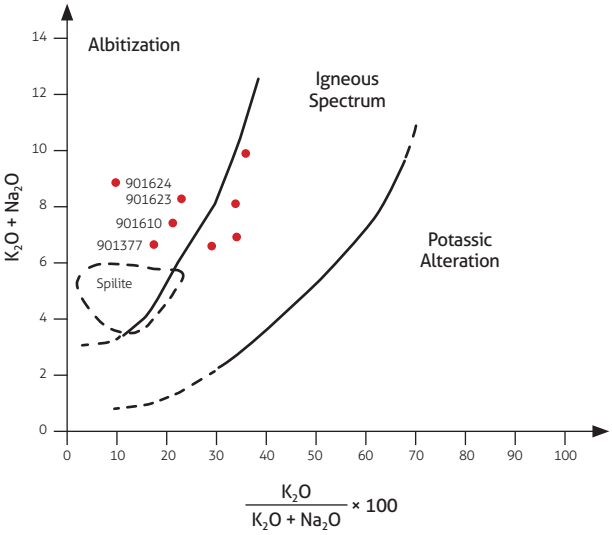

Figure 4. Samples of the La Quinta Formation for identifying alteration according to the diagram of Hughes (1972)

(Figure 5A). The samples IGM 901382, IGM 901437, IGM 901624, IGM 901625 and IGM 901609 are classified in the alkaline series, and the samples IGM 901625, IGM 901377 and IGM 901623 are classified in the subalkaline series. The TAS diagram is similar to that obtained in the model classification of the rocks in the diagram of Streckeisen (1978). In the Nb/Y vs. Zr/Ti diagram (Winchester and Floyd, 1977), the samples of lavas and pyroclastic rocks primarily correspond to the fields of andesites and subalkaline rhyodacites (Figure 5B). The rocks of the La Quinta Formation are metaluminous, and some reach the field of peraluminous rocks (IGM 901609, IGM 901610, IGM 901623), with A/CNK values ranging from 0.7 to 1.3. The A/NK values range from 1 to 2 (Figure 5C). The rocks show a wide dispersion in the SiO_2 vs. K_2O diagram and are distributed in the fields of normal-to-high-K calc-alkaline rocks (Figure 5D).

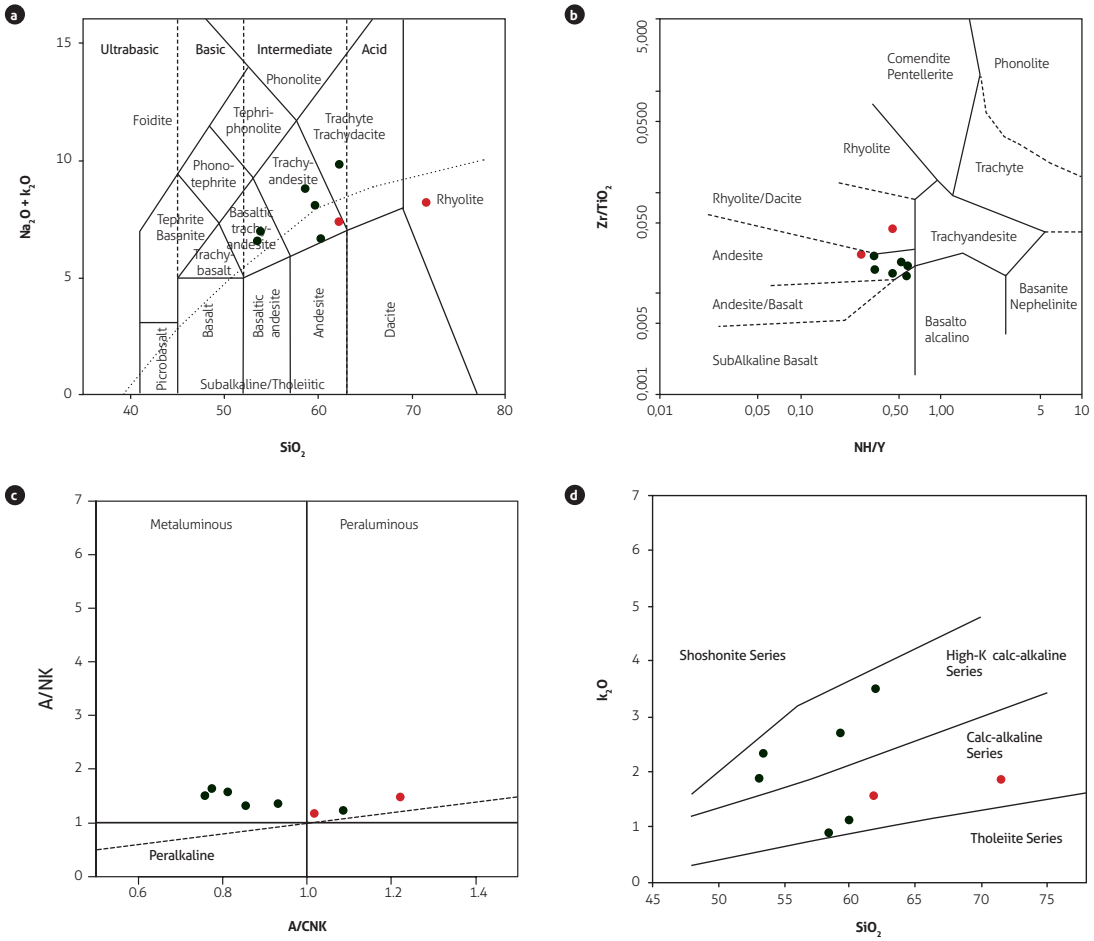

Figure 5. Classification diagram of volcanic rocks of the La Quinta Formation; lavas in black and tuffs in red
A) TAS diagram (Le Bas et al., 1986). B) Winchester and Floyd (1977) classification diagram. C) Shand classification diagram. D) SiO_2 vs. K_2O diagram (Peccerillo and Taylor, 1976)

5.1 Trace elements

The behavior of these elements is analyzed considering the SiO_2 content of the rocks and the chemical classification to determine whether there are relationships between the patterns of rare-earth elements (REE), trace elements and SiO_2 content.

The chondrite-normalized (Nakamura, 1974) REE diagrams of basaltic trachyandesites show a parallel pattern, with a negative slope and with a light-REE enrichment of 70 to 100 times. The $(La/Yb)_N$ ratio ranges from 6.7 to 7.8 and has no Eu anomalies, and the Eu/Eu* ratio is approximately 1. The patterns of trachyandesites and trachydacites are subparallel, and these rocks are slightly more depleted of Tm, Yb and Lu than basaltic trachyandesites. The Eu anomaly ranges from 0.56 to 0.97, and the $(La/Yb)_N$ ratio ranges from 7.3 to 16.8. The rhyolitic tuff has a pattern with an even more negative slope and higher light-REE enrichment, between 300 and 400 times, and further heavy-REE depletion, with Eu and Ce anomalies, indicating plagioclase fractionation and possible contribution of sedimentary material to the source. In the rhyolitic tuff, the Eu/Eu* ratio is 0.7, and the $(La/Yb)_N$ ratio is 46.6 (Figure 6A, C and E). The higher values of the $(La/Yb)_N$ ratio in rhyolite could represent greater contributions from the crust and periods of higher magma flux and/or thicker crust. Lower values of the $(La/Yb)_N$ ratio could indicate greater contributions of mantle materials to the magma and periods of lower magmatic flux (Girardi et al., 2008).

The lavas of the La Quinta Formation, in the normal mid-ocean ridge basalt (NMORB)-normalized trace element diagram (Sun and McDonough, 1989), show negative Nb and Ti anomalies and positive anomalies and high values of Cs, Rb, Ba, Th, K and Pb, which suggests affinity with the continental crust (convergent margins), where these highly incompatible elements abound. The high values of Ba and Rb may result from their mobilization from fluids that interact with magma in the subduction zone. All of these features are characteristic of magmas generated in arc settings (Pearce et al., 1984; Pearce, 1996), with gradual depletion of large-ion lithophile elements (LILE) and enrichment in high-field-strength elements (HFSE; Figure 6). The basaltic trachyandesitic, trachyandesitic and dacitic lavas show similar multielement patterns, with higher Cs, Rb and Ba mobility in trachyandesites and with negative Nb and Ti and positive K and Pb anomalies. The andesitic pyroclastic rocks have multielement patterns in trace elements similar to those of lavas, suggesting that they are cogenetic (Figure 6B and D). The sample of rhyolitic tuff shows a different pattern, with more pronounced negative Nb, P and Ti anomalies (Figure 6F), suggesting at least three magmatic events, as proposed by Cano et al. (2017).

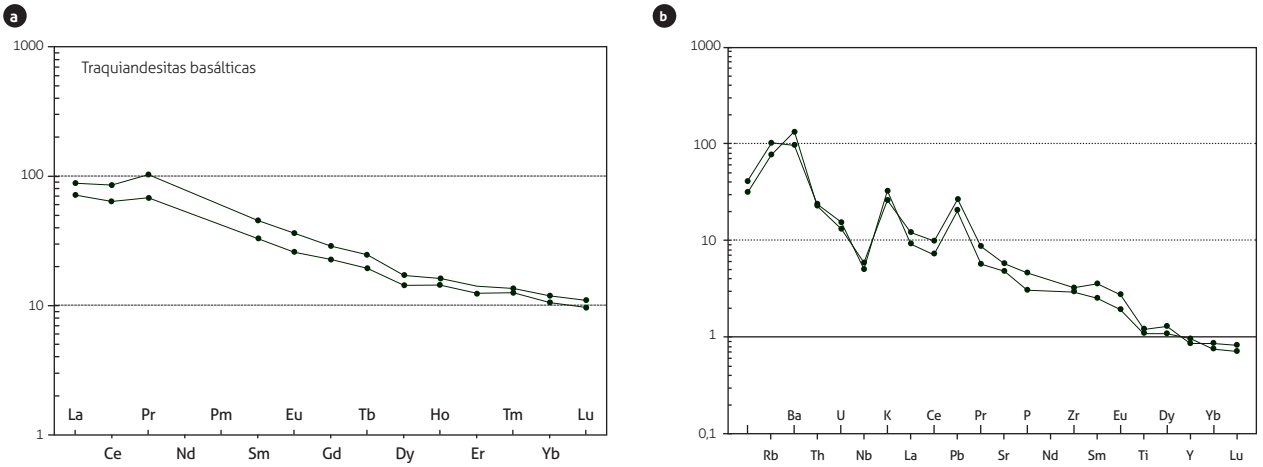

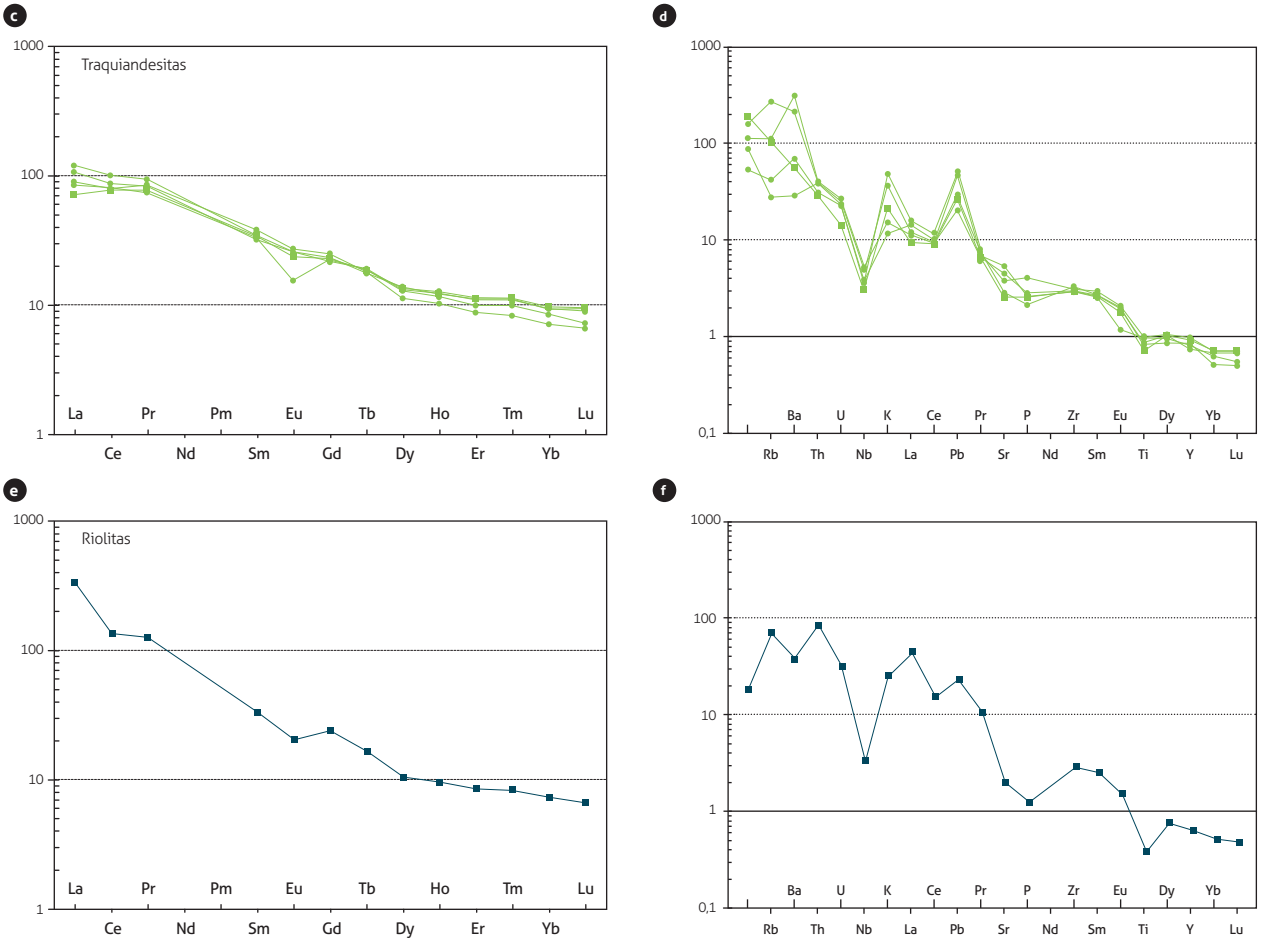

Figure 6. Multielement diagrams corresponding to volcanic and pyroclastic rocks of the La Quinta Formation
A, C, E) Chondrite-normalized REE diagrams (Nakamura, 1974). B, D, F) NMORB-normalized multielement diagrams (Sun and McDonough, 1989)

5.2 Tectonic setting discrimination

The presence of basaltic trachyandesites, trachyandesites, dacites and calc-alkaline rhyolites, together with Nb and Ti anomalies in the multielement diagrams and negative slopes in the REE diagrams, suggests that the volcanic rocks of the La Quinta Formation were generated in an arc setting. The lavas and pyroclastic rocks of the La Quinta Formation, in the Sr/Y vs $(La/Yb)_N$ diagram (Condie and Kröner, 2013), are plotted in the field of continental volcanic arcs, with enrichment in $(La/Yb)_N$ as the rocks become more differentiated (Figure 7). Basaltic trachyandesites, trachyandesites and rhyolites are grouped separately, and rhyolite is plotted outside the field, although in other diagrams, such as that of Pearce (2008), rhyolite falls within the field of arcs.

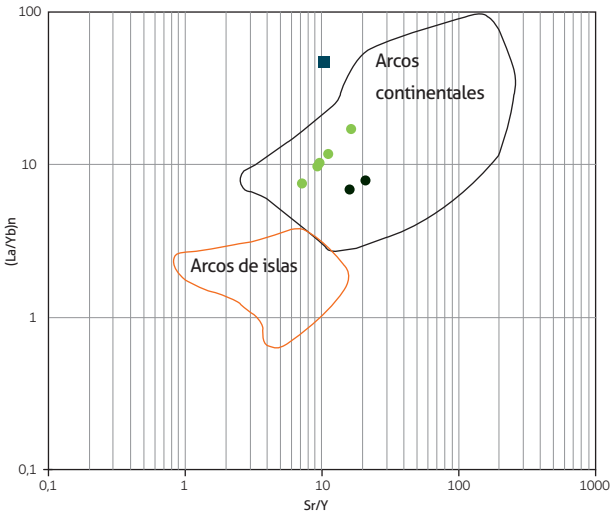

Figure 7. Nb/Yb vs Th/Yb diagram of Condie and Kröner (2013) for rock samples from the La Quinta Formation

6. Geochronology

For the geochronological analysis of the volcanic rocks of the La Quinta Formation, six rocks were analyzed using the U-Pb zircon LA-ICP-MS method. The U-Pb ages reported by González et al. (2015 a, b) were collected and are outlined in Table 4, and the corresponding spatial locations are shown in Figure 1. The reported ages are calculated with the Pb^{206}/U^{238} ratio. In general, all the ages show dispersion in each of the dated samples. This phenomenon is well-documented in igneous systems, due to the long crystallization of zircon within the magmatic system (Schoene et al., 2015) or to Pb loss and the presence of older inherited zircons in the magma (antecrystals). The crystallization age of each rock is calculated considering the presence or absence of populations of ages according to the probability density diagram and the observable distribution in the Tera-Wasserburg diagram, which could suggest populations of antecrystals. For this purpose, cathodoluminescence images and the age of each zircon are analyzed, as well as the locations of zircon ablations, for which the younger zircon populations are separated from the zircon populations of the magmatic system that could correspond to the ages of the antecrystals. Three ages are determined in the rocks that show high dispersion of ages according to the Pb^{206}/U^{238} ratio: the age of the entire population, the age of the likely antecrystals and the youngest age of likely crystallization. These ages are analyzed in the discussion.

Table 4. Summary of U-Pb ages determined by LA-ICP-MS in zircon samples of the La Quinta Formation

Sample No.	W Longitude	N Latitude	Rock	Age (Ma)	MSWD	Inheritances	Reference
GOE-1045a	1148285	1701812	Trachydacite	188.3 ± 2.2	3.9	1,902.2 ± 70 (n = 1); 1,138-1,191 (n = 2); 1,010.2-1,097 (n = 5); 856.2 ± 21.6 (n = 1); 931.1 ± 22 (n = 1); 613.5 ± 15; 210-218 (n = 3)	Present study
GR-6849	1147831	1694625	Tuff*	179.5 ± 2.1	4.3	1.974.3; 1,369-1.311 (n = 3); 1,283-1,209 (n = 3); 1,076-926.3 (n = 5); 992-926.3 (n = 4); 873.3-855.9; 623 ± 25.6; 556-551 (n = 3); 287.7 ± 8 (n = 1)	Present study
GR-6851	1156113	1709417	Trachyandesite	188.3 ± 2.5	6.6	1,913.8 ± 39.7 (n = 1); 1,361.1 ± 31 (n = 1), 892.6-996.2 (n = 2); 625.4-605.2 (n = 2); 226.2-203.5 (n = 4)	Present study
GOE-1057	1124017	1660152	Vitreous tuff*	175.5 ± 1.4	5.3	1,263.2 ± 33 (n = 1); 956.2-969.5 (n = 2).	Present study
GZ-6903	1123566	1659592	Dacite*	174.8 ± 1.2	3.4	1,515 ± 55.6 (n = 1); 1,465.7 ± 55 (n = 1); 1,343-1,322 (n = 2); 1,278.8-1,202 (n = 5); 1,167-1,153 (n = 5); 1,087-1,004 (n = 7); 993-906 (n = 19); 882.8-852 (n = 4); 269-252 (n = 4)	Present study
GR-6854	1116457	1652853	Trachyandesite	—		1,615 ± 40 (n = 1); 1,578-1,537 (n = 3); 1,487.8 ± 45 (n = 1); 1,559-1,487 (n = 3); 1,359-1,295 (n = 3); 1,266-1,199 (n = 5); 1,072-1,013 (n = 6)	Present study
U-Pb ages in previous studies							
DQB-0058r	1100929	1590508	Tuff	181 ± 1.1	1.2		González et al., 2015a
DQB-0060r	1101194	1589892	Rhyolite	180 ± 1	3.1		González et al., 2015a
DQB-0061r	1100 988	1589202	Rhyolite	177 ± 1	1.7		González et al., 2015a
ABE-oo75ra	1100882	1585343	Dacite	181 ± 4	4.5		González et al., 2015a

* Petrographic classification.

The sample GOE-1045A corresponds to a dacite according to the petrographic classification and to a trachydacite according to the chemical classification. There are two populations of zircons in this rock: one of colorless, flattened and elongated prismatic zircons (stems), with sizes ranging from 80 to 110 microns in length, and a second population of oval zircons, with sizes ranging from 20 to 100 microns. In cathodoluminescence (CL) images, the prismatic crystals show the typical oscillatory zonation of igneous zircons (Figure 8E and F), and the oval zircons correspond to inherited zircons (cathodoluminescence supplementary files). A total of 52 ablations were performed in 54 zircons (supplementary table), disregarding discordances greater than 10% in the data interpretation. The age of the entire set of zircons is calculated as 188.3 ± 2.2, with a mean square weighted deviation

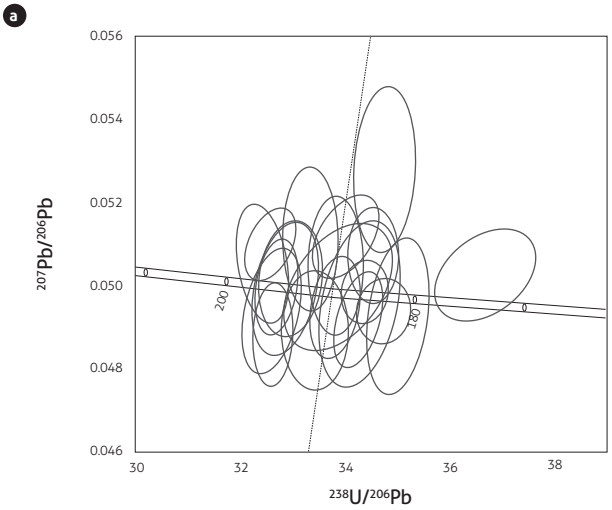

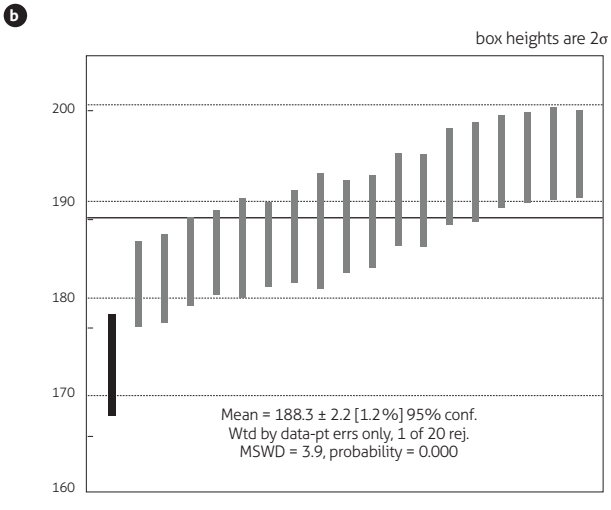

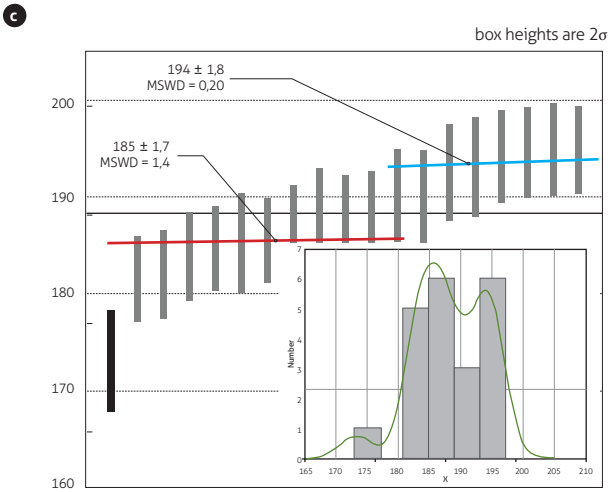

Ablación - circón	Edad	2S
GOE_1045_A_24	181,62	4,55
GOE_1045_A_49	182,21	4,60
GOE_1045_A_45	182,89	4,47
GOE_1045_A_1	183,94	4,41
GOE_1045_A_53	184,85	4,35
GOE_1045_A_31	185,37	5,11
GOE_1045_A_51	185,53	4,41
GOE_1045_A_47	186,54	4,78
GOE_1045_A_42	187,13	5,97
GOE_1045_A_3	187,63	4,60
GOE_1045_A_52	187,98	4,54
GOE_1045_A_8	190,21	4,92
GOE_1045_A_30	190,26	4,66

Ablación - circón	Edad	2S
GOE_1045_A_7	192,66	5,04
GOE_1045_A_27	193,13	5,04
GOE_1045_A_54	194,37	4,60
GOE_1045_A_44	194,70	4,65
GOE_1045_A_18	194,96	4,92
GOE_1045_A_2	195,00	4,48
GOE_1045_A_20	195,76	4,73

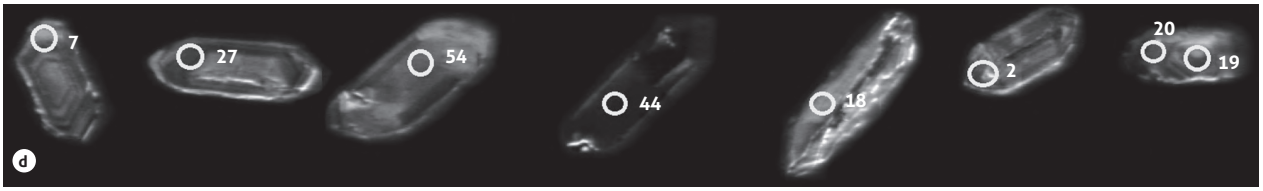

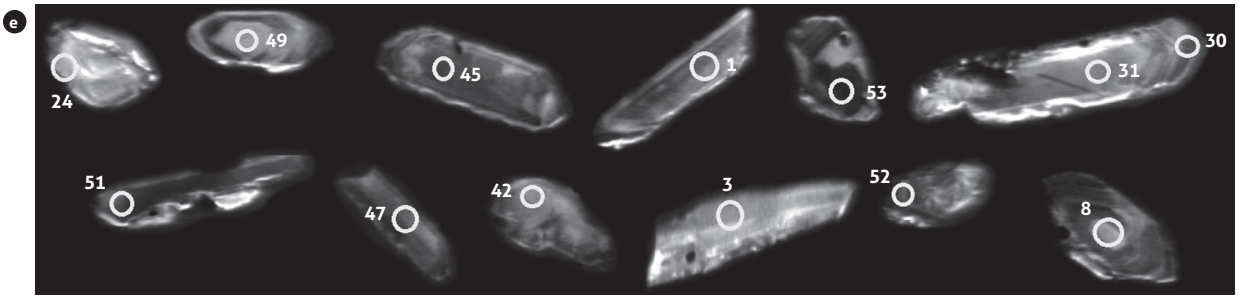

Figure 8. Results of U-Pb zircon dating of the sample GOE-1045A
A) Tera-Wasserburg Concordia diagram. B) Mean age. C) Mean ages of the "populations" and tables of the ages of each zircon. Black vertical bars correspond to values rejected by the Isoplot software in the mean age calculations. The age of the likely antecrystals is indicated in blue, and the crystallization age of the younger rock zircons is indicated in red. D) Cathodoluminescence image of older zircons in the population, indicating crystallization. E) Cathodoluminescence image of younger zircons

(MSWD) = 3.9 from twenty data points (Figure 8A and B), which is interpreted as the likely rock crystallization age. The probability density diagram presents two likely populations with two different ages: the population of previous zircons of the igneous system (or antecrystals) present a mean age of 194.4 ± 1.8 with MSWD = 0.20 (n=8), and the population of younger zircons present an mean age of 185.7 ± 1.7 with MSWD = 1.4 (n = 13), corresponding to the Pliensbachian (Figure 8C). A comparison of the cathodoluminescence images of the oldest and the youngest zircons yields no differences, which prevented us from identifying antecrystals (Figure 8D and E). Most of the ablations in the young and old zircons are applied to the crystal cores. The Th/U ratio ranges from 0.6 and 1.7. These values are in line with the typical ratios of igneous zircons (Rubatto, 2002), finding inherited zircons from the Triassic (n = 3), Neoproterozoic (n = 9), Mesoproterozoic (n = 9) and Paleoproterozoic (n = 1).

The sample GR-6851 corresponds to an andesite according to the petrographic classification and to a trachyandesite according to the chemical classification. The zircons of this rock are short, flattened, prismatic and euhedral, showing few stems and needles, with round and slightly oval ends and with sizes smaller than 100 microns, and some are fractured. In the cathodoluminescence (CL) images, the flattened crystals have oscillatory zonation, and the stems show a parallel pattern typical of igneous zircons (Figure 9D and E; supplementary file). A total of 48 ablations were performed in 55 zircons (supplementary table) disregarding discordances greater than 10% in the data interpretation. The age of the entire set of zircons is 188.3±2.5, with MSWD = 6.6 from twenty-two data points (Figure 9A and B), which is interpreted as a likely rock crystallization age. The probability density diagram presents two probable populations with two different ages: the population of the previous zircons of the igneous or anticrystal system present a mean age of 191.6 ± 1.7 with MSWD = 2 (n=16), and the population of younger zircons present an average age of 181.2 ± 1.7 with MSWD = 1.4 (n = 6), which corresponds to the Pliensbachian (Figure 9C). A comparison of the cathodoluminescence images of the oldest and youngest zircons yields no differences, which prevented us from identifying any antecrystals (Figure 9D and E). Most of the ablations in the young and old zircons are applied to the crystal cores, and the crystals subjected to multiple ablations yield very similar ages for the rims and cores. The Th/U ratio ranges from 0.58 to 1.6, which is in line with the typical ratios of igneous zircons (Rubatto, 2002), demonstrating inherited zircons from the Triassic (n = 4), Neoproterozoic (n = 4), Mesoproterozoic (n = 2) and Paleoproterozoic (n = 1).

The sample GR-6849 corresponds to a tuff according to the petrographic classification and to a rhyolite according to the chemical classification. The zircons of this rock correspond to two populations: one of short and stem-like, inequigranular, prismatic and euhedral crystals and another of sparse subrounded zircons of oval shapes. In the cathodoluminescence (CL) images, the prismatic crystals show oscillatory zonation, and some have inherited cores; the stem-like crystals show the typical parallel arrangement of igneous zircons. A total of 61 ablations were performed on 51 zircons (supplementary table), and discordances greater than 10% were disregarded in the data interpretation. A single weighted average age of 179.5 ± 2.1 with MSWD = 4.3 is assessed from 28 data points. This age is interpreted as the rock crystallization age and corresponds to the Toarcian (Figure 10A and B). The Th/U ratio ranges from 0.6 to 1.7, which is in line with the typical ratios of igneous zircons (Rubatto, 2002), demonstrating inherited zircons from the Permian (n = 1), Neoproterozoic (n = 11), Mesoproterozoic (n = 7) and Paleoproterozoic (n = 2).

Sample GZ-6903 corresponds to a dacite according to the petrographic classification. The zircons of this rock are part of at least two populations: one of short prismatic euhedral crystals with a few stem-like equigranular crystals and the other of oval zircons. In the cathodoluminescence (CL) images, the prismatic crystals demonstrate the oscillatory zonation typical of igneous zircons, and the oval crystals seem to have metamorphic overgrowths. A total of 69 ablations were performed in 50 zircons (supplementary Table), and discordances greater than 10% were disregarded in the data interpretation. A single weighted average age of 175.2 ± 2.3 with MSWD = 1.02 is calculated from nine data points, which is interpreted as the rock crystallization age and corresponds to the Aalenian (Figure 10C and D). The Th/U ratio ranges from 0.57 and 1.5, which is in line with the typical ratios of igneous zircons (Rubatto, 2002), demonstrating inherited zircons from the Triassic (n = 2), Permian (n = 2), Neoproterozoic (n = 24) and Mesoproterozoic (n = 25).

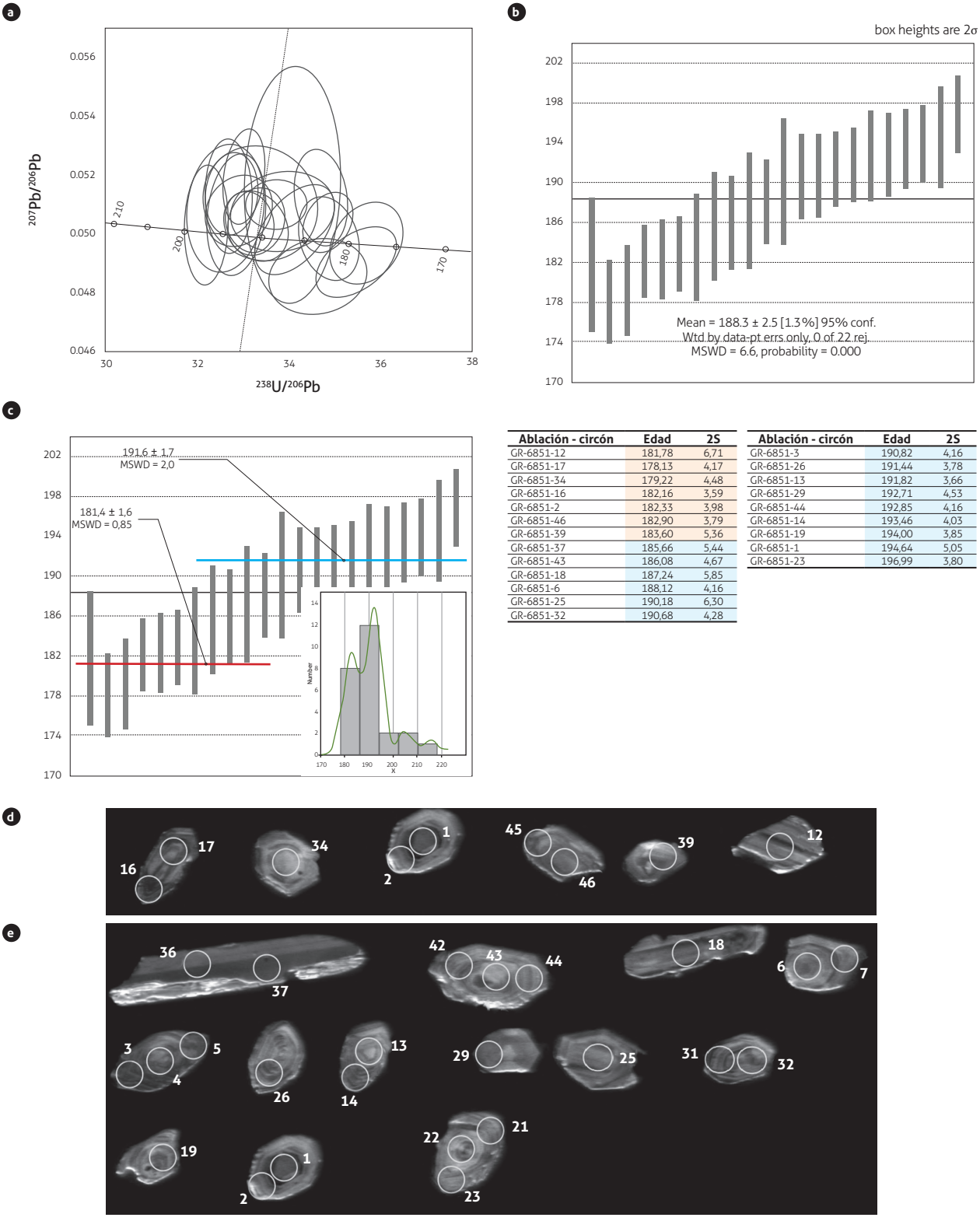

Ablación - circón	Edad	2S
GR-6851-12	181,78	6,71
GR-6851-17	178,13	4,17
GR-6851-34	179,22	4,48
GR-6851-16	182,16	3,59
GR-6851-2	182,33	3,98
GR-6851-46	182,90	3,79
GR-6851-39	183,60	5,36
GR-6851-37	185,66	5,44
GR-6851-43	186,08	4,67
GR-6851-18	187,24	5,85
GR-6851-6	188,12	4,16
GR-6851-25	190,18	6,30
GR-6851-32	190,68	4,28

Ablación - circón	Edad	2S
GR-6851-3	190,82	4,16
GR-6851-26	191,44	3,78
GR-6851-13	191,82	3,66
GR-6851-29	192,71	4,53
GR-6851-44	192,85	4,16
GR-6851-14	193,46	4,03
GR-6851-19	194,00	3,85
GR-6851-1	194,64	5,05
GR-6851-23	196,99	3,80

Figure 9. Results for U-Pb zircon dating of sample GR-6851
A) Tera-Wasserburg Concordia diagram. B) Mean age. C) Mean ages of the "populations" and tables of ages of each zircon. The ages of the likely antecrystals are shown in blue, and the crystallization ages of the younger zircons are shown in red. D) Cathodoluminescence images of the younger zircons. E) Cathodoluminescence images of the older zircons of the population, indicating crystallization

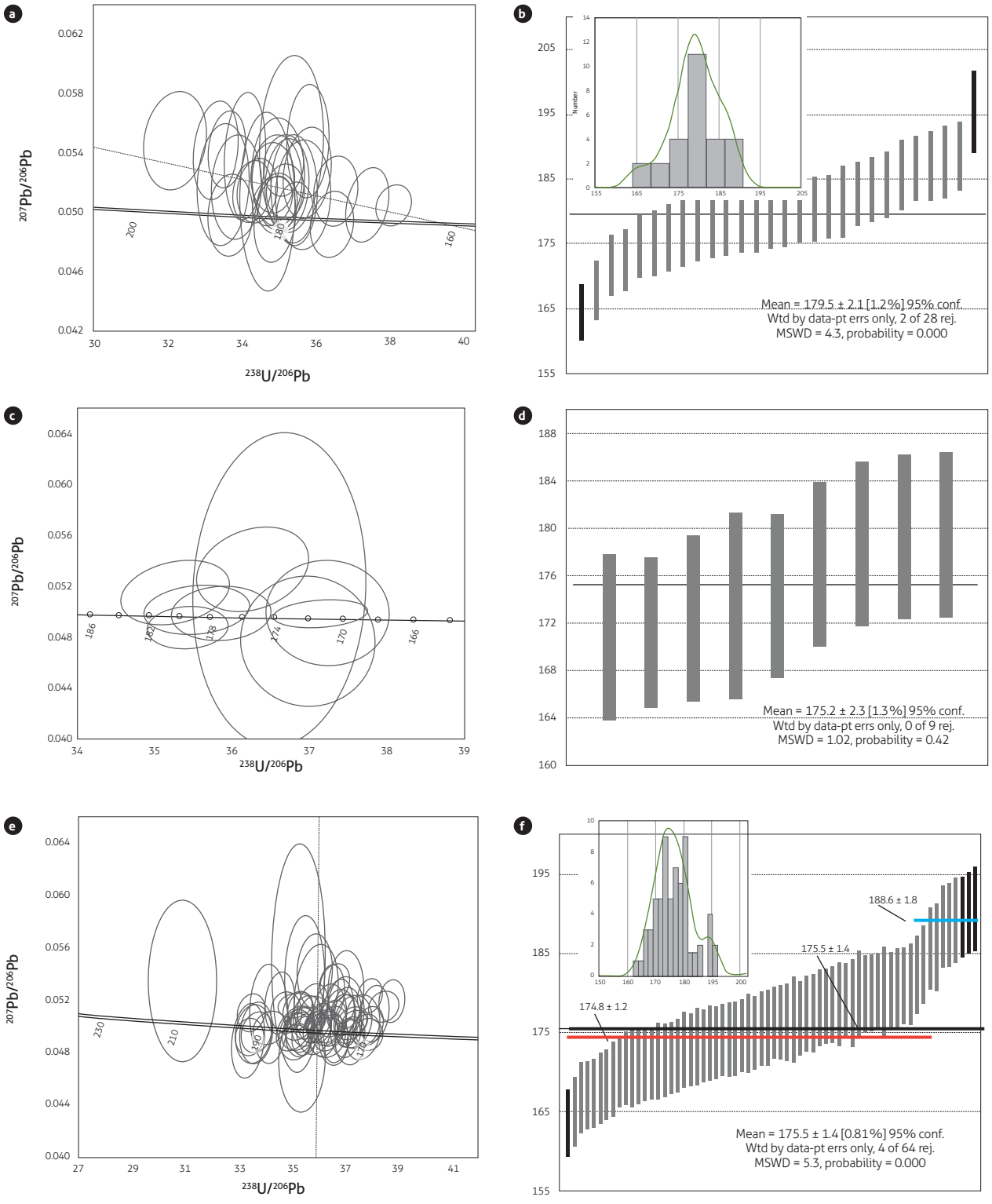

Figure 10. Results for U-Pb zircon dating
A) Tera-Wasserburg Concordia diagram of sample GR-6849. B) Mean age and probability density diagram of the zircons that define the age of sample GR-6849. C) Wetherill Concordia diagram of sample GZ-6903. D) Mean age of sample GZ-6903. E) Tera-Wasserburg Concordia diagram of sample GOE-1057. F) Mean age and probability density diagram of the zircons that define the age of sample GOE-1057 (the ages of all the zircons are shown in black; the ages of the possible antecrystals are shown in blue, and the crystallization ages of the younger zircons are shown in red). The black vertical bars in B and F correspond to values rejected by the Isoplot software in the calculation of the mean age

Sample GOE-1057 corresponds to a tuff according to the petrographic classification. The zircons of this rock are prismatic, short and equigranular, with sizes ranging from 50 to 100 microns. In the cathodoluminescence (CL) images, the zircons that define the age show oscillatory zonation, and some have complex zonation (cathodoluminescence supplementary file). A total of 94 ablations were performed in 60 zircons (supplementary table), disregarding discordances greater than 10% in the data interpretation. The age of the entire set of zircons is 175.5 ± 1.4 with MSWD = 5.3, as assessed from 64 data points (Figure 10E and F), which is interpreted as the likely rock crystallization age. The probability density diagram shows two likely populations with two different ages (Figure 10E): the population of previous zircons of the igneous system or antecrystals yields a mean age of 188.6 ± 1.8 with MSWD = 0.51 (n=8), and the population of younger zircons yields a mean age of 174.8 ± 1.2 with MSWD = 3.4 (n = 56), corresponding to the Aalenian (Figure 10F). A comparison of the cathodoluminescence images of the young and old zircons shows that the oldest ages are found for crystal rims or in fractured crystals, and some crystals have younger cores (cathodoluminescence supplementary file, supplementary table). The Th/U ratio ranges from 0.51 to 2.26, which is in line with the ratios typical of igneous zircons (Rubatto, 2002), demonstrating inheritances from the Triassic (n = 1), Neoproterozoic (n = 2) and Mesoproterozoic (n = 1).

6.1 Inheritances

To determine the populations of inherited zircons in the volcanic rocks of the La Quinta Formation, the inheritance results of six samples dated using the U-Pb zircon method are considered (GOE-1045a, GR-6851, GR-6849, GZ-6903, GOE-1057 and GR-6854); the ages of each sample are integrated and grouped. Data with discordances > 10% up to 800 Ma and discordances > 5% in ages older than 800 Ma are disregarded, leaving 112 data points that meet the condition for analysis.

The inheritances of each sample are shown in the Concordia diagrams of Figure 11, which includes the samples that do not meet the concordance criteria. The populations of inherited zircons in the volcanic rocks of the La Quinta Formation are shown in Figure 12, and some zircons characteristic of these populations are shown in Figure 13. The oldest population dates back to ~1.911 Ma (n = 3), with one concordant data point and two discordant data points, and two important populations date back to the Mesoproterozoic, at ~1.549 Ma and ~1.354, with three younger populations of ~1.247 Ma, ~1.153 and ~1.068 Ma. The most representative populations of the Neoproterozoic are dated between ~983 Ma and ~871 Ma, with two younger populations between ~618 and ~553 Ma. Four concordant data points, 287.6 ± 8.2, 269.9 ± 10, 258.8 ± 10 and 251.9 ± 9.4 Ma, are identified in the Permian. The eight Triassic zircons have a mean age of 210.3 ± 5.8. The Mesoproterozoic populations have Th/U ratios below and above 0.3, which suggests that the zircons have an igneous and metamorphic basement. The Neoproterozoic populations have Th/U ratios > 0.3, which suggests that they are mostly igneous zircons (Rubatto, 2002). The Permian and Triassic zircons generally have Th/U ratio > 1 and are thus igneous zircons (Figure 12Q and R and Figure 13A and B).

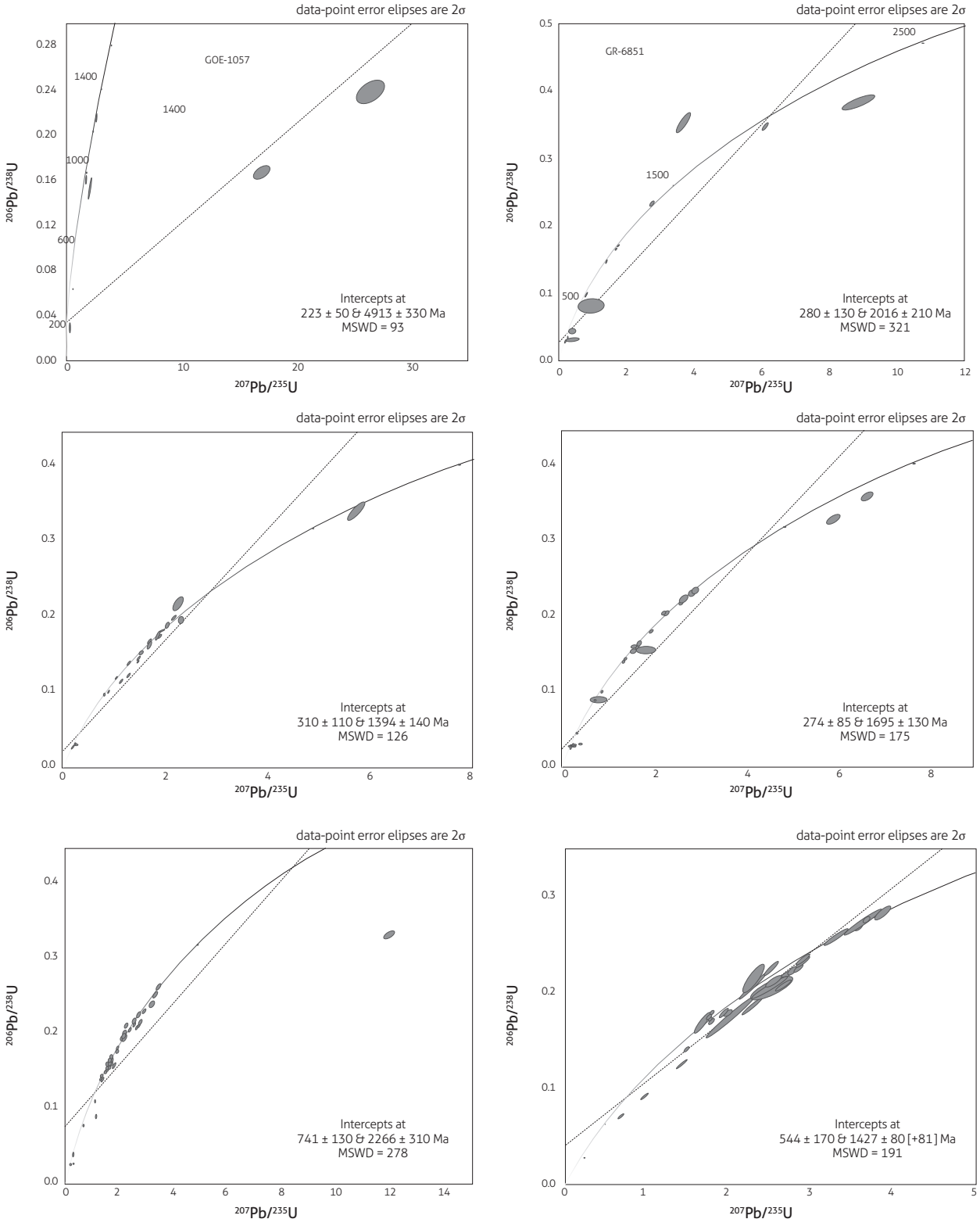

Figure 11. Concordia diagrams with all inherited age data per sample

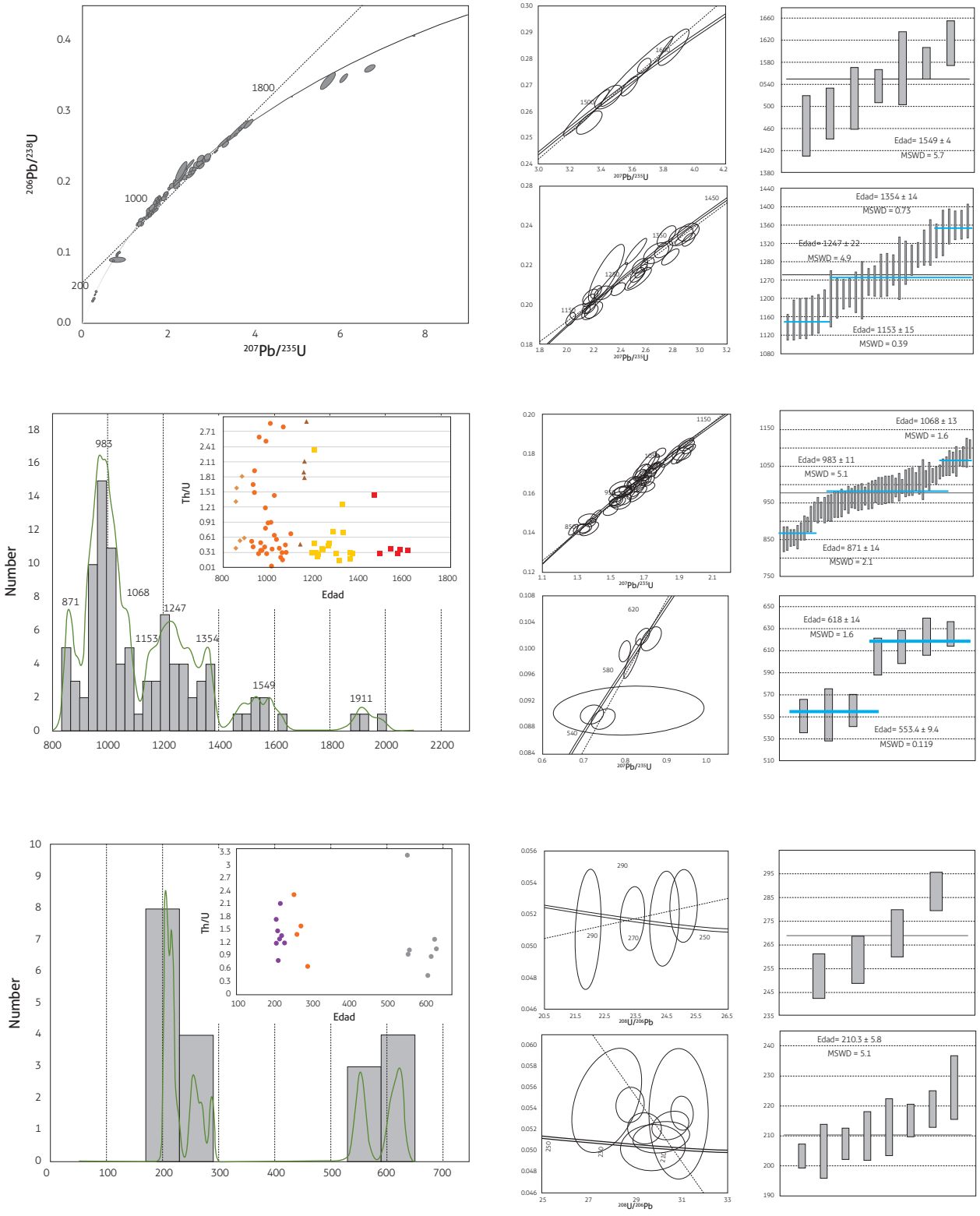

Figure 12. U/Pb geochronology of inherited zircons of the La Quinta Formation. Concordia, probability density, weighted average age and Th/U vs. age diagrams

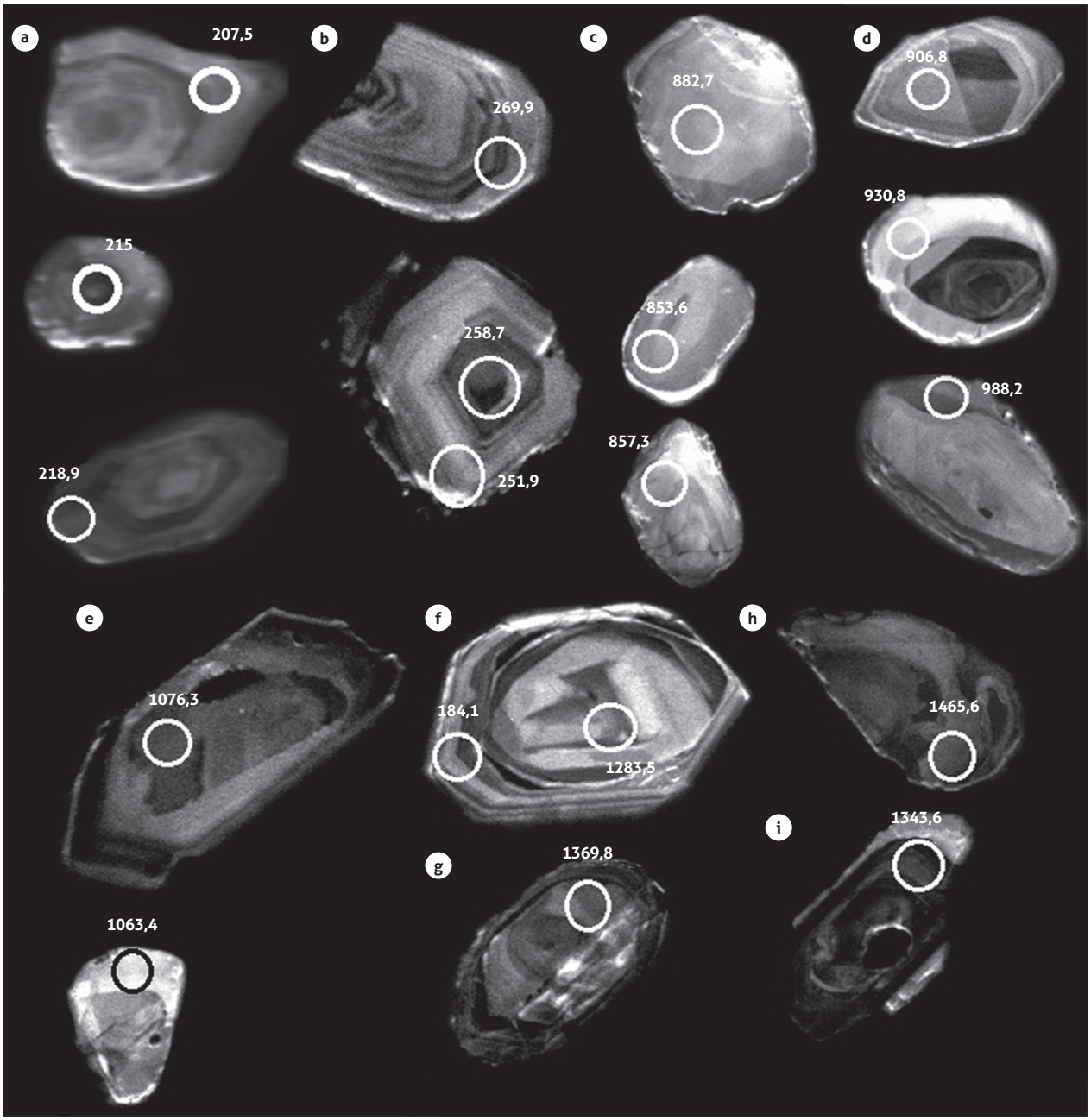

Figure 13. Cathodoluminescence images of representative xenocrystals from different populations
A and B) Triassic and Permian igneous xenocrystals with concentric texture. C) Homogeneous luminescent xenocrystals with weak internal structure. D) Crystals with metamorphic overgrowth rims around inherited cores. E) Inherited cores truncated by concentric and clear growth rims. F, G, H, I) Mesoproterozoic inherited nuclei, in some cases, with Jurassic igneous rims

7. Discussion

7.1 Ages and correlations

The crystallization ages assessed in some samples show high dispersion in the data, which suggests the presence of older zircons (antecrystals) or Pb loss. The zircon structure, shape and texture, which determine the crystallization age, show no differences according to the cathodoluminescence images for their differentiation.

The Pb^{206}/U^{238} ages that determine the crystallization of samples GOE-1045A and GR-6851 range from ~15 Ma to ~18 Ma. Most of these ages are assessed in zircon cores, with similar ages for the rims and cores when tested, suggesting that the differences in age do not result from Pb loss. Thus, these two samples likely contain a population of antecrystals, and the crystallization age is represented in the younger population; however, the information is considered insufficient, and therefore, the crystallization age of these two rocks is that of the entire population that meets the selection criteria described above. Sample GOE-1057 has a population of older ages (nine data points), which are located on the rims of zircon crystals and on zircons with internal fracturing, with younger ages in the cores of some zircons than on the rims, suggesting Pb loss and the absence of antecrystals at these more remote ages. For this reason, we consider the crystallization age of this sample to be 174.8 ± 1.2 Ma with MSWD = 3.4 and hence slightly younger than the weighted average age of the entire population, removing these eight ages from the calculation.

The data from this study indicate that the volcanism of the La Quinta Formation, in the Perijá mountain range, was active from the Lower to the Middle Jurassic. The ages suggest that the volcanism began in ~191 Ma (samples GOE-1045A and GR-6851) and continued until at least ~163 Ma (according to the U-Pb age reported by Barret et al., 2008 in Venezuela), with at least three likely periods of volcanic activity: ~188 Ma, ~179-181 Ma and ~173-175 Ma, which correspond to the crystallization ages of the rocks of the La Quinta Formation (Table 4). A comparison of the duration and episodes of crystallization of the volcanic rocks in units correlated with the La Quinta Formation, and which are part of this arc, such as the Jurassic vulcanites of the Sierra Nevada de Santa Marta (Quandt et al., 2018; Rodríguez et al., 2019b), Noreán Formation (Correa et al., 2019) and Saldaña Formation (Rodríguez et al., 2016), shows that the period of volcanic activity is virtually the same in the different volcanic units that make up the arc or fall within the crystallization period of the arc (Table 5). Furthermore, this period matches the duration of plutonism described by Rodríguez et al. (2018) and Rodríguez et al. (2020) in VSM and in SNSM. Although the geochronological data collected in the La Quinta Formation are not abundant, the petrographic and chemical composition of the rocks and the U-Pb ages suggest that the volcanism of the La Quinta Formation evolved from basic to acidic and from metaluminous to peraluminous, initially generating lava flows of basaltic trachyandesites and subsequently trachyandesites and dacites and ultimately becoming explosive and generating rhyolites and rhyolitic pyroclastic rocks in this region. This volcanism occurred in a subaerial setting, developing hematite, which stained the rocks a reddish color. The dates estimated in previous studies using the U-Pb method on volcanic rocks indicate ages ranging from 176 to 182 Ma (González et al., 2015 a, b) on the western flank of the Perijá mountain range and of 163 ± 5 Ma in Venezuela (Dasch, 1982). Barrett et al. (2008) located this unit between the Lower and Middle Jurassic, according to fossil evidence of *Ornithischian Lesothosaurus* sp. and reptile remains (in Nova et al., 2012).

The comparison of the geochronology, geochemistry and petrography results of this study with those reported for the Noreán Formation of the Santander massif in the San Lucas mountain range (Ingeominas-UIS, 2006a, 2006c, 2006d, 2006e; Leal Mejía, 2011; González et al., 2015a, 2015b and Correa Martínez et al., 2019), for the volcanic units of Sierra Nevada de Santa Marta (Guatapurí and Corual formations, Caja de Ahorros, La Paila and Los Clavos ignimbrites, Los Tábanos Triassic spilites, keratophyric porphyries and rhyodacites and Golero rhyolites) (Tschanz et al., 1969a; Maze, 1984; Quandt et al., 2018, Rodríguez et al., 2019c), for Ipapure-Cerro de La Teta rhyodacites in Upper Guajira (Radelli, 1960; Rodríguez and Londoño, 2002; Zuluaga et al., 2015) and for the Saldaña Formation and Pitalito vulcanites in the Upper Magdalena Valley (Rodríguez et al., 2016; Zapata et al., 2016) shows that all the volcanic rocks of these units are correlated with the volcanic rocks of the La Quinta Formation.

Table 5. Comparison between the crystallization period of volcanic arc units and periods of increased crystallization, based on U-Pb zircon ages

Lithological unit	Activity lapse	Crystallization episodes	Source
Saldaña Formation and Pitalito vulcanites	~190 to ~164 Ma	~190-186 Ma, ~183-178 Ma, ~173-168 Ma	Rodríguez et al. (2016)
Noreán Formation	~194 to ~175 Ma	~192 Ma, ~185 Ma, ~175 Ma	Correa et al. (2019)
Volcanic units of SNSM	~196 to ~165 Ma	~195 Ma, ~186 Ma, ~178-175 y ~168 Ma	Rodríguez et al. (2019b)
La Quinta Formation	~196 to ~164 Ma	~188 Ma, ~179-181 Ma, ~173-175 Ma	Present study
Cerro de La Teta and Ipapure rhyodacites	~ 184 to ~181		Zuluaga et al. (2015)

The U-Pb zircon geochronology results of the volcanic units show similar crystallization periods and geochemical behavior of major and trace elements suggesting that they were formed from the same continental volcanic arc (Rodríguez et al., 2016; 2018, 2019b, Correa et al, 2019, Quandt et al., 2018), which was subsequently dispersed along the paleomargin of northern South America (Bayona et al., 2010; Villagómez et al., 2015; Zapata et al., 2016; Zuluaga et al., 2015, Rodríguez et al., 2019a).

7.2 Inheritance and basement

The presence of xenocrystals and inherited zircon cores in the rocks of the La Quinta Formation is most likely related to the melting of older wall rocks. This process commonly occurs in magmatic systems. The formation of antecrystals, which is more debatable and difficult to determine, was found in some of the rocks analyzed in this study, which is in line with the crystallization episodes of the arc (Table 5).

The ages of the inherited zircons in the volcanic rocks of the La Quinta Formation match the ages and inheritances described by Ibáñez Mejía et al. (2015) for the Putumayo orogen. These authors suggest that the inherited zircons with ages older than 0.9 Ga possibly derived from metasedimentary rocks of the Mesoproterozoic basement and were contributed to by an older Cratonic domain. In our case, the inherited zircons were incorporated into Jurassic magmas, which produced the La Quinta Formation, among others, through melting of the Putumayo orogen crust. Ages between 1.15 and 1.10 Ga, according to Ibáñez Mejía et al. (2015), are associated with accretion of arc edges against the continental margin, triggering an early metamorphic event, and ages of approximately 0.99 Ga have been interpreted as the Amazonia incorporation into the core of Rodinia during the collision with the Baltic (Ibáñez Mejía et al., 2015). This would largely explain the oldest inheritances of the volcanic arc of 0.9 Ga, which would be contributed to the arc by the basement of the Putumayo orogen that belongs to the Chibcha Terrane (Restrepo et al., 2009). This terrane currently spans across part of the Cordillera Oriental [Eastern Ranges] and the easternmost section of the Cordillera Central [Central Andes] and consists of a Neoproterozoic crystalline basement (Putumayo orogen), Paleozoic marine sedimentary sequences and intrusions and volcanic rocks of arcs formed during the Carboniferous-Permian and the Lower-to-Middle Jurassic. After the formation of the arcs, the Chibcha Terrane was divided into blocks scattered along the paleomargin of northern South America, as we currently know it (Rodríguez et al., 2019a).

The ages of 618 and 553 Ma are similar to the inheritances described by Rodríguez et al. (2019a) in the plutons of the Permian arc, which, according to Nova et al. (2018), possibly correspond to the zircons of units included in the Mixteco and Maya blocks of Mexico. The source of the Triassic igneous xenocrystals is unknown; most likely, they are related to minor igneous bodies still unidentified in the Chibcha Terrane and in general older than plutonic rocks of intrusions dated between the Triassic and the Lower Jurassic of the Santander massif.

A comparison of the ages of the xenocrystals and inherited zircon cores of the La Quinta Formation with other correlated volcanic units suggests that all these volcanic units have similar zircon inheritance, which would indicate that they shared the same preexisting basement, on which all the arc units were emplaced: the Noreán Formation has zircon inheritances from the Mesoproterozoic (~1400 Ma, n = 1) and from the period between the Mesoproterozoic and Neoproterozoic (~1.050 and 950 Ma, n = 3) (Correa Martínez et al., 2019); the Saldaña Formation has inheritances from the Mesoproterozoic (~1.460, ~1.570 and ~1.630 Ma), Neoproterozoic

(~906 to ~1.060 Ma and ~510 Ma), Permian (~270 Ma) and Triassic (~223 Ma) (Rodríguez et al., 2016; Zapata et al., 2016); the Jurassic volcanic rocks of the Sierra Nevada de Santa Marta have Mesoproterozoic, Neoproterozoic, Paleozoic, Permian and Triassic xenocrystals, as well as ages contemporary with Pan-African orogeny events during the Devonian (400-650 Ma) (Rodríguez et al., 2019c).

7.3 Tectonic model

Different arc models have been proposed for Jurassic magmatism: Bayona et al. (2010), based on paleomagnetic data, consider that blocks moved northward relative to a point on the craton and formed an oblique-subduction margin along the South American paleomargin. Villagómez et al. (2015), similar to Bayona et al. (2010), conclude that the Jurassic blocks of the Upper Magdalena, Cordillera Central [Central Andes], San Lucas mountain range and Sierra Nevada de Santa Marta are allochthons formed in an arc and in a back-arc and the Jurassic rocks of the Santander massif are autochthonous and related to a rift; Spikings et al. (2015) postulate that the westward shift in Jurassic magmatism over time is due to slab rollback and/or trench retreat; Bustamante et al. (2016) and Quandt et al. (2018) embrace the idea of highly oblique subduction; the former explain the compositional changes by reduced sediment melting and long-term source evolution (proposed by Leal Mejía, 2011); Zapata et al. (2016) consider the volcanic and plutonic rocks to share the same arc history and to be related to a fragmented Jurassic magmatic belt; Zuluaga et al. (2015) discuss the relationship between the plutons and Jurassic volcanic rocks of La Guajira and conclude that they were formed in the same axis, which would imply that there was no back-arc and that they formed within the arc; Rodríguez et al. (2018) consider the arc to be represented by volcanic and plutonic rocks that were formed in the Upper Magdalena Valley during three high-activity magmatic pulses (from 188 to 186 Ma, from 183 to 178 Ma and from 173 to 168 Ma), that the plutons tended to rejuvenate from west to east, that the north of the Ibagué Batholith is not part of this arc and that this batholith was emplaced in an Upper Jurassic orogen (Blanco Quintero et al., 2014, Rodríguez et al., 2020). These authors attribute the compositional changes and the migration of the plutons to erosion of the accretionary prism due to the increased water flow from the subduction slab, consequently decreasing the *solidus* temperatures; Rodríguez et al. (2020) propose three magmatic arcs for the Jurassic magmatism of the northern Andes, each one formed at different periods, with their own chemical and petrographic composition and emplaced in different orogens.

The geochemistry and geochronology data presented here show the correlation between the volcanic units that make up the different blocks of the northern Andes (Saldaña Formation, Pitalito vulcanites, Noreán Formation, SNSM Jurassic volcanic units, La Quinta Formation and Cerro de La Teta and Ipapure rhyodacites), which suggests that from Ecuador through the Upper Magdalena Valley to La Guajira, volcanism was generated in a similar time span of ~30 Ma, from 195 Ma to 164 Ma, and that the pulses or episodes of peak magmatic activity were virtually identical in these units and in their plutonic equivalents, in contrast to an oblique subduction model, considering multiple arcs.

According to some authors, the Jurassic units correspond to a single arc that evolved from east to the west over an extended period of time. Based on the above, oblique subduction is postulated considering the Jurassic plutonism and volcanism data of the Upper Magdalena Valley (Rodríguez et al., 2016, Zapata et al, 2016; Bustamante et al., 2016; Rodríguez et al., 2018), San Lucas mountain range (Leal Mejía, 2011; Correa et al., 2019), Sierra Nevada de Santa Marta (Tschanz et al., 1969a; Quandt et al., 2018 y Rodríguez et al., 2019b) and Upper Guajira (Zuluaga et al., 2015), which show similar composition and spatial behavior and considerably different chemical and petrographic composition from the Triassic-Jurassic units of the Santander massif (Rodríguez et al., 2017, 2020) and from the north of the Ibagué Batholith.

The analysis of the data of the Upper Magdalena Valley and Sierra Nevada de Santa Marta shows coincidences when describing the compositional variation in the plutons of these two blocks (Tschanz et al., 1969; Jaramillo and Escovar, 1980; Núñez et al., 1996), corroborating published petrographic and geochemical results (Rodríguez et al., 2018 y Rodríguez et al., 2019b). The studies by Jaramillo and Escovar (1980) and by Núñez et al. (1996) describe eastward macroscopic and compositional changes in plutons in the Upper Magdalena Valley and show

that the bodies are more acidic and granitic in the same direction. Tschanz et al. (1969) separated the plutons of Sierra Nevada de Santa Marta into two batholith belts, a central belt and southeastern belt, and they described their macroscopic differences, stating that the southeastern belt was granitic.

In this context and considering the volume of information published, the arc to which the La Quinta Formation belongs shows eastward compositional and temporal migration that was most likely caused by erosion of the trench subduction front as the Farallones plate slid under the continental paleomargin during the ~30 Ma years of the duration of the arc. This continental arc is characterized by erosion, with eastward compositional migration and rejuvenation.

The continental margin, in the northern Andes, has been an accretion margin of blocks or terranes. Much of this accretion is represented by the metamorphic sequences of the Cordillera Central [Central Andes] and by the volcanic rocks of the Cordillera Occidental [West Andes]. In some periods, the margin has behaved as an erosional margin. In this study, the margin was considered erosional between the Lower and Middle Jurassic, during the formation of this Jurassic arc.

8. Conclusions

The La Quinta Formation is a volcano-sedimentary unit composed mainly of detrital sedimentary rocks (conglomerates, sandstones and mudstones) and subordinate chemical sedimentary (limestones) and extrusive and pyroclastic volcanic rocks. The extrusive rocks have a basaltic, andesitic, dacitic and rhyolitic composition, and the pyroclastic rocks are crystal-vitreous and lithic tuffs of ash and lapilli size and agglomerates. The chemical classification of the extrusive rocks based on higher oxides matches the modal classification. The tuffs are chemically classified as dacites and rhyolites.

The chemistry results from this study and from previous studies indicate that the volcanic rocks were formed in a subduction-related setting in a volcanic-plutonic arc with compositional variations and eastward rejuvenation related to an erosional continental margin arc.

The ages suggest that the volcanism began in ~191 Ma (Sinemurian) and continued until ~164 Ma, with at least three periods of increased volcanic activity: 186 Ma (Pliensbachian), 179-181 Ma (Toarcian) Ma and 173-175 (Toarcian), and continued until the Middle Jurassic (Callovian).

The periods of peak volcanic activity are correlated with similar periods in volcanic units during the Lower and Middle Jurassic in the Upper Magdalena Valley (Saldaña Formation and Pitalito Vulcanites), the San Lucas mountain range (Noreán Formation), Sierra Nevada de Santa Marta (Guatapurí and Corual formations, Caja de Ahorros, La Paila and Los Clavos ignimbrites, Triassic spilites, keratophyric porphyries, Los Tábanos Rhyodacite and Golero Rhyolite), and the Cocinas mountain range (Ipapure-Cerro La Teta Rhyodacite). All these units, including the La Quinta Formation, have similar chemical and petrographic compositions; in these units, the inherited zircons mark similar populations and were formed from the same Plutonic volcanic arc along the South American paleomargin on a crystalline basement consisting of Neoproterozoic rocks, Paleozoic sedimentary units and Permian arc plutons, which appear in tectonic blocks as we know them today.

The lack of xenocrystals with Ordovician ages in all the correlated volcanic units of the Lower and Middle Jurassic indicates that the La Quinta Formation did not develop in the basement of the Famatinian orogen of the Santander massif but was instead established in rocks of the Neoproterozoic basement of the Putumayo orogen and in intrusions of the Permian arc predating the Lower and Middle Jurassic arc.

Acknowledgments

We would like to thank the Servicio Geológico Colombiano for funding the project, the SGC Petrography and Chemistry laboratories for preparing the thin sections and for the chemical analyses of the samples, respectively, the SGC Geochronology Laboratory for the U-Pb zircon dating of six samples, the geologist Gilberto Zapata for his help with field sampling, Tomás Correa for translating the abstract of the article, Juan Pablo Zapata for making the figure of the general geological map, and the reviewers for their comments, which allowed us to improve the manuscript.

References

Arias, A., & Morales, C. (1999). *Geología del departamento de Cesar*. Bogota: Ingeominas.

Barrett, M., Butler, R., Moore-Fay, S., Novas, F., Moody, J., Clark, J., & Sánchez-Villagra, M. (2008). Dinosaur remains from the La Quinta Formation (Lower or Middle Jurassic) of the Venezuelan Andes. *Paläontologische Zeitschrift*, 82, 163-177. https://doi.org/10.1007/BF02988407

Bayona, G., Jiménez, G., Silva, C., Cardona, A., Montes, C., Roncancio, J., & Cordani, U. (2010). Paleomagnetic data and K–Ar ages from Mesozoic units of the Santa Marta massif: A preliminary interpretation for block rotation and translations. *Journal of South American Earth Sciences*, 29 (4), 817-831. https://doi.org/10.1016/j.jsames.2009.10.005

Blanco Quintero, I. F., García Casco, A., Toro, L. M., Moreno, M., Ruiz, E. C., Vinasco, C. J., & Morata, D. (2014). Late Jurassic terrane collision in the northwestern margin of Gondwana (Cajamarca Complex, eastern flank of the Central Cordillera, Colombia). *International Geology Review*, 56 (15), 1852-1872. https://doi.org/10.1080/00206814.2014.963710

Bustamante, C., Cardona, A., Bayona, G., Mora, A., Valencia, V., Gehrels, G., & Vervoort, J. (2010). U-Pb LA-ICP-SM Geochronology and regional correlation of middle Jurassic intrusive rocks from the Garzon massif, upper Magdalena valley and Central cordillera, southern Colombia. *Boletín de Geología*, 32 (2), 93-109.

Bustamante, C., Archanjo, C., Cardona, A., Valencia, V., & Vervoort, J. (2016). Late Jurassic to Early Cretaceous plutonism in the Colombian Andes: a record of long-term arc maturity. *GSA Bulletin*, 128 (11-12), 1762-1779 https://doi.org/10.1130/B31307.1.

Cano, N. A., Molano, J. C., Guerrero, N. M., Sepúlveda, M. J., Prieto, D., Murillo, H., & Patiño, R. (2017). Petrología de los miembros volcánicos de la Formación La Quinta. Abstracts. XVI Congreso de Geología. Santa Marta.

Cediel, F., Mojica, J., & Macía, C. (1980). Definición estratigráfica del Triásico en Colombia, Suramérica. Formaciones Luisa, Payandé y Saldaña. *Newsletters on Stratigraphy*, 9 (2), 73-104. https://doi.org/10.1127/nos/9/1980/73

Cediel, F., Mojica, J., & Macía, C. (1981). Las formaciones Luisa, Payandé y Saldaña: sus columnas estratigráficas características. *Geología Norandina*, 3, 11-19.

Condie, K. C., & Kröner, A. (2013). The building blocks of continental crust: Evidence for a major change in the tectonic setting of continental growth at the end of the Archean. *Gondwana Research*, 23 (2), 394-402. https://doi.org/10.1016/j.gr.2011.09.011

Correa Martínez, A. M., Rodríguez, G., Arango, M. I., & Zapata García, G. (2019). Petrografía, geoquímica y geocronología U-Pb de las rocas volcánicas y piroclásticas de la Formación Noreán al NW del macizo de Santander, Colombia. *Boletín de Geología*, 41 (1), 29-54. https://doi.org/10.18273/revbol.v41n1-2019002

Coyner, S. J., Kamenov, G. D., Mueller, P. A., Rao, V., & Foster, D. A. (2004). FC-1: A zircon reference standard for the determination of Hf isotopic compositions via laser ablation ICP-MS. *American Geophysical Union, Fall Meeting.* San Francisco.

Dasch, L. E. (1982). *U-Pb geochronology of the Sierra de Perijá* (Ph. D. thesis). Case Western Reserve University.

Forero, S. (1970). Estratigrafía del Precámbrico en el flanco occidental de la serranía de Perijá. *Geología Colombiana*, 7, 7-78.

Forero, A. (1972). Estratigrafía del Precretácico en el flanco occidental de la serranía de Perijá. *Geología Colombiana*, 7, 7-78.

Geoestudios. (2006). Cartografía geológica cuenca Cesar-Ranchería. Final inform.

Girardi, V. A. V., Teixeira, W., Bettencourt, J. S., Andrade, S., Navarro, M. S., & Sato, K. (2008). Trace element geochemistry and Sr-Nd characteristics of Mesoproterozoic mafic intrusive rocks from Rondônia, Brazil, SW Amazonian craton: Petrogenetic and tectonic inferences. *Episodes*, 31 (4), 392-400. https://doi.org/10.18814/epiiugs/2008/v31i4/004

González, H., Maya, M., Camacho, J., Cardona, O. D., & Vélez, W. (2015a). *Elaboración de la cartografía geológica de un conjunto de planchas a escala 1:100.000 ubicadas en cuatro bloques del territorio nacional, identificados por el Servicio Geológico Colombiano. Plancha 41: Becerril*. Bogota: Servicio Geológico Colombiano.

González, H., Maya, M., García, J. F., Gómez, J. P., Palacio, A. F., & Vélez, W. (2015b). *Elaboración de la cartografía geológica de un conjunto de planchas a escala*

1:100.000 ubicadas en cuatro bloques del territorio nacional, identificados por el Servicio Geológico Colombiano. Plancha 42: serranía de Perijá. Bogotá: Servicio Geológico Colombiano.

Hernández, M. (2003). *Memoria explicativa geología plancha 48, Jagua de Ibirico. Esc 1:100.000*. Bogotá: Ingeominas.

Hellstrom, J., Paton, C., Woodhead, J. D., & Hergt, J. M. (2008). Iolite: Software for spatially resolved LA-(quad and MC) ICP-MS analysis. In: P. Sylvester (ed.), *Laser Ablation ICP-MS in the Earth sciences: Current practices and outstanding issues* (pp. 343-348). Vancouver: Mineralogical Association of Canada.

Hughes, C. J. (1972). Spilites, keratophyres and the igneous spectrum. *Geological Magazine,* 109 (6), 513-527. https://doi.org/10.1017/S0016756800042795.

Ibáñez Mejía, M., Pullen, A., Arenstein, J., Gehrels, G., Valley, J., Ducea, M., Mora, A., Pecha, M., & Ruiz, J. (2015). Unraveling crustal growth and reworking processes in complex zircons from orogenic lower-crust: The Proterozoic Putumayo Orogen of Amazonia. *Precambrian Research*, 267, 285-310. https://doi.org/10.1016/j.precamres.2015.06.014

Ingeominas. (2002). *Atlas geológico digital de Colombia. Versión 1.1, plancha 5-06. Escala 1: 500.000.* Bogotá: Ingeominas.

Ingeominas-UIS. (2006a). *Cartografía geológica de 9.600 km² de la serranía de San Lucas: planchas 55 (El Banco), 64 (Barranco de Loba), 85 (Simití) y 96 (Bocas del Rosario). Aporte a su evolución geológica*. Memoria explicativa de la Plancha 85: Simití. Bucaramanga: Ingeominas.

Ingeominas-UIS. (2006b). *Geología de la plancha 55: El Banco. Escala 1:100.000. Mapa Geológico.* Bogotá y Bucaramanga: Ingeominas.

Ingeominas-UIS. (2006c). *Cartografía geológica de 9.600 km² de la serranía de San Lucas: planchas 55 (El Banco), 64 (Barranco de Loba), 85 (Simití) y 96 (Bocas del Rosario). Aporte a su evolución geológica.* Memoria explicativa de la plancha 55: El Banco. Bucaramanga: Ingeominas.

Ingeominas-UIS. (2006d). *Cartografía geológica de 9.600 km² de la serranía de San Lucas: planchas 55 (El Banco), 64 (Barranco de Loba), 85 (Simití) y 96 (Bocas del Rosario). Aporte a su evolución geológica.* Memoria explicativa de la plancha 64: Barranco de Loba. Bucaramanga: Ingeominas.

Ingeominas-UIS. (2006e). Cartografía geológica de 9.600 km² de la serranía de San Lucas: planchas 55 (El Banco), 64 (Barranco de Loba), 85 (Simití) y 96 (Bocas del Rosario). Aporte a su evolución geológica. Memoria explicativa de la plancha 96: Bocas del Rosario. Bucaramanga: Ingeominas.

Invemar, Ingeominas, Ecopetrol, ICP y Geosearch. (2007). *Geología de las planchas 11, 12, 13, 14, 18, 19, 20, 21, 25, 26,27, 33 y 34. Proyecto: "Evolución geohistórica de la Sierra Nevada de Santa Marta"*. Bogotá: Ingeominas.

Janoušek, V., Farrow, C. M., & Erban, V. (2006). Interpretation of whole-rock geochemical data in igneous geochemistry: Introducing Geochemical Data Toolkit (GCDkit). *Journal of Petrology*, 47 (6), 1255-1259. https://doi.org/10.1093/petrology/egl013.

Jaramillo, L., & Escovar, R. (1980). *Cinturones de pórfidos cupríferos en las cordilleras colombianas. Simposio sobre metalogénesis en Latinoamérica*. 17p, México D.F.

Kundig, E. (1938). Las rocas precretáceas de los Andes centrales de Venezuela, con algunas observaciones sobre su tectónica. *Venezuela Boletín de Geología y Mine*ría, 2 (2), 3.

Leal Mejía, H. (2011). *Phanerozoic gold metallogeny in the Colombian Andes: A tectono-magmatic approach* (Ph. D. Thesis). University of Barcelona.

Leal Mejía, H., Shaw, R. P., & Melgarejo, J. C. (2019). Spatial-temporal migration of granitoid magmatism and the Phanerozoic tectono-magmatic evolution of the Colombian Andes. In: F. Cediel y R. P. Shawn (eds.), *Geology and tectonics of Northwestern South America* (pp. 253-410). Frontiers in Earth Sciences. Springer, Cham. https://doi.org/10.1007/978-3-319-76132-9_5.

Le Bas, M., Le Maitre, R., Streckeisen, A., & Zanettin, B. (1986). A chemical classification of volcanic rocks based on the total alkali-silica diagram. *Journal of Petrology*, 27 (3), 745-750. https://doi.org/10.1093/petrology/27.3.745

Le Maitre, R. W., Streckeisen, A., Zanettin, B., Le Bas, M. J., Bonin, B., Bateman, P., & Lamere, J. (2002). Igneous rocks: A classification and glossary of terms: Recommendations of the International Union of Geological Sciences. In: *Subcommission on the Systematics of Ig-*

neous Rocks. Cambridge University Press. https://doi.org/10.1017/CBO9780511535581

Ludwig, K. R. (2012). User's manual for Isoplot 3.75- 4.15. A Geochronological Toolkit Microsoft Excel. Berkeley Geochronology Center, Special Publication, 5.

Maze, W. (1984). Jurassic La Quinta Formation in the Sierra de Perijá, Northwestern Venezuela: Geology and tectonic environment of red beds and volcanic rocks. In: W. Bonini, R. Hargraves y R. Shagam (eds.). *The Caribbean-South American Plate boundary and regional tectonics* (pp. 263-282). McLean: Geological Society of America, v. 162. https://doi.org/10.1130/MEM162-p263.

Miller, J. B. (1960). Directrices tectónicas en la sierra de Perijá. *Boletín Geológico de Venezuela*, publicación especial, n.º 3, t. II.

Mojica, J., & Kammer, A. (1995). Eventos jurásicos en Colombia. *Geología Colombiana*, 19, 165-172.

Mojica, J., Kammer, A., & Ujueta, G. (1996). El Jurásico del sector noroccidental de Suramérica y guía de la excursión al valle superior del Magdalena (nov. 1-4/95), regiones de Payandé y Prado, departamento del Tolima, Colombia. *Geología Colombiana*, 21, 3-41.

Mojica, J., & Dorado, J. (1987). El Jurásico anterior a los movimientos intermálmicos en los Andes colombianos. Parte A: Estratigrafía. In: W. Volkheimer (ed.), *Bioestratigrafia de los sistemas regionales del Jurásico y Cretácico de América del Sur* (pp. 49-110). Mendoza: Comité Sudamericano del Jurásico y Cretácico, v. 1.

Nakamura, N. (1974). Determination of REE, Ba, Fe, Mg, Na and K in carbonaceous and ordinary chondrites. *Geochimica et Cosmochimica Acta*, 38 (5), 757-775. https://doi.org/10.1016/0016-7037(74)90149-5.

Nova, G., Montaño, P., Bayona, G., Rapalini, A., & Montes, C. (2012). Paleomagnetismo en rocas del Jurásico y Cretácico Inferior en el flanco occidental de la serranía del Perijá: contribuciones a la evolución tectónica del NW de Suram**é**rica. *Boletín de Geología*, 34 (2), 117-138.

Nova, G., Bayona, G., Silva, J., Cardona, A., Rapalini, A., Montaño, P., Eisenhauer, A., Dussan, K., Valencia, V., Ramírez, V., & Montes, C. (2018). Jurassic break-up of the Peri-Gondwanan margin in Northern Colombia: Basin formation and implications for terrane transfer. *Journal of South American Earth Sciences*, 89, 92-117. https://doi.org/10.1016/j.jsames.2018.11.014

Núñez A., Bocanegra, A., & Gómez, J. (1996). Los plutones jurásicos del valle superior del Magdalena. *VII Congreso Colombiano de Geología*. Bogotá, Colombia.

Paton, C., Woodhead, J. D., Hellstrom, J. C., Hergt, J. M., Greig, A., & Maas, R. (2010). Improved laser ablation U-Pb zircon geochronology through robust downhole fractionation correction. *Geochemistry, Geophysics, Geosystems*, 11 (3), 1-36. https://doi.org/10.1029/2009GC002618.

Pastor Chacón, A., Reyes Abril, J., Cáceres Guevara, C., Sarmiento, G., Cramer, T. (2013). Análisis estratigráfico de la sucesión del Devónico-Pérmico al oriente de Manaure y San José de Oriente (serranía del Perijá, Colombia). *Geología Colombiana*, 38, 5-24.

Pearce, J. A., Harris, N. B., & Tindle, A. G. (1984). Trace Element Discrimination Diagrams for the Tectonic Interpretation of Granitic Rocks. *Journal of Petrology*, 25 (4), 956-983. https://doi.org/10.1093/petrology/25.4.956

Pearce, J. A. (1996). A user's guide to basalt discrimination diagrams. In D. A. Wyman (ed.), *Trace element geochemistry of volcanic rocks: Applications for massive sulphide exploration* (pp. 79-113). Winnipeg: Geological Association of Canada. Short Course Notes v. 12.

Pearce, J. A. (2008). Geochemical fingerprinting of oceanic basalts with applications to ophiolite classification and the search for Archean oceanic crust. *Lithos*, 100 (1-4), 14-48. https://doi.org/10.1016/j.lithos.2007.06.016.

Peña Urueña, M. L., Muñoz Rocha, J. A., & Urueña, C. L. (2018). Laboratorio de Geocronología en el Servicio Geológico Colombiano: avances sobre datación U-Pb en circones mediante la técnica LA-ICP-MS. *Boletín Geológico*, 44, 39-56. https://doi.org/10.32685/0120-1425/boletingeo.44.2018.7

Petrus, J. A., & Kamber, B. S. (2012). Vizual age: A novel approach to laser ablation ICP-MS U-Pb geochronology data reduction. *Geostandards and Geoanalytical Research*, 36 (3), 247-270. https://doi.org/10.1111/j.1751-908X.2012.00158.x.

Peccerillo A., & Taylor, T. S. (1976). Geochemistry of Eocene calc-alkaline volcanic rocks from Kastamonu area, Northern Turkey. *Contributions to Mineralogy and Petrology*, 58, 63-81. https://doi.org/10.1007/BF00384745

Quandt, D., Trumbull, R., Altenberger, W., Cardona, A., Romer, R., Bayona, G., Ducea, M., Valencia, V., Vásquez, M., Cortés, E., & Guzmán, G. (2018). The geochemistry and geochronology of Early Jurassic igneous rocks from the Sierra Nevada de Santa Marta, NW Colombia, and tectono-magmatic implications. *Journal of South American Earth Sciences*, 86, 216-230. https://doi.org/10.1016/j.jsames.2018.06.019

Radelli, L. (1960). El basamento cristalino de la península de la Guajira. *Boletín Geológico*, 8 (1-3), 5-23.

Radelli, L. (1962). Acerca de la geología de la serranía de Perijá entre Codazzi y Villanueva (Magdalena-Guajira, Colombia). *Geología Colombiana*, 1, 23-42.

Renne, P. R., Swisher, C. C., Deino, A. L., Karner, D. B., Owens, T. L., & De Paolo, D. J. (1998). Intercalibration of standards, absolute ages and uncertainties in 40Ar/39Ar dating. *Chemical Geology*, 145 (1-2), 117-152. https://doi.org/10.1016/S0009- 2541(97)00159-9.

Restrepo, J. J., Ordóñez Carmona, O., Martens, U., Correa, A. M. (2009). Terrenos, complejos y provincias en la cordillera Central de Colombia. XII Congreso Colombiano de Geología.

Rodríguez, G., & Londoño, A. C. (2002). Mapa geológico del departamento de La Guajira. *Geología, recursos minerales y amenazas potenciales, Escala*, *1:250.000.* Bogotá: Ingeominas.

Rodríguez, G., Arango, M. I., Zapata, G., & Bermúdez, J. G. (2015). Características petrográficas, geoquímicas y edad U-Pb de los plutones jurásicos del valle superior del Magdalena. Poster. XV Congreso Colombiano de Geología.

Rodríguez, G., Arango, M. I., Zapata, G., & Bermúdez, J. G. (2016). Catálogo de unidades litoestratigráficas de Colombia, Formación Saldaña. Cordilleras Central y Oriental, Tolima, Huila, Cauca y Putumayo. Medellín: Servicio Geológico Colombiano.

Rodríguez, G., Zapata, G., Correa Martínez, A. M y Arango M. (2017). *Caracterización del magmatismo triásico-jurásico del macizo de Santander*. Medellín: Servicio Geológico Colombiano.

Rodríguez, G., Arango, M. I., Zapata, G., & Bermúdez, J. G. (2018). Petrotectonic characteristics, geochemistry, and U-Pb geochronology of Jurassic plutons in the Upper Magdalena Valley-Colombia: Implications on the evolution of magmatic arcs in the NW Andes. *Journal of South American Earth Sciences*, 81, 10-30. https://doi.org/10.1016/j.jsames.2017.10.012.

Rodríguez García, G., Correa Martínez, A. M., Zapata Villada, J. P., & Obando Erazo, G. (2019a). Fragments of a Permian arc on the western margin of the Neoproterozoic basement of Colombia. In: Gómez, J., & Mateus Zabala, D. (eds.), *The geology of Colombia*, vol. 1: *Proterozoic-Paleozoic*. Publicaciones Geológicas Especiales 35. Bogotá: Servicio Geológico Colombiano. https://doi.org/10.32685/ pub.esp.35.2019.10.

Rodríguez, G., Zapata Villada, J. P., Ramírez, D. A, Correa Martínez, A. M., Obando, G., Muñoz, J. A, Rayo, L., & Ureña, C. L. (2019b). *Magmatismo jurásico de la Sierra Nevada de Santa Marta*. Medellín: Servicio Geológico Colombiano.

Rodríguez, G., Correa Martínez, A. M., Zapata, G., Arango, M. I., Obando Erazo, G., Zapata Villada, J. P., & Bermúdez, J. G. (2020). Diverse Jurassic magmatic arcs of the Colombian Andes: Constraints from petrography, geochronology and geochemistry. In: Gómez, J., & Pinilla–Pachon, A.O. (eds.), *The Geology of Colombia*, vol. 2 Mesozoic. Publicaciones Geológicas Especiales 36. Bogotá: Servicio Geológico Colombiano. https://doi.org/10.32685/pub.esp.36.2019.04

Rubatto, D. (2002). Zircon trace element geochemistry: Partitioning with garnet and the link between U-Pb ages and metamorphism. *Chemical Geology*, 184 (1-2), 123-138. https://doi.org/10.1016/S0009-2541(01)00355-2.

Schoene, B., Samperton, K. M., Eddy, M. P., Keller, G., Adatte, T., Bowring, S. A., Khadri, S. F. R., & Gertsch, B. (2015). U-Pb geochronology of the Deccan Traps and relation to the end-Cretaceous mass extinction. *Science*, 347 (6218), 182-184. https://doi.org/10.1126/science.aaa0118

Shand, S. J. (1943). *Eruptive rocks: Their genesis, composition, classification, and their relation to ore-deposits with a chapter on meteorite.* New York: John Wiley & Sons.

Sláma, J., Košler, J., Condon, D. J., Crowley, J. L., Gerdes, A., Hanchar, J. M., Horstwood, M. S. A., Morris, G. A., Nasdala, L., Norberg, N., Schaltegger, U., Schoene, B., Tubrett, M. N., & Whitehouse, M. J. (2008). Plešovice zircon: A new natural reference material for U-Pb and Hf isotopic microanalysis. *Chemical Geology*, 249 (1-2), 1-35. https://doi.org/10.1016/j.chemgeo.2007.11.005.

Spikings, R., Cochrane, R., Villagómez, D., Van der Lelij, R., Vallejo, C., Winkler, W., & Beate, B. (2015). The geological history of Northwestern South America: From Pangaea to the early collision of the Caribbean Large Igneous Province (290-75 Ma). *Gondwana Research*, 27 (1), 95-139. https://doi.org/https://doi.org/10.1016/j.gr.2014.06.004.

Stacey, J. S., & Kramers, J. D. (1975). Approximation of terrestrial lead isotope evolution by a two-stage model. *Earth and Planetary Science Letters*, 26 (2), 207-221. https://doi.org/10.1016/0012-821X (75) 90088-6.

Streckeisen, A. (1978). IUGS Subcommission on the Systematics of Igneous Rocks: Classification and nomenclature of volcanic rocks, lamprophyres, carbonatites and melilitic rocks; recommendation and suggestions. *Neues Jahrbuch für Mineralogie - Abhandlungen*, 134, 1-14.

Sun, S. S., & McDonough, W. F. (1989). Chemical and isotopic systematics of oceanic basalts: Implications for mantle composition and processes. In: A. D. Sanders y M. J. Norry (eds.), *Magmatism in oceanic basins* (pp. 313-345). Special Publication 42. Oxford: Geological Society of London.

Trumpy, D. (1943). Pre-Cretaceous of Colombia. *GSA Bulletin*, 54, 1281-1304. https://doi.org/10.1130/GSAB-54-1281

Tschanz, C., Jimeno, A., & Cruz, J. (1969). *Geology of the Sierra Nevada de Santa Marta area, Colombia*. Informe interno n.º 1829. Bogotá: Ingeominas.

Tschanz, C. M., Marvin, R. F., Cruz B., J., Mehnert, H. H., & Cebula, G. T. (1974). Geologic evolution of the Sierra Nevada de Santa Marta, northeastern Colombia. *GSA Bulletin*, 85 (2), 273-284. https://doi.org/10.1130/0016-7606(1974)85<273:GEOTSN>2.0.CO;2

Villagómez, D. (2010). *Thermochronology, geochronology and geochemistry of the Western and Central Cordilleras and Sierra Nevada de Santa Marta, Colombia: The tectonic evolution of NW South America* (Ph. D. thesis). University of Geneva.

Villagómez, D., Martens, U., & Pindell, J. (2015). Are Jurassic and some older blocks in the Northern Andes in-situ or far-travelled? Potential correlations and new geochronological data from Colombia and Ecuador. Resumen, Conferencia Simposio: Tectónica Jurásica en la parte noroccidental de Suramérica y bloques adyacentes.

Weisbord, N. (1926). Venezuelan Devonian fossils. *Bulletins of American Paleontology*, 11 (46), 223-272.

Wiedenbeck, M., Allé, P., Corfu, F., Griffin, W. L., Meier, M., Oberli, F., Von Quadt, A., Roddick, J. C., & Spiegel, W. (1995). Three natural zircon standards for U-Th-Pb, Lu-Hf, trace element and REE analyses. *Geostandards Newsletter*, 19 (1), 1-23. https://doi.org/10.1111/j.1751-908X.1995.tb00147.x.

Wiedenbeck, M., Hanchar, J. M., Peck, W. H., Sylvester, P., Valley, J., Whitehouse, M.… Zheng, Y. F. (2004). Further characterisation of the 91500 zircon crystal. *Geostandards and Geoanalytical Research*, 28 (1), 9-39. https://doi.org/10.1111/j.1751-908X.2004.tb01041.x

Winchester, J. A., & Floyd, P. A. (1977). Geochemical discrimination of different magma series and their differentiation products using immobile elements. *Chemical Geology*, 20, 325-343. https://doi.org/10.1016/0009-2541(77)90057-2.

Woodhead, J. D., & Hergt, J. M. (2007). A Preliminary appraisal of seven natural zircon reference materials for in situ Hf isotope determination. *Geostandards and Geoanalytical Research*, 29, 183-195. https://doi.org/10.1111/j.1751-908x.2005.tb00891.x

Zapata García, G.; Rodríguez, G., & Arango, M. I. (2017). Petrografía, geoquímica y geocronología de rocas metamórficas aflorantes en San Francisco, Putumayo, y la vía Palermo-San Luis, asociadas a los complejos La Cocha-río Téllez y Aleluya. *Boletín Ciencias de la Tierra*, 41, 48-65. https://doi.org/10.15446/rbct.n41.58630

Zapata, S., Cardona, A., Jaramillo, C., Valencia, V., & Vervoort, J. (2016). U-Pb LA-ICP-MS geochronology and geochemistry of Jurassic volcanic and plutonic rocks from the Putumayo region (Southern Colombia): Tectonic setting and regional correlations. *Boletín de Geología*, 38 (2), 21-38. http://dx.doi.org/10.18273/revbol.v38n2-2016001

Zuluaga, C., Pinilla, A., & Mann, P. (2015). Jurassic silicic volcanism and associated continental-arc basin in Northwestern Colombia (Southern boundary of the Caribbean plate). In: C. Bartolini y P. Mann (eds.), *Petroleum geology and potential of the Colombian Caribbean margin*, AAPG memoir, vol. 108 (pp. 137-160). Tulsa: American Association of Petroleum Geologists.

SUPPLEMENTARY TABLES

Tabla 1.

AnalysisName	U (ppm)1	Th (ppm)1	Th/U	$^{207}Pb/^{206}Pb$	±2σ	$^{207}Pb/^{235}U$	±2σ	$^{206}Pb/^{238}U$	±2σ abs3	Correlación errores	% disc. (6/8-7/5)	$^{206}Pb/^{238}U$ Edad (Ma)	±2s	$^{207}Pb/^{235}U$ Edad (Ma)	±2σ	$^{207}Pb/^{206}Pb$ Edad (Ma)	±2σ	Best age	Unc 2σ
GOE___1045_A_56	4550	6250	1,37	0,102	0,002	0,253	0,007	0,018	0,001	0,772	115,29	114,1	4,1	229,2	5,4	1656	42	106,46	4,46
GOE___1045_A_14	2770	2046	0,74	0,074	0,002	0,257	0,008	0,025	0,000	0,117	51,15	158,3	1,8	231,7	6,5	1052	60	153,29	3,70
GOE___1045_A_26	1728	5500	3,18	0,088	0,003	0,317	0,009	0,026	0,000	0,1	74,97	167,4	2,3	279	7,1	1369	73	159,45	4,09
GOE___1045_A_13	579	780	1,35	0,051	0,001	0,189	0,004	0,027	0,001	0,676	1,43	173,4	3,7	175,7	3,6	216	39	173,23	5,23
GOE___1045_A_24	177,3	189,1	1,07	0,050	0,002	0,194	0,006	0,029	0,000	0,146	-0,89	181,6	2,4	180	4,9	171	73	181,62	4,55
GOE___1045_A_49	171,2	219	1,28	0,053	0,002	0,210	0,007	0,029	0,000	0,302	5,92	182,9	2,5	193	5,6	308	70	182,21	4,60
GOE___1045_A_45	407	266	0,65	0,050	0,001	0,196	0,003	0,029	0,000	0,657	-0,60	183	2,2	181,8	2,8	197	32	182,89	4,47
GOE___1045_A_1	223,2	274	1,23	0,050	0,001	0,203	0,004	0,029	0,000	0,522	1,77	184	2	187,2	3,7	196	44	183,94	4,41
GOE___1045_A_53	697	475	0,68	0,050	0,001	0,2	0,003	0,029	0,000	0,616	0,13	184,8	1,9	185,1	2,7	182	28	184,85	4,35
GOE___1045_A_31	150,5	158	1,05	0,05	0,002	0,200	0,006	0,029	0,001	0,213	-0,41	185,4	3,3	184,6	5,3	191	70	185,37	5,11
GOE___1045_A_51	220	241,9	1,10	0,050	0,001	0,198	0,004	0,029	0,000	0,178	-1,15	185,5	2	183,4	2,9	172	40	185,53	4,41
GOE___1045_A_47	353	237	0,67	0,051	0,001	0,208	0,003	0,029	0,000	0,473	2,61	186,8	2,7	191,4	2,8	234	37	186,54	4,78
GOE___1045_A_42	240	149,9	0,62	0,052	0,001	0,204	0,006	0,030	0,001	0,524	0,47	187,6	4,5	188	4,6	274	55	187,13	5,97
GOE___1045_A_3	169	159	0,94	0,051	0,001	0,206	0,006	0,030	0,000	0,387	1,26	187,9	2,3	190	5	223	63	187,63	4,60
GOE___1045_A_52	369	363	0,98	0,050	0,001	0,202	0,004	0,030	0,000	0,276	-0,73	187,9	2,2	186,6	3,4	170	47	187,98	4,54
GOE___1045_A_8	205,7	351	1,71	0,049	0,001	0,202	0,006	0,030	0,000	0,530	-1,90	190,1	2,9	186,6	4,8	155	57	190,21	4,92
GOE___1045_A_30	323	271	0,84	0,051	0,002	0,212	0,006	0,030	0,000	0,392	2,39	190,6	2,4	194,8	5,3	262	70	190,26	4,66
GOE___1045_A_7	345	334	0,97	0,050	0,001	0,21	0,005	0,030	0,000	0,478	0,44	192,7	2,9	193,5	4,5	202	54	192,66	5,04
GOE___1045_A_27	340	246	0,72	0,050	0,001	0,210	0,005	0,030	0,000	0,270	-0,07	193,2	2,9	193	4,4	207	58	193,13	5,04
GOE___1045_A_54	350	300	0,86	0,049	0,001	0,211	0,004	0,031	0,000	0,288	-0,14	194,2	1,9	194,1	3,4	154	48	194,37	4,60
GOE___1045_A_2	234,4	220,9	0,94	0,049	0,001	0,206	0,005	0,031	0,000	0,336	-2,31	194,6	1,8	190,5	3,8	130	45	195,00	4,48
GOE___1045_A_18	195	182	0,93	0,049	0,001	0,209	0,005	0,031	0,000	0,175	-1,21	194,7	2,7	192,6	4	151	48	194,96	4,92
GOE___1045_A_44	765	2530	3,31	0,051	0,001	0,216	0,003	0,031	0,000	0,447	1,95	194,9	2,3	198,5	2,5	236	31	194,70	4,65
GOE___1045_A_20	269	162,2	0,60	0,050	0,001	0,215	0,006	0,031	0,000	0,652	0,89	195,8	2,3	197,5	5,2	210	56	195,76	4,73
GOE___1045_A_19	184,5	190,3	1,03	0,063	0,002	0,277	0,009	0,032	0,000	0,385	25,43	200,7	2,4	247,8	6,8	719	57	197,56	4,79
GOE___1045_A_22	171	277	1,62	0,054	0,002	0,249	0,013	0,032	0,001	0,368	10,30	204,9	5,6	225	11	370	100	203,99	6,90
GOE___1045_A_15	84,7	94	1,11	0,063	0,003	0,284	0,013	0,032	0,001	0,471	25,33	205,1	4,7	253,1	9,8	703	94	201,94	6,22
GOE___1045_A_46	138	110,5	0,80	0,052	0,001	0,235	0,009	0,033	0,001	0,781	1,83	210,3	6,8	213,9	7,1	290	49	210,06	8,15
GOE___1045_A_48	111,7	144	1,29	0,050	0,002	0,233	0,012	0,034	0,001	0,722	-0,49	213	8	212	9,8	202	81	213,04	9,42
GOE___1045_A_9	257	353	1,37	0,055	0,002	0,260	0,008	0,035	0,001	0,508	7,26	220,2	3,7	234,9	6,1	416	63	219,00	5,94

AnalysisName	U (ppm)1	Th (ppm)1	Th/U	$^{207}Pb/^{206}Pb$	±2σ	$^{207}Pb/^{235}U$	±2σ	$^{206}Pb/^{238}U$	±2σ abs3	Correlación errores	% disc. (6/8-7/5)	$^{206}Pb/^{238}U$ Edad (Ma)	±2s	$^{207}Pb/^{235}U$ Edad (Ma)	±2σ	$^{207}Pb/^{206}Pb$ Edad (Ma)	±2σ	Best age	Unc 2σ
GOE___1045_A_43	132	127	0,96	0,216	0,046	1,29	0,35	0,037	0,004	0,979	295,00	239	22	740	160	2480	450	187,34	22,43
GOE___1045_A_17	5,3	9	1,70	0,16	0,13	0,4	1,1	0,062	0,036	0,071	107,20	380	210	700	550	2000	1300	337,84	202,56
GOE___1045_A_23	157	141	0,90	0,058	0,001	0,8	0,012	0,100	0,001	0,380	-2,47	611,8	7,9	598,3	6,6	537	38	613,47	15,02
GOE___1045_A_21	464	188,7	0,41	0,062	0,001	0,893	0,012	0,103	0,002	0,802	2,77	631,1	9,5	647,7	6,6	692	23	630,25	16,11
GOE___1045_A_37	415	101,4	0,24	0,070	0,001	1,144	0,027	0,118	0,003	0,935	8,68	718	17	774	13	929	19	712,15	22,31
GOE___1045_A_6	419	28,2	0,07	0,062	0,001	1,044	0,014	0,122	0,002	0,761	-2,30	741	10	725,7	7,2	671	20	742,79	18,35
GOE___1045_A_55	179	86,5	0,48	0,074	0,001	1,281	0,028	0,126	0,003	0,880	11,06	762	14	837	13	1044	26	753,62	20,99
GOE___1045_A_29	193	254	1,32	0,065	0,001	1,282	0,022	0,142	0,002	0,703	-2,22	853	12	837,2	9,8	773	24	856,20	21,66
GOE___1045_A_36	588	169,6	0,29	0,074	0,001	1,466	0,02	0,143	0,002	0,711	6,89	863	10	916,3	8,1	1041	24	857,22	20,29
GOE___1045_A_11	645	127,9	0,20	0,073	0,001	1,476	0,026	0,148	0,003	0,902	3,93	889	15	920	11	999	20	885,22	24,33
GOE___1045_A_50	89,2	36,6	0,41	0,072	0,001	1,532	0,031	0,156	0,002	0,531	1,28	933	11	943	12	978	28	931,06	21,99
GOE___1045_A_41	419,5	175,2	0,42	0,073	0,001	1,679	0,031	0,165	0,004	0,813	1,71	984	22	1000	12	1015	28	983,20	29,94
GOE___1045_A_28	257,4	232,5	0,90	0,072	0,001	1,685	0,02	0,169	0,002	0,700	-0,76	1009	11	1002,5	7,5	975	20	1010,17	23,63
GOE___1045_A_16	105,6	152,7	1,45	0,071	0,001	1,7	0,023	0,172	0,002	0,731	-1,72	1023	12	1008,3	8,8	969	22	1025,92	24,76
GOE___1045_A_25	1257	266,2	0,21	0,077	0,001	1,894	0,029	0,178	0,003	0,734	2,66	1054	14	1079	10	1127	22	1051,01	25,71
GOE___1045_A_40	400	124,3	0,31	0,074	0,001	1,852	0,042	0,179	0,005	0,901	0,74	1058	25	1067	14	1049	19	1059,16	33,21
GOE___1045_A_12	152,9	103	0,67	0,075	0,001	1,942	0,038	0,186	0,002	0,796	-0,27	1097	11	1095	13	1075	24	1097,92	25,15
GOE___1045_A_34	134,1	63,6	0,47	0,077	0,001	2,034	0,03	0,193	0,003	0,557	-0,65	1137	14	1131	11	1110	25	1138,37	27,36
GOE___1045_A_39	40,7	46,3	1,14	0,083	0,002	2,308	0,045	0,200	0,004	0,281	4,18	1173	22	1217	13	1260	38	1168,14	32,80
GOE___1045_A_33	330	99,9	0,30	0,078	0,001	2,172	0,038	0,203	0,003	0,750	-1,70	1189	13	1171	12	1139	24	1191,31	28,40
GOE___1045_A_32	154	88	0,57	0,073	0,001	2,239	0,084	0,222	0,008	0,681	-8,77	1289	40	1191	27	1015	24	1305,55	50,03
GOE___1045_A_35	258	193	0,75	0,121	0,001	5,73	0,14	0,345	0,01	0,849	1,72	1911	50	1935	21	1968	20	1902,26	70,84
GOE___1045_A_4	0,017	0,055	3,24	no value	NAN	no value	NAN	no value	NAN	NaN	#VALUE	no value	NAN	no value	NAN	no value	NAN	#VALUE	#VALUE
GOE___1045_A_5	0,002	0,038	21,11	no value	NAN	no value	NAN	no value	NAN	NaN	#VALUE	no value	NAN	no value	NAN	no value	NAN	#VALUE	#VALUE
GOE___1045_A_10	0,010	0,037	3,56	no value	NAN	no value	NAN	no value	NAN	NaN	#VALUE	no value	NAN	no value	NAN	no value	NAN	#VALUE	#VALUE
GOE___1045_A_38	0,002	0,011	5	no value	NAN	no value	NAN	no value	NAN	NaN	#VALUE	no value	NAN	no value	NAN	no value	NAN	#VALUE	#VALUE

Table 2.

AnalysisName	U (ppm)1	Th (ppm)1	Th/U	$^{207}Pb/^{206}Pb$	±2σ	$^{207}Pb/^{235}U$	±2σ	$^{206}Pb/^{238}U$	±2σ	Correlación errores	% Error 6/8 2S	% disc. (6/8-7/5)	$^{206}Pb/^{238}U$ Edad (Ma)	±2σ	$^{207}Pb/^{235}U$ Edad (Ma)	±2σ	$^{207}Pb/^{206}Pb$ Edad (Ma)	±2σ	Best age	Unc 2σ
GOE___1057_37	1756	230	2,53	0,109	0,003	0,237	0,008	0,016	0,000	0,526	2,92	135,12	99,4	2,9	215,8	6,1	1785	54	91,78	3,51
GOE___1057_73	396	52	1,69	0,055	0,005	0,179	0,012	0,024	0,001	0,085	2,12	13,57	150,7	3,2	170	13	440	150	149,69	4,80
GOE___1057_69	324	59	2,21	0,069	0,005	0,227	0,015	0,024	0,001	0,123	2,83	40,36	151,9	4,3	208	14	820	140	148,20	5,53
GOE___1057_86	233	83	3,23	0,069	0,011	0,218	0,029	0,025	0,001	0,1	2,80	31,12	157,1	4,4	201	20	620	190	153,29	6,01
GOE___1057_55	1343	92	1,43	0,058	0,001	0,202	0,004	0,025	0,000	0,501	1,63	17,80	159,9	2,6	186,3	3,4	534	37	158,15	4,51
GOE___1057_20	82,6	4,6	1,69	0,082	0,009	0,255	0,017	0,025	0,001	0,1	4,16	48,70	160,9	6,7	229	14	1010	190	154,00	7,52
GOE___1057_74	90,2	9,6	1,73	0,061	0,005	0,217	0,016	0,026	0,000	0,014	1,71	24,45	163,8	2,8	201	14	550	140	161,51	4,77
GOE___1057_87	82,9	5,1	1,96	0,092	0,009	0,322	0,03	0,026	0,001	0,144	2,13	68,89	164	3,5	262	20	1130	160	155,13	5,22
GOE___1057_81	643	44	1,13	0,052	0,001	0,185	0,005	0,026	0,000	0,245	0,97	4,98	164,3	1,6	171,8	4,1	269	54	163,65	4,17
GOE___1057_13	1331	110	1,63	0,052	0,001	0,185	0,004	0,026	0,000	0,437	1,21	4,26	165,5	2	172,1	3,3	255	39	165,07	4,35
GOE___1057_56	207	14	0,80	0,047	0,013	0,19	0,027	0,026	0,001	0,1	2,10	10,12	166,5	3,5	184	18	-210	400	167,09	6,07
GOE___1057_80	708	65	1,11	0,051	0,002	0,185	0,006	0,026	0,000	0,159	1,26	2,98	167,1	2,1	171,8	5,4	237	66	166,83	4,43
GOE___1057_28	843	22	1,16	0,052	0,001	0,190	0,004	0,026	0,000	0,298	0,95	5,66	167,7	1,6	176,6	3,4	284	43	167,15	4,23
GOE___1057_52	846	21	1,01	0,051	0,001	0,182	0,004	0,026	0,000	0,299	1,07	1,59	167,7	1,8	170,1	3,5	206	47	167,44	4,30
GOE___1057_72	466	21	1,20	0,056	0,002	0,204	0,007	0,026	0,000	0,104	1,31	12,43	168	2,2	187,4	6,2	385	72	166,69	4,47
GOE___1057_11	881	33	1,11	0,049	0,001	0,180	0,004	0,026	0,000	0,454	1,25	-0,30	168,1	2,1	167,6	3,5	169	44	168,11	4,43
GOE___1057_64	46,1	2,9	1,36	0,075	0,008	0,271	0,028	0,026	0,001	0,1	2,38	45,22	168,2	4	236	23	780	210	162,51	5,65
GOE___1057_14	1510	120	1,47	0,049	0,001	0,182	0,004	0,026	0,000	0,505	1,25	0,96	168,5	2,1	170,2	3,1	165	35	168,58	4,43
GOE___1057_45	282	16	1,01	0,049	0,002	0,183	0,008	0,027	0,000	0,266	1,48	1,06	169,1	2,5	171	6,5	145	76	169,20	4,70
GOE___1057_31	95,5	6,9	1,49	0,054	0,004	0,199	0,014	0,027	0,000	0,048	1,71	11,10	169,3	2,9	187	12	330	140	168,32	4,97
GOE___1057_59	2026	91	1,89	0,050	0,001	0,186	0,003	0,027	0,000	0,473	1,06	1,73	170,1	1,8	173	2,6	198	33	170,06	4,36
GOE___1057_47	99,8	10	1,90	0,061	0,004	0,226	0,016	0,027	0,001	0,038	2,06	22,23	170,2	3,5	205	13	540	140	167,71	5,31
GOE___1057_23	440	6,1	0,67	0,050	0,002	0,186	0,006	0,027	0,000	0,303	1,64	1,84	170,6	2,8	173,8	5,2	172	64	170,65	4,87
GOE___1057_15	407	24	1,83	0,049	0,002	0,181	0,006	0,027	0,000	0,269	1,23	-1,51	170,8	2,1	168,4	4,8	137	59	170,99	4,50
GOE___1057_21	1278	52	0,96	0,050	0,001	0,187	0,004	0,027	0,000	0,361	1,35	1,75	170,8	2,3	173,6	3,1	207	38	170,62	4,61
GOE___1057_30	88,6	4	1,25	0,055	0,004	0,209	0,016	0,027	0,000	0,129	1,81	14,86	170,9	3,1	195	13	380	140	169,78	5,10
GOE___1057_34	1689	67	2,02	0,050	0,001	0,184	0,003	0,027	0,000	0,339	1,17	0,25	171,3	2	171,6	2,9	183	38	171,17	4,49
GOE___1057_24	191	32	0,69	0,05	0,002	0,187	0,008	0,027	0,000	0,187	1,34	1,96	171,7	2,3	175	7,1	218	83	171,64	4,63
GOE___1057_46	262,5	8,1	0,99	0,050	0,002	0,191	0,008	0,027	0,000	0,372	1,57	2,65	171,7	2,7	176,1	7,1	213	80	171,55	4,81
GOE___1057_63	196	11	1,55	0,053	0,002	0,197	0,009	0,027	0,000	0,270	1,45	6,94	171,9	2,5	182,8	8	301	92	170,94	4,75
GOE___1057_35	1361	34	1,18	0,051	0,001	0,191	0,003	0,027	0,000	0,326	1,16	3,22	172,2	2	177,5	2,9	215	40	171,96	4,48

AnalysisName	U (ppm)1	Th (ppm)1	Th/U	$^{207}Pb/^{206}Pb$	±2σ	$^{207}Pb/^{235}U$	±2σ	$^{206}Pb/^{238}U$	±2σ	Correlación errores	% Error 6/8 2S	% disc. (6/8-7/5)	$^{206}Pb/^{238}U$ Edad (Ma)	±2σ	$^{207}Pb/^{235}U$ Edad (Ma)	±2σ	$^{207}Pb/^{206}Pb$ Edad (Ma)	±2σ	Best age	Unc 2σ
GOE___1057_27	834	170	2,18	0,051	0,001	0,191	0,005	0,027	0,000	0,300	1,28	2,59	172,5	2,2	176,7	4	243	51	172,24	4,55
GOE___1057_29	224	16	0,93	0,049	0,002	0,188	0,009	0,027	0,000	0,103	1,44	0,40	173,3	2,5	174	7,3	162	89	173,30	4,77
GOE___1057_10	330	10	1,49	0,052	0,002	0,193	0,007	0,027	0,000	0,168	1,44	2,94	173,4	2,5	178	6	264	74	172,91	4,74
GOE___1057_91	347	17	1,67	0,121	0,007	0,458	0,028	0,027	0,000	0,389	1,44	136,72	173,5	2,5	374	19	1880	100	157,99	4,62
GOE___1057_5	705,1	17	1,11	0,049	0,001	0,183	0,005	0,027	0,000	0,264	1,21	-1,60	173,7	2,1	171	4,3	162	55	173,79	4,56
GOE___1057_26	1213	110	1,62	0,053	0,001	0,201	0,005	0,027	0,000	0,296	1,21	7,20	173,7	2,1	185,4	3,8	318	43	172,94	4,54
GOE___1057_54	1031	8	0,51	0,050	0,001	0,190	0,005	0,027	0,000	0,512	1,32	1,39	173,9	2,3	176,2	3,9	207	44	173,78	4,67
GOE___1057_2	863	8,9	0,62	0,049	0,001	0,183	0,005	0,027	0,000	0,357	1,09	-1,89	174,1	1,9	170,9	3,9	141	49	174,19	4,50
GOE___1057_19	63,8	2,1	1,33	0,075	0,007	0,275	0,023	0,027	0,001	0,1	2,47	46,88	174,4	4,3	248	18	890	180	168,84	5,95
GOE___1057_39	445	26	1,67	0,050	0,002	0,190	0,005	0,027	0,000	0,186	1,32	1,33	174,4	2,3	176,6	4,5	216	60	174,28	4,68
GOE___1057_92	472	22	1,47	0,053	0,002	0,199	0,007	0,027	0,000	0,199	1,09	6,35	174,5	1,9	184,5	5,7	334	73	173,49	4,48
GOE___1057_33	375,4	32	2,26	0,051	0,002	0,194	0,007	0,027	0,000	0,298	1,32	3,01	174,6	2,3	179,6	5,6	212	65	174,34	4,68
GOE___1057_50	1816	56	1,52	0,049	0,001	0,188	0,004	0,027	0,000	0,611	1,20	0,12	174,6	2,1	174,9	3,3	161	34	174,69	4,55
GOE___1057_44	1827	42	1,20	0,049	0,001	0,187	0,003	0,028	0,000	0,427	1,14	-0,93	174,8	2	173,4	2,9	140	36	175,03	4,55
GOE___1057_57	524	8,8	0,91	0,049	0,001	0,187	0,006	0,027	0,000	0,359	1,54	-0,86	174,8	2,7	173,5	4,7	135	54	175,01	4,94
GOE___1057_58	1887	90	1,24	0,050	0,001	0,189	0,003	0,028	0,000	0,520	1,25	0,19	175,6	2,2	175,9	2,9	172	34	175,57	4,67
GOE___1057_32	349,9	27	1,56	0,050	0,002	0,189	0,006	0,028	0,000	0,268	1,31	0,31	175,7	2,3	176,3	5,3	179	65	175,76	4,75
GOE___1057_67	2832	93	2,12	0,055	0,001	0,213	0,003	0,028	0,000	0,483	1,19	11,80	176,4	2,1	195,8	2,9	417	34	175,14	4,58
GOE___1057_16	1131	63	1,62	0,050	0,001	0,192	0,004	0,028	0,000	0,433	1,19	1,09	176,5	2,1	178,3	3	185	37	176,37	4,61
GOE___1057_97	985	25	0,70	0,051	0,001	0,193	0,004	0,028	0,000	0,242	0,96	1,82	176,5	1,7	179,5	3,5	212	44	176,30	4,48
GOE___1057_66	912	47	1,07	0,049	0,001	0,191	0,004	0,028	0,000	0,376	1,24	0,23	176,8	2,2	177,3	3,6	162	44	176,90	4,68
GOE___1057_61	118,1	12	1,63	0,051	0,003	0,2	0,013	0,028	0,001	0,1	1,92	5,22	177	3,4	186	12	270	130	176,77	5,41
GOE___1057_8	42,6	1,6	1,15	0,059	0,007	0,227	0,027	0,028	0,001	0,100	2,26	14,13	177,2	4	200	23	430	210	175,24	5,95
GOE___1057_25	179	19	1,13	0,054	0,002	0,209	0,009	0,028	0,000	0,266	1,47	8,53	177,3	2,6	191,5	7,8	347	87	176,45	4,86
GOE___1057_43	839	41	0,77	0,059	0,003	0,231	0,016	0,028	0,000	0,698	1,46	16,19	177,6	2,6	204	11	448	88	175,57	4,92
GOE___1057_68	461	14	1,15	0,051	0,002	0,197	0,007	0,028	0,000	0,159	1,46	3,33	178	2,6	183,5	5,5	216	65	177,59	4,87
GOE___1057_75	827	31	0,88	0,052	0,001	0,197	0,005	0,028	0,000	0,471	1,35	3,02	178,1	2,4	182,9	3,9	277	45	177,54	4,79
GOE___1057_51	1365	15	0,90	0,050	0,001	0,194	0,004	0,028	0,000	0,476	1,35	0,89	178,2	2,4	179,8	2,9	182	35	178,21	4,80
GOE___1057_53	432	18	1,06	0,051	0,001	0,197	0,006	0,028	0,000	0,317	1,23	1,83	178,7	2,2	181,7	4,8	239	56	178,43	4,67
GOE___1057_71	1442	65	1,13	0,050	0,001	0,195	0,004	0,028	0,000	0,529	1,29	1,12	178,7	2,3	180,6	3,6	203	39	178,59	4,80

AnalysisName	U (ppm)1	Th (ppm)1	Th/U	$^{207}Pb/^{206}Pb$	±2σ	$^{207}Pb/^{235}U$	±2σ	$^{206}Pb/^{238}U$	±2σ	Correlación errores	% Error 6/8 2S	% disc. (6/8-7/5)	$^{206}Pb/^{238}U$ Edad (Ma)	±2σ	$^{207}Pb/^{235}U$ Edad (Ma)	±2σ	$^{207}Pb/^{206}Pb$ Edad (Ma)	±2σ	Best age	Unc 2σ
GOE___1057_85	843	55	1,19	0,050	0,001	0,192	0,005	0,028	0,000	0,203	1,17	-0,39	179	2,1	178,4	4,2	172	51	179,10	4,68
GOE___1057_40	314	67	1,64	0,052	0,004	0,208	0,016	0,028	0,000	0,168	1,73	8,02	179,2	3,1	193	14	330	150	178,67	5,24
GOE___1057_38	152	27	1,24	0,047	0,003	0,185	0,013	0,028	0,001	0,232	2,00	-4,08	179,6	3,6	173	11	80	120	180,36	5,56
GOE___1057_4	280,7	4,2	0,97	0,049	0,002	0,196	0,008	0,028	0,000	0,225	1,33	0,82	179,9	2,4	181,5	6,9	172	77	180,02	4,82
GOE___1057_94	899	47	1,14	0,050	0,001	0,195	0,006	0,028	0,001	0,463	1,83	0,23	179,9	3,3	180,4	4,9	178	54	179,98	5,37
GOE___1057_83	674	45	0,97	0,049	0,001	0,194	0,006	0,028	0,000	0,391	1,17	-0,23	180,2	2,1	179,9	5	155	54	180,32	4,74
GOE___1057_7	46,8	1,8	1,37	0,054	0,007	0,216	0,028	0,028	0,001	0,116	2,27	7,56	180,3	4,1	193	23	160	220	179,44	6,12
GOE___1057_84	847	34	0,81	0,051	0,001	0,200	0,005	0,028	0,000	0,308	1,27	2,95	180,4	2,3	185,4	4,2	242	51	180,08	4,79
GOE___1057_93	1786	100	1,11	0,050	0,001	0,196	0,004	0,028	0,000	0,514	1,27	0,76	180,5	2,3	181,8	3,2	205	37	180,44	4,80
GOE___1057_89	834	12	0,87	0,049	0,001	0,192	0,005	0,028	0,000	0,333	1,27	-1,46	180,8	2,3	178,4	4	142	48	181,04	4,81
GOE___1057_36	1750	160	1,62	0,051	0,001	0,203	0,004	0,028	0,000	0,624	1,44	3,57	181	2,6	187,2	3,2	232	36	180,75	4,98
GOE___1057_78	966	30	0,82	0,05	0,001	0,195	0,005	0,029	0,000	0,322	1,55	0,05	181,2	2,8	181,3	4,2	190	53	181,21	5,12
GOE___1057_77	965	51	0,99	0,051	0,001	0,203	0,006	0,029	0,000	0,430	1,37	2,51	182,8	2,5	187	4,9	259	55	182,43	4,92
GOE___1057_48	145,1	14	0,97	0,060	0,004	0,229	0,016	0,029	0,001	0,345	2,24	15,16	183	4,1	208	14	590	130	180,61	5,93
GOE___1057_42	451	34	0,84	0,052	0,002	0,207	0,007	0,029	0,000	0,160	1,36	3,95	184	2,5	190,9	6	260	68	183,64	4,93
GOE___1057_62	56,4	1,4	1,20	0,061	0,005	0,245	0,022	0,029	0,001	0,249	2,37	21,33	185,5	4,4	222	18	520	170	182,97	6,22
GOE___1057_96	921	24	0,62	0,051	0,001	0,202	0,005	0,029	0,000	0,463	1,40	0,14	185,9	2,6	186	3,9	222	43	185,75	5,11
GOE___1057_6	154	11	1,03	0,051	0,003	0,206	0,013	0,029	0,001	0,277	1,72	0,62	186,1	3,2	187	11	260	120	185,84	5,46
GOE___1057_76	711	44	0,92	0,05	0,001	0,203	0,005	0,030	0,000	0,342	1,38	-0,57	188,6	2,6	187,5	4,6	191	51	188,58	5,11
GOE___1057_12	226	18	1,12	0,050	0,002	0,203	0,008	0,030	0,000	0,247	1,48	-1,00	188,7	2,8	186,8	6,7	183	78	188,69	5,25
GOE___1057_95	354	19	0,99	0,050	0,002	0,203	0,008	0,030	0,000	0,313	1,58	-1,04	189,3	3	187,4	6,7	187	74	189,38	5,37
GOE___1057_82	657	11	1,02	0,051	0,001	0,210	0,005	0,030	0,000	0,324	1,26	1,87	189,8	2,4	193,2	4,4	213	50	189,65	5,05
GOE___1057_49	647	18	1,14	0,049	0,001	0,203	0,005	0,030	0,000	0,385	1,26	-1,62	190,2	2,4	187,2	4,4	145	51	190,28	5,06
GOE___1057_1	476	13	0,97	0,056	0,002	0,227	0,008	0,030	0,000	0,287	1,21	10,52	190,4	2,3	208,5	6,9	440	75	188,66	4,97
GOE___1057_90	211,6	8,8	0,92	0,049	0,002	0,202	0,010	0,030	0,000	0,114	1,47	-2,78	190,6	2,8	185,4	8	135	91	190,71	5,27
GOE___1057_79	128,7	9	1,20	0,053	0,005	0,239	0,024	0,032	0,001	0,336	3,46	4,92	205,2	7,1	215	20	310	180	204,92	8,88
GOE___1057_41	243	2,2	0,14	0,087	0,003	1,95	0,14	0,154	0,008	0,967	4,70	15,83	915	43	1048	51	1305	67	904,80	48,99
GOE___1057_17	385	2,4	0,28	0,074	0,001	1,637	0,024	0,160	0,002	0,589	1,04	2,82	959	10	983,2	9,3	1038	26	956,23	24,28
GOE___1057_18	161,2	2,2	0,35	0,074	0,001	1,661	0,031	0,163	0,002	0,389	1,13	2,63	972	11	995	12	1038	35	969,53	24,84
GOE___1057_60	6,3	0,85	5,87	0,731	0,023	17	0,57	0,169	0,005	0,527	2,80	1227,95	1001	28	2937	32	4810	53	221,17	37,68
GOE___1057_9	995	27	0,44	0,086	0,001	2,557	0,038	0,217	0,003	0,714	1,26	2,04	1268	16	1289	11	1322	22	1263,24	33,23
GOE___1057_70	3,86	0,4	3,85	0,806	0,029	26,5	1	0,240	0,008	0,511	3,10	1346,55	1385	43	3363	38	4977	66	232,48	61,27

Table 3.

AnalysisName	U (ppm)1	Th (ppm)1	Th/U	$^{207}Pb/^{206}Pb$	±2σ	$^{207}Pb/^{235}U$	±2σ	$^{206}Pb/^{238}U$	±2σ	Correlación errores	% Error 6/8 2S	% disc. (6/8-7/5)	$^{206}Pb/^{238}U$ Edad (Ma)	±2σ	$^{207}Pb/^{235}U$ Edad (Ma)	±2σ	$^{207}Pb/^{206}Pb$ Edad (Ma)	±2σ	Best age	Unc 2σ
GR___6849_37	2640	2410	0,91			0,187	0,004	0,025	0,001	0,690	3,26	9,07	160,078	5,222	174,6	3,5	358	37	160,08	5,22
GR___6849_49	538	357	0,66			0,200	0,010	0,025	0,000	0,285	2,98	14,60	160,477	4,790	183,9	8,1	467	93	160,48	4,79
GR___6849_55	1464	1272	0,87			0,180	0,004	0,026	0,000	0,291	2,57	1,96	164,580	4,238	167,8	3,5	197	46	164,58	4,24
GR___6849_47	323,1	188,5	0,58			0,184	0,007	0,026	0,000	0,043	2,68	1,76	167,941	4,504	170,9	6,1	203	82	167,94	4,50
GR___6849_14	845	624	0,74			0,192	0,007	0,027	0,000	0,246	2,73	3,49	171,803	4,683	177,8	6,2	213	74	171,80	4,68
GR___6849_33	350,5	236,2	0,67			0,184	0,007	0,027	0,000	0,233	2,75	-1,10	172,607	4,752	170,7	5,9	181	73	172,61	4,75
GR___6849_34	259	255	0,98			0,201	0,010	0,028	0,000	0,157	2,85	6,38	175,226	4,999	186,4	8,2	298	95	175,23	5,00
GR___6849_22	217	157,8	0,73			0,209	0,012	0,028	0,000	0,147	2,72	8,74	174,813	4,756	190,1	9,9	340	110	174,81	4,76
GR___6849_41	148	104,7	0,71			0,226	0,016	0,028	0,001	0,109	3,02	19,44	174,142	5,257	208	13	540	130	174,14	5,26
GR___6849_50	219	135,2	0,62			0,196	0,012	0,028	0,001	0,251	2,96	2,57	176,073	5,203	180,6	9,9	220	110	176,07	5,20
GR___6849_13	478	471	0,99			0,212	0,01	0,028	0,000	0,119	2,77	10,65	175,960	4,866	194,7	8,4	373	94	175,96	4,87
GR___6849_12	834	1328	1,59			0,192	0,007	0,028	0,000	0,293	2,64	-0,00	177,605	4,687	177,6	5,9	184	69	177,60	4,69
GR___6849_44	207,6	272	1,31			0,199	0,012	0,028	0,000	0,265	2,79	2,87	177,503	4,954	182,6	9,8	240	110	177,50	4,95
GR___6849_11	152,3	129,3	0,85			0,211	0,019	0,028	0,001	0,137	3,18	7,17	177,290	5,632	190	16	260	160	177,29	5,63
GR___6849_58	97,6	61,8	0,63			0,26	0,03	0,028	0,001	0,016	3,52	29,55	174,451	6,139	226	23	650	210	174,45	6,14
GR___6849_54	266	255	0,96			0,201	0,01	0,028	0,000	0,170	2,77	3,16	178,264	4,942	183,9	8,5	273	96	178,26	4,94
GR___6849_39	645	308	0,48			0,200	0,006	0,028	0,000	0,309	2,65	3,65	178,671	4,733	185,2	5,2	275	58	178,67	4,73
GR___6849_19	648	502	0,77			0,207	0,007	0,028	0,000	0,296	2,72	6,61	178,601	4,857	190,4	5,7	287	64	178,60	4,86
GR___6849_17	247,1	231,2	0,94			0,206	0,012	0,028	0,000	0,248	2,93	5,18	179,699	5,264	189	10	250	110	179,70	5,26
GR__6849_3	190,4	212,2	1,11			0,203	0,011	0,028	0,000	0,257	2,89	3,48	179,843	5,197	186,1	9,3	280	100	179,84	5,20
GR___6849_10	436	327	0,75			0,194	0,009	0,028	0,000	0,072	2,74	-0,14	180,349	4,950	180,1	8	178	93	180,35	4,95
GR__6849_6	578	350,5	0,61			0,205	0,008	0,028	0,000	0,384	2,77	5,03	180,430	4,992	189,5	6,9	259	74	180,43	4,99
GR___6849_51	883	551	0,62			0,199	0,005	0,028	0,000	0,255	2,69	1,71	180,812	4,864	183,9	4,6	201	54	180,81	4,86
GR___6849_28	78,9	44,65	0,57			0,2	0,02	0,029	0,001	0,236	3,02	1,85	181,636	5,479	185	16	180	170	181,64	5,48
GR___6849_40	78,6	38,8	0,49			0,211	0,064	0,029	0,001	0,1	8,26	21,77	172,457	14,241	210	40	-750	960	172,46	14,24
GR__6849_4	172,3	154,8	0,90			0,235	0,014	0,029	0,000	0,316	2,89	18,66	181,185	5,244	215	12	500	120	181,18	5,24
GR___6849_18	616	360	0,58			0,205	0,007	0,029	0,000	0,254	2,70	3,08	182,874	4,929	188,5	6,2	233	68	182,87	4,93
GR___6849_32	459	491	1,07			0,205	0,007	0,029	0,000	0,189	2,68	2,83	183,508	4,924	188,7	5,8	265	69	183,51	4,92
GR___6849_46	182,8	203	1,11			0,216	0,014	0,029	0,000	0,082	2,76	8,60	184,162	5,080	200	11	300	110	184,16	5,08
GR___6849_15	369	397	1,08			0,209	0,012	0,029	0,001	0,232	2,90	6,50	185,732	5,390	197,8	9,5	310	100	185,73	5,39
GR___6849_56	315	169,2	0,54			0,202	0,010	0,029	0,000	0,258	2,81	0,18	187,168	5,256	187,5	7,9	194	87	187,17	5,26

AnalysisName	U (ppm)1	Th (ppm)1	Th/U	$^{207}Pb/^{206}Pb$	±2σ	$^{207}Pb/^{235}U$	±2σ	$^{206}Pb/^{238}U$	±2σ	Correlación errores	% Error 6/8 2S	% disc. (6/8-7/5)	$^{206}Pb/^{238}U$ Edad (Ma)	±2σ	$^{207}Pb/^{235}U$ Edad (Ma)	±2σ	$^{207}Pb/^{206}Pb$ Edad (Ma)	±2σ	Best age	Unc 2σ
GR___6849_7	535	572	1,07			0,221	0,009	0,030	0,000	0,157	2,67	8,63	186,686	4,979	202,8	7,1	368	81	186,69	4,98
GR___6849_20	141,1	125,2	0,89			0,212	0,014	0,030	0,001	0,181	2,94	6,53	187,732	5,526	200	12	310	120	187,73	5,53
GR___6849_30	222	156	0,70			0,223	0,011	0,030	0,000	0,1	2,81	8,16	188,617	5,308	204	9,5	340	100	188,62	5,31
GR___6849_5	82,7	67,8	0,82			0,229	0,025	0,030	0,001	0,228	3,25	13,48	189,462	6,155	215	20	350	180	189,46	6,16
GR___6849_48	46,9	35,1	0,75			0,265	0,036	0,030	0,001	0,047	3,78	22,57	188,456	7,127	231	29	420	240	188,46	7,13
GR___6849_43	70,1	55,1	0,79			0,261	0,033	0,031	0,001	0,045	3,40	22,03	190,935	6,495	233	26	470	220	190,93	6,49
GR___6849_16	376	242	0,64			0,234	0,012	0,031	0,001	0,301	3,22	7,90	195,559	6,304	211	10	328	98	195,56	6,30
GR___6849_31	74,4	56	0,75			0,4	0,035	0,031	0,001	0,238	3,38	79,24	186,899	6,313	335	24	1360	160	186,90	6,31
GR___6849_23	142	92	0,65			0,321	0,019	0,046	0,001	0,055	2,84	-2,32	287,671	8,172	281	15	220	110	287,67	8,17
GR___6849_8	248,7	809	3,25			0,748	0,024	0,089	0,001	0,374	2,75	2,54	550,984	15,129	565	14	546	67	550,98	15,13
GR___6849_9	286	295	1,03			0,72	0,023	0,09	0,001	0,248	2,62	-1,08	555,994	14,540	550	14	519	63	555,99	14,54
GR___6849_53	10,34	9,68	0,94			0,81	0,15	0,091	0,003	0,1	4,28	3,40	552,250	23,655	571	87	430	310	552,25	23,66
GR___6849_52	423	549	1,30			0,864	0,02	0,102	0,002	0,525	2,69	1,28	623,006	16,788	631	11	605	44	623,01	16,79
GR___6849_60	466	178,3	0,38			1,351	0,021	0,142	0,002	0,476	2,59	1,25	855,917	22,205	866,6	9	890	31	855,92	22,20
GR___6849_61	390	209,5	0,54			1,384	0,025	0,145	0,002	0,426	2,61	0,77	873,267	22,771	880	11	904	36	873,27	22,77
GR___6849_36	94,7	49,4	0,52			1,563	0,047	0,155	0,003	0,352	2,76	3,31	926,298	25,551	957	18	1001	55	926,30	25,55
GR___6849_42	9,36	3,07	0,33			1,83	0,17	0,157	0,004	0,049	3,54	10,88	922,606	32,651	1023	65	1020	200	922,61	32,65
GR___6849_35	85,5	29,31	0,34			1,581	0,048	0,161	0,002	0,310	2,65	-0,89	963,584	25,555	955	19	957	64	963,58	25,55
GR___6849_21	1330	662	0,50			1,664	0,039	0,162	0,004	0,862	3,10	2,46	965,250	29,970	989	15	1054	25	965,25	29,97
GR___6849_59	147,8	40,8	0,28			1,695	0,037	0,167	0,002	0,342	2,62	1,41	992,047	25,991	1006	14	1020	42	992,05	25,99
GR___6849_38	402	124,9	0,31			1,959	0,031	0,182	0,002	0,650	2,50	2,39	1076,323	26,878	1102	11	1139	26	1076,32	26,88
GR___6849_26	110,5	31,5	0,29			2,276	0,053	0,206	0,003	0,383	2,63	-0,24	1209,876	31,864	1207	16	1189	45	1209,88	31,86
GR___6849_27	389	85,9	0,22			2,225	0,033	0,207	0,003	0,565	2,58	-1,90	1214,080	31,276	1191	11	1158	25	1214,08	31,28
GR___6849_45	218,5	157,1	0,72			2,606	0,044	0,221	0,003	0,448	2,55	1,44	1283,531	32,716	1302	12	1316	32	1283,53	32,72
GR___6849_1	74,2	10,1	0,14			2,672	0,077	0,226	0,004	0,477	2,92	0,57	1311,547	38,288	1319	21	1348	51	1311,55	38,29
GR___6849_2	69,5	12,76	0,18			2,857	0,074	0,235	0,004	0,471	2,82	0,84	1357,604	38,238	1369	20	1394	48	1357,60	38,24
GR___6849_29	146,9	40,2	0,27			2,913	0,066	0,237	0,004	0,393	2,71	1,18	1369,841	37,083	1386	16	1371	37	1369,84	37,08
GR___6849_24	198	112,4	0,57			5,95	0,11	0,332	0,005	0,698	2,74	8,14	1816,164	49,845	1964	16	2089	23	1816,16	49,84
GR___6849_25	206,3	87,4	0,42			6,694	0,096	0,363	0,005	0,656	2,65	5,05	1974,315	52,418	2074	13	2135	20	1974,32	52,42
GR___6849_57	-0,000	0,017	-9081,75			no value	NAN	no value	NAN		#VALUE	#VALUE	#VALUE	#VALUE	no value	NAN	no value	NAN	#VALUE	#VALUE

Table 4.

AnalysisName	U (ppm)1	Th (ppm)1	Th/U	$^{207}Pb/^{206}Pb$	±2σ abs	$^{207}Pb/^{235}U$	±2σ abs2	$^{206}Pb/^{238}U$	±2σ abs3	Correlación errores	% Error 6/8 2S	% disc. (6/8-7/5)	$^{206}Pb/^{238}U$ Edad (Ma)	±2σ	$^{207}Pb/^{235}U$ Edad (Ma)	±2σ4	$^{207}Pb/^{206}Pb$ Edad (Ma)	±2σ5	Best age	Unc 2σ
GR___6851_47	107	257,9	2,41	0,060	0,002	0,205	0,009	0,025	0,001	0,360	2,86	19,35	158,19	4,52	188,8	7,3	623	85	158,19	4,52
GR___6851_17	578	345,8	0,60	0,050	0,001	0,192	0,005	0,028	0,001	0,467	2,34	0,09	178,13	4,17	178,3	4,1	179	52	178,13	4,17
GR___6851_34	292,9	248	0,85	0,050	0,001	0,191	0,004	0,028	0,001	0,539	2,50	-1,13	179,22	4,48	177,2	3,3	170	51	179,22	4,48
GR___6851_2	453,4	778	1,72	0,050	0,001	0,197	0,006	0,029	0,000	0,662	2,18	0,20	182,33	3,98	182,7	5,1	192	55	182,33	3,98
GR___6851_16	659	543	0,82	0,051	0,001	0,199	0,004	0,029	0,000	0,423	1,97	1,34	182,16	3,59	184,6	3	218	34	182,16	3,59
GR___6851_46	252,2	298	1,18	0,051	0,001	0,204	0,006	0,029	0,000	0,579	2,07	2,85	182,90	3,79	188,1	5,4	231	53	182,90	3,79
GR___6851_39	267,8	168,9	0,63	0,049	0,001	0,193	0,006	0,029	0,001	0,730	2,92	-2,23	183,60	5,36	179,5	5,2	159	43	183,60	5,36
GR___6851_43	184,2	130,9	0,71	0,050	0,001	0,203	0,005	0,029	0,001	0,329	2,51	1,03	186,08	4,67	188	4,1	198	60	186,08	4,67
GR___6851_37	32,5	25,3	0,78	0,053	0,003	0,209	0,014	0,029	0,001	0,322	2,93	3,42	185,66	5,44	192	12	310	130	185,66	5,44
GR___6851_36	27,7	31,5	1,14	0,060	0,004	0,244	0,016	0,029	0,001	0,296	2,62	19,94	184,25	4,82	221	13	570	150	184,25	4,82
GR___6851_18	227	237	1,04	0,052	0,001	0,207	0,007	0,030	0,001	0,759	3,12	1,90	187,24	5,85	190,8	5,7	264	50	187,24	5,85
GR___6851_6	339,3	448	1,32	0,051	0,001	0,209	0,004	0,030	0,000	0,751	2,21	2,17	188,12	4,16	192,2	3,5	220	38	188,12	4,16
GR___6851_25	188	101,8	0,54	0,050	0,002	0,211	0,010	0,030	0,001	0,742	3,31	2,01	190,18	6,30	194	8	208	66	190,18	6,30
GR___6851_3	353	406,7	1,15	0,050	0,001	0,209	0,005	0,030	0,000	0,519	2,18	0,88	190,82	4,16	192,5	3,9	196	39	190,82	4,16
GR___6851_32	214	140,1	0,65	0,050	0,001	0,208	0,006	0,030	0,001	0,731	2,25	0,69	190,68	4,28	192	4,8	207	46	190,68	4,28
GR___6851_26	193,9	138,7	0,72	0,050	0,001	0,210	0,005	0,030	0,000	0,672	1,98	0,87	191,44	3,78	193,1	4	207	48	191,44	3,78
GR___6851_13	208,2	155,4	0,75	0,052	0,001	0,217	0,005	0,030	0,000	0,201	1,91	3,90	191,82	3,66	199,3	4,6	286	59	191,82	3,66
GR___6851_22	169,5	135,8	0,80	0,056	0,002	0,235	0,009	0,030	0,000	0,164	2,04	12,52	191,25	3,91	215,2	7,5	448	85	191,25	3,91
GR___6851_29	298	180	0,60	0,051	0,001	0,213	0,005	0,030	0,001	0,601	2,35	1,61	192,71	4,53	195,8	4,4	235	44	192,71	4,53
GR___6851_44	110,7	149,2	1,35	0,052	0,001	0,213	0,007	0,030	0,000	0,292	2,16	2,05	192,85	4,16	196,8	5,8	261	63	192,85	4,16
GR___6851_14	216	133,2	0,62	0,051	0,001	0,216	0,005	0,031	0,000	0,497	2,08	2,66	193,46	4,03	198,6	4,5	260	55	193,46	4,03
GR___6851_4	230,2	188,8	0,82	0,058	0,003	0,246	0,014	0,031	0,001	0,186	2,81	15,96	192,30	5,41	223	11	480	110	192,30	5,41
GR___6851_19	196	135,1	0,69	0,051	0,002	0,216	0,007	0,031	0,000	0,418	1,99	2,43	194,00	3,85	198,7	6,1	231	68	194,00	3,85
GR___6851_1	185	165,8	0,90	0,050	0,002	0,215	0,008	0,031	0,001	0,450	2,59	1,57	194,64	5,05	197,7	7	206	78	194,64	5,05
GR___6851_31	333	460	1,38	0,056	0,001	0,236	0,005	0,031	0,000	0,529	1,80	10,72	194,46	3,51	215,3	4,1	448	43	194,46	3,51
GR___6851_23	148,1	129,6	0,88	0,050	0,002	0,215	0,007	0,031	0,000	0,294	1,93	0,46	196,99	3,80	197,9	6,2	206	78	196,99	3,80
GR___6851_45	165	336	2,04	0,089	0,006	0,372	0,025	0,031	0,000	0,296	2,11	70,47	187,71	3,96	320	18	1370	140	187,71	3,96
GR___6851_12	89,8	79,9	0,89	0,123	0,009	0,53	0,05	0,031	0,001	0,742	3,69	135,44	181,78	6,71	428	32	1950	130	181,78	6,71
GR___6851_21	167,7	209,5	1,25	0,056	0,002	0,246	0,01	0,032	0,000	0,182	2,11	11,62	199,70	4,22	222,9	8,4	443	90	199,70	4,22
GR___6851_8	305	378	1,24	0,068	0,02	0,4	0,17	0,032	0,003	0,451	9,54	33,73	200,41	19,11	268	81	600	340	200,41	19,11
GR___6851_35	14,8	49,7	3,36	0,079	0,007	0,36	0,03	0,032	0,002	0,142	5,30	57,35	197,01	10,45	310	23	1170	190	197,01	10,45

AnalysisName	U (ppm)1	Th (ppm)1	Th/U	$^{207}Pb/^{206}Pb$	±2σ abs	$^{207}Pb/^{235}U$	±2σ abs2	$^{206}Pb/^{238}U$	±2σ abs3	Correlación errores	% Error 6/8 2S	% disc. (6/8-7/5)	$^{206}Pb/^{238}U$ Edad (Ma)	±2σ	$^{207}Pb/^{235}U$ Edad (Ma)	±2σ4	$^{207}Pb/^{206}Pb$ Edad (Ma)	±2σ5	Best age	Unc 2σ
GR___6851_9	305	536	1,76	0,054	0,001	0,238	0,007	0,032	0,000	0,505	1,94	6,47	203,53	3,95	216,7	5,5	369	44	203,53	3,95
GR___6851_7	243	360	1,48	0,052	0,001	0,237	0,006	0,033	0,001	0,609	2,57	3,97	207,47	5,34	215,7	5,1	298	51	207,47	5,34
GR___6851_20	119,5	253,1	2,12	0,052	0,001	0,245	0,008	0,034	0,001	0,676	2,48	3,10	215,32	5,34	222	6,2	276	61	215,32	5,34
GR___6851_42	65,6	77,3	1,18	0,06	0,002	0,285	0,011	0,035	0,001	0,381	2,65	17,53	216,21	5,72	254,1	8,9	593	66	216,21	5,72
GR___6851_24	37,9	45,4	1,20	0,057	0,004	0,272	0,019	0,036	0,002	0,238	4,69	7,86	226,22	10,61	244	15	460	140	226,22	10,61
GR___6851_5	13,6	33,6	2,47	0,066	0,006	0,403	0,089	0,045	0,004	0,166	7,87	26,43	280,80	22,10	355	46	780	220	280,80	22,10
GR___6851_10	1,68	1,25	0,74	0,088	0,03	0,96	0,32	0,083	0,009	0,1	11,51	21,74	492,87	56,75	600	190	880	710	492,87	56,75
GR___6851_11	1	1,24	1,24	0,208	0,044	2,77	0,75	0,093	0,013	0,455	15,12	173,94	470,91	71,21	1290	190	2440	590	470,91	71,21
GR___6851_33	748	326	0,44	0,061	0,001	0,819	0,017	0,099	0,002	0,873	2,77	0,32	605,18	16,76	607,1	9,6	630	21	605,18	16,76
GR___6851_27	228,8	243,6	1,06	0,060	0,001	0,844	0,014	0,102	0,001	0,555	1,82	-0,39	625,41	11,39	623	7,5	607	31	625,41	11,39
GR___6851_40	101,4	60,1	0,59	0,069	0,001	1,413	0,025	0,149	0,002	0,798	2,15	0,16	892,58	19,19	894	11	907	24	892,58	19,19
GR___6851_48	213,8	191	0,89	0,074	0,001	1,691	0,022	0,167	0,002	0,604	1,85	0,87	996,22	18,43	1004,9	8,5	1034	22	996,22	18,43
GR___6851_15	194,6	127,3	0,65	0,074	0,001	1,76	0,026	0,173	0,002	0,655	1,85	0,54	1025,05	18,97	1030,6	9,3	1044	23	1025,05	18,97
GR___6851_28	117,5	36,1	0,31	0,086	0,001	2,75	0,057	0,235	0,004	0,606	2,31	-1,48	1361,14	31,43	1341	15	1326	31	1361,14	31,43
GR___6851_41	245	88,9	0,36	0,127	0,001	6,095	0,074	0,349	0,005	0,769	2,07	3,93	1913,82	39,67	1989	11	2051	14	1913,82	39,67
GR___6851_30	11,3	2,83	0,25	0,075	0,002	3,68	0,19	0,355	0,013	0,882	3,96	-24,20	2059,48	81,57	1561	40	1064	56	2059,48	81,57
GR___6851_38	613	105	0,17	0,165	0,005	8,83	0,39	0,386	0,009	0,843	2,914	14,485	2022,10	58,93	2315	43	2508	54	2022,10	58,93

Table 5.

AnalysisName	U (ppm)1	Th (ppm)1	Th/U	$^{207}Pb/^{206}Pb$	±2σ abs	$^{207}Pb/^{235}U$	±2σ abs2	$^{206}Pb/^{238}U$	±2σ abs3	Correlación errores	% Error 6/8 2S	% disc. (6/8-7/5)	$^{206}Pb/^{238}U$ Edad (Ma)	±2σ	$^{207}Pb/^{235}U$ Edad (Ma)	±2σ4	$^{207}Pb/^{206}Pb$ Edad (Ma)	±2σ5	Best age	Unc 2σ
GR___6854_7	70,8	127,3	1,80	0,060	0,003	0,234	0,008	0,029	0,001	0,1	2,41	17,24	182,10	4,40	213,5	6,9	560	100	182,10	4,40
GR___6854_16	709	258	0,36	0,068	0,001	0,683	0,027	0,073	0,003	0,932	3,64	18,95	445,58	16,21	530	17	882	23	445,58	16,21
GR___6854_3	1920	148	0,08	0,074	0,001	0,964	0,036	0,093	0,003	0,918	3,36	21,50	562,98	18,90	684	18	1045	18	562,98	18,90
GR___6854_5	784	62,7	0,08	0,081	0,001	1,428	0,061	0,127	0,004	0,978	3,51	18,73	756,34	26,55	898	26	1230	21	756,34	26,55
GR___6854_29	740	189	0,26	0,088	0,002	2,72	0,22	0,221	0,014	0,986	6,11	3,02	1280,39	78,19	1319	61	1386	40	1280,39	78,19
GR___6854_21	377,4	81,9	0,22	0,076	0,001	1,488	0,024	0,142	0,002	0,887	2,25	9,01	848,74	19,07	925,2	9,9	1094	19	848,74	19,07
GR___6854_15	143	4,2	0,03	0,072	0,002	1,675	0,075	0,170	0,009	0,927	5,39	-1,76	1013,89	54,64	996	29	978	45	1013,89	54,64
GR___6854_26	423	159,1	0,38	0,076	0,001	1,782	0,027	0,171	0,003	0,736	2,26	2,17	1015,91	22,91	1038	10	1095	24	1015,91	22,91
GR___6854_2	257	145	0,56	0,074	0,001	1,764	0,022	0,174	0,002	0,571	1,83	-0,22	1034,39	18,95	1032,1	8,2	1039	25	1034,39	18,95
GR___6854_14	507	166	0,33	0,082	0,003	2,03	0,25	0,177	0,018	0,986	9,81	5,11	1041,78	102,17	1095	89	1227	62	1041,78	102,17
GR___6854_13	244	96	0,39	0,073	0,001	1,752	0,027	0,176	0,003	0,751	2,19	-1,67	1047,41	22,96	1029,9	9,1	1017	22	1047,41	22,96
GR___6854_8	167,7	70	0,42	0,08	0,001	1,981	0,048	0,180	0,003	0,646	2,21	4,68	1058,51	23,37	1108	16	1194	35	1058,51	23,37
GR___6854_27	1300	197	0,15	0,079	0,001	1,935	0,043	0,180	0,004	0,942	2,63	3,10	1060,12	27,90	1093	15	1163	17	1060,12	27,90
GR___6854_22	154,7	71,5	0,46	0,073	0,001	1,793	0,024	0,181	0,002	0,429	1,87	-2,79	1072,54	20,09	1042,6	8,9	1017	30	1072,54	20,09
GR___6854_31	462	151	0,33	0,087	0,001	2,29	0,11	0,188	0,008	0,957	4,25	9,68	1098,67	46,72	1205	34	1344	35	1098,67	46,72
GR___6854_11	172	63,5	0,37	0,087	0,004	2,52	0,21	0,206	0,01	0,784	5,16	6,29	1198,57	61,86	1274	65	1342	82	1198,57	61,86
GR___6854_28	206	98,9	0,48	0,086	0,003	2,47	0,2	0,206	0,01	0,977	5,15	4,36	1199,67	61,82	1252	57	1330	62	1199,67	61,82
GR___6854_12	736	474	0,64	0,092	0,001	2,667	0,08	0,209	0,005	0,955	2,68	9,28	1205,21	32,33	1317	22	1471	18	1205,21	32,33
GR___6854_19	358	94	0,26	0,080	0,001	2,29	0,14	0,208	0,011	0,977	5,10	-1,40	1219,08	62,13	1202	40	1199	30	1219,08	62,13
GR___6854_9	335,8	126,9	0,38	0,086	0,001	2,52	0,051	0,213	0,004	0,940	2,31	3,47	1237,06	28,61	1280	16	1343	19	1237,06	28,61
GR___6854_4	422	152,1	0,36	0,087	0,002	2,539	0,08	0,213	0,005	0,802	2,67	3,35	1239,49	33,11	1281	23	1376	28	1239,49	33,11
GR___6854_30	30,5	14,7	0,48	0,079	0,002	2,3	0,11	0,216	0,012	0,840	5,36	-4,55	1266,63	67,85	1209	32	1154	47	1266,63	67,85
GR___6854_6	343,9	96,7	0,28	0,091	0,001	2,777	0,052	0,224	0,003	0,762	2,15	4,12	1295,57	27,89	1349	14	1437	21	1295,57	27,89
GR___6854_23	390	123,8	0,32	0,092	0,001	2,847	0,045	0,227	0,003	0,821	2,13	4,80	1307,22	27,83	1370	12	1469	20	1307,22	27,83
GR___6854_25	117,7	82,1	0,70	0,081	0,001	2,521	0,065	0,227	0,005	0,913	2,76	-3,69	1325,89	36,60	1277	19	1223	20	1325,89	36,60
GR___6854_20	226	68,5	0,30	0,090	0,001	2,899	0,073	0,236	0,004	0,930	2,34	1,47	1359,97	31,78	1380	19	1416	20	1359,97	31,78
GR___6854_10	282	84	0,30	0,092	0,002	3,31	0,12	0,259	0,007	0,960	3,06	-0,53	1487,85	45,54	1480	30	1471	31	1487,85	45,54
GR___6854_18	346	127,1	0,37	0,096	0,001	3,584	0,042	0,270	0,003	0,779	1,94	0,56	1537,13	29,88	1545,7	9,3	1557	18	1537,13	29,88
GR___6854_17	340	94,9	0,28	0,095	0,001	3,63	0,19	0,275	0,011	0,972	4,23	-1,40	1569,90	66,43	1548	44	1529	30	1569,90	66,43
GR___6854_1	362	132,5	0,37	0,097	0,001	3,679	0,035	0,277	0,002	0,610	1,79	-0,75	1578,36	28,21	1566,6	7,6	1565	14	1578,36	28,21
GR___6854_24	381	132	0,35	0,099	0,001	3,869	0,08	0,285	0,006	0,827	2,50	-0,56	1615,00	40,30	1606	17	1601	23	1615,00	40,30

Table 6.

AnalysisName	U (ppm)1	Th (ppm)1	Th/U	$^{207}Pb/^{206}Pb$	±2σ s	$^{207}Pb/^{235}U$	±2σ	$^{206}Pb/^{238}U$	±2σ	Correlación errores	% Error 6/8 2S	% disc. (6/8-7/5)	$^{206}Pb/^{238}U$ Edad (Ma)	±2σ	$^{207}Pb/^{235}U$ Edad (Ma)	±2σ	$^{207}Pb/^{206}Pb$ Edad (Ma)	±2σ	Best age	Unc 2σ
GZ___6903_52	281	545	0,52	0,049	0,003	0,185	0,013	0,027	0,000	0,269	1,70	-0,55	170,8	2,9	170	11	160	120	170,95	6,99
GZ___6903_29	1852	2228	0,83	0,050	0,001	0,185	0,004	0,027	0,000	0,480	1,28	0,53	171,3	2,2	172,2	3,2	175	39	171,29	6,32
GZ___6903_51	396	940	0,42	0,059	0,003	0,223	0,011	0,027	0,000	0,181	1,69	20,05	171,9	2,9	203,9	8,9	555	98	169,84	6,90
GZ___6903_68	196	140	1,40	0,048	0,004	0,178	0,016	0,027	0,001	0,230	1,92	-2,60	172	3,3	168	13	110	140	172,49	7,02
GZ___6903_69	68,7	39,4	1,74	0,050	0,010	0,195	0,038	0,027	0,001	0,062	2,41	-3,21	174,1	4,2	168	32	160	270	173,57	7,86
GZ___6903_36	299,2	236,5	1,27	0,054	0,003	0,203	0,01	0,028	0,000	0,079	1,59	7,31	175,6	2,8	187,2	8,6	310	100	174,44	6,94
GZ___6903_16	411	614	0,67	0,051	0,002	0,192	0,007	0,028	0,000	0,319	1,47	0,68	177,3	2,6	178,3	6,2	212	72	177,09	6,95
GZ___6903_28	499	760	0,66	0,050	0,002	0,195	0,006	0,028	0,000	0,325	1,51	0,64	178,8	2,7	179,9	5,5	196	64	178,75	6,95
GZ___6903_8	904	1320	0,68	0,050	0,002	0,190	0,006	0,028	0,000	0,330	1,17	-1,19	179,6	2,1	177,2	4,8	202	59	179,34	6,95
GZ___6903_19	296	200,8	1,47	0,053	0,002	0,202	0,008	0,028	0,000	0,136	1,61	3,21	180,2	2,9	185,3	6,7	301	83	179,53	6,93
GZ___6903_10	530	714	0,74	0,080	0,005	0,317	0,02	0,028	0,000	0,285	1,49	57,80	180,7	2,7	274	15	1090	110	173,64	6,79
GZ___6903_63	91	70,9	1,28	0,056	0,004	0,295	0,019	0,039	0,001	0,141	1,83	6,53	245,5	4,5	260	15	370	130	244,06	10,02
GZ___6903_48	384,6	165	2,33	0,052	0,002	0,289	0,011	0,040	0,001	0,366	1,47	2,20	252,1	3,7	257,5	8,7	273	72	251,95	9,39
GZ___6903_47	207	148	1,40	0,051	0,003	0,292	0,014	0,041	0,001	0,193	1,58	0,08	258,7	4,1	259	12	234	95	258,78	10,04
GZ___6903_35	457	286	1,60	0,052	0,002	0,305	0,010	0,043	0,001	0,232	1,37	0,09	270	3,7	270,2	7,5	263	68	269,96	10,00
GZ___6903_26	236,4	90,6	2,61	0,062	0,002	0,676	0,019	0,080	0,001	0,381	1,35	6,68	494,5	6,7	525	11	653	57	492,12	18,77
GZ___6903_64	1213	840	1,44	0,092	0,002	1,143	0,023	0,092	0,002	0,748	2,47	41,76	567	14	773	11	1448	31	545,30	23,29
GZ___6903_21	922	38,8	23,76	0,072	0,001	1,111	0,018	0,112	0,002	0,627	1,32	11,99	683,6	9	757,4	8,6	973	29	676,28	25,37
GZ___6903_49	136,7	34,3	3,99	0,068	0,002	1,329	0,04	0,142	0,002	0,270	1,41	0,51	854	12	858	17	861	59	853,60	32,21
GZ___6903_12	158	37,1	4,26	0,071	0,002	1,375	0,044	0,142	0,003	0,605	1,99	2,76	856	17	876	19	958	54	852,46	33,84
GZ___6903_5	165,2	103,4	1,60	0,069	0,002	1,347	0,035	0,142	0,002	0,347	1,17	0,66	858	10	863	15	893	54	857,38	31,61
GZ___6903_15	1669	197,4	8,45	0,071	0,001	1,381	0,022	0,143	0,002	0,718	1,39	2,56	861	12	879,6	9,5	945	24	857,64	32,08
GZ___6903_11	90,5	49,6	1,82	0,069	0,002	1,366	0,045	0,147	0,002	0,339	1,36	-0,31	883	12	880	19	863	63	882,77	32,74
GZ___6903_30	191,9	16,35	11,74	0,071	0,002	1,498	0,035	0,151	0,002	0,427	1,21	2,44	908	11	929	15	957	45	906,90	33,76
GZ___6903_9	442	266	1,66	0,072	0,001	1,526	0,029	0,156	0,002	0,578	1,18	0,67	933	11	938	12	980	32	931,74	34,23
GZ___6903_14	162,7	33,5	4,86	0,072	0,002	1,541	0,038	0,156	0,002	0,430	1,39	1,42	934	13	944	15	962	45	930,80	34,85
GZ___6903_54	234	120,8	1,94	0,072	0,002	1,579	0,036	0,157	0,002	0,329	1,38	2,53	940	13	961	14	988	47	937,33	34,80
GZ___6903_67	181	121	1,50	0,073	0,002	1,588	0,046	0,157	0,003	0,703	1,81	2,63	940	17	962	18	1014	42	937,36	36,50
GZ___6903_3	207,6	12,88	16,12	0,071	0,001	1,535	0,036	0,158	0,002	0,495	1,27	-0,19	945	12	944	15	938	41	945,75	34,84
GZ___6903_20	395,3	118,4	3,34	0,075	0,001	1,632	0,029	0,159	0,002	0,609	1,16	3,58	951	11	981	11	1056	29	947,13	34,68
GZ___6903_66	837	114	7,34	0,075	0,001	1,663	0,041	0,160	0,003	0,822	1,89	5,00	953	18	998	16	1051	27	950,47	37,53

AnalysisName	U (ppm)1	Th (ppm)1	Th/U	$^{207}Pb/^{206}Pb$	±2σ s	$^{207}Pb/^{235}U$	±2σ	$^{206}Pb/^{238}U$	±2σ	Correlación errores	% Error 6/8 2S	% disc. (6/8-7/5)	$^{206}Pb/^{238}U$ Edad (Ma)	±2σ	$^{207}Pb/^{235}U$ Edad (Ma)	±2σ	$^{207}Pb/^{206}Pb$ Edad (Ma)	±2σ	Best age	Unc 2σ
GZ___6903_18	262,2	63,2	4,15	0,082	0,001	1,812	0,052	0,160	0,004	0,835	2,09	10,72	956	20	1046	19	1257	32	944,70	38,37
GZ___6903_34	163	62,6	2,60	0,070	0,002	1,566	0,045	0,160	0,002	0,386	1,36	-0,35	958	13	956	17	928	49	959,37	36,01
GZ___6903_37	308	95,7	3,22	0,072	0,001	1,622	0,036	0,162	0,002	0,434	1,24	1,18	967	12	977	14	1001	40	965,57	35,32
GZ___6903_50	198,9	50,6	3,93	0,072	0,002	1,593	0,035	0,162	0,002	0,433	1,24	-0,13	968	12	967	14	970	43	968,31	35,93
GZ___6903_44	88,1	7,55	11,67	0,069	0,002	1,558	0,052	0,163	0,003	0,395	1,65	-2,26	970	16	952	20	892	63	973,99	37,20
GZ___6903_56	113,7	19,86	5,73	0,075	0,002	1,698	0,049	0,163	0,002	0,411	1,23	3,85	976	12	1007	19	1066	52	969,67	35,83
GZ___6903_27	355	450	0,79	0,071	0,001	1,631	0,028	0,165	0,002	0,546	1,32	-0,01	984	13	984	11	959	31	984,09	36,46
GZ___6903_25	90,7	75,9	1,19	0,073	0,002	1,637	0,047	0,165	0,002	0,312	1,32	-0,24	985	13	982	18	1007	57	984,34	37,03
GZ___6903_38	188	56	3,36	0,072	0,002	1,653	0,045	0,165	0,003	0,360	1,42	0,14	986	14	988	17	983	47	986,63	37,03
GZ___6903_42	81,3	19,69	4,13	0,073	0,002	1,664	0,051	0,166	0,003	0,525	1,52	0,78	988	15	996	20	986	56	988,25	37,60
GZ___6903_24	214,7	85,3	2,52	0,075	0,001	1,718	0,031	0,166	0,002	0,554	1,11	2,75	990	11	1015	12	1057	30	987,80	36,34
GZ___6903_55	200	59,4	3,37	0,071	0,002	1,646	0,042	0,166	0,002	0,400	1,31	-0,91	992	13	984	16	930	49	993,07	37,08
GZ___6903_45	567	145	3,91	0,072	0,001	1,676	0,03	0,169	0,002	0,692	1,29	-0,61	1004	13	998	11	997	27	1004,08	36,95
GZ___6903_43	106,6	32,7	3,26	0,073	0,002	1,691	0,041	0,169	0,002	0,352	1,29	-0,42	1008	13	1004	16	1005	47	1008,25	37,54
GZ___6903_62	641	223,1	2,87	0,072	0,001	1,706	0,026	0,169	0,002	0,598	1,19	0,21	1008	12	1010,2	9,4	992	27	1008,06	36,95
GZ___6903_23	192	50,2	3,82	0,074	0,002	1,72	0,042	0,170	0,002	0,459	1,18	0,57	1013	12	1018	15	1033	42	1012,25	37,49
GZ___6903_22	167,4	47,7	3,51	0,072	0,001	1,693	0,035	0,172	0,003	0,379	1,37	-1,54	1021	14	1007	13	971	39	1022,75	38,12
GZ___6903_53	168,2	59,8	2,81	0,077	0,002	1,914	0,045	0,180	0,003	0,297	1,31	1,75	1065	14	1082	15	1113	46	1063,44	39,59
GZ___6903_7	330,1	80,6	4,10	0,078	0,001	1,948	0,035	0,184	0,002	0,584	1,19	1,19	1089	13	1100	12	1128	31	1087,06	39,49
GZ___6903_39	136,6	71,4	1,91	0,080	0,002	2,177	0,052	0,196	0,003	0,481	1,39	1,86	1155	16	1175	16	1187	41	1153,52	43,27
GZ___6903_65	68,5	32,31	2,12	0,078	0,002	2,104	0,063	0,197	0,003	0,374	1,39	-0,79	1155	16	1148	21	1126	57	1157,12	43,41
GZ___6903_46	198,8	110,3	1,80	0,081	0,002	2,206	0,055	0,197	0,004	0,627	1,64	2,28	1160	19	1184	17	1225	38	1157,59	44,33
GZ___6903_2	446	130,9	3,41	0,080	0,001	2,168	0,036	0,198	0,003	0,597	1,20	0,54	1165	14	1170	11	1196	27	1163,70	42,67
GZ___6903_1	230,3	79	2,92	0,08	0,001	2,171	0,04	0,199	0,002	0,458	1,11	0,31	1169	13	1171	13	1201	32	1167,36	42,11
GZ___6903_4	365	155	2,35	0,078	0,001	2,182	0,047	0,205	0,003	0,589	1,33	-2,60	1200	16	1171	15	1144	35	1202,32	44,43
GZ___6903_40	354	72,4	4,89	0,084	0,001	2,388	0,043	0,208	0,003	0,562	1,15	2,16	1218	14	1241	13	1290	29	1214,79	44,15
GZ___6903_13	728	260	2,80	0,092	0,001	2,656	0,039	0,211	0,003	0,634	1,14	7,89	1233	14	1315	11	1464	23	1218,89	44,86
GZ___6903_6	313	54,7	5,72	0,078	0,001	2,26	0,046	0,213	0,003	0,581	1,29	-4,03	1245	16	1201	14	1130	32	1251,38	46,07
GZ___6903_41	327	75,5	4,33	0,085	0,001	2,534	0,046	0,215	0,003	0,596	1,27	2,01	1255	16	1278	13	1316	27	1252,84	46,28
GZ___6903_61	545	79,9	6,82	0,092	0,001	2,742	0,059	0,216	0,004	0,786	1,67	7,31	1259	21	1336	16	1467	26	1244,93	48,17
GZ___6903_60	836	114,7	7,29	0,091	0,001	2,77	0,045	0,218	0,003	0,650	1,26	6,80	1272	16	1347	12	1444	24	1261,29	46,55
GZ___6903_31	245	73	3,36	0,085	0,001	2,551	0,046	0,220	0,003	0,564	1,25	0,64	1281	16	1287	13	1318	29	1278,78	47,39

AnalysisName	U (ppm)1	Th (ppm)1	Th/U	$^{207}Pb/^{206}Pb$	±2σ s	$^{207}Pb/^{235}U$	±2σ	$^{206}Pb/^{238}U$	±2σ	Correlación errores	% Error 6/8 2S	% disc. (6/8-7/5)	$^{206}Pb/^{238}U$ Edad (Ma)	±2σ	$^{207}Pb/^{235}U$ Edad (Ma)	±2σ	$^{207}Pb/^{206}Pb$ Edad (Ma)	±2σ	Best age	Unc 2σ
GZ___6903_33	207	164	1,26	0,087	0,002	2,728	0,056	0,228	0,003	0,591	1,36	1,38	1326	18	1341	15	1351	33	1322,73	49,52
GZ___6903_59	1090	59,6	18,29	0,091	0,001	2,914	0,038	0,233	0,003	0,673	1,11	3,19	1350	15	1386,5	9,9	1441	19	1343,69	48,71
GZ___6903_57	135,4	119,7	1,13	0,095	0,002	3,198	0,078	0,242	0,004	0,562	1,43	4,70	1395	20	1454	19	1532	38	1388,68	52,95
GZ___6903_58	288	198,5	1,45	0,093	0,001	3,329	0,066	0,256	0,004	0,681	1,23	1,52	1469	18	1488	15	1493	26	1465,69	54,66
GZ___6903_17	228	45,6	5,00	0,096	0,002	3,449	0,072	0,265	0,004	0,654	1,19	-0,20	1517	18	1512	16	1539	30	1515,09	55,69
GZ___6903_32	280	101,4	2,76	0,259	0,003	11,94	0,18	0,335	0,005	0,672	1,18	66,31	1863	22	2600	14	3233	19	1563,32	62,89

Boletín Geológico

SERVICIO GEOLÓGICO COLOMBIANO

Boletín Geológico
Editorial Policy

About the journal

The *Boletín Geológico* is a serial scientific publication of the *Servicio Geológico Colombiano* (SGC), active since 1953, aiming to promote and disseminate research in the Earth sciences. The *Boletín Geológico* publishes original and non-published scientific manuscripts of research, reflections, reviews, data and case reports on the Earth sciences.

Objective and scope

To disseminate scientific knowledge in the following fields of research:

- Stratigraphy, sedimentology, structure and evolution of basins.
- Geochemistry, geophysics, volcanology, igneous and metamorphic petrology.
- Tectonics, seismotectonic and geodynamic modeling.
- Hydrogeology, oceanography and geothermal energy.
- Economic geology, mineralogy, metallogenesis, hydrocarbon genesis and reservoirs.
- Geomorphology, geological hazards, environmental geology, soil research, climate change and geological heritage.
- Paleontology, paleoclimatology, Quaternary geology and geoarchaeology.
- Software applications and artificial intelligence in Earth sciences.

The *Boletín Geológico* may also publish compilations, short notes and issues on the state of knowledge and special research on critical issues of relevance in the region.

Frequency and publication date

Annual publication with online publishing in June of each year.

Publication costs

The contents of the journal are freely available without charge to readers and can be reused after download with proper bibliographic reference.

The journal does not charge authors any fees for sending or receiving their article, for the derived editorial process, or for publishing. It is completely funded by the Servicio Geológico Colombiano.

Open Access Statement

Authorship

The authorship of a postulated article should include those who actively and substantially contributed to the intellectual content and the analysis or interpretation of the data; as such, the authors are publicly responsible for the article submitted. The list and order of the authors should be reviewed before submitting the work the first time for publication. After submitting an article, authorship changes are not accepted.

Assignment of copyright to the Servicio Geológico Colombiano

The authors of an article approved for publication transfer copyright ownership rights to the Servicio Geológico Colombiano for its subsequent dissemination, reproduction and distribution in the printed and digital media available to the Servicio Geológico Colombiano, as well as for its inclusion in national or international databases and indexes.

Author requirements

Understand the editorial policy of the *Boletín Geológico* and the derived processes and be in agreement with them.

Include all the people who contributed to the preparation of the manuscript as authors.

Abide by all ethical guidelines for authors and reviewers.

In the event that the reviewers of the article/publication suggest the need to make changes or adjustments before their approval, the authors agree to make such adjustments in the time required by the *Boletín Geológico*.

The obligations of the authors are included in the letter of authorship found at the journal website: https://revistas.sgc.gov.co/index.php/boletingeo

Peer-review process

All articles are subject to a strict review process by two national or international referees. The mere submission and receipt of articles does not guarantee their subsequent publication.

First, compliance with all key items for submission outlined by the *Boletín Geológico* in the author guidelines are verified. Subsequently, the review process begins, which is completely anonymous for reviewers and authors. Once complete, in a period of no longer than three weeks, the authors must address the suggestions and corrections made. In the event a suggestion is not incorporated, the authors should provide a detailed explanation in an additional letter. If the two

reviewers recommend rejecting the article, the article will not be published. If the two reviewers' recommendations are in disagreement, the article will be subjected to a third review. If publication is recommended, but changes and a second review are required, the revised version will be sent to a reviewer assigned by the editor for approval.

The reviewers must sign a confidentiality agreement and a declaration of conflict of interest, if applicable, to safeguard the proper use of the information.

The estimated time between the delivery date of an article and its publication is on the order of six calendar months.

Review format

The reviewers use the article review form of the *Boletín Geológico* that is available at the journal website: https://revistas.sgc.gov.co/index.php/boletingeo

Declaration of ethics and good practices for editors

Responsibility for the content of the journal

The editor must assume responsibility for everything he or she publishes and must have established procedures and policies to guarantee the quality of the material published and maintain the integrity of the published record.

Editorial independence and integrity

An important part of the responsibility for making fair and impartial decisions is defending the principle of editorial independence and integrity.

Separating decision-making from commercial considerations

The editor makes decisions based only on academic merit and assumes full responsibility for his or her decisions.

Relationship of the editor with the director of the journal

The editor and those responsible for the journal have no role in content decisions for commercial or political reasons. The editor should not be removed from his or her duties due to any journal content unless there is editorial misconduct or the result of an independent investigation has concluded that the editor's decision to publish was contrary to the scientific-academic mission of the journal.

Journal metrics and decision making

The editor does not attempt to inappropriately influence the journal's ranking by artificially increasing any metric. For example, it is not appropriate to require that references to the articles of that journal be included, except for purely academic reasons. The editor must ensure that the articles are reviewed for purely academic reasons and that the authors are not pressured to cite specific publications for nonacademic reasons.

Ethical guidelines for authors and reviewers

Both reviewers and authors should understand and accept the international standards of research ethics issued by the Committee on Publication Ethics regarding plagiarism and peer review, which are the standards that the *Boletín Geológico* adheres to, namely:

Fabrication and falsification of data

The fabrication of data means that the researcher did not actually perform the study but instead falsified the data. Data falsification means that the researcher performed the experiment but then changed some of the data.

Plagiarism

Taking the ideas and work of other scientists without giving them credit is considered unfair and dishonest behavior. Copying a phrase from someone else's manuscript, even one that has been previously published, without a proper citation is considered plagiarism; every author should use their own words.

Multiple presentations

It is not ethical to send the same manuscript to more than one journal at the same time. Doing so wastes the time of the editors and peer reviewers and can harm the reputation of the authors and the journal in which the article is duplicated since the publication will have to be withdrawn.

Redundant publications (or "salami" publications)

This refers to the publication of many very similar manuscripts based on the same experiment. The combination of the results in a very solid document is of greater interest for a selective journal. It is recommended that the editor reject a weak document when it is suspected of being a slice of "salami".

Contribution or incorrect attribution of an author

All the authors listed must have made a significant scientific contribution to the research in the manuscript and must have approved all the claims. Do not forget to list all those who made an important scientific contribution, including students and laboratory technicians. Do not "gift" authorship to those who did not contribute to the article.

Identification of unethical practices

Tools and procedures are used to identify the authors who engage in unethical behavior. If an unethical practice is confirmed, the manuscript can be rejected without review, and your institution will be informed of the incident.

Archiving and preservation

The *Boletín Geológico* uses the LOCKSS system as a storage system that allows the creation of permanent archives for conservation and restoration purposes.

Instructions to Authors

Authorship

Authorship should be attributed to those who have actively and substantially contributed to the intellectual content of the article and to its data analysis or interpretation; therefore, the authors are responsible for the content of the submitted article. The list and order of authors must be reviewed before submission, since after submitting the article author changes are not accepted.

Transfer of patrimonial copyright to the Servicio Geológico Colombiano

The authors of an article approved for publication will transfer the patrimonial copyright to the Servicio Geológico Colombiano for its subsequent publication, reproduction and distribution in any print and online media the Servicio Geológico Colombiano may choose and for its inclusion in databases and in national or international citation indexes.

Obligations of the authors

- Know the editorial policy of the Geological Bulletin and the derived processes, and agree with them.
- Include as authors all the people who contributed to the writing of the manuscript.
- Abide by all ethical guidelines for authors and evaluators.
- In the event that the evaluators of the article/publication suggest the need to make changes or adjustments before their approval, the authors undertake to make such adjustments in the times required by the Geological Bulletin.

The authors' obligations will be included in the authorship letter found at the journal website: https://revistas.sgc.gov.co/index.php/boletingeo

Submission criteria

All articles submitted for consideration for publication must meet the following submission criteria:

- Articles must be sent in Word format by this web page, in the "Submit articles" tab of the Instructions to authors.
- The title, in Spanish and English, should be concise and reflect the subject matter.
- The name, highest academic title and complete institutional affiliation of each author and the email of the corresponding author must be included.
- The abstract and keywords must be included in both Spanish and English. Images must be attached as individual graphics files, with a minimum resolution of 300 dpi.

Editorial guidelines

Tables

Tables must be submitted in an editable format, not as images, and they must be accompanied by an explicit legend and source. They must be referenced in the text, and they must be essential to explain or further support the argument of the article.

Figures

Figures, such as diagrams, photographs or maps, should be sent in graphics files with a minimum resolution of 300 dpi. Each figure must be cited in the text and be accompanied by an explanatory legend that includes the source.

Images from sources other than the authors of the article must have the permission from the authors of the original image, be free of copyright conflicts or have a Creative Commons license (for further information, please refer to: https://co.creativecommons.org/). Maps, aerial photographs and satellite images should include a graphic scale.

Citations

The citation format of Boletín Geológico is American Psychological Association (APA) style. In the text, citations must include the author's name and date of publication, and all references must be listed in the references section.

When several works by the same author are cited, they must be organized in chronological order and will be shown separated by a comma: (Groat, 2014).

When a reference has two authors, the surnames of both authors must be cited and separated by the conjunction "&": (Pokrovski & Dubessy, 2014).

When the reference has three or more authors, only the first author must be cited, followed by the abbreviation "et al.": (Feneyrol et al., 2013).

In the case of a corporate author, the name of the organization must be written the first time with the acronym in parentheses, followed by the year; subsequently, only the acronym will be mentioned (Servicio Geológico Colombiano (SGC), 2017).

When citing several references, they must be chronologically sorted and separated by semicolons: (Mantilla et al., 2013; Van der Lelij et al., 2016; Rodríguez et al., 2017). When a specific page of a reference is cited, the page number must be included after the year and be preceded by the abbreviation p., or pp. in the case of several pages: (Groat, 2014, p. 48).

Quotes

When the quote is shorter than forty words, it must be written within the paragraph, in quotation marks and without italics. The reference must be included at the end of the quote (Groat, 2014, p. 48).

When the quote is longer than forty words, it must be written in a separate paragraph, with a 2.5-cm left indent, without quotation marks or italics and with a font size one point smaller than the body text. The reference must be included at the end of the quotation (Groat, 2014, p. 48).

References

According to the APA format, only the first letter (initial) of the first names of the authors is provided. In the case where two surnames are included, they must not be separated by a hyphen. References must be written in single-space format and with a 1-cm hanging indent (in a hanging indent, the first line of the paragraph is not indented, and all subsequent lines are indented, in this

case, 1 cm). If the documents have a Digital Object Identifier (DOI), this identifier must be included at the end of the reference.

Books

Only the first letter (initial) of the first word and of proper names, if any, in the titles of books are capitalized. The titles should be italicized, and the subtitle separated from the title by a colon, not by a period. In Spanish, the first letter of a word following a colon is written in uppercase font; in English, this letter is capitalized.

The information provided must strictly match that included in the following examples and follow the same rules of punctuation between each element of the reference:

Lee, M. S. (2012). *Mass Spectrometry Handbook* (Vol. 1). New Jersey: Wiley.

Bormann, P. (2013). *New Manual of Seismological Observatory Practice 2 (NMSOP-2)*. Potsdam: Deutsches GeoForschungsZentrum. https://doi.org/10.2312/GFZ.NMSOP-2_DS_3.1.

Book chapters

Book chapters follow the same rules as those of book titles, except for one difference: the titles of book chapters must not be italicized. The title of the book must be italicized and preceded by the preposition "In".

The information provided must strictly match that included in the following examples and follow the same rules of punctuation between each element of the reference:

Horstwood, M. (2008). Data reduction strategies, uncertainty assessment and resolution of LA–(MC–) ICP–MS isotope data. In P. Sylvester (Ed.), *Laser ablation–ICP–MS in the Earth Sciences: Current practices and outstanding issues*. Vancouver: Mineralogical Association of Canada.

Reimann, C., Birke, M., Demetriades, A., Filzmoser, P., & O'Connor, P. (2014). The gemas project - concept and background. In C. Reimann, A. Demetriades, M. Birke & I. Schoeters (Eds.). *Chemistry of Europe's Agricultural Soils, Part A*. Hannover: Bundesanstalt fur Geowissenschaften und Rohstoffe.

Journal articles

Titles of journal articles follow the same rules as those of titles of book chapters, except for one difference: the first letters of all meaningful words (first word, names, verbs and adjectives) of titles of journal articles must be written in uppercase font and italicized, but they must not be preceded by the preposition "In".

The information provided must strictly match that included in the following examples and follow the same rules of punctuation between each element of the reference:

Domeier, M. & Torsvik, T. (2014). Plate tectonics in the late Paleozoic. *Geoscience Frontiers*, 5 (3): 303-350. https://doi.org/10.1016/j.gsf.2014.01.002.

Konstantinou, K. (2015). Tornillos modeled as self-oscillations of fluid filling a cavity: application to the 1992-1993 activity at Galeras volcano, Colombia. *Physics of the Earth and Planetary Interiors*, 238: 23-33. https://doi.org/10.1016/j.pepi.2014.10.014.

Thesis works

Saylor, J. (2008). *The Late Miocene Through Modern Evolution of the Zhada Basin, South-Western Tibet*. (Ph. D. Thesis). The University of Arizona, Tucson.

Conferences, seminars and others

The titles of talks given in these contexts are written without italics, and only the first letter of the first word and proper nouns, if included, are capitalized. All meaningful words in event names are capitalized.

The information provided must strictly match that included in the following example and follow the same rules of punctuation between each element of the reference:

Sulochana, V., Francis, A. & Tickle, A. (2015). Morphology based radon processed neural network for transmission line fault detection. *2015 International Conference on Advances in Computing, Communications and Informatics* (ICACCI).

Maps

The information provided must strictly match that included in the following example and follow the same rules of punctuation between each element of the reference:

Bacchin, M., Miligan, P. R., Wynne, P. & Tracey, R. (2008). *Gravity anomaly map of the Australian region*, 3rd edn, 1:5,000,000. Geoscience Australia, Canberra.

Web pages

EURAQUEM/CITAC. (2016). *Guide to quality in analytical chemistry an aid to accreditation*. Retrieved from www.eurachem.org.

Suggested links

- Keywords in the Geosciences: https://www.americangeosciences.org/georef/georef-thesaurus-lists
- Creative Commons: https://co.creativecommons.org/

CONTENIDO

bg

SERVICIO GEOLÓGICO COLOMBIANO

El futuro es de todos | Minenergía

ISSN 0120-1425 46
9 770120 142003